TECHNISCHE UNIVERSITÄT MÜNCHEN

Fakultät für Chemie

Microporous Ni catalysts for selective 1-butene dimerization

Laura Löbbert

Vollständiger Abdruck der von der Fakultät für Chemie der Technischen Universität München zur Erlangung des akademischen Grades einer

Doktorin der Naturwissenschaften (Dr. rer. nat.)

genehmigte Dissertation.

Vorsitzender:	Prof. Dr. Roland A. Fischer
Prüfer der Dissertation:	1. Prof. Dr. Johannes A. Lercher
	2. Prof. Dr. Klaus Köhler
	3. Prof. Garry L. Haller, Ph.D.

Die Dissertation wurde am 02.12.2021 bei der Technischen Universität München eingereicht und durch die Fakultät Chemie am 08.02.2022 angenommen.

"There is no sadder sight in the world than to see
a beautiful theory killed by a brutal fact."

Thomas Henry Huxley (1825 – 1895)

Für meine Familie

Statutory declaration

I hereby declare that I have written this thesis at the Chemistry Department of the Technische Universität München under the guidance and supervision of Prof. Johannes Lercher and that I have used only the aids in accordance with the examination regulations.

This thesis is a result of my own independent work, and all direct or indirect sources used are acknowledged or marked as references.

………………………………………………..

Laura Löbbert

Acknowledgement

At this point I would like to thank all the people who have accompanied me during my doctorate and have contributed to this work.

First, I would like to express my deep gratitude to *Prof. Johannes A. Lercher* for supervising my work in his research group. Johannes, thank you for giving me the chance to work on a challenging and exciting topic. With your mentorship, support and constant incentive throughout my time in your group, I received most valuable scientific encouragement.

I am also very grateful to my supervisors throughout this work. I warmly thank *Ricardo Bermejo de Val*, who supervised me during the first two years of my thesis. Thank you for your very appreciated comments and suggestions. Special thanks also goes to *Maricruz Sanchez-Sanchez*, for her scientific input and support during the last 1.5 years. Thank you to *Yue Liu* for his guidance on the MOF project. I really admire your ability to always come up with a new theory, whenever the latest analysis challenged our last hypothesis. I would like to thank *Rachit Khare* for his expertise on XAFS measurements, his ideas, and new perspectives that he brought into the project. In addition, *Prof. Andreas Jentys* always had an open ear for my questions on IR spectra or other issues.

Additionally, I am grateful to EVONIK Industries for initially funding the project. Special thanks goes to *Johannes Knossalla* and *Stephan Peitz* for the fruitful discussions.

I would also like to thank our many collaborators from abroad. *Oliver Gutiérrez*, *Jian Zheng*, and *Julian Schmid* from *PNNL*, thank you for laying the foundation of this project by providing freshly prepared MOF catalysts. Many thanks to *Donald Camaioni* (*PNNL*) for helping with the development of the adsorption models. *Prof. Laura Gagliardi*, *Prof. Ilja Siepmann*, *Prof. Matthew Neurock* for the scientific discussions and the successful collaboration. *Saumil Chheda*, I really enjoyed working with you (no matter on which continent you were) and I really appreciated the virtual meetings that significantly moved the MOF projects forward. I specially thank *Ruixue Zhao*. As a member of the TUM MOF team, thank you for your scientific support in spontaneous Friday evening meetings and participation in numerous craft activities.

Thank you to our great technicians *Xaver Hecht*, *Muhammad Iqbal*, *Martin Neukamm* and *Andreas Marx*. Thanks to you, the setups last much longer and technical problems in our groups are solved much faster. In general, I would like to thank all the technicians and

scientific staff members from TUM who maintain the research operation and analyze our samples using different techniques (in my case elemental analysis and X-ray photoelectron spectroscopy). I owe special thanks to *Michi* and *Robert* from the Feinmechanik at TUM for their help with the reactor and BPR in difficult times. A big thank you also goes to *Bettina Federmann*, *Stefanie Seibold*, and *Kateryna Kryvko* for the administrative, organizational, and financial work.

During the last years, many students have helped me with my research work. I would like to thank *Matthias Bauer*, *Manuel Botta*, *Munirah Amir*, *Mengjie Zhou*, *Hendrik Hoeft*, *Lawrence Tseng Hsin*, *Renato de Rosa*, *Mira Eggl*, and *Abelina Ellert* for their input during their internships or theses. Keep up the good work!

Above all, I would like to thank the entire working group for the great time we spent together, which went far beyond the daily laboratory routine. A warm thank you goes to *Ehrmi* who introduced me to the topic and helped me getting started; to *Verena* and *Christoph* for helping with the reactor in the beginning and who always shared some Swagelok parts with me; to *Martina* for many discussions on and off topic; to my *Lab girls* (Tessi, Martina, Mirjam, Madita and Simon) for the cookie and cake breaks; to the *Chemistry Comedy Club* (Martl, Ferdi, Christoph, Roli, Lara, Fipsie, Kuba, Insu, Lei, Karen, Alex, Nikki, Lennart, Florian, Yong, Felix, Daniel) for the challenging (political) discussions during lunch breaks and scientific contributions in the lab; to the *Sweet girls* (Lingli, Guanhua, Fuli, Iris) for sharing their culture and their favorite Chinese and German sweets; and to the whole group for our well-known TC2-barbecues.

A warm thank you goes to my friends and family for sharing the ups and downs of life outside TC2. Thank you to everyone, who provided the necessary balance with most enjoyable evenings, sport activities and unforgettable experiences. Special shout out to my friends from LMU and my volleyball team. Additionally, I would like to thank *Anni* and *Sophia*, *Marisa* and *Mona* for listening to science problems without even liking chemistry.

My biggest thank you goes to my family. To my parents, *Anita* and *Gerd*, for inspiring me every day and supporting me no matter what. To my sister *Arnelle*, for taking the time to listen whenever science would not agree with me and always being in my corner.

My warmest thank you goes to *Niklas*. Thank you for your challenging questioning, always accompanied by motivating encouragement and unconditional support despite distance and work stress.

Abstract

The industrially applied Ni catalysts supported by amorphous aluminosilicates for the dimerization of n-alkenes suffer from low selectivity to linear dimers. Ni^{2+} in well-ordered microporous catalysts such as zeolites and metal-organic frameworks are promising candidates to limit the ability to form branched alkenes. The best catalysts show high Ni activity while controlling the selectivity by excluding Brønsted acid sites. The thesis reports an in-depth study of the nature of the active Ni site, the adsorption of butene, and the role of the constraints on the mechanism for the reaction rates and selectivities.

Zusammenfassung

Die für die Dimerisierung von n-Alkenen industriell eingesetzten Ni-Katalysatoren auf amorphen Alumosilikaten zeigen geringe Selektivitäten für lineare Dimere. Ni^{2+} in gut geordneten, mikroporösen Katalysatoren wie Zeolithen oder metallorganischen Gerüstverbindungen sind vielversprechende Kandidaten, um die Bildung von verzweigten Alkenen zu begrenzen. Die besten Katalysatoren weisen eine hohe Ni-Aktivität auf und kontrollieren gleichzeitig die Selektivität, indem sie Brønsted-Säuren ausschließen. In dieser Arbeit werden die Beschaffenheit der aktiven Ni-Stelle, die Adsorption von Buten und der Einfluss des Trägers auf den Mechanismus für die Reaktionsraten und Selektivitäten untersucht.

List of symbols and abbreviations

°C	degree Celsius
σ^2	Debye-Waller-factor
ΔH_{ads}	adsorption enthalpy
ΔG_{ads}	adsorption free energy
Å	Ångström
AAS	atom absorption spectroscopy
Al	Aluminum
ASA	silica alumina
BAS	Brønsted acid sites
BDC	benzenedicarboxylate
BET	Brunauer-Emmett-Teller
Cat	catalyst
CHA	Chabazite
cm	centimeter
cm^{-1}	reciprocal centimeter
CN	coordination number
CO	carbon monoxide
$C_{X\ (X=2,3,4,8,12,16)}$	molecules containing X (X=2,3, 4,8,12,16) carbon atoms
d	interatomic distance
DFT	density functional theory
DMA	dimethylamine
DMF	dimethylformamide
DS	defect site
DSC	differential scanning calorimetry
E_a	activation energy
EFAl	extra-framework aluminum
eq	equilibrium
eV	electronvolt
EXAFS	extended X-ray absorption fine structure
FAU	Faujasite
FCC	fluid catalytic cracking
FT	Fourier-transformed
FWHM	full width at half maximum
g	gram
GC	gas chromatography
H_2	hydrogen
h	hour(s)
ICP-AES	inductively coupled plasma-atomic emission spectroscopy

Im	Imaginary
IR	infrared
K	Kelvin
kJ	kilojoule
LAS	Lewis acid sites
M	metal
mbar	millibar
mg	milligram
MHz	megahertz
min	minute(s)
MFI	Zeolite ZSM-5
mL	milliliter(s)
mmol	millimole(s)
MOF	metal-organic framework
MR	membered ring
MTBE	methyl *tert*-butyl ether
N_2	Nitrogen
Na	Sodium
Ni	Nickel
$Ni(NO_3)_2$	Nickel nitrate
NiO	Nickel oxide
$NiOAc_2$	Nickel acetate
NMR	nuclear magnetic resonance
p	pressure
PBU	primary building unit
PFR	plug flow reactor
PXRD	powder X-ray diffraction
RDS	rate-determining step
RT	room temperature
S	selectivity
s	second(s)
SBU	secondary building unit
SEM	scanning electron microscopy
Si	silicon
SiC	silicon carbide
SiO_2	silica
synair	synthetic air
T	temperature
TBA	*tert*-butyl alcohol
TGA	thermogravimetric analysis
TMAdaOH	*N,N,N*-trimethyl-1-adamantyl-ammonium hydroxide
TOF	turnover frequency
TOS	time on stream
TPD	temperature-programmed desorption

UiO-66	$Zr_6O_4(OH)_4$(1,4-benzene dicarboxylate)$_6$
WHSV	weight hourly space velocity
wt.%	weight percent
X	conversion
XAFS	X-ray absorption fine spectroscopy
XANES	X-ray absorption near edge spectroscopy
XAS	X-ray absorption spectroscopy
XES	X-ray emission spectroscopy
XRD	X-ray diffraction
Y	yield

Table of Contents

1 Introduction

1.1. Valorization of butene

The formation of new C-C bonds during oligomerization of short-chained olefins (C_2-C_4) presents an attractive route to provide C_6-C_{10} as highly desired intermediates for the industrial production of fuels and chemicals.[1,2] Butenes, for example, form as byproducts during various refinery or cracking processes of butane, naphtha, or gas oil.[3,4] Dimerization and alkylation reactions are widely used to valorize these butenes into branched and linear octenes (**Figure 1.1**).[5,6] The highly branched dimers are blended into an isooctane mixture and commercially applied as fuel additives.[6] On the other hand, linear octenes are used as solvents, lubricants, or comonomers in the production of low-density polyethylene (LLDPE). Additionally, they can be hydroformulated and hydrogenated to alcohols and, upon further esterification, used as plasticizers for polyvinylchloride on an industrial scale.[3]

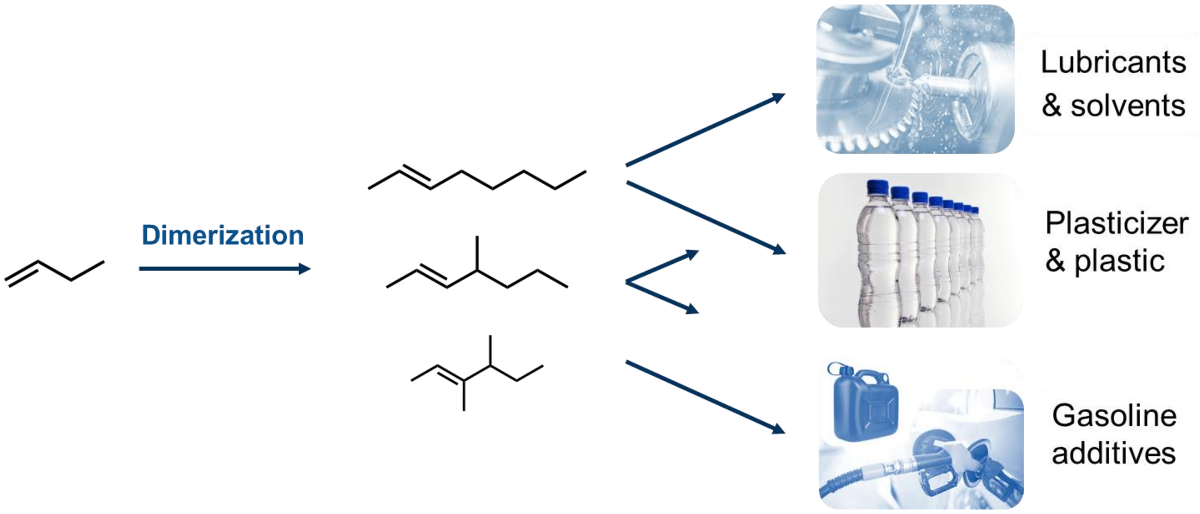

Figure 1.1: Valorization of butene.

1.1.1 Industrial butene dimerization

The C_4 cut from the cracking processes cannot be separated into its components economically by distillation as the boiling points of the different fractions are too similar.[3] **Figure 1.2** displays the process indicated diagram for the typical industrial steps to separate the C_4 cut. First, butadiene is extracted *via* distillation with selective solvents. The remaining fraction termed Raffinate I contains isobutene, which is separated and used as a reactant for methyl *tert*-butyl ether (MTBE) production. The remaining *Raffinate II* is separated from 1-butene, resulting in the *Raffinate III* fraction. *Raffinate II* and *III* are used as reactants for dimerization and oligomerization in both homogeneous and heterogeneous processes.[3,6–9]

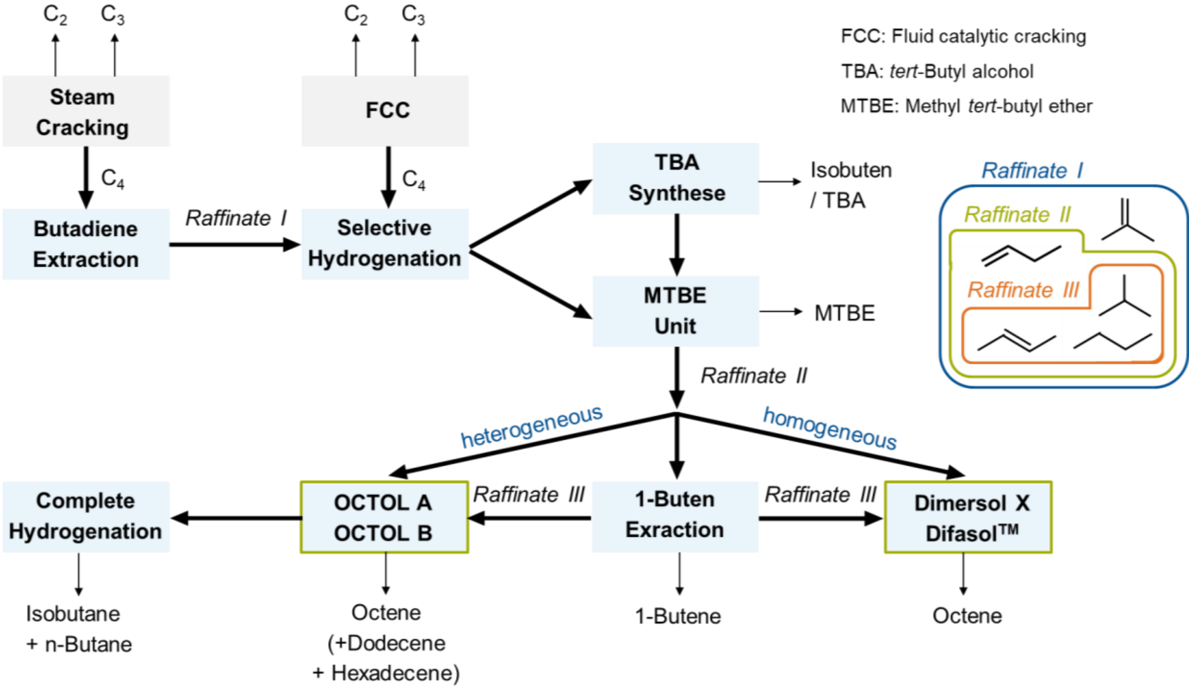

Figure 1.2: Process indicated diagram for upgrading C4-cut for a typical refinery or petrochemical plant. Cracking processes are shown in grey, separation units in blue (dimerization and oligomerization processes are shown with green border).

The dimerization of butenes to octenes has been first industrially implemented by the *Institut Français du Pétrole* in the so-called *Dimersol X^TM^* process in the 1970s.[7,10] In this homogeneous process, an aluminum alkyl compound activates a Ziegler-type catalyst based on nickel (or a nickel complex), which catalyzes butene conversions of up to 80% and dimer selectivities of 85%.[5,7,11] Limitations as catalyst recyclability or the dependency of the conversion on the initial feed concentration could be greatly overcome by the *Difasol™* process.[5] This biphasic liquid-liquid technology, provided by *IFP* in 1987, uses ionic liquids as a solvent for the nickel catalyst. The resulting reaction system allows dimer selectivities up to 95% at conversions comparable to the *Dimersol X™* process (70-80%). However, low selectivities (5-7%) of the desired linear n-octene within the dimer fraction remain the major drawback.[5]

The Hüls AG, today *Evonik Industries*, developed a heterogeneous system in the 1980s, known as the *OCTOL* process, in which the selectivity of linear dimerization products could be increased due to the low acidity of the catalyst. The oligomerization of butenes is catalyzed by nickel oxide on aluminosilicates ($NiO-Al_2O_3/SiO_2$) and achieves n-octene selectivities of 13% (conversion up to 45%, dimer selectivities of 85%).[6,9,11] Heterogeneous catalysis promises economic advantages by solvent-free processes, easy separation of products and catalyst, and catalyst recyclability.[12] However, it still suffers from lower activities and selectivities than its homogenous counterpart.[1] This has led to an immense interest in this field during the last decades.

1.1.2 Active sites in alkene dimerization

Type of Catalysis – Brønsted acid or Lewis acid catalysis

Homogeneous C-C formation during butene dimerization, and alkene oligomerization in general, is mainly catalyzed by two classes – organoaluminum compounds and transition metal complexes (containing primarily Ti, Zr, or Ni). The two main catalyst groups for heterogeneous oligomerization reactions are acidic solid catalysts or supported transition metals such as nickel-based catalysts.[1,13] Brønsted acidic solid catalysts contain supported phosphoric acid, zeolites, silica alumina, and microporous sulfonic resins.[12]

Brønsted acid sites (BAS) catalyze branched dimer formation, skeletal and internal isomerization, cracking, disproportionation, hydrogen transfer, and cyclization reactions, eventually leading to the exclusion of linear dimers.[14–17] The degree of branching and the chain length of the products were found to depend on the pore size of porous zeolite/ aluminosilicate catalysts, decreasing branching with decreasing pore size.[1,17–20] Additionally, the side reactions on BAS produce large hydrocarbons and coke, which causes pore blockage and promote, therefore, fast deactivation.[21]

Alkene dimerization and oligomerization have also been carried out heterogeneously over transition metals such as WO_3 and ReO_3,[22] $TaCl_5$ or supported Ce,[23] Cr,[24,25] Co,[23,26–28] and Ni.[12,29] *Sanati et al.* have provided a thorough overview of heterogeneous catalysts tested in alkene oligomerization.[30] Ni has been the most studied transition metal since the discovery of the `Nickel effect` by *Ziegler et al.* in the 1950s.[31,32] It describes the tendency of Ni to catalyze alkene dimerization while preventing long-chained oligomers by polymerization.[32]

Active Ni site

As homogeneous Ni complexes are well-defined species and generally easy to characterize, literature has widely agreed on the matter of active sites. Nickel(II)-hydrides or alkyl species have been suggested to participate as active species in alkene reactions by nearly all homogeneous investigations.[29] In comparison to homogeneous catalysis, identifying the active Ni site in heterogeneous oligomerization reactions is still controversially debated, as the chemical environment of the support and different Ni species lead to ambiguity regarding the nature of the elementary steps before alkene coordination and during the oligomerization process.[12,29] The large heterogeneity of nickel species, including various oxidation states on the catalyst support, significantly impedes meaningful conclusions from experimental work especially considering that the active site might be a minority species.[33,34] A deeper understanding of the reaction pathway is therefore lacking, which is why a broad consensus of the catalytic cycle has not been reached so far. This will be addressed in a later section.

Most intriguing in heterogeneous catalysis is the fact that the formation of the active Ni site does not require any type of cocatalyst, contrarily to Ziegler-type homogeneous systems, which are activated with alkylaluminum species. This emphasizes the important role of the support.[29,35] Nickel-based catalysts are prepared by impregnation, deposition, or exchange with Ni^{2+} salts or precursors. During the subsequent high-temperature treatment, which is necessary for activation, Ni can adapt to different electronic configurations like Ni^0, Ni^+, or Ni^{2+}. Therefore, the activation treatment complicates the localization, distribution, and identification of the active nickel species.[29,36] In the following, an overview will be provided over the different active (and inactive) Ni sites so far suggested in the literature.

In the early days, highly dispersed Ni^0[37] or NiO[38–40] were proposed as the active sites for ethene dimerization. Lately, however, more research groups conclude that Ni^0[33,41,42] and NiO[43] are inactive in alkene oligomerization (especially in butene dimerization) and that these species can form upon deactivation.[34,35,44–46]

The widely accepted Cossee-Arlman mechanism in homogeneous catalysis proposes a Ni-hydride species, or after alkene adsorption, the subsequent Ni-alkyl species as active site (see **Figure 1.3a** and **b**).[47,48] *Feldblyum et al.* and *Chauvin et al.* proposed the same active species (and the same mechanism) in homogeneous and heterogeneous catalysis based on similar product selectivities.[29] Nickel-hydride species were observed in heterogeneous catalysts using low-temperature IR or isotopic exchange experiments.[21,49] While some groups report the formation of the active Ni-hydride species through the reaction of the originally Ni cations with BAS during thermal activation,[33,50] *Moussa et al.* strictly ruled out the formation during thermal treatment, as the Ni-H species was only observed after contacting ethene with the Ni-based catalyst.[49]

Monovalent Ni^+-cations (see **Figure 1.3c**) have been repeatedly proposed as active sites (or intermediate in the active site generation), especially in heterogeneous ethene dimerization. These suggestions are mostly based on the observation of Ni^+ in electron paramagnetic resonance spectroscopy or infrared (IR) spectroscopy using CO as probe molecules or a combination of both techniques.[42,43,58,46,51–57] However, all here cited studies based on CO-IR have performed the measurements, including the CO adsorption step at room temperature (or even elevated temperatures).[51–54] However, adsorption of CO at room temperature was shown to induce the reduction of Ni^{2+}-cations to Ni^+-cations, thus calling into question any conclusion about the nature of the Ni site based solely on these adsorption experiments.[59] In addition, literature disagrees on whether catalytic activity correlates with Ni^+ content or not.[34,42,56,57] Other researchers have even described Ni^+-cations as spectators without significance for activity.[35,59]

Single Ni^{2+}-cations in ion-exchange positions in zeolites or MCM-41 (see **Figure 1.3d**) are proposed by other groups to function as active sites.[60–65] The oxidation state was revealed by NO adsorption experiments[63] or X-ray absorption near edge spectroscopy (XANES) studies.[61,62] The latter suggested the preservation of the oxidation state throughout the reaction. However, the exact mechanistic course involving only Ni^{2+}-species remains unclear. *Moussa et al.* suggested Ni^{2+}-cations other than Ni^{2+}-cations in ion-exchange positions as the reason for high activity based on observations in CO-IR at liquid nitrogen temperatures. Specifically, Ni^{2+}-cations interacting with silanols or aluminols and those located on the surface of very small NiO nanoparticles were suggested as active sites.[49,66]

Both, Ni^+ and dehydrated Ni^{2+} have been proposed as active sites by *Lallemand et al.* upon evaluating the influence of thermal treatment on the oxidation state of nickel in Ni-Y and Ni-MCM-41 *via* IR spectroscopy of adsorbed CO.[67]

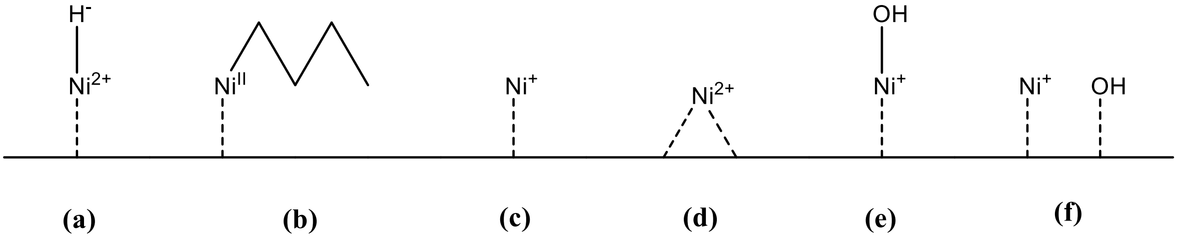

Figure 1.3: Ni active sites for alkene dimerization proposed in literature.

Recently, an active $[Ni^{II}OH]^+$ species (see **Figure 1.3e**) has been identified by *Iglesia* and coworkers. They observed increasing rates in ethene dimerization with increasing Ni^{2+}/BAS_0 in a mesoporous Al-MCM-41 catalyst until Ni^{2+}/BAS_0 ratio of 1.[15,68] This is of particular interest, as the catalysts seem highly active, even at subambient temperatures.

A similar species, namely $[Ni^IOH]$ (see **Figure 1.3f**), was proposed by *Brückner et al.* as the active species in a Ni^I/Ni^{II} redox shuttle mechanism in amorphous aluminosilicate (ASA). Hereby, the hydroxide could be a dangling hydroxide on the Ni to balance the charge (as the species in **Figure 1.3c**). As suggested by the authors, the OH could also be a nearby bridging Si-OH-Al (BAS), which is part of the zeolite framework.[44,69] All in all, the OH group is necessary to stabilize the Ni^+ species, and the proton also participates in the catalytic cycle.

Similarly, the influence of BAS on the Ni activity has been repeatedly pointed out by many other groups. BAS catalyze dimerization on their own, as mentioned before. However, some studies assume that the BAS in close proximity to the Ni site are crucial for activating or generating the active Ni site.[52,53] Other groups consider the BAS to be part of the active site or that at least both nickel and acid sites are required for the reaction.[51,70–72]

1.2 Approaches for supporting Ni cation oligomerization catalysts for heterogeneous olefin oligomerization

The design of well-defined supports is extremely important for stabilizing the active species and controlling productivities and selectivities for alkene oligomerization. Many different strategies were developed to support Ni molecular catalysts, e.g., the heterogenization of homogeneous catalysts. Literature provides plenty of approaches to heterogenize homogeneous catalysts, including nickel complexes immobilized on solid supports (e.g., polymers, metal–organic framework, inorganic porous materials) and liquid supports (e.g., fluorous solvent, nonaqueous ionic liquids). Also, a combination of solid and liquid supports (e.g., supported ionic liquid phase catalysis) have been tested. These supports are summarized elsewhere.[29] This thesis will focus on solid supports for Ni-promoted olefin oligomerization, especially on amorphous aluminosilicates (ASAs), zeolites, and metal-organic frameworks (MOFs).

1.2.1 Amorphous and mesoporous aluminosilicates

Amorphous aluminosilicates (ASAs) have been identified as the most active catalysts for alkene oligomerization. They are therefore used as catalysts in the industrial *OCTOL* process, as mentioned earlier.[6] Additionally, they are applied in many other industrial applications due to their functional physicochemical properties. ASA is an inorganic amorphous mixed oxide of alumina and silica with high mesoporous porosity, large surface areas, superior thermal stability, and good ion exchange capability.[73] It is a three-dimensional framework of tetrahedrally coordinated Si and Al connected by shared O-atoms. In contrast to other aluminosilicates, however, ASAs do not have a long-range order. The tetrahedra of the fourfold coordinated Al^{3+} are negatively charged and need to be charge-balanced by either protons or alkali metal cations (see **Figure 1.4**).[74–76] They provide, therefore both, Lewis and Brønsted acidity. ASA as the support in industrial butene oligomerization has been under thorough investigation.[34,44,45,77,78] Changes in the acidic properties of the ASA support induced by steam-treating were reported to alter BAS and Lewis acid sites (LAS). The decrease of BAS on ASA and weak Al^{3+}-LAS reduces the catalytic activity for the Brønsted-acid-catalyzed C-C formation but did not affect the Ni activity. On the weak Al^{3+} sites, medium-strong Ni^{2+} sites are formed that are active in the oligomerization reaction. Their octene isomer distribution is not influenced by remaining BAS on the support.[78]

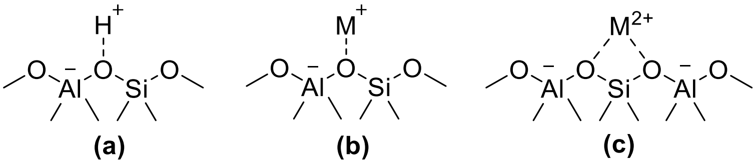

Figure 1.4: Structure of zeolitic aluminosilicate with negative framework charge compensated by different species. a) Brønsted acid site (BAS), b) monovalent metal ion M^+, and c) divalent metal ion M^{2+} on paired Al-site.

Numerous nickel species, including various oxidation states on the catalyst support, are often present simultaneously on the ASA support. This significantly impedes meaningful conclusions from experimental work especially considering that the active site might be a minority species.[33,34] Homogeneously distributed nickel species of one kind supported by a well-characterized and ordered environment are beneficial to gain further insight into the active species.

Mesoporous aluminosilicates have a regular ordered system of mesopores with pore sizes of 2-50 nm.[79] They have been investigated in alkene oligomerization resulting in high activities and selectivities.[62,68,72]

1.2.2 Zeolites

Zeolites are, besides ASA and mesoporous aluminosilicates, a group of aluminosilicates. In contrast to the other two, they are crystalline and microporous materials with well-defined pore size distributions and channel systems.[80,81] They consist, like the other aluminosilicates, of SiO_4 and AlO_4^- tetrahedra, which are referred to as primary building units (PBU). Connecting these PBU to larger entities, termed secondary building units (SBU), gives rise to the multi-dimensional structure of the zeolites.[82–84] **Figure 1.5** illustrates the binding of PBU to the smallest possible SBU, a 4-membered ring (MR).

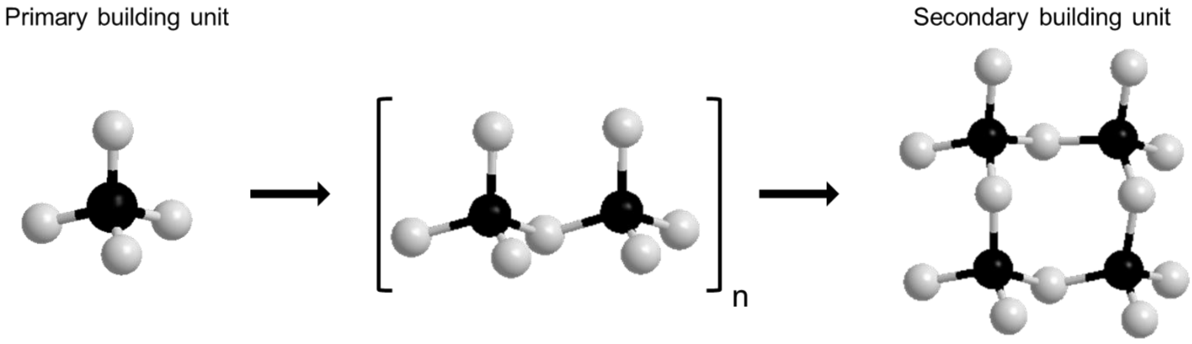

Figure 1.5: Structure of zeolites composing of primary building units that assemble to secondary building units (exemplarily a 4-member ring is illustrated here).

Substitution of the Si with Al introduces negatively charged AlO_4^- tetrahedra to the lattice, similar as described before for ASA. The negative charges must be compensated by extra-framework cations, e.g., protons (leading to BAS) or monovalent metal cations.[82] Two Al tetrahedra in close proximity to each other, only separated by one or two SiO_4 units, are termed as ´Al pair´ and allow the introduction of bivalent metal cations (see **Figure 1.4c**).[85–87]

Zeolites are divided into three classes. Small-pore zeolites, e.g., CHA, feature pore sizes of 8-MR in the range of 0.30-0.45 nm. The pores of medium-pore zeolites, e.g., MFI, consist of 10-MR and range from 0.45-0.60 nm, while large-pore zeolites, e.g., FAU, contain openings of 12-MR ranging from 0.60-0.80 nm.[82,88]

The frameworks for the three examples of CHA, MFI and FAU are depicted in **Figure 1.6**.

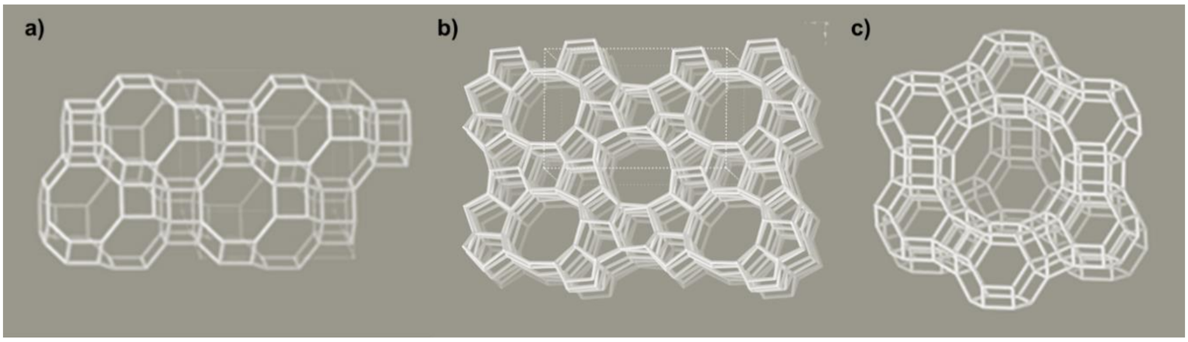

Figure 1.6: Framework of a) CHA exhibiting a 6MR channel system, b) MFI featuring a 2-dimensional 10MR system, and c) FAU with a 3-dimensional framework consisting of 12MR pores (images adapted from [89]).

Zeolites feature high hydrothermal stability, tunable acidity, as well as low production costs and offer, therefore, the same advantages as ASA for the application as catalyst supports. In addition, their channel system introduces shape selectivity to numerous catalytic reactions.[90,91] In the case of alkene dimerization, it has been reported that zeolites shift the product distribution to linear dimers and shorter oligomers.[61]

1.2.3 Metal-organic frameworks

Metal-organic frameworks (MOFs) were discovered three decades ago and have attracted tremendous attention since then.[92–94] They are porous and crystalline materials consisting of inorganic metal nodes interconnected by organic linkers. [92,93] These materials feature outstanding properties, such as exceptional porosity (up to 90% free volume and BET areas of 1000-7000 $m^2 \cdot g^{-1}$)[95,96] and accurate and flexible structure tunability on a molecular level.[97–101] Besides a wide range of applications, they have been lately tested as supports for Ni oligomerization catalysts.

In this thesis, Zr-based UiO-66 is one of the most promising candidates as a catalyst due to its high thermal, chemical, and mechanical stability.[102–104] The exceptional strength is suggested to result from the high degree of network connection, as each zirconium node (Zr_6O_8) is connected to 12 other nodes *via* 12 benzene-1,4-dicarboxylate (BDC) linkers in contrast to many other MOFs with 6- or 8-fold connected nodes.[105–107] The two carboxylate groups on each BDC linker connect two nodes emerging to a vast network. Mathematically, six BDC linkers belong to one node resulting in the electroneutral formula $Zr_6O_4(OH)_4(OOC\text{-}C_6H_4\text{-}COO)_6$. **Figure 1.7** (top row) shows the MOF structure built from the node and the organic linkers.

Recent work has shown that this 12-fold connected framework of UiO-66 has a significant fraction of missing linkers.[105,108,109] The missing linkers cause defect sites on the node, which act as solid acids (see **Figure 1.7**, bottom right for the structure of defect site). In contrast, the ideal UiO-66 does not feature acidic properties.[110] Numerous studies aimed to characterize the type, concentration, and (de-)hydration degree of the defect sites[105,110–115] and their influence on catalytic activity.[116–118] The degree of hydration determines whether the site acts as Brønsted acid or the undercoordinated Zr^{4+} site is free of ligands and takes part in the reaction as a Lewis acid center.[107,110,119,120]

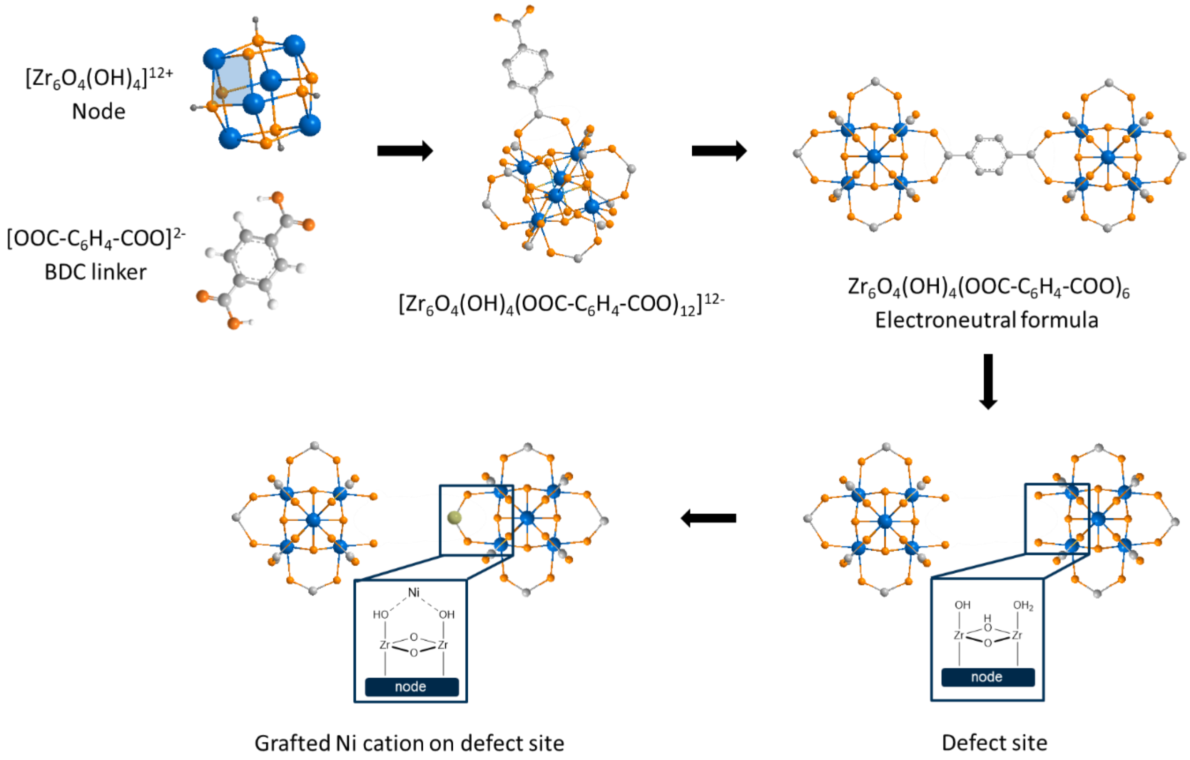

Figure 1.7: Structure of the UiO-66-MOF. Each Zr_6O_8 node is connected to 12 BDC linkers and each linker connects two nodes, resulting in the electroneutral formula on the top right. A missing BDC linker creates a defect site (bottom right), onto which transition metals as Ni can be grafted (bottom left). Color code: blue (Zr), orange (O), grey (C), white (H), green (Ni).

Lately, introducing other Lewis acids such as Ni or Co into MOFs has attracted growing interest in enhancing activity in alkene oligomerization. The groups of A. Bell[121], S. Kaskel[122], and M. Dincă[123–125] have synthesized MOFs with catalytically active Ni nodes (Ni as part of the node) for ethene or propene oligomerization. Some of them even exceed the activities of their homogeneous counterpart.[124] The catalytic metal sites can also be deposited on the MOF nodes *via* three types of post-synthetic modifications, e.g., installing catalytic metalloligands, anchoring molecularly defined catalysts to the MOF pores[126–128], or grafting metal cations or metal clusters onto (the defect site of) the node.[129–133] The deposition of single metal cations onto the node is exemplarily illustrated in **Figure 1.7** (bottom left).

The insertion of isolated metal atoms is of particular interest in the oligomerization of alkene because monodisperse compounds exhibit high catalytic activity and are conceptually easier to characterize.[124,128,134–136] The use of MOFs is advantageous compared to other supports because of the possibility to deposit high metal loadings with low aggregation[132,137] while simultaneously featuring easy separation and recyclability.[137–139] Additionally, the well-defined structure of the MOF allows detailed mechanistic studies of supported heterogeneous metal catalysts.[134]

Single metal sites have been introduced into MOFs by atomic layer deposition in MOFs[129,130,133] (AIM) or solvothermal deposition in MOFs (SIM).[140–144] *Farha*, *Hupp*, and collaborators have explored Ni in MOFs installed by AIM for ethene dimerization with remarkable selectivities towards the dimerization products.[129,130] However, the exact molecular structure of the active Ni site has yet to be elucidated.

Despite their enormous potential, MOFs have been so far not investigated in butene dimerization.

1.3 Mechanisms in alkene oligomerization

Polyolefin chains can form with varying numbers *n* of reacting molecules. Hereby, the C-C formation is referred to as dimerization if n = 2, oligomerization if 2 < n < 100, and polymerization if n > 100.[1] In Ni catalyzed butene oligomerization, oligomers mostly contain n = 3-4 monomers.

In general, polymerization oligomerization reactions consist of three steps: initiation, propagation, and termination.[145] The initiation described for polymerization is comparable to the active site generation described in oligomerization. The second step represents the chain growth (propagation), and the third step terminates the reaction. Oligomerization reactions are often described solely with the last two steps.[1] The rate constants for chain propagation and chain termination k_P and k_T affect the activation barriers for C-C-coupling and product desorption or β-hydride elimination.[146] The dimensions of the two rate constants decide whether polymerization, oligomerization, or dimerization occurs. If $k_P >> k_T$, numerous insertion steps will occur, and polyolefins are formed, leading to polymerization. If $k_P \approx k_T$, the reaction results in oligomerization, and $k_P << k_T$ leads to dimerization.[147] This is illustrated in **Figure 1.8** for the example of butene.

Various Ni-based catalysts favor chain termination over propagation and have been applied, therefore, in various dimerization processes.[32,148]

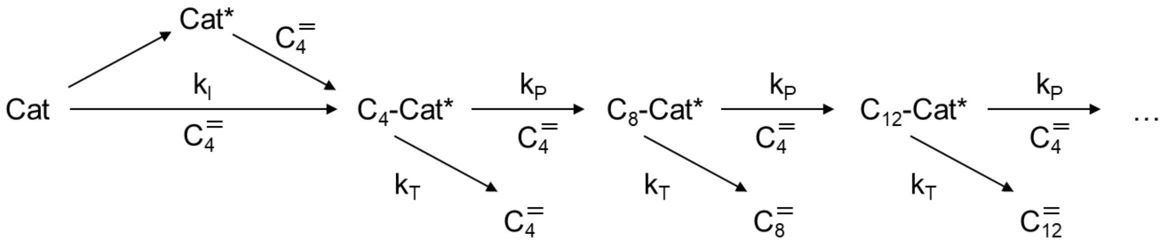

Figure 1.8: Mechanistic steps for polymerization, oligomerization, and dimerization. The initiation is depicted with the rate constant k_I, chain propagation with the rate constant k_P and chain termination with the rate constant k_T (adapted from [147,149]).

In the following, different dimerization mechanisms will be discussed. We will focus first on the Brønsted acid-catalyzed mechanism before passing on to the Nickel-catalyzed mechanisms, which have been so far proposed in the literature.

1.3.1 Brønsted acid-catalyzed mechanism

BAS in zeolites can catalyze dimerization *via* the formation of alkoxide species as intermediates (see **Scheme 1.1**).[20,150–152] 1-Butene adsorbs onto the active BAS **(a)** by hydrogen bonding to form a π-complex **(b)**. BAS can induce isomerization forming the π-complex of 2-butene **(c)**. Both π-bonded alkenes can be transformed into the alkoxides **(d)** and **(e)**, which are dimerized upon further butene adsorption. The intermediate between the π-complex and the alkoxide is a positively charged carbenium ion.[150]

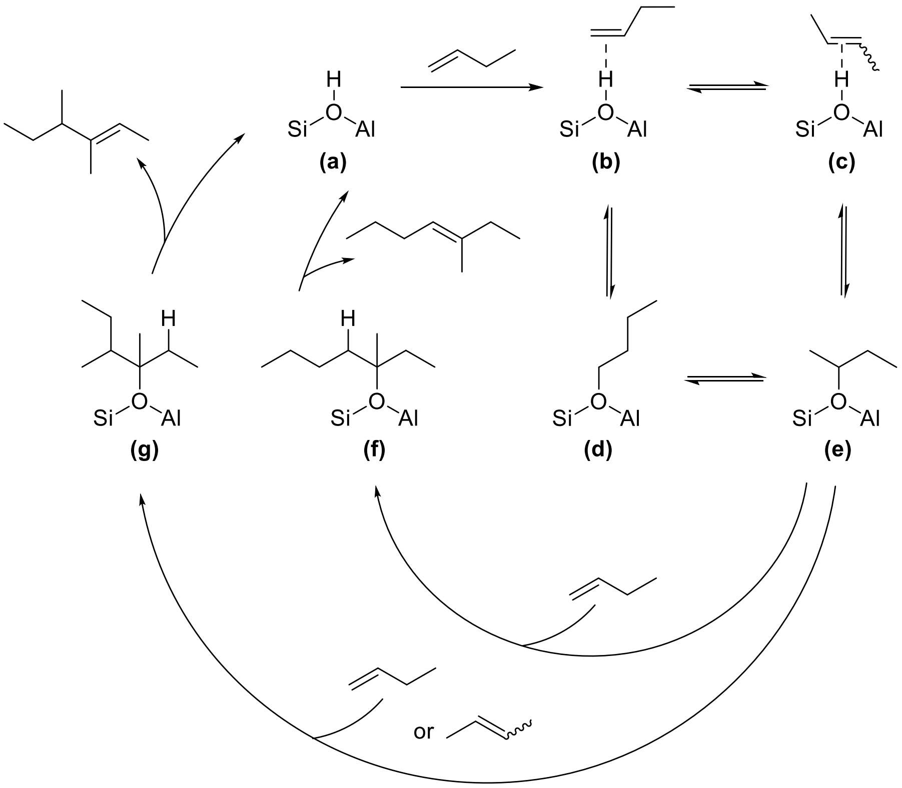

Scheme 1.1: Schematic illustration of Brønsted acid-catalyzed mechanism for butene dimerization.

Scheme 1.1 illustrates two exemplary dimerization pathways, both starting from the secondary butoxide **(e)**, which is covalently bound to the support *via* an internal carbon atom. These two pathways are more likely than a further reaction of the primary butoxide **(d)**, as the formation of the latter would involve the generation of a primary carbenium ion as intermediate, which is less stable than the secondary. Therefore, Brønsted acid-catalyzed dimerization exclusively results in branched products.

The formation of a di- or monobranched dimer depends on the attack of the second butene.[149] If it attacks via the C1 atom, a monobranched alkoxide **(f)** forms, and upon deprotonation, methylheptene is released. If the second butene molecule attacks *via* the C2 atom, the dibranched alkoxide **(g)** forms and dimethylhexene is desorbed. A fast isomerization to 2-butene increases the production of dimethylhexene, as the produced 2-butene will only attack *via* the C2 atom.

1.3.2 Cossee-Arlman mechanism or Coordination-insertion mechanism

The Cossee-Arlman mechanism was first described by Cossee[153] and Arlman[154] in 1964, and since then, it has been often extensively studied in homogeneous alkene oligomerization.[1,11,148,155–157] Recently, it has been used more often to describe the oligomerization mechanism also in heterogeneous catalysis.[21,33,35,48]

The metal center maintains the same oxidation state (+II for Ni) throughout the catalytic cycle (see **Scheme 1.2**).[21] Activators or co-catalysts such as Al-alkyl compounds on the Ni **(a)** are normally required in homogeneous catalysis to generate the active nickel hydride or nickel alkyl species.[148,157,158] The alkene adsorbs onto the nickel hydride by coordination of the double bond to the nickel **(b)** and subsequent formation of a β-agostic monomer species **(c)**. A second butene molecule is coordinated to the Ni site **(d)** and inserted into the Ni-carbon bond **(f)** *via* the transition state **(e)**. Subsequently, the β-agostic butyl species forms **(g)**. Upon β-hydride elimination, the nickel hydride species forms to which the dimer is coordinated. Finally, the dimer desorbs, which regenerates the active site **(b)**, and the catalytic cycle restarts.

In summary, the cycle involves three fundamental steps: alkene coordination, alkene insertion into the nickel hydride (or alkyl intermediate), and β-hydride elimination.[29] Therefore, the Cossee-Arlman mechanism is often referred to as the coordination-insertion mechanism.

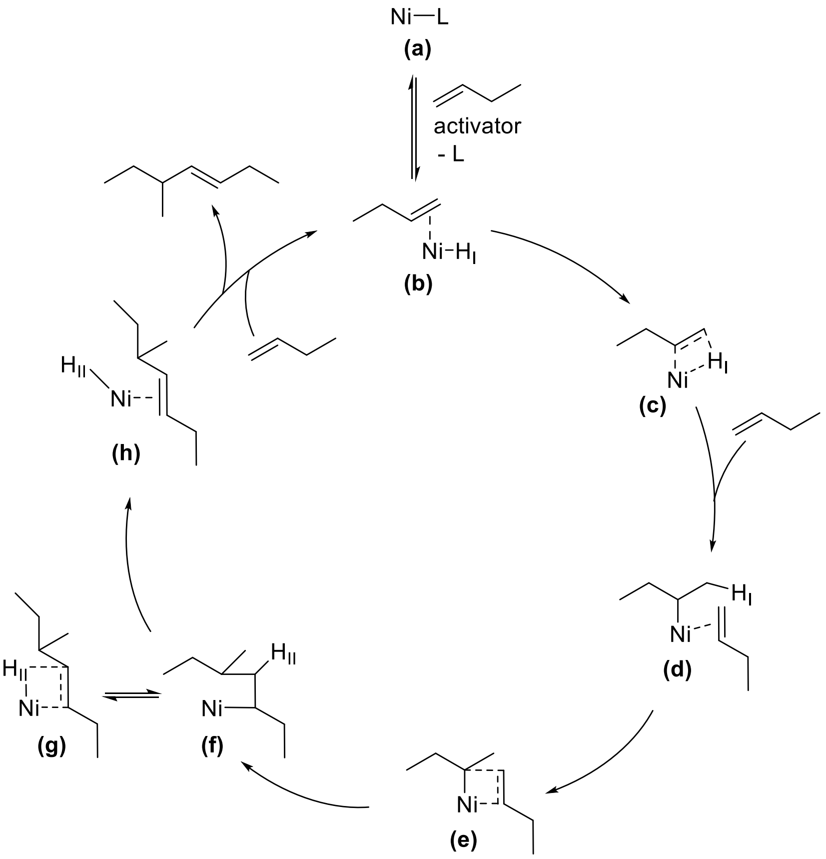

Scheme 1.2: Cossee-Arlman dimerization mechanism.

As previously mentioned, the function of the cocatalyst in homogeneous systems is to alkylate the metal center. This creates the first metal-carbon bond, which can initiate the oligomerization *via* the classical Cossee-Arlman mechanism.[49] It is often suggested that the butene adsorbs before the dimer desorbs, which facilitates the desorption resulting in butene-assisted dimer desorption.[21] The active site is then often proposed to be the Ni-alkyl hydride species, as shown in **Scheme 1.2**. In heterogeneous catalysis, the active site is assumed to form in-situ without any activators or co-catalysts.[21,49] However, the exact mechanism for the active site formation has not been clarified for heterogeneous catalysis. *Joshi et al.* observed a decrease in the induction period with increasing alkene pressure and concluded that the reactant assists the active site formation.[21] Theoretical calculations propose that the active [Ni-ethyl-ethene]$^+$ can be formed in situ from Ni^{2+} or [NiOH]$^+$ precursors by ethene deprotonation and simultaneous BAS formation.[33]

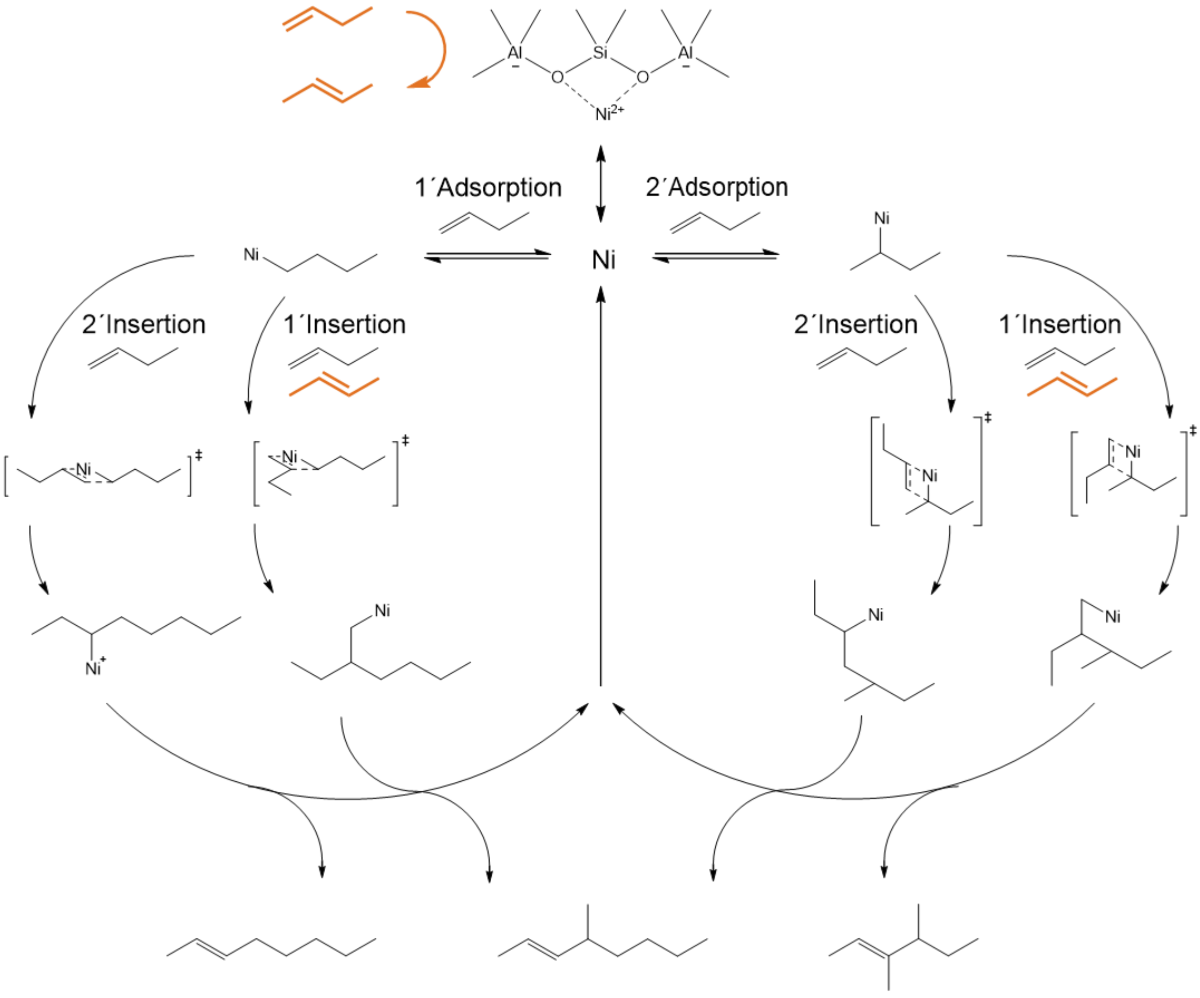

Scheme 1.3: Transition states and intermediates in the Cossee-Arlman mechanism. 1´Adsorption and 2´adsorption of the first butene molecules as well as 1´insertion and 2´insertion of second butene molecules lead to different branching degrees of the products, resulting in dimethylhexenes, methylheptenes, and linear octenes. The position of the double bond is just exemplary and can adopt any internal position.

Contrarily to the Brønsted acid-catalyzed mechanism, the Ni-catalyzed mechanism generates all dimer isomers, including the linear octenes in butene dimerization. Regarding the Cossee-Arlman mechanism, the selectivity is determined by the orientation of both butene molecules before insertion into the Ni-C bond.[149,159] The initial adsorption with the C1 or C2 atom and the orientation of the second butene molecule upon adsorption, will decide the degree of branching of the products. The different possibilities are illustrated in **Scheme 1.3**, resulting in linear octene, methylheptene, and dimethylhexene.

1.3.3 Metallacycle mechanism

The Cossee-Arlman mechanism is often compared to the Metallacycle oligomerization mechanism, illustrated in **Scheme 1.4** for the example of butene. It suggests a metal center with two vacant adsorption sites as active site **(a)**, allowing the coordination of two butene molecules **(b)**.[29] Then, oxidative coupling (with respect to the metal) occurs, which describes the formation of two M-C bonds and an additional C-C bond while the metal is oxidized, increasing its oxidation state by two. This leads to a metallacyclopentane intermediate **(c)**. A *β*-hydride elimination **(d)** and a subsequent reductive elimination release the dimer and regenerate the active site.[21,29,148,160,161] Instead of proceeding stepwise, it has also been suggested that the product elimination occurs *via* a concerted 3,5-hydrogen shift.[160]

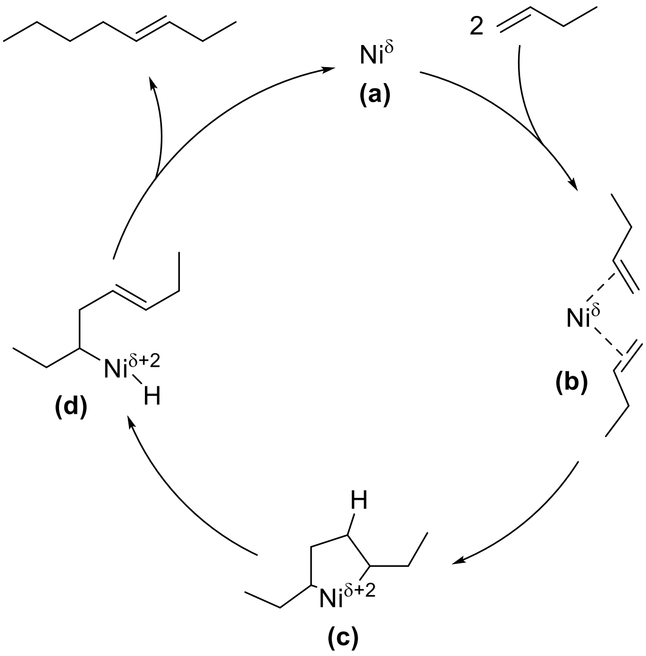

Scheme 1.4: Schematic illustration of the metallacycle mechanism for butene dimerization.

The orientation of the monomers during the coordination determines the selectivity of the products. A statistical ratio for linear, mono- and dibranched dimers can be expected despite massive sterical hindrances.[149] In ethene oligomerization, the mechanism solely results in *α*-alkenes, as little or no isomerization of the *α*-alkene occurs due to the short-lived metal hydride.[160,162] The constrained geometry of the metallacyclopentane ring initiates additional ethylene insertion and further chain growth. However, the resulting metallacycloheptane is quite unstable against further chain growth and favors the elimination of the trimer.[160] Therefore, the metallacycle often leads to trimerization.

For Cr-based catalysts, the metallacycle has been identified as the dominant mechanism mostly in homogeneous but also in heterogeneous catalysis.[163,164] *Köhn et al.* and others have suggested that several chromium oxidation couples are possible [Cr^{I}/Cr^{III}, Cr^{II}/Cr^{IV}, maybe more],[164–166] while density functional theory (DFT) calculations indicate that the high oxidation state +III and +IV are not stable for Ni.[33] Computational research concludes that the high energy barriers in heterogeneous ethene dimerization strongly disfavor the metallacycle.[33] So far, no clear evidence of the metallacycle has been provided for heterogeneous Ni catalysts.[29]

1.3.4 Proton-transfer mechanism or Phillips-type mechanism

The following mechanism depicted in **Scheme 1.5** has been proposed by *Delley et al.* for the Phillips catalyst, a silica-supported chromium oxide (CrO_x/SiO_2),[24,167] which is why it has been referred to as a Phillips-type mechanism. Later, *Bernales et al.* have investigated it in a computational study as one of three possible mechanisms in heterogeneous ethene dimerization over a Co-decorated MOF.[131] Recently, *Moussa et al.* suggested it to be the prevailing mechanism in a Ni-zeolite for ethene dimerization.[49]

The active site is a single metal site **(a)**, to which the butene coordinates **(b)**. In the next step, a metal vinyl species forms **(c)**, which is characteristic of the mechanism. *Delley*, *Bernales*, and coworkers did not discuss the oxidation states of the metal within the cycle or a possible charge within the support.[24,131] However, it seems plausible that the butene forms a covalent bond to the metal *via* a nucleophilic attack, possibly leading to a partial reduction of the metal. The proton released from the butene is accepted by the support balancing the negative charge in the framework. The insertion of the second butene into the metal-vinyl species proceeds according to the Cossee-Arlman mechanism and leads to a metal-octenyl. Finally, the proton is transferred to the alkene, which desorbs from the site. The metal is thereby reset to its original oxidation state and can recurrently participate in the catalytic cycle. Due to the repeated proton transfers, this cycle is also referred to as the proton-transfer mechanism.[33]

Moussa et al. suggested a slightly different catalytic cycle, which resembles more the Cossee-Arlman cycle than the Phillips-type mechanism, as no proton is transferred, but a hydride. However, the involvement of a vinyl species is the reason why it is discussed in this section.

The C-H bond activation occurs *via* oxidative addition of the alkene to the metal center leading to a Metal-alkenyl-hydride species.[49] As mentioned above, this species is also referred to as the Cossee-Arlman site. The second ethene is inserted into the nickel-hydride, the Cossee-Arlman site, and proceeds *via* the Cossee-Arlman insertion step. Upon reductive elimination, the dimer desorbs, and the active site is regenerated. The proposal of this catalytic cycle is based on IR measurements that show the emergence of a nickel-hydride species together with a vinyl species during the initial activation and dimerization of ethene.

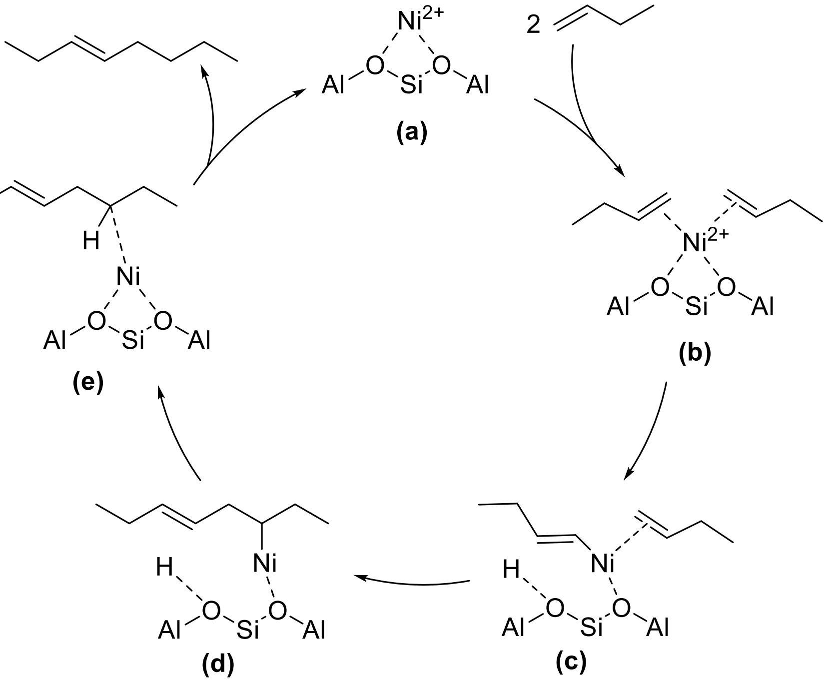

Scheme 1.5: Schematic illustration of butene dimerization *via* the proton-transfer mechanism.

However, DFT calculations suggest that the initiation through the vinyl species is much too slow in the Cr-based catalysts.[131,168] In addition, the transfer of the proton to the oxygen coordinated to the metal is not possible in zeolites, as DFT calculations resulted in a nickel-vinyl-ethene species that moves to the neighboring oxygen pair instead.[33]

Theoretical studies to discriminate between the Cossee-Arlman mechanism, the metallacycle, and the proton-transfer mechanism reveal the Cossee-Arlman mechanism as the most likely mechanism for heterogeneous ethene dimerization.[33] The computational results imply that the structures and relative energetics of the active Ni^{II} site in the zeolite and essential intermediates during the heterogeneous catalytic cycle are similar to those in homogeneous catalysis. These findings encourage the search for heterogeneous catalysts with the same high activity as their homogeneous counterparts.[33]

1.3.5 Ni^I /Ni^{II} -redox shuttle mechanism

The redox shuttle mechanism (**Scheme 1.6**) has been just recently proposed by *Rabeah et al.*[44] in 2016 and has so far been rarely discussed. The active site is a [Ni^IOH] site **(a)**, where the hydroxide is attached to the Ni or part of the zeolite structure in close proximity to the Ni. The butene interacts with the Ni as a π-complex and reacts reversibly with a neighboring BAS to form a carbocation **(b)**. The carbocation is electron-poor and oxidizes the Ni^+ to a Ni^{2+}-alkyl intermediate **(c)** by creating a metal-carbon bond. A second butene molecule coordinates **(d)** and is inserted into the metal-carbon bond **(e)**. Upon β-hydride shift, the olefin is formed by reductive elimination, and the active site is regenerated.

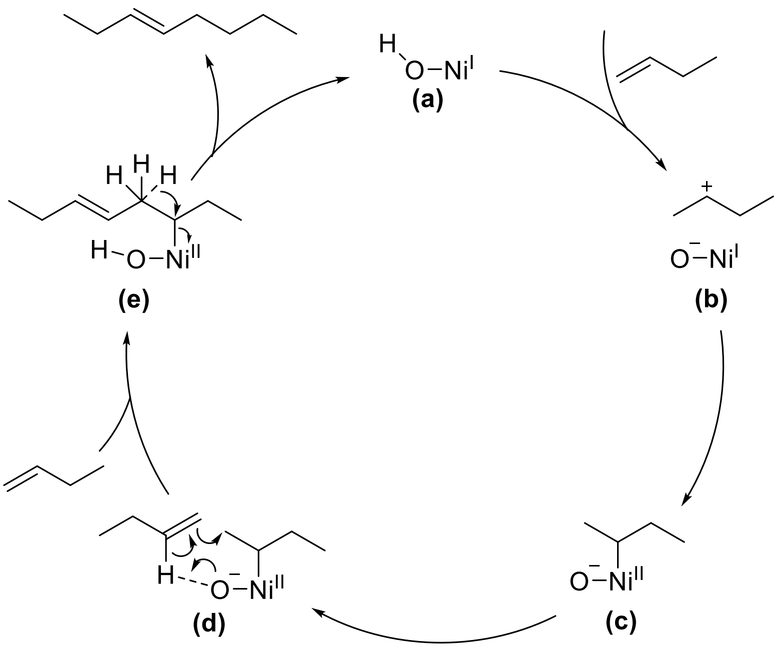

Scheme 1.6: Redox shuttle mechanism proposed by *Rabeah et al.* (adapted from [44]).

This mechanism was based on electronic paramagnetic resonance (EPR) and in situ XANES measurements indicating the transformation of Ni^+ to Ni^{2+} species when butene was adsorbed. A BAS near the Ni was discovered to be essential, as no activity could be observed for catalysts featuring exclusively Ni^+ sites but no BAS.[44] In addition, the BAS help remove the Cp ligand from the $Ni(Cp)_2$ precursor to form the active Ni^+ single sites while preventing agglomeration. In summary, the BAS are proposed to stabilize the active sites and are necessary for high activity due to their participation in the catalytic cycle.[44,69]

1.4 Strategies towards active, selective, and scalable heterogeneous nickel-based dimerization catalysts

In this section, different strategies are addressed to optimize heterogeneous Ni catalysts towards activities and selectivities that resemble the performance in homogeneous catalysts.

Temperature and pressure are crucial parameters for high activities and selectivities in oligomerization reactions. A positive kinetic effect of the alkene pressure on the rate has been observed in several studies.[12,49,50,61,72,169] Especially the analysis of *Rabeah et al.* highlighted the importance of pressure, as the active Ni site was only stabilized in ASA at butene pressures higher than 2 bar. Lower pressures resulted in the formation of inactive Ni^0 agglomerates.[44] Reaction orders between 1 and 2 were observed for Ni-aluminosilicates in short-alkene oligomerization[2,60,61,68] with the tendency of lower reaction orders in mesopores compared to microporous catalysts.[35]

Brogaard et al. measured apparent activation energies (E_a) of 34-37 $kJ \cdot mol^{-1}$ in ethene dimerization on a Ni-based zeolite independent of the pressure. These results suggest that the dimerization mechanism is the same for a wide pressure range (4-26 bar). The free energy ΔG of 58 $kJ \cdot mol^{-1}$, derived from experiments, agrees reasonably well with the computed results of 71 $kJ \cdot mol^{-1}$.[170] Other studies on ethene dimerization revealed activation energies E_a of 42-58 $kJ \cdot mol^{-1}$.[171] *Ehrmaier et al.* reported an activation energy of 73 $kJ \cdot mol^{-1}$ for butene dimerization under high-pressure conditions.[61] In general, the activation energies are influenced by the type of alkene reactant and the reaction conditions.

In addition, the reaction conditions determine the state of aggregation of the reactant. *Agirrezabal-Telleria et al.* applied subambient temperature and pressures below 10 bar to install intrapore liquids within a Ni-based mesoporous aluminosilicate catalyst. These intrapore liquids confer extremely high stability, selectivity, and activity to the catalyst.[2,68] Such conditions presumably facilitate the coordination of multiple ethene molecules on the active site, thereby enhancing dimerization rates.

The Ni loading strongly affects activity and selectivity in alkene dimerization,[59] as pointed out before. The Ni loading regulates the type of Ni species present, which influences the activity massively. This is discussed in **Section 1.1.2** in detail.

Heterogeneous Ni-based dimerization catalysts do not require external chemical activation by cocatalysts, but they are often treated under high temperatures to remove adsorbed water ligands on the Ni.[29] In various catalysts, an activation period can be observed. *Minar et al.* suggested Ni migration from inaccessible to accessible position in Ni-Na-FAU catalysts as the reason for this activation.[60]

In addition, the acidic and electronic properties of Ni can be altered by different anions of the nickel precursor salts or by introducing cocations.[8,45,172,173] *Nkosi et al.* showed that the acidity of a Ni-Na-FAU catalyst, determined by ammonia temperature-programmed desorption (TPD) studies, varies for different sources of nickel and that those catalysts with lower acid strength exhibit higher butene oligomerization activities.[8] A linear relationship was found between the acid concentration and the Sanderson electronegativity of Ni-Na-FAU catalysts partially exchanged with alkali and alkaline-earth cations. The activity increased thereby with higher acidities contradicting the findings form the TPD studies.[172] *Ehrmaier et al.* concluded instead that a higher Sanderson electronegativity of the cocations in Ni-based zeolites and ASA increases 1-butene double-bond isomerization and, therefore, controls the dimer selectivity while showing only minor influence on activity.[45,174] It should be mentioned that the effect of increasing free volumes around the Ni site induced by different cocations leading to lower steric constraints and hence increasing activity, as suggested by *Mlinar et al.*[159], was not considered in these studies.

While ethene or propene are not affected by double bond isomerization, butene can isomerize from 1-butene to cis- and trans-2-butene and vice versa. This isomerization significantly changes the reaction behavior, as the position of the adsorbed C-atom influences the branching of the products. In addition, 2-butene dramatically reduces dimerization activity as it has been suggested to induce rapid deactivation.[61]

Acidic properties of the catalyst or catalyst support are essential parameters to adjust to reach high catalytic performances. On one side, BAS catalyze oligomerization themselves, thereby promoting selectivity towards long-chained and branched products as well as deactivation.[14–21] However, a small amount of remaining BAS does not seem to influence the selectivity negatively.[78] On the other side, they have been suggested to be crucial as part of the active site or active site generation, as we described earlier in detail. This implies that a balanced Ni/BAS ratio can significantly improve the dimerization activity without decreasing the linear dimer formation.

The study by *Lallemand et al.* compared two zeolites with different textural and acidic properties in ethene dimerization. A Ni-MCM-36 catalyst with a more open porosity was more active at any temperature than a Ni-MCM-22 even though it showed lower acidity than the MCM-22 catalyst.[175,176] This implies that structural and textural properties like porosity of the catalyst and the catalyst support play a critical role in the performance in dimerization. As mentioned before, the channel systems of zeolites can induce shape selectivity towards linear dimers.[159,177] ASA is less selective but has been reported to be more active than zeolites, possibly due to a lack of pore diffusion limitations within the zeolite channels.[8] It was observed that the activity of Ni^{2+} cations increased with the increment of the pore size in different meso- and microporous aluminosilicates, leading the authors to conclude that the activity of Ni^{2+} cations increased with larger free volume near the site.[62,159] The ratio of the inner and external surface and, therefore, the crystal size dramatically affects the catalyst´s activity, selectivity, and lifetime and can control diffusion limitations.[178,179]

Multiple studies report that microporous zeolites undergo rapid deactivation due to coking caused by the formation of higher oligomers. These large carbon chains seem to adhere firmly to the active site, leading to site blocking and eventually pore blocking. Large pore diameters are therefore predicted to limit deactivation by increasing the product´s desorption rate.[8,29,180] The reaction of two nearby Ni-olefin complexes has been suggested to lead to site blockage and, thereby, deactivation of both sites.[60]

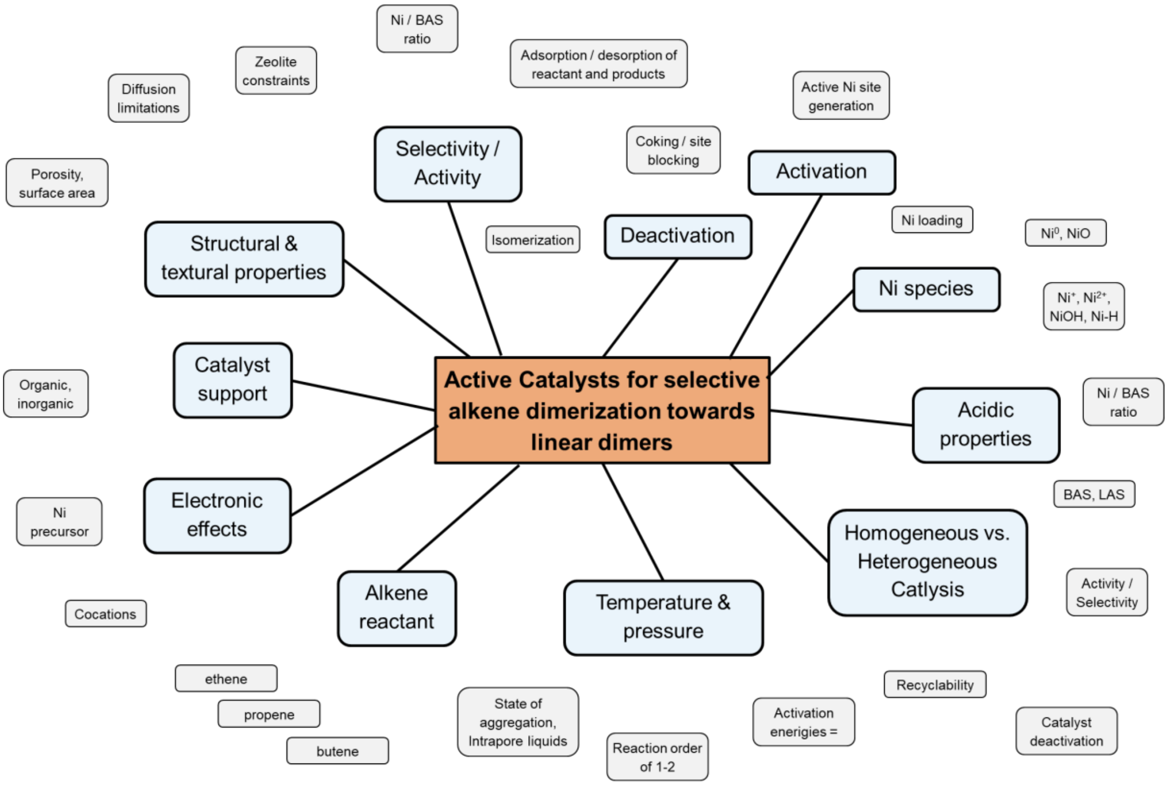

Figure 1.9: Critical parameters to adjust for highly active catalysts for selective alkene dimerization towards linear dimers.

Homogeneous catalysis has been successfully implemented for ethene, propene, and butene oligomerization on an industrial scale, while efficient heterogeneous Ni-based catalysts are only available for butene dimerization.[29] Homogeneous catalysts were preferred on ethylene or propylene feeds as the active Ni complexes can be precisely tuned *via* the ligand leading to fine control of the selectivity. Compared with homogeneous systems, the properties of the heterogeneous oxide supports (alumina, aluminosilicates) often induce double bond isomerization and co-oligomerization of the primary products. However, supporting Ni with heterogeneous oxide supports enables olefin oligomerization under milder conditions than applying raw solid acids [29]

When comparing different olefin reactants, dimerization rate constants increase with increasing alkene size (ethene < propene < butene) on Ni active sites and on BAS.[2,177]

All the above-described parameters influencing activity and selectivity in butene dimerization are summarized in **Figure 1.9**. They require careful consideration when designing an efficient Ni dimerization catalyst.

1.5 Scope of the thesis

The selective dimerization of butene to linear octenes is a valuable method to valorize C_4-olefins into important intermediates to produce solvents, lubricants, and plasticizers. Research, however, focuses mainly on ethene or propene oligomerization, while only a few studies investigate the dimerization of butene. These studies on butene dimerization apply mainly to amorphous or mesoporous aluminosilicates. Many different Ni species and remaining BAS on the catalyst surface lead to an ambiguity concerning the nature of the active site.

Metal-organic frameworks can be precisely tuned and synthesized to stabilize single Ni^{2+} cations homotopically. They present, therefore, excellent model catalysts for dimerization reactions. Comparison to different zeolite constraints allows more profound insights into the influence of the Ni´s immediate environment. In support of understanding the crucial parameters for manufacturing a highly active and selective Ni catalyst, the following points shall be addressed:

1) The activity of homotopic single Ni sites in MOFs is compared to the performance of metal oxo complexes consisting of Ni cations and allows conclusions regarding the active site. DFT calculations combined with indirect spectroscopic measurements and kinetic analyses indicate that the dimerization follows a Cossee-Arlman mechanism.

2) The immediate local environment of active single Ni cations supported in MOFs, thereby the influence of neighboring aqua or hydroxyl ligands will be studied and compared to the performance of other metal cations. Butene adsorption properties are investigated and compared to values calculated by DFT. Correlations of adsorption free energies and rates are explored and indicate the tremendous influence of the first mechanistic cycle step on dimerization activity. The Cossee-Arlman mechanism shall be investigated for all metals, putting differences in activity into perspective.

3) The active site in Ni-based zeolites shall be investigated and reveal single Ni^{2+} cations as the active species. Zeolites with different pore sizes are analyzed according

to their influence of various local Ni environments on activity and selectivity in butene dimerization. The performance will be compared to the Ni-MOF and a Ni-ASA (similar to the catalyst used in industry). Reasons for activity differences are to be explored.

This work, therefore, offers a comprehensive insight into the possibilities of MOFs and microporous zeolites as supports for Ni-catalyzed butene dimerization. The here-reported mechanistic studies allow deeper insights into the catalytic cycle for heterogeneous Ni-based butene dimerization and pave the way for further understanding essential parameters to custom-tailor Ni performances.

2 Metal-organic framework supported single-site Ni catalysts for butene dimerization

This chapter is based on unpublished results. The manuscript will be submitted promptly. The project is a joint effort of Dr. Jian Zheng, Saumil Chheda, Dr. Navneet Khetrapal, Dr. Carlo Alberto Gaggioli, Julian Schmid, Dr. Oliver Y. Gutiérrez, Dr. Ricardo Bermejo-Deval, Radha Kishan Motkuri, John L. Fulton, Dr. Mahalingam Balasubramanian, Prof. J. Ilja Siepmann, Prof. Matthew Neurock, Prof. Laura Gagliardi, and Prof. Johannes A. Lercher and me. I carried out the catalytic experiments as well as parts of the catalyst characterization.

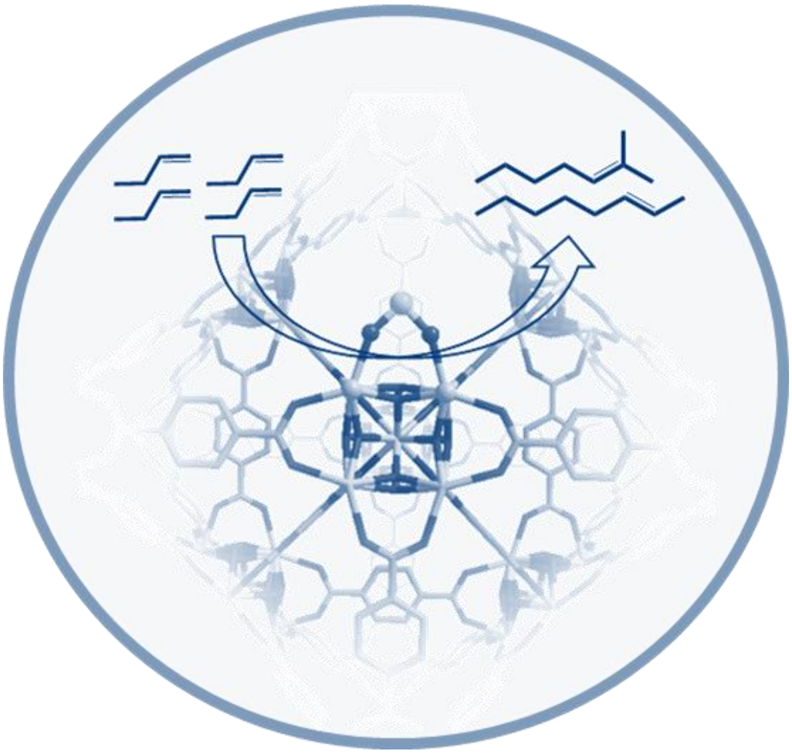

Homotopic sites in a well-controlled environment are not only ideal systems for mechanistic studies but also allow to optimally control catalytic transformations. Sites having only a single metal cation and sites consisting of metal oxo complexes with few nickel cations supported on the nodes of UiO-66 metal-organic framework (Ni-UiO-66) are studied for 1-butene dimerization. Monomeric Ni sites, which bind to the Zr_6 node *via* two Zr-OH(μ_3) linkages, are active and selective for the dimerization of butene to linear and mono branched

C_8 isomers. Ni oxo complexes with few Ni cations show lower activity and promote the oligomerization of intermediately formed C_8 isomers. Kohn-Sham density function theory calculations combined with indirect spectroscopic measurements and kinetic analyses indicate that dimerization follows a Cossee-Arlman reaction mechanism.

2.1 Introduction

The wide availability of shale gas has significantly increased its utilization for producing light alkenes (C_2-C_4) *via* steam cracking and dehydrogenation.[181,182] The selective dimerization of alkenes, such as butene, into higher hydrocarbons has emerged in turn as a viable route for the production of fuels, lubricants, and surfactants.[3,183] Current dimerization processes, which use transition-metal complexes in solution, show high sensitivity to impurities in the feed, suffer from low lifetime and require involved catalyst-product-solvent separation processes.[29,160]

Heterogeneous catalysts obtained by depositing organometallic ligands into porous solid materials, e.g., zeolites, metal-organic frameworks (MOFs), or covalent organic frameworks, have been considered as alternatives to the conventional homogeneous catalysts for the dimerization of butene but have not been commercially implemented.[124,126,128,132,184] It should be noted that most of these supported catalysts require solvents and alkyl aluminum compounds as cocatalysts to initiate the catalytic cycle.[160,185,186]

Alkene dimerization may be catalyzed by Brønsted (BAS) and Lewis acid sites (LAS) without the presence of an initiator.[68] Dimerization catalyzed by BAS usually leads to branched dimers *via* carbenium ion transition states which provide low barrier paths to isomerization.[187,188] Dimerization on LAS, such as supported Ni^{2+}, Co^{2+}, and Cr^{3+}, has shown higher selectivity to linear and mono-branched dimers.[26,61,170,189] LAS sites are also known to moderate and control isomerization steps. Thus, efficient catalysts should, in principle, be free of strong BAS[45,61,174] while maintaining a high concentration of active LAS sites.[190]

MOFs with discrete oxide nodes are conceptually ideal catalyst supports, as the node surface and the substantial spacing between nodes allows for the stabilization of metal atoms/cations and establishes a homotopic environment for active centers. The increased node spacing also eliminates the interactions between bound intermediates that form at different sites. Zr_6-based MOFs (e.g., UiO-66 and NU-1000) have excellent chemical and thermal stability, required to ensure regeneration and robust handling.[191–193] Previous studies show that Ni-containing MOFs are more selective to linear olefin products than Ni-exchanged aluminosilicates for propene oligomerization.[121]

Different reaction mechanisms have been proposed for alkene dimerization, i.e., the Cossee-Arlman, the metallacycle, and the proton-transfer mechanism.[131] The aspects of the nature and structure of potentially active Ni species in dimerization reactions are beginning to be discussed vividly in the literature.[24,33,34,194]

In this work, we report on the synthesis, characterization, and density functional theory (DFT) studies of homotopic single-atom and clustered Ni cations stabilized at under-coordinated nodes of UiO-66 ($Zr_6O_4(OH)_4$(1,4-benzene dicarboxylate)$_6$). We report on studies of the effects of the local structure, the nuclearity, and the chemical environment of Ni sites on their catalytic behavior and characterize the most favorable reaction pathway for the dimerization of butene.

2.2 Results and Discussion

Thermal gravimetric analysis (**Figure 6.1**) and ^{1}H-NMR (**Figure 6.2**) show that the synthesized UiO-66 has one benzene dicarboxylate (BDC) linker missing per Zr_6 node.[195,196] The missing linker defect sites are occupied by -OH/-OH_2 groups and are potential sites for chemical functionalization.[119,141,195,197] We used a double-solvent impregnation method (see scheme in **Figure 2.7** and section 2.4.2 on catalyst synthesis) to functionalize these defect sites resulting in Ni-UiO-66 with varying Ni loadings (1.3 wt.% (Ni/Zr_6 molar ratio = 0.34), 2.5 wt.% (Ni/Zr_6 = 0.67), 5.0 wt.% (Ni/Zr_6 = 1.37), and 10.0 wt.% (Ni/Zr_6 = 2.90)). These materials are denoted as 1.3%Ni-UiO-66, 2.5%Ni-UiO-66, 5%Ni-UiO-66, and 10%Ni-UiO-66, respectively (**Table 6.3**).

Powder X-ray diffraction (PXRD) confirmed that the crystal structure of UiO-66 was retained after Ni deposition (**Figure 6.3**). The surface areas and pore volumes of the UiO-66 decreased (**Figure 6.4** and **Table 6.4**) and the total volume of pores with diameter of ~1.6 nm decreased with increasing Ni loading (**Figure 6.4b**). This suggests that Ni was anchored in the large pores of the MOF. The thermal gravimetric and mass spectrometry analysis showed that Ni-UiO-66 is stable up to 400 ºC in inert atmosphere (**Figure 6.5**). This is consistent with the N_2-sorption and XRD results for 2.5%Ni-UiO-66 after treatment at various temperatures (**Figure 6.6**). IR spectra showed that the intensity of the Zr-OH_2 band at 3630 cm^{-1} decreases after Ni deposition, which suggests that Ni interacts with the -OH_2 groups on the Zr_6 nodes (**Figure 6.7**).[198]

2.2.1 Performance in butene dimerization

The dimerization of 1-butene on 2.5%Ni-UiO-66 presented an induction period of ~8 h time on stream (TOS) at 200 °C until a maximum conversion of ~1% was reached. This induction period decreased to ~3 h TOS at 230 °C (**Figure 2.1a**) after achieving a maximum conversion of ~2%. Finally, no induction period was observed at 250 °C, in which the conversion monotonously decreased from ~5%. We speculate that the induction period in this case was completed within the time (1h) before the first measurement point. The observed induction periods suggest that the active sites for dimerization are generated in the presence of butene (likely the formation of an alkyl species, see below). Over 90% of the products by weight were C_8 isomers (**Figure 6.8**). The rest were mostly C_{12} olefins (< 10%) and trace amounts of C_{16} products (< 0.5%). Octene (60 - 70%) and methylheptene (30 - 40%) were the dominate dimers among the C_8 isomers. A small concentration of dimethylhexene was also observed (< 1%) and is hypothesized to be formed *via* double-bond isomerization to 2-butene followed by dimerization.[174] The selectivities to n-octene and methylheptene were nearly constant with TOS (**Figure 6.8**), suggesting that deactivation resulted from the loss of active sites.[60,61] The N_2-sorption and IR spectra of the spent catalysts support deactivation by pore blocking (**Figure 6.10** and **Figure 6.11**).

The apparent activation energy (E_a) of 1-butene dimerization, based on the maximum rate of 1-butene conversion, was measured to be 58±5 kJ·mol^{-1} (**Figure 2.1a**). This value is close to those reported for alkene dimerization on Ni-zeolites and higher than those reported in systems with mass transfer limitations (~30 kJ·mol^{-1}).[199,200] The first-order kinetics with respect to 1-butene (**Figure 2.1b**) suggests that the reaction is compatible with a Cossee-Arlman mechanism.[153,170,201] The oxidative coupling of two alkene molecules, in contrast, is typically the rate-determining step (RDS) in reactions that proceed *via* the metallacycle path and would result in second order kinetics.[160]

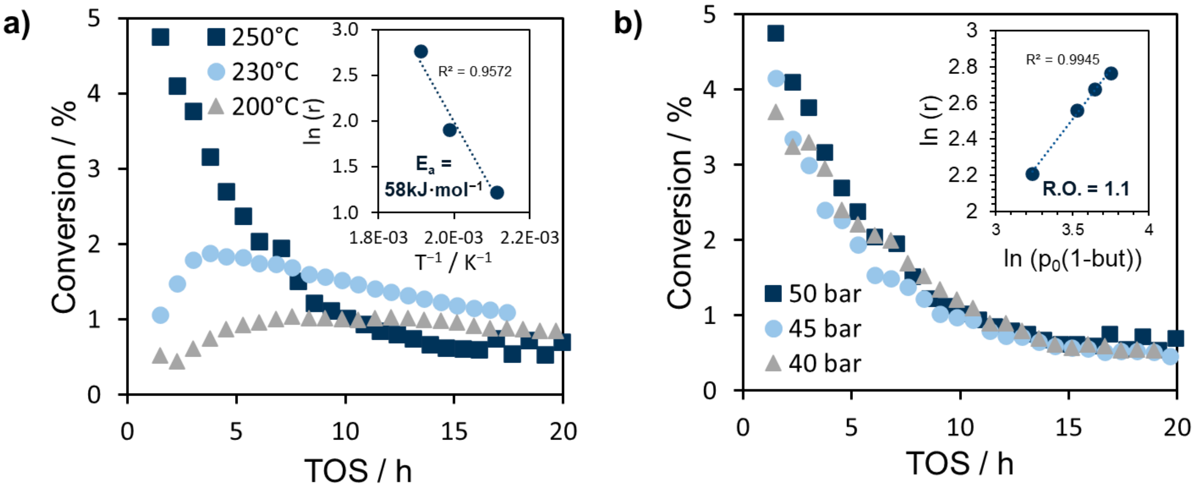

Figure 2.1: a) 1-Butene conversion on 2.5%Ni-UiO-66 at varying reaction temperature against TOS. The inset shows the Arrhenius plot. b) Rate of 1-butene consumption on 2.5%Ni-UiO-66 against various partial pressures of 1-butene plotted on a log-log plot (Reaction conditions: T = 200-250 °C, p = 30-50 bar, WHSV = 8.4 h^{-1}).

The impact of Ni loading on butene dimerization was studied at 250 °C (Figure 2.2**a**). The consumption rate of 1-butene normalized to the weight of the catalyst increased linearly with increasing Ni loading up to 5.0 wt.%. A further increase did not impact the butene consumption rate. The rates normalized to the Ni content (Figure 2.2**a**) were nearly identical for 1.3%Ni-UiO-66 and 2.5%Ni-UiO-66 ($\sim 3.7 \cdot 10^{-3} \pm 0.3 \cdot 10^{-3}$ $\mathrm{mol_{butene} \cdot mol_{Ni}^{-1} \cdot s^{-1}}$) and decreased by ~30% and ~70% on the samples with 5.0 and 10.0 wt.% of Ni, respectively.

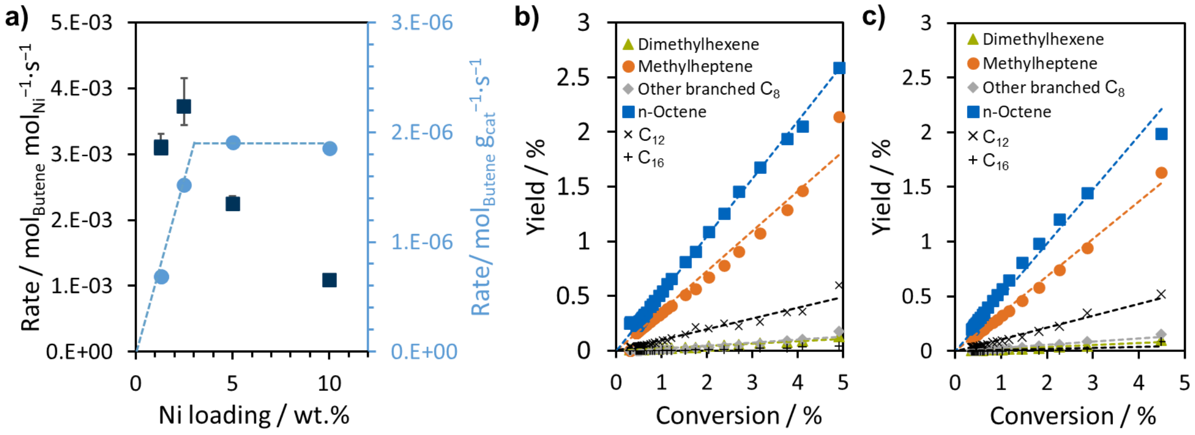

Figure 2.2: a) Rate of 1-butene consumption as a function of Ni concentration in Ni-UiO-66 based on the mass of catalysts (blue) and based on the molar Ni amount(black). Yield/conversion plot of collected products at different levels of 1-butene conversion on b) 2.5%Ni-UiO-66 and c) 10%Ni-UiO-66 (Reaction conditions: $T = 250$ °C, $p = 50$ bar, WHSV = 8.4 $\mathrm{h^{-1}}$).

The linear decrease of the reaction rate with increasing Ni loading above 2.5 wt.% was paralleled by an increase of the concentrations of butene trimers (C_{12}) and tetramers (C_{16}) due to the addition of butene to the primary C_8 products (Figure 2.2**b** and **c**). This suggests that with increasing Ni concentration, new active sites form, which tend to prefer addition of a further alkene over desorption.

2.2.2 Structure elucidation with X-ray absorption spectroscopy

Ni K-edge X-ray absorption near-edge structure (XANES) and extended X-ray absorption fine structure (EXAFS) were used to assess the structural differences among Ni species (**Figure 2.3a**). All Ni-UiO-66 materials showed similar XANES spectra indicating the same oxidation state and coordination geometry of Ni sites (**Figure 6.13**). The comparison of edge position between Ni-UiO-66 and reference compounds (and the $\chi(k)$ EXAFS spectra shown in **Figure 6.15**) indicates that Ni exhibits features in between those of α-Ni(OH)$_2$ and NiO. Thus, the oxidation state of Ni is +II, which is further supported by the X-ray emission spectra (XES) reported in **Figure 6.14**. The lower intensity of the white line of Ni-UiO-66 than that of α-Ni(OH)$_2$ and NiO suggests that there are fewer scatters in the first shell of Ni in the MOF than on the reference. In addition, the 1s→3d electronic transition pre-edge peak at 8333-8334 eV in Ni-UiO-66 is more intense than those of the references (inset in **Figure 2.3a**). The intensity of this pre-edge peak is related to a defined tetrahedral coordination of the Ni cation. Thus, the large intensity further supports the existence of Ni sites with low coordination numbers in the activated Ni-UiO-66 samples (i.e., tetrahedral coordination preferred over octahedral coordination).[190] 10%Ni-UiO-66 exhibited a weaker pre-edge peak and a closer shape to that of α-Ni(OH)$_2$ than to the other MOF samples. This suggests that there is a higher proportion of square planar and/or octahedral Ni sites in 10%Ni-UiO-66 than in materials with lower Ni loading.

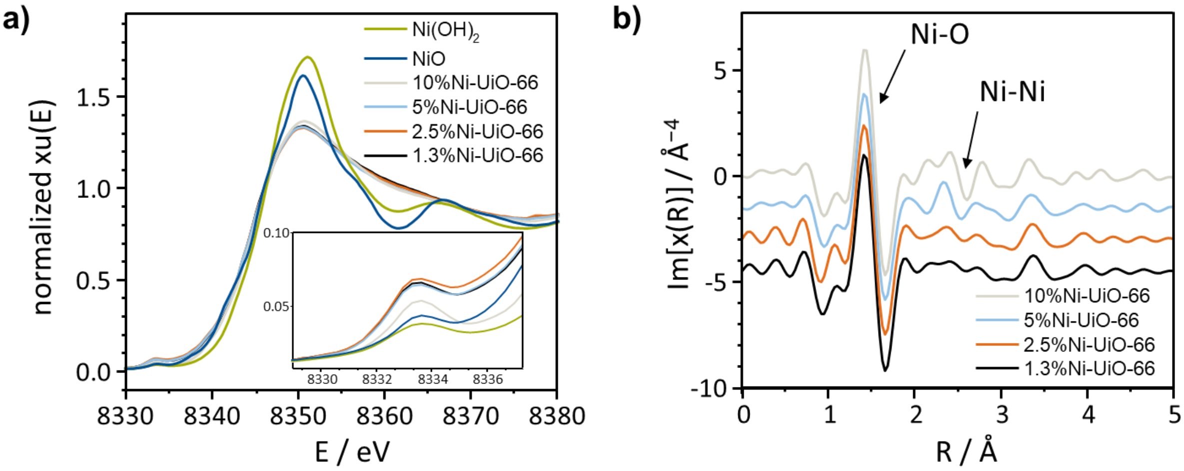

Figure 2.3: a) Normalized Ni-XANES spectra and b) k^3-weighted Ni-EXAFS Im[$\chi(R)$] spectra of the as-prepared Ni-UiO-66 and reference compounds. The inset of a) shows the pre-edge feature corresponding to the 1s → 3d electronic transition for the Ni.

Figure 2.3b shows the phase-uncorrected k^3-weighted imaginary $\chi(R)$ spectra of the Ni-UiO-66 materials. The first feature at 1.4 -1.6 Å is assigned to the Ni-O single scattering. We note that the distance of Ni-O in the activated MOF sample is 0.15 Å shorter compared to that of α-Ni(OH)$_2$ and NiO (**Figure 6.15**). The amplitude of Ni-O peak in 2.5%Ni-UiO-66 is weaker by 20-30% than the six-fold-coordinated reference compounds, which indicates that fewer O atoms are coordinated in the first shell of Ni in activated Ni-UiO-66 as compared to the reference Ni compounds, i.e., 3 - 4 O atoms. The Ni-Ni single scattering feature (2.4 - 2.6 Å) in 2.5%Ni-UiO-66 is much weaker than that of α-Ni(OH)$_2$ and NiO. This indicates the presence of Ni in clusters with few Ni atoms or as isolated Ni sites. Inspection of the k^3-weighted imaginary part of EXAFS spectra shows that the intensity of the Ni-Ni feature increases with increasing Ni loading.

The experimental data were fitted with a modified Ni(OH)$_2$ model obtained by using the FEFF9 code (see **Section 2.4.4** for details). The fitting confirmed a first Ni-O shell with the average distance of 1.91-1.92 Å for all MOF samples (**Table 2.1**). The average coordination numbers (CN) were ~3 for 1.3%Ni-UiO-66 and 2.5%Ni-UiO-66, which increased to 3.6 for 10%Ni-UiO-66. The values fit for the Ni-Ni path at ~2.98 Å in 1.3%Ni-UiO-66 and 2.5%Ni-UiO-66 were negligible, suggesting that Ni is predominantly present in isolated monomeric structures. The Ni-Ni scattering had an average coordination number of 0.9 ± 0.5 for 1%-Ni-UiO-66. Fitting with a Ni-O-Zr path for the MOF samples provided only minor improvement to the fit quality and did not change the parameters for Ni-Ni and Ni-O. This suggests that Ni–Zr interactions are significantly disordered.[202] The conclusion of having isolated Ni sites in low Ni loading materials (e.g., 1.3%Ni-UiO-66 and 2.5%Ni-UiO-66) and clusters in 10%Ni-UiO-66, can be correlated with the concentration of Ni in the MOF. The molar ratios of Ni to Zr$_6$ nodes are 0.34, 0.67 and 2.90 for 1.3%Ni-UiO-66, 2.5%Ni-UiO-66 and 10%Ni-UiO-66, respectively (**Table 6.3**).

Table 2.1: Average interatomic distances (R), coordination number (CN) and Debye-Waller factors (DWF) determined for Ni ions in Ni-UiO-66 by fitting the experimental k^3-weighted spectrum

Sample	Path	CN	R/Å	DWF
1.3%Ni-UiO-66	Ni-O	3.2 (3)	1.912 (21)	0.0059(13)
	Ni-Ni	-	-	-
2.5%Ni-UiO-66	Ni-O	3.0 (4)	1.908 (15)	0.0077(11)
	Ni-Ni	-	-	-
5%Ni-UiO-66	Ni-O	3.4 (4)	1.912(36)	0.0063 (19)
	Ni-Ni	0.3(2)	2.972 (29)	0.0106 (20)

10%Ni-UiO-66	Ni-O	3.6 (5)	1.917 (36)	0.0094 (11)
	Ni-Ni	0.9(5)	2.979 (14)	0.0121 (29)

We measured XANES and EXAFS spectra of 2.5%Ni-UiO-66 at different stages of the activation procedure. The XANES of freshly prepared 2.5%Ni-UiO-66 overlaps with that of Ni^{II} ions in water (**Figure 6.16a**). Upon activation in He, the intensity of the white line significantly decreases (**Figure 6.16b**), suggesting that the Ni site is dehydrated. As Ni^{II} ions in water have six H_2O molecules in the first shell forming octahedral $Ni(H_2O)_6^{2+}$ species,[203] we propose a 6-fold coordinated octahedral Ni species in the freshly prepared 2.5%Ni-UiO-66 (see **Figure 6.17a**). Note that the FEFF simulated EXAFS spectra for the proposed model match well with the experimental spectra (**Figure 6.17b** and **Figure 6.17c**). Four water molecules desorbed from 2.5%Ni-UiO-66 upon heating at 300 °C (**Figure 6.5** and **Figure 6.17**) as illustrated in **Figure 6.18**. Based on these observations and the fitting parameters determined by EXAFS for the dehydrated Ni structure in 2.5%Ni-UiO-66, we optimized a series of formate-truncated cluster models for mononuclear Ni ions supported on the nodes of UiO-66 (see **Figure 6.23** and section on cluster models in the SI) using DFT (M06L/def2TZVPP/def2SVP level of theory). The DFT-optimized cluster model that best reproduces the experimental EXAFS data is shown in **Figure 2.4a**. In this structure, the Ni ion binds to the Zr_6 node in a square planar type structure *via* two Zr-(μ_3)OH-Ni linkages and an extra -OH ligand on the Ni that orients away from the Zr_6 node. The O atom in this terminal -OH, together with Ni and O atoms in one Zr-(μ_3)OH-Ni bond, forms a nearly straight line. The calculated Ni-O distance is 1.9 Å, close to the experimental value of 1.908 Å (**Table 2.1**). The simulated EXAFS spectra for the Ni-UiO-66 cluster model are in good agreement with the experiments (**Figure 2.4b**). The close match of the paths in Im[$\chi(R)$] and the oscillation in x(k) plots indicates that majority of the Ni species are single metal ions bound to the nodes of UiO-66 as represented by the computationally defined structures.

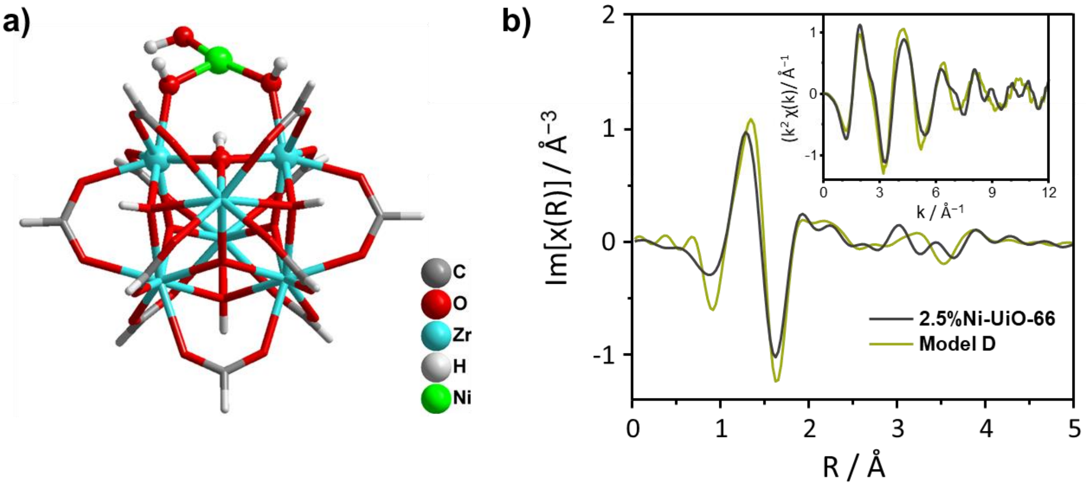

Figure 2.4: a) Best DFT-optimized structure of Ni species on the MOF. (b) k^2-weighted Ni-EXAFS Im[$\chi(R)$] spectra for 2.5%Ni-UiO-66 and the DFT-optimized model. Inset show the respective x(k) plots.

2.2.3 Catalytic mechanism for butene dimerization

This optimized Ni-UiO-66 cluster model was applied to examine the 1-butene dimerization mechanism using DFT (M06L/def2TZVPP/def2SVP level of theory). **Scheme 6.1**, **Figure 2.5b** or **Scheme 6.2** and **Scheme 6.3** depict three possible mechanisms for 1-butene dimerization, i.e., proton-transfer, Cossee-Arlman, and metallacycle reaction mechanisms (simply named as Cycle I, II, and III).[131] The proton-transfer mechanism (**Scheme 6.1**) proceeds by the activation of the node (**structure Node A**) by a proton transfer from the adsorbed butene (**structure PA**) to the hydroxide on the metal to form water which desorbs from the node, leaving a Ni-vinyl type intermediate (**structure PB**). This is followed by the coordination of a second 1-butene molecule to the active metal site (**structure PC**). The vinyl species subsequently inserts into the Ni-C bond of the adsorbed butene (**structure PD**) with a free energy barrier of $\Delta G^{\neq}$= 86 kJ·mol^{-1} (**Figure 6.25**) to form the C-C bond. This is followed by a proteolytic H transfer to the bound alkenyl intermediate to form the dimer product adsorbed on the metal (**structure PE**) with a free energy barrier of at least $\Delta G^{\neq}$= 120 kJ·mol^{-1} (**Figure 6.25**). Desorption of the bound higher olefin yields the dimerization product regenerating the bare metal site (**structure PF**). Adsorption of another 1-butene on this bare metal site (**structure PG**) is followed by the activation of a C-H bond in butene to form the M-vinyl reactive species (**structure PB**) which regenerates the active site for the next catalytic cycle.

The activation of butene to form the bound vinyl is calculated here to be the rate determining step (RDS), with a Gibbs free energy activation barrier $\Delta G^{\neq}$ = 152 kJ·mol^{-1} (**Figure 6.25**).

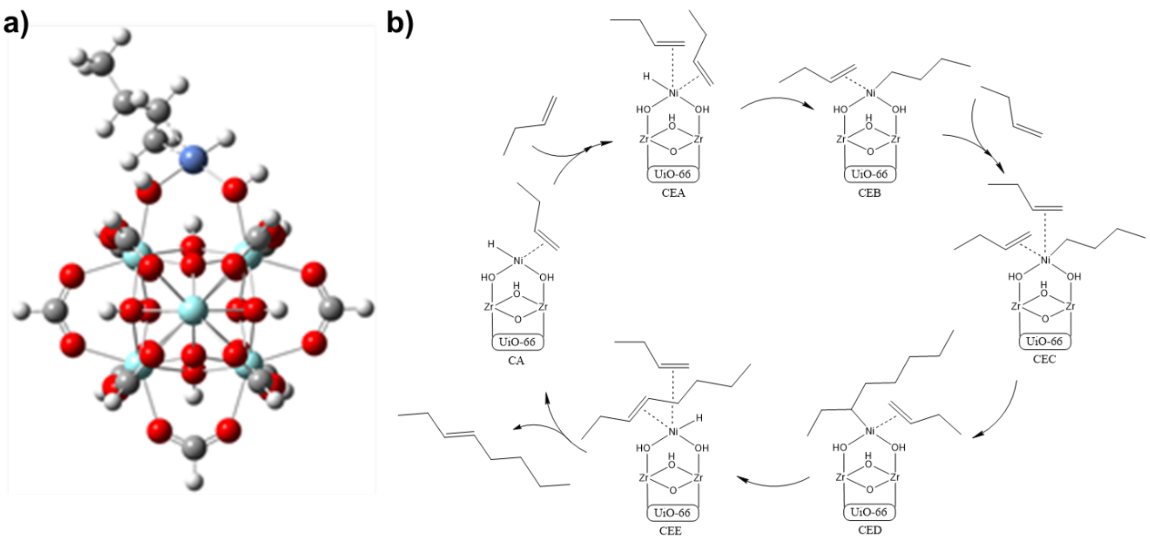

Figure 2.5: a) Cluster model of Ni-H active site in Ni-UiO-66, and b) proposed Cossee-Arlman reaction mechanism for the dimerization of 1-butene catalyzed by Ni-H active site in Ni-UiO-66 catalyst in the presence of a physisorbed 1-butene molecule. Color code: Zr (cyan), Ni (blue), O (red), C (grey), H (white).

The Cossee-Arlman mechanism shown in **Scheme 6.2**, requires an initial process to generate a metal hydride intermediate to drive the catalytic cycle. This can proceed by the same initial step as that presented above for the proton-transfer mechanism and will be discussed later. 1-Butene subsequently adsorbs at the metal hydride (M-H) site (**structure CA**). The hydride inserts into the adsorbed 1-butene to form the M-butyl intermediate (**structure CB**, $\Delta G^{\neq}$= 20 kJ·mol^{-1}, **Figure 6.26**). This step is followed by the adsorption of a second 1-butene at the M-butyl active site (**structure CC**). The butyl group subsequently inserts into the M-C bond of the adsorbed 1-butene to form the corresponding M-octyl structural isomer (**structure CD**), with an intrinsic Gibbs free energy barrier of $\Delta G^{\neq}$= 95 kJ·mol^{-1} (**Figure 6.26**). The measured rates were found to be first order with respect to 1-butene. As such the apparent activation energy should be measured with respect to bound alkyl intermediate (**structure CB**). The DFT apparent activation enthalpy for the C-C bond formation from the M-butyl intermediate (**Figure 6.26**) was calculated to be 23 kJ·mol^{-1}. The M-octyl species subsequently undergoes a β-hydride elimination to form the adsorbed 1-octene product (**structure CE**, $\Delta G^{\neq}$= 57 kJ·mol^{-1}, **Figure 6.26**). The 1-octene product desorbs to complete the catalytic cycle and regenerate the M-H reactive site. Thus, the C-C insertion to form the M-octyl species is likely the rate-determining step in this mechanism.

The rather low apparent activation barrier calculated here ($\Delta H^{\neq}$ = 23 kJ·mol^{-1}) results from the coordinative unsaturation of the Ni center and the idealized nature of the reaction environment. Previous high pressure olefin dimerization studies carried out in zeolites[2] indicate that the olefins condense and form a solvation shell that enhances the catalytic activity. At the present high-pressure reaction conditions (p=50 bar, T=250 °C) butene is physisorbed in the MOF pores. Preliminary Gibbs Ensemble Monte Carlo simulations indicate that there are up to 16 butene molecules within the unit cell of UiO-66 with at least 2 molecules that reside in the central cavity between the nodes. To provide a more representative model of the active Ni sites under reaction conditions, we introduce an additional physisorbed 1-butene molecule. This model is also more consistent with those used in homogeneous olefin oligomerization catalysis to model the associative displacement of the resulting oligomer to propagate a new chain.[204] The additional 1-butene coordinates to the active M-H site to form the square planar $Ni(ZrOH)_2OH$(1-butene) complex shown in **Figure 2.5a** which is consistent with the resting state structure for homogenous Ni systems. The Cossee-Arlman mechanism in the presence of the physisorbed 1-butene molecules is shown in **Figure 2.5b** and the corresponding standard free energies and the enthalpies for each intermediate and TS are shown in **Figure 2.6** (and **Figure 6.26**). The rate limiting step still involves C-C coupling with an intrinsic free energy of 87 kJ·mol^{-1}. The apparent activation enthalpy for this system increases to 48 kJ·mol^{-1} (**Figure 6.26**), which is in reasonable agreement with the experimental value of 58±5 kJ·mol^{-1}.

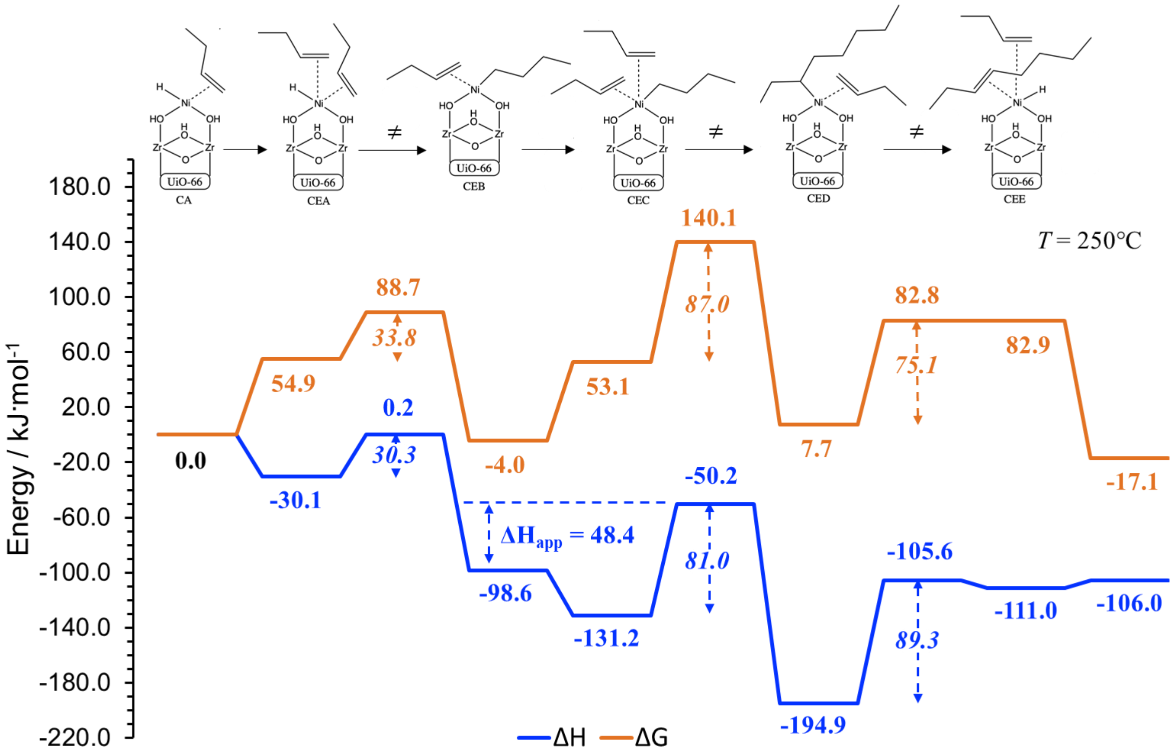

Figure 2.6: Standard free energy diagram (red) and enthalpy diagram (blue) for the dimerization of 1-butene catalyzed by Ni-UiO-66 at T = 250 °C and p = 1 bar, following the Cossee-Arlman reaction mechanism in the presence of a physisorbed 1-butene molecule.

The metallacycle mechanism (**Scheme 6.3**, Cycle III) proceeds by the adsorption of two 1-butene molecules to the active metal center (**structure MC**). This is followed by the oxidation of the metal to form a substituted metallacycle (**structure MD**), overcoming a free energy barrier of $\Delta G^{\neq}$= 214 kJ·mol^{-1} (**Figure 6.27**). The metallacycle intermediate subsequently undergoes a β-hydride elimination, H transfer, and metal reduction steps to form the dimer olefin product adsorbed on the metal (**structure ME**). Desorption of the product regenerates the active metal site for subsequent cycles.

The free energy barriers of the RDS for the investigated reaction pathways suggest that 1-butene dimerization is catalyzed by Ni-UiO-66 *via* a Cossee-Arlman mechanism (Cycle II). It cannot be ruled out that the proton transfer mechanism (Cycle I) acts as a path for the generation of the active site for the Cossee-Arlman mechanism.

In the proton transfer mechanism, the C-C insertion of the vinyl species into the adsorbed 1-butene generates the M-octenyl intermediate (or its structural isomer, **structure PD**, **Scheme 6.1**). If this insertion step is followed by a β-hydride elimination step, it can form an octadiene and generate the desired Ni-H active site (structure **M-H**, **Scheme 6.4**). The free energy diagram for the formation of this M-H from the proton-transfer pathway on Ni-UiO-66 is shown in **Figure 6.28** and indicates a free energy barrier ($\Delta G^{\neq}$) of 64 kJ·mol^{-1} for the β-hydride elimination step. The β-hydride elimination step (to form **M-H**) competes with the proton transfer step in Cycle I (to form dimer olefin product) and has a free energy barrier lower than the latter step by at least 56 kJ·mol^{-1}, suggesting that the formation of the Ni-H active site for the Cossee-Arlman reaction mechanism is favored. Therefore, the observed induction period for 1-butene conversion on stream is attributed to the *in-situ* generation of Ni-H active sites in the presence of 1-butene for dimerization.

2.3 Conclusion

UiO-66 based catalysts with single and few Ni cation metal oxo clusters at undercoordinated zirconia nodes of UiO-66 have been synthesized by varying the molar ratio of Ni atoms to the zirconia nodes during synthesis. Upon activation at 300 °C in inert gas, both single-atom and sites containing multiple Ni cations were observed and were found to be catalytically active for dimerization of 1-butene without a cocatalyst. While the single Ni atom-based catalysts showed high selectivity to linear octene and methylheptene (>90%), the catalysts with more Ni cations per site produced more trimers and tetramers. X-ray absorption spectroscopy and DFT calculations suggest that Ni in the as-synthesized Ni-UiO-66 has a local structure with octahedral geometry of Ni^{2+}. Four H_2O molecules on the Ni cations are removed upon activation, which leads to the formation of a partially dehydrated mononuclear Ni site attached to the Zr_6 node of UiO-66 MOF *via* two μ-OH groups. The oxidation state of Ni^{2+} remains unchanged in this process. DFT studies for the 1-butene dimerization mechanism suggest the Cossee-Arlman reaction mechanism to be energetically favored. The in-situ formation of the Ni-H active site in the presence of 1-butene for dimerization following the Cossee-Arlman mechanism is found to be more favorable over the parallel dimerization of 1-butene following the proton-transfer mechanism at the hydroxyl Ni site based on the computed free energies. The observed induction period during dimerization is attributed to the transition of the hydroxyl Ni site to a Ni-H site for 1-butene dimerization. The high olefin pressures assist in the rate-limiting C-C bond formation and chain termination.

2.4 Experimental work

2.4.1 UiO-66 MOF synthesis

UiO-66 MOF was synthesized *via* a solvent-thermal route described in the literature.[196,205] In a typical process, 8.39 g $ZrCl_4$ (36 mmol, Sigma-Aldrich) was dissolved in 50 mL N,N-dimethyl-formamide (DMF) by rigorous stirring in a autoclave (2 L, Parr). Subsequently, 66.6 mL of 37 wt.% HCl aqueous solution was added into the reactor until the mixture became clear. 8.31 g terephthalic acid (50 mmol, Sigma-Aldrich) was separately dissolved in 500 mL DMF by stirring. The solution of terephthalic acid was then added slowly into the autoclave, which was then sealed and kept at 80 °C for 18 h. The resulting product was separated, washed with DMF for three times and acetone for five times, and dried in a vacuum oven at 80 °C for 12 h. The yield of UiO-66 was around 86%.

2.4.2 Catalyst synthesis

Ni-UiO-66 samples with various Ni loadings were prepared *via* a double-solvent impregnation method. In this method, the highly hydrophilic Zr_6 nodes of the MOFs attract metal aqua complexes.

In a typical experiment (see **Figure 2.7**), UiO-66 was degassed under vacuum (10^{-3} mbar) at 250 °C for 4 h to remove the impurities (e.g., residual DMF solvent, physically adsorbed water). Subsequently, 1.0 g of degassed UiO-66 was transferred into a glass jar containing 80 mL hexane. Ultrasonic treatment was required to disperse the MOF. Under intensive stirring, 0.6 mL $Ni(NO_3)_2$ (0.7 M) aqueous solution was dropped into the mixture. The volume of added solution is equivalent to that of the pore volume of UiO-66. The mixture was further stirred for several hours until a light green suspension formed. After impregnation, the product was separated by centrifugation, collected, and dried at 90 °C in a vacuum oven for 12 h. The dried sample was further heated in a helium flow at 250 °C for 4 h to remove the nitrate species. Ni loading in the MOF was varied by adjusting the concentration of Ni ions in the initial aqueous solution.

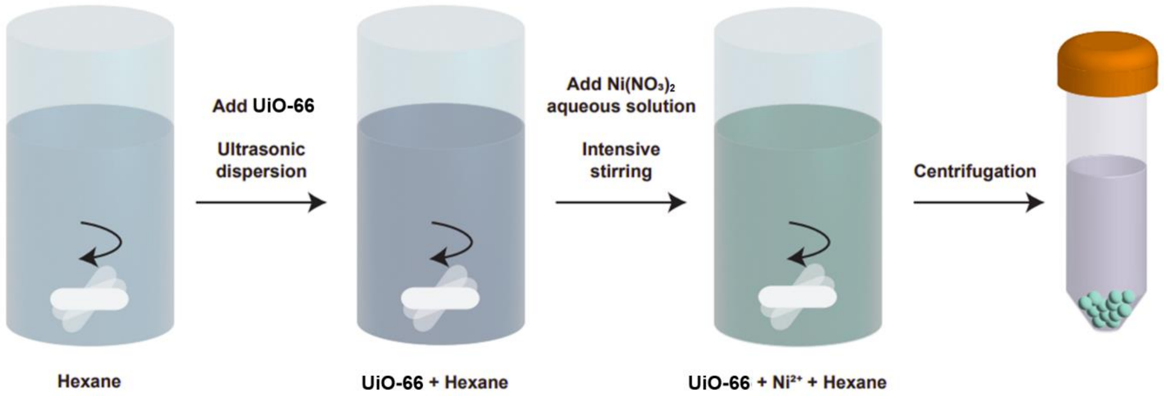

Figure 2.7: Schematic route for the synthesis of Ni-UiO-66 *via* the double-solvent impregnation method.

The Ni-ZrO_2 catalyst was synthesized by incipient wetness impregnation. $Zr(OH)_4$ nanopowder (<100 nm, monoclinic, 20-30 $m^2 \cdot g^{-1}$) was purchased from MELChemicals (Product code: MELCat 631/01). In a typical procedure, 6 mL aqueous solution of $Ni(NO_3)_2$ (1.6 M) was added stepwise and in small quantities to 1.0 g $Zr(OH)_4$. The resulting Ni-$Zr(OH)_4$ precursor was calcined in air at 550 °C for 6 h to obtain Ni-ZrO_2.

2.4.3 Material characterization

The elemental composition of the catalysts was determined by inductively coupled plasma-atomic emission spectroscopy (ICP-AES, Perkin Elmer 7300DV). The samples were digested in an HNO_3/HCl/HF/H_2O mixture followed by H_3BO_3 addition for extra HF treatment before the ICP-AES tests.

Proton nuclear magnetic resonance (^1H NMR) spectroscopy was also used to determine residual DMF and formate species in the parent UiO-66 MOF. Typically, 20 mg of UiO-66 was dissolved in 1 mL of 1 M NaOH solution in D_2O. The mixture was left to digest for 24 h. The data were recorded with a 400 MHz spectrometer. The OH-based procedure dissolves only the organic parts of the MOF (e.g., linker, solvent, formate), while the inorganic component sinks to the bottom as ZrO_2 and does not interfere with the spectra. Quantification of the organic portion was obtained by calculating the integrated peak area of each portion.

Powder X-ray Diffraction (PXRD) was used to analyze the phase composition and structure of fresh and used Ni-UiO-66. Experiments were performed with a Rigaku MiniFlex 600 X-ray diffractometer (XRD). The diffraction patterns were collected in the 2θ range of 1-40° with a step size of $2°\cdot min^{-1}$ under ambient conditions.

Physisorption experiment with N_2 to determine surface areas and pore volumes was measured at liquid N_2 temperature on a Micromeritics ASAP 2020 instrument. The total pore volume was investigated by single-point adsorption close to $p/p_0 = 0.99$.

Thermogravimetric Analysis (TGA) and differential scanning calorimetry (TG-DSC) analyses were performed on a SENSYS EVO TG-DSC (SETARAM Instrumentation). The dehydration degree of Ni-UiO-66 was determined under vacuum (10^{-3} mbar). There is an online mass spectrometry connected to the vacuum chamber to probe the desorbed water molecules. The samples were heated at the ramp rate of $5\ °C\cdot min^{-1}$ from room temperature to 500 °C. For determining the amount of linker missing, the samples were heated at the ramp rate of $1\ °C\cdot min^{-1}$ under air from room temperature to 700 °C.

Infrared spectra (IR) of the MOFs were recorded on a ThermoScientific Nicolet FTIR spectrometer equipped with CaF_2 windows and an MCT detector with a resolution of $4\ cm^{-1}$. 64 scans were accumulated for each spectrum. The samples for IR measurements were prepared as self-supporting thin wafers with a density of approximately 2-3 $mg\cdot cm^{-2}$. They were placed into the IR cell and activated by evacuation to $1.0\cdot 10^{-6}$ mbar and subsequent treatment at 300 °C (ramp rate of $5\ °C\cdot min^{-1}$).

Ni X-ray emission spectroscopy (XES) was performed on a laboratory EasyXAFS XES150 system equipped with a 100 W X-ray generator (W or Pd anode). The system has a full XES energy range from 5 keV to 12 keV. A Si (511) monochromator was configured to scan the Ni-UiO-66 from 8.2 keV to 9.9 keV.

The X-ray absorption spectroscopy experiment of Ni-UiO-66 was carried out at the Pacific Northwest Consortium/X-ray Science Division bending-magnet beamline at the Advanced Photon Source at Argonne National Laboratory or on beamlines 2-2 at Stanford Synchrotron Radiation Lightsource. All experiments were performed in transmission mode. A harmonic rejection mirror was installed to reduce harmonic effects. A Ni foil was placed before the sample cell as a reference for calibration of the photon. To assure the dehydration of the catalyst during measurements, the samples were activated in helium at 200 °C or 300 °C and loaded into a thin-walled glass capillary (0.02 mm) in an argon glove box. The capillary end was sealed with a propane flame. The XAS data were processed using ATHENA, as part of the XAFS software package,[206] to remove the background from the $\chi(k)$ oscillations. The Fourier transform of the k-space EXAFS data were fitted to X-ray determined structure using Artemis. For the fitting, α-Ni(OH)$_2$ was used as starting model. Parts of the Ni-O-Ni scattering paths were modified to Ni-O-Zr and calculated by (FEFF9). The fits to the Ni K-edge EXAFS $\chi(k)$ data were weighted by k^2 and windowed between 2.0 Å^{-1} < k < 12.0 Å^{-1} using a Hanning window with dk = 1.0 Å^{-1}.

2.4.4 EXAFS spectra simulation

The EXAFS spectra of DFT-optimized Ni models were simulated as described somewhere else in literature.[205] Ab initio scattering theory was applied with approximate global disorder parameters (T = 25 °C).[207] The computed coordinates were used to generate the primary input for the ab initio EXAFS scattering code (FEFF9) that includes all the single and multiple scattering paths out to 6 Å. This results in several hundred scattering paths for each Ni atom in the structure.[192] The bond disorder at 25 °C is considered by setting a universal value of the Debye-Waller factor (σ^2 = 0.0035). The obtained spectra for each Ni atom in the cluster are then averaged, and an overall E_0 is applied to match experimental values (oscillations in $\chi(k)$ converge at k = 0). While the global Debye-Waller factor is a reasonable estimate of the first shell disorder, it is an overestimation of the order in the higher shells, which manifests as an over-prediction of these amplitudes, although the atom positions predicted by the theory are correctly represented.

2.4.5 Catalytic testing

The procedure and set-up for the catalytic tests in butene dimerization are similar to those described in the literature.[61,174]

A fixed bed plug flow reactor (PFR (i.d. = 3.9 mm)), connected to an online GC analysis unit (Agilent HP 6890, equipped with a 50 m HP-1 column) was used to test the catalytic performances.[61,174] Before GC analysis, the product stream was hydrogenated over a Pt/Al_2O_3 catalyst with hydrogen. A syringe pump (ISCO Model 500 D) introduced a mixture of 15% isobutane and 85% 1-butene, a Eurotherm 2416 apparatus regulated the temperature, and a Tescom backpressure regulator controlled the pressure. The lines immediately before and after the reactor were kept at 150 °C.

The catalyst was pressed and sieved into pellet sizes of 180-250 µm. Before weighing, the catalyst was dried at 100 °C for 1 h. The catalyst bed was diluted with SiC and fixed in the isothermal zone of the reactor. After activation at 300 °C for 1 h (rate 5 $°C \cdot min^{-1}$) in N_2, the reactor was cooled to reaction temperature, while the bypass was flushed with the feed. Then the desired flow rate was set, and after a minimum of three stabile GC measurements of the bypass, the flow was redirected into the reactor, and the GC measurements of the reaction were started.

Standard measurement conditions were 200-250 °C and 30-50 bar with a feed flow rate of 0.04 $mL \cdot min^{-1}$. Catalyst loading was 150 mg. The activation energy was determined between 200 and 250 °C at 50 bar with a weight hourly space velocity (WHSV) of 8.4 h^{-1}. The reaction order was measured at 30, 40, 45, and 50 bar of 1-butene, at 250 °C, and a WHSV of 8.4 h^{-1}.

Conversion, selectivity, and yield were calculated according to the following equations:

$$X = \frac{n(\text{butene})_{\text{in}} - n(\text{butene})_{\text{out}}}{n(\text{butene})_{\text{in}}} \qquad \textbf{(Eq. 2.1)}$$

$$S = \frac{n(\text{product})_{\text{out}}}{n(\text{butene})_{\text{in}} - n(\text{butene})_{\text{out}}} \cdot \frac{|\nu_{\text{butene}}|}{\nu_{\text{product}}} \qquad \textbf{(Eq. 2.2)}$$

$$Y = \frac{n(\text{product})_{\text{out}}}{n(\text{butene})_{\text{in}}} \cdot \frac{|\nu_{\text{butene}}|}{\nu_{\text{product}}} \qquad \textbf{(Eq. 2.3)}$$

2.4.6 Computational Details

All DFT computations were performed using the Gaussian 16 software package[208] employing the M06-L local density functional[209] and a def2-SVP basis set for C, O, and H atoms and a def2-TZVPP basis set for Ni and Zr metal atoms.[210,211]

The associated Stuttgart/Dresden (SDD) effective core potential was employed for the core electrons in Zr. An ultrafine grid was employed for performing the numerical integrations. Ni was investigated in an oxidation state of +II as both closed shell singlet and open shell triplet system. Vibrational frequencies were computed at the optimized geometries for calculating the enthalpic and entropic contributions as well as for determining the nature of the stationary point. All intermediates had real vibrational frequencies, while the transitions states had only one imaginary vibrational frequency. Vibrational frequencies below 50 cm^{-1} were corrected to 50 cm^{-1} while computing free energies. Electronic energies, enthalpies, and standard free energies of the reaction intermediates and transition states were computed relative to the isolated Ni-UiO-66 structure and gas phase 1-butene molecules according to the following equation:

$$\Delta X\ (X = E, H, G) = X_{intermediate/TS} - X_{Ni-UiO-66} - n_{1-butene}X_{1-butene} \qquad \textbf{(Eq. 2.4)}$$

2.4.7 Cluster models

All computations of the reaction mechanism were performed on finite cluster models extracted from previously optimized periodic structures of UiO-66 MOF. The benzoate linkers of the MOF were replaced by formate linkers to reduce the cluster size for computations. The positions of the C atoms of the formate linkers were held fixed during all optimizations to mimic the structural rigidity of the MOF. One of the formate linkers coordinated to the Zr_6O_8 node of UiO-66 was replaced by -OH and H_2O ligands representing the missing linker defect while maintaining the overall charge neutrality of the cluster model.

3 Influence of adsorption on butene dimerization activity of single metal cations on UiO-66 nodes

This chapter is based on unpublished results. The manuscript will be submitted promptly. The project is a joint effort of Saumil Chheda, Dr. Jian Zheng, Dr. Navneet Khetrapal, Julian Schmid, Dr. Ruixue Zhao, Dr. Carlo A. Gaggioli, Donald M. Camaioni, Dr. Ricardo Bermejo-Deval, Dr. Oliver Gutiérrez, Dr. Yue Liu, Prof. J. Ilja Siepmann, Prof. Matthew Neurock, Prof. Laura Gagliardi, Prof. Johannes A. Lercher. I performed the catalyst characterization, the catalytic experiments as well as the adsorption studies.

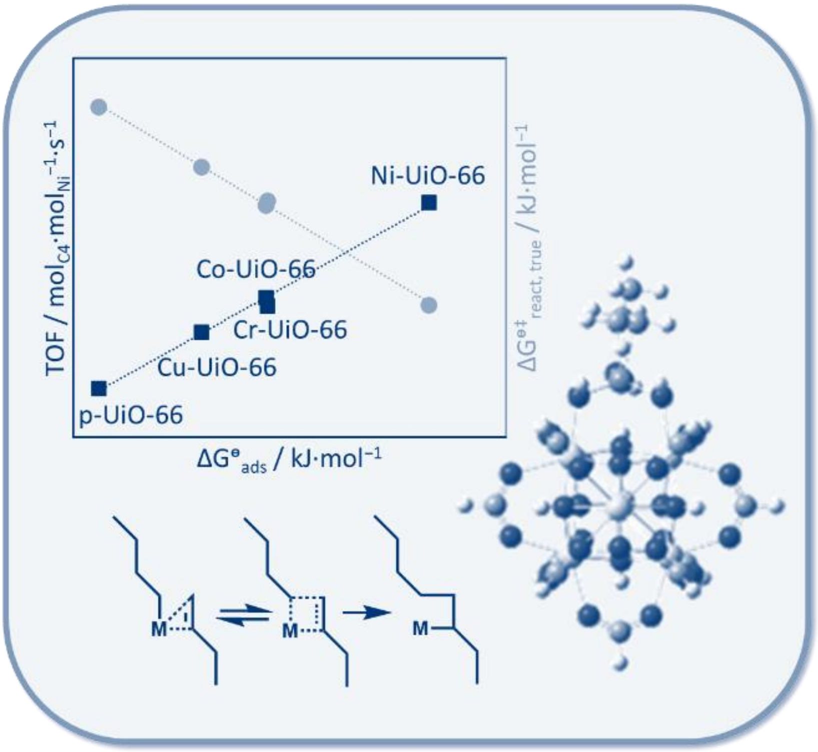

Grafting metal cations onto sites generated by a missing linker in zirconium-based metal-organic frameworks (MOFs), such as UiO-66, produces a uniquely well-defined and homotopic catalytically active site. We present here the synthesis and characterization of a group of UiO-66 based catalysts with Ni, Co, Cu, and Cr for dimerization of alkenes. The H-D exchange *via* D_2O adsorption followed by IR spectroscopy showed that the last molecular water ligand desorbs from the sites after evacuation at 300 °C leading to M(OH)-UiO-66 structures. Adsorption of 1-butene followed by IR spectroscopy, calorimetry, and density functional theory is used to characterize the interactions of an alkene with the metal cation sites, active for alkene oligomerization. For the most active Ni-UiO-66, the removal of molecular water from the active site significantly increases the butene adsorption enthalpy and almost doubles the catalytic activity for 1-butene dimerization in comparison to the presence of water ligands. Other M-UiO-66 (M = Co, Cu, and Cr) exhibit one to three orders of magnitude lower catalytic activities. Catalytic activity correlates linearly with the free adsorption energy of butene. Density functional theory calculations probing the Cossee-Arlman mechanism for all metals support differences in activity, providing a molecular level understanding of the metal site as the active center for 1-butene dimerization.

3.1 Motivation

Metal-organic frameworks (MOFs) are porous and crystalline materials built from inorganic metal nodes and organic linkers that have attracted growing attention in the last three decades.[92,93] These materials feature outstanding properties, such as exceptional porosity (up to 90% free volume and BET areas of 1000 – 7000 $m^2 \cdot g^{-1}$)[95,96] and accurate and versatile structure tunability on a molecular level.[97–101] Moreover, these porous materials can be used to design well-defined isolated single-atom or low-nuclearity metal sites for adsorption and catalysis.[139,212] Therefore, they find applications in a wide range of processes ranging from gas separation and storage,[105,213] chemical sensing,[214,215] (photo-)catalysis[216,217] to drug delivery.[218,219]

Among the variety of different MOFs, the Zr-based UiO-66 is one of the most promising candidates as a catalyst owing to its high thermal, chemical, and mechanical stability.[102–104] UiO-66 has been investigated as catalyst or catalyst support in a wide variety of catalytic reactions, such as esterification of carboxylic acids,[118,119] Diels-Alder condensation,[220] alkene (de-)hydrogenation[142,221], and methane oxidation.[192,222] It has been suggested that the exceptional stability results from the high degree of network connectivity, as each zirconium node (Zr_6O_8) is connected to 12 benzene-1,4-dicarboxylate (BDC) linkers in contrast to many other MOFs with 6- or 8-fold connected nodes.[105–107]

However, recent work has shown that this 12-fold connected framework of UiO-66 has a significant fraction of missing linkers.[105,108,109] These materials act as solid acids. In contrast, the defect-free UiO-66 does not feature acidic properties.[110] This change in properties has triggered a large number of investigations of the sites resulting from missing linkers, frequently dubbed as "defect sites".[105,110–114] A first investigation into the defect sites provided direct structural evidence for the defects by high-resolution neutron powder diffraction.[105] Numerous studies followed to characterize the type, concentration, and (de-)hydration degree of the sites[105,115,197] and their influence on the catalytic activity.[116–118] The degree of hydration determines whether these sites exhibit Brønsted or Lewis acidity, where the undercoordinated Zr^{4+} sites form the Lewis acid center.[107,110,119,120]

Lately, great efforts were made to introduce also other Lewis acids such as transition metal Ni^{2+} or Co^{2+} into MOFs to enable catalytic reactions like short alkene oligomerization. Herein we will examine the introduction of Ni, Co, Cu and Cr into UiO-66 and the adsorption and catalytic dimerization of 1-butene. *Bell et al.*[121], *Kaskel et al.*[122], *Dincă et al.*[123–125] have synthesized different Ni-based MOFs where Ni is part of the node structure and have reported high catalytic activities for light alkene (ethene or propene) oligomerization. Some of the reported activities exceed those of their homogeneous counterpart.[124] The catalytic metal sites can also be deposited on the surface of the MOF nodes through three types of post-synthetic modification, i.e., employing catalytic metalloligands, anchoring molecularly defined catalysts to the MOF pores[126–128], or grafting metal cations or clusters of metal cations within the MOF.[129–133]

Inserting isolated metal atoms has been of particular interest in alkene oligomerization, as mono-dispersed catalysts show interesting catalytic activity and are conceptually more straightforward to characterize.[124,128,134–136] The use of MOFs as support offers several advantages over other conventional substrates, such as deposition of high metal loadings with low aggregation,[132,137] while simultaneously featuring easy separation and good recyclability.[137–139] Additionally, the well-defined structure of the MOF allows detailed mechanistic studies of supported heterogeneous metal catalysts.[134]

In the case of alkene oligomerization, the dimerization pathway in a Ni-MOF is generally thought to follow the Cossee-Arlman reaction mechanism, in which the alkene coordinates to a nickel hydride species and is subsequently inserted to form an alkyl intermediate. A second alkene coordinates and is similarly inserted into the Ni-alkyl bond. The dimer desorbs upon β-H elimination and the active site is regenerated.[131,134,154,223,224] However, for butene dimerization, different Ni species in the environment of different pores lead to an ambiguity with respect to the nature of the active site and elementary steps in the mechanism.

Single metal sites have been introduced into MOFs by atomic layer deposition in MOFs[129,130,133] (AIM) or solvothermal deposition in MOFs.[140–144] Farha, Hupp and collaborators have explored Ni in MOFs installed by AIM for ethene dimerization with remarkable selectivities towards the dimerization products.[129,130] However, the exact molecular structure of the active Ni sites remained unknown.

Therefore, we carry out detailed structural characterization to provide atomic-scale insights for Ni, Co, Cu, and Cr installed into UiO-66 by a new solvothermal deposition technique together with a study of the evolution of this structure with increasing activation temperature.[207] Infrared (IR) spectra of adsorbed D_2O show the aqua ligand and the degree of hydration of the metal on the node, which strongly influences the adsorption of butene and catalytic activity in butene dimerization. These identified structures, as well as the measured adsorption properties of butene, i.e., the heat of adsorption, were also supported by density functional theory (DFT) calculations. It is shown experimentally and theoretically that the Ni-UiO-66 exhibits higher activity than the Co-, Cu-, or Cr-based UiO-66 catalysts for 1-butene dimerization.

3.2 Results and Discussion

3.2.1 Structure of parent-UiO-66

Thermogravimetric analysis (TGA) of the parent material (p-UiO-66) was used to quantify the concentrations of defect sites (DS) and missing linkers. The p-UiO-66 has one missing linker per six linkers that are counted for each node (**Figure 6.29**), as the node shares only one link to the next node and each node has twelve sites for linking to a node. This leads to an average of two defect sites per node. Elemental analysis (**Table 3.1**) showed remaining chlorine and nitrogen in the samples. The presence of chlorine is attributed to residues from the $ZrCl_4$ precursor[225] or residual HCl from washing after synthesis, while nitrogen is attributed to remaining molecules of the solvent dimethylformamide (DMF). Considering the remaining chlorine and DMF to block parts of the defect sites (based on the strong computed enthalpies for the binding of chlorine (ΔH = −98 kJ·mol^{-1}) and DMF (ΔH = −126 kJ·mol^{-1}) on the defect site (see **Figure 6.30** in **Section S1.3**), the investigated p-UiO-66 is estimated to have 0.78 $mol_{DS}{\cdot}mol_{node}^{-1}$ free defect sites (**Table 3.1**). The detailed calculations for the free defect sites and residues per node are given in the SI (**Table 6.9** in **Section 6.2.1**).

Table 3.1: Count of free defect sites in the p-UiO-66 after thermal treatment at 300 °C in flowing N_2.

	p-UiO-66
Defect sites / mol·mol_{node}^{-1}	2.0
Cl / mol·mol_{node}^{-1}	0.60
N / mol·mol_{node}^{-1}	0.62
Free Defect sites / mol·mol_{node}^{-1}	0.78

Subtracting the Cl and N contents from the total defect sites results in the free defect site concentration.

The presence of remaining water molecules on the nodes was investigated by IR spectroscopy using the H-O-H deformation band (1600-1650 cm^{-1}) as indicator of the presence of molecular water. The high concentration of aromatic rings in BDC linkers, however, leads to strong infrared absorption at 1300-1650 cm^{-1}, which prevents the direct use of this method. Therefore, the water molecules were exchanged for D_2O. While the IR spectra of the fully D-exchanged UiO-66 (activated at 250 °C for 1h, introduction of 10 mbar

D_2O for 15 min and evacuation of 30 min, spectra taken at 50 °C) indicated the full exchange by showing only OD stretching vibrations (2708 cm^{-1}), the D-O-D deformation vibration band (1200 cm^{-1}) was not observed. Thus, we conclude that molecularly adsorbed water was not present on p-UiO-66 (after activation **Figure 6.31**, SI). Previous work in our group using H_2O^{18} adsorption/desorption has shown the presence of only one hydroxyl species on the defect site after activation at 250 °C, corroborating the structure in **Figure 3.1** for the free defect sites on the node.

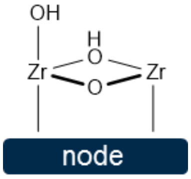

Figure 3.1: Structure of the defect site in UiO-66 upon activation at 250 °C.

Hydroxyl groups observable by IR spectroscopy after activation between 250-350 °C are compiled in **Figure 3.2**. Four bands were observed at 3683, 3673, 3647, and 3621 cm^{-1}. The band at 3673 cm^{-1} has been assigned to the vibration of the bridging μ_3-OH group.[108] The other three bands are hypothesized to originate from the terminal OH groups that interact with chlorine or by perturbation of the DMF solvent.[225] The intensity of the OH band decreased with increasing activation temperature from 250 to 350 °C. After 350 °C, the OH band at 3673 cm^{-1} disappeared thus indicating the removal of the hydroxyl groups. A DFT-based simulated IR spectrum (see **Figure 3.2**, spectrum in orange) obtained as a linear combination of different species hypothesized to be present in the defective UiO-66 sample, weighted by the amount of each type of species as tabulated in **Table 3.1** (for exact procedure see **Section 6.2.2** in SI), shows good agreement with the IR spectra (within 20 cm^{-1}) obtained experimentally. This good agreement allows to firmly attribute the stretching bands to the different functional groups of terminal -OH and μ_3-OH groups from the vacant defect (activated UiO-66), chlorine-containing defect sites (UiO-66-HCl), and DMF-containing defect sites (UiO-66-DMF).

The peak at 3673 cm^{-1} is attributed to the bridging μ_3-OH stretch of in the parent UiO-66. The terminal-OH stretch of the missing linker defect site occurs at 3704 cm^{-1}. The 3648 cm^{-1} band is attributed to the vibrations of the μ_3-OH groups in the defect plane of the vacant Zr defect site. The bands at 3632 and 3560 cm^{-1} correspond to the stretching bands of the terminal -OH and the μ3-OH bonded at the Cl-containing defect site (see **Section 6.2.2** of SI for the individual IR spectrum of each model and its corresponding assignments).

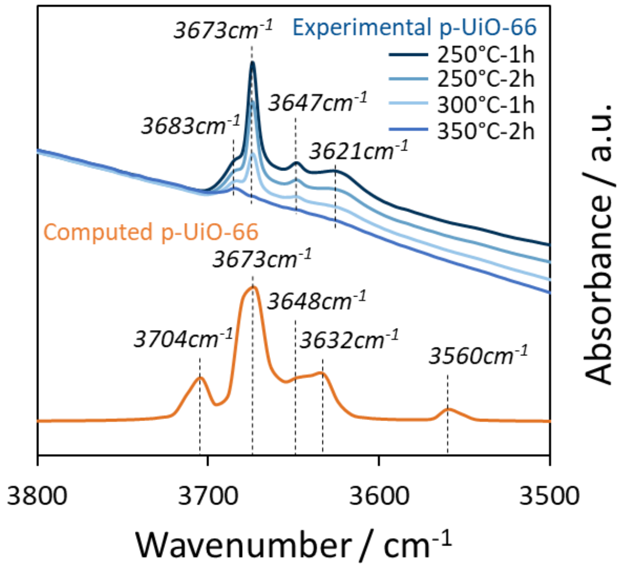

Figure 3.2: Experimental IR spectra of the p-UiO-66 after different activation procedures (blue graphs) and DFT-based simulated IR spectrum (orange graph).

The weight loss quantified by thermogravimetry (TG) at 350 °C indicates a composition of $Zr_6O_7BDC_5$ that is free of OH groups.[112] This is supported by the disappearance of the OH bands (3500-3700 cm^{-1}) after activation at 350 °C (**Figure 3.2**). After activation at 300 °C, both TG and IR spectra indicate a partially hydroxylated node suggesting a composition of $Zr_6O_6BDC_5(OH)_2$. Based on these results, we derive a detailed analysis of the hydroxylation of the p-UiO-66 node (**Figure 3.3**) after the increasing activation temperatures.

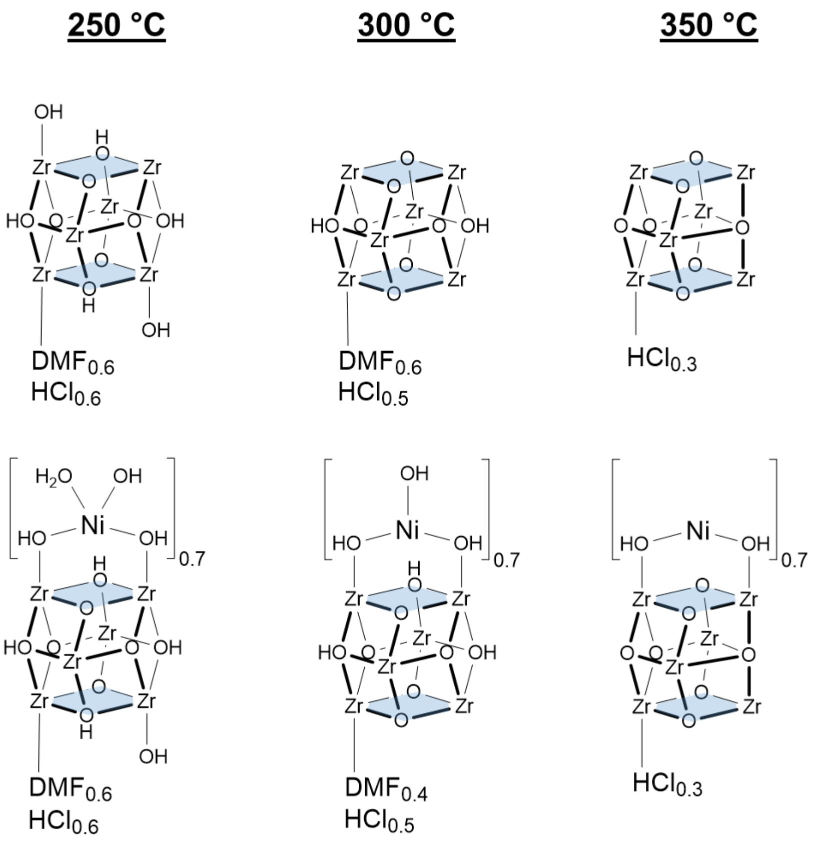

Figure 3.3: Proposed structures of the p-UiO-66 and the Ni-UiO-66 MOFs at different activation temperatures. Blue planes correspond to the defect sites, and white planes correspond to planes to which a BDC linker is connected.

3.2.2 Structure of Ni-UiO-66 and other M-UiO-66 (M = Co, Cu, Cr)

The environment of Ni and the other metals, Co, Cu and Cr, on the nodes of the M-UiO-66 will be discussed next. Elemental analysis showed the presence of Cl and N in concentrations similar to the p-UiO-66 (see **Table 6.10**, SI). At a loading of Ni of 2.5 wt.%, corresponding to 0.69 mol_{Ni} per node, it is presumed that single Ni^{2+} cations are attached at the free defect sites of p-UiO-66. The absence of Ni-Ni scattering in extended X-ray absorption fine structure spectroscopy (EXAFS) shows unequivocally the presence of single Ni^{2+} sites (**Figure 6.36**, SI).

IR spectroscopy and TG allowed to quantify molecularly sorbed water and hydroxyl groups on Ni and the node, respectively (see **Figure 3.4a**; similar analysis can be found for the other M-UiO-66 in section 2.3 of the SI). Assuming that after oxidative treatment at 700 °C only ZrO_2 and NiO are present (and setting the corresponding weight as 100%), the observed weight of 195% at 350 °C corresponded to a composition of $Zr_6O_7BDC_5Ni_{0.7}(OH)_{1.4}$. The IR spectrum after activation at 350 °C in **Figure 3.4b** shows a small band at 3673 cm^{-1}, attributed to Zr-OH groups. We hypothesize that these OH groups bridge between Zr and the Ni (**Figure 3.3**) and are required to balance the charge of Ni^{2+}. Thus, in contrast to p-UiO-66, OH groups are still present at 350 °C. Elemental analysis (EA) suggests that additionally 0.3 mol Cl are present per node (see **Table 6.10**, SI) after activation at 350 °C. This leads to a composition of $Zr_6O_7BDC_5Ni_{0.7}(OH)_{1.4}(H_2O)_{0.7}(HCl)_{0.3}$, corresponding to a weight of 196.5% compared to the oxidic core.

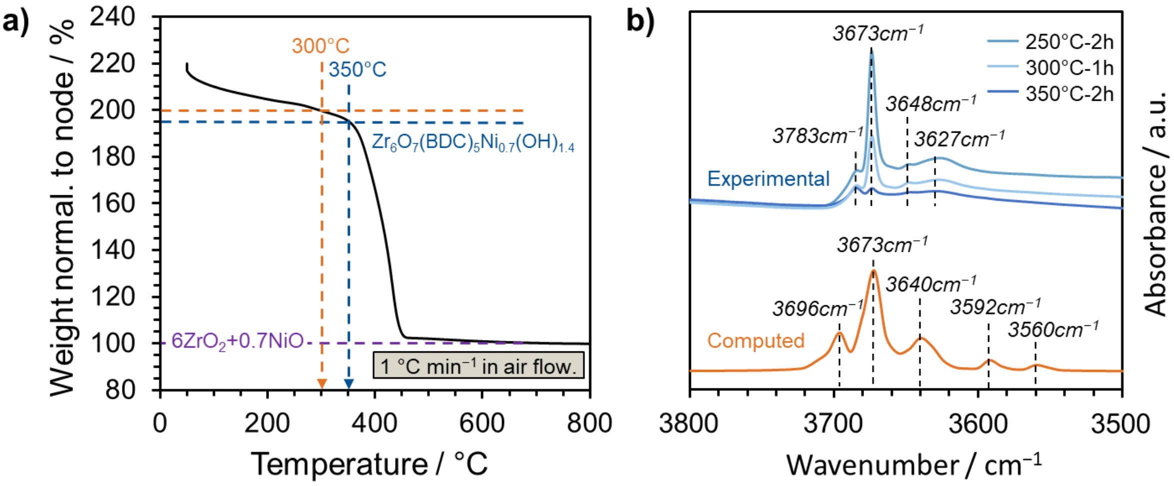

Figure 3.4: Determination of the 2.5%Ni-UiO-66 structure at different temperatures. a) TGA curve. The weight was normalized to the end weight. b) Experimental IR spectra of Ni-UiO-66 after different activation temperatures (blue graphs) and DFT-based simulated IR spectrum (orange graph).

A DFT-based cumulative IR spectrum (**Figure 3.4b**) was calculated using cluster models for the Ni-containing nodes, free defect sites, Cl-containing defect sites, and DMF-containing defect sites (see **Figure 3.3**) representing the node structure after activation at 300 °C. The ratio of these sites was determined *via* EA (see **Table 6.10**, SI) and used for the weights of the composite IR spectrum. The simulated IR spectrum (**Figure 3.4b**) shows good agreement with the experimental IR spectrum for 2.5%Ni-UiO-66 and corroborates the presence of hydroxyl groups by the peaks in the 3592-3696 cm^{-1} OH stretching region.

As the water concentration was challenging to be determined accurately by gravimetry, the IR spectra of D-exchanged Ni-UiO-66 was used to determine remaining hydroxyl and water ligands on the Ni. The H-D exchange of Ni-UiO-66 was performed following the same procedure as described above for p-UiO-66. All OH bands were converted to OD bands, confirming a complete exchange. As visible in **Figure 3.5**, the D-O-D vibration on the Ni (or NiO) at 1160 cm^{-1} [226,227] was present at low activation temperatures up to 250 °C. This indicates the presence of a remaining aqua ligand on the Ni (as depicted in **Figure 3.5**, bottom right). When activating at temperatures equal to or above 300 °C, the corresponding band disappeared, indicating the desorption of the aqua ligand. In addition, the Ni-OD vibrations[226,227] at 2454, 2474, 2678, and 2696 cm^{-1} diminished gradually in intensity with increasing temperature. As evidence for molecular water was not present after activation at 300 °C, we conclude that the desorption of water indicated by gravimetry stems from the combination of an OH group and a nearby proton (in **Figure 3.5**, middle right). TGA further implies that another water molecule desorbs upon activation at 350 °C. Therefore, we assume that the remaining Ni-OD vibration observed after activation at 350 °C is caused by bridging Ni-OD-Zr groups (**Figure 3.5**, top right). However, the remaining low intensity of the IR bands at 2680-2720 cm^{-1} does not allow to accurately determine the number of terminal OD groups that have desorbed.

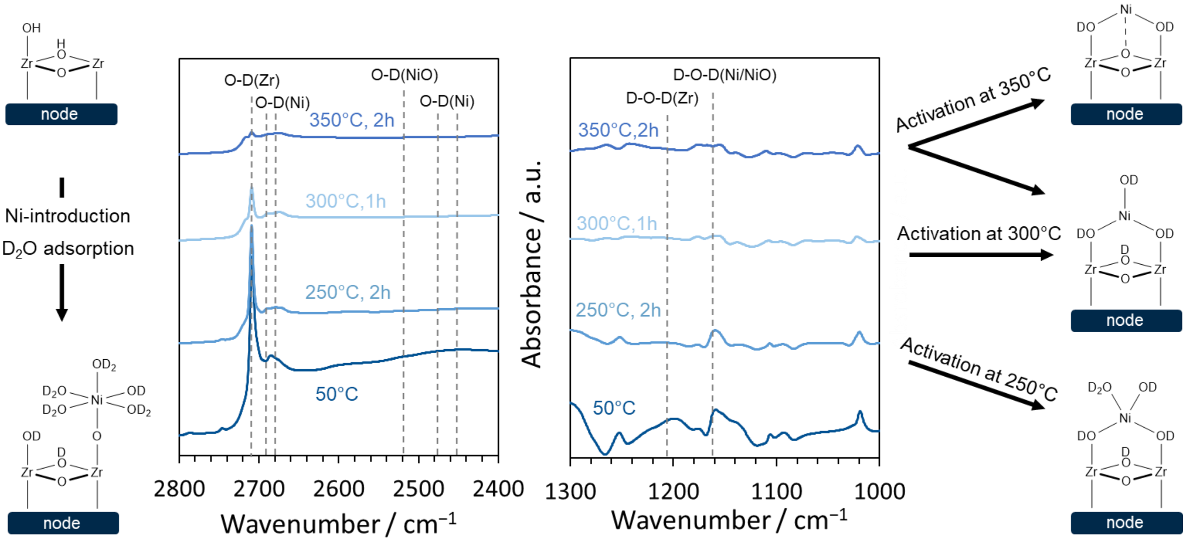

Figure 3.5: D_2O adsorption, followed by IR spectroscopy shows the O-D and D-O-D vibration on Ni^{2+}. This leads to the conclusion that the degree of hydration decreases with increasing activation temperature resulting in the indicated structures.

A similar analysis for Co-UiO-66 is described in the SI (**Figure 6.38**, SI), also demonstrating the elimination of aqua ligands after activation above 300 °C. In analogy with Ni-UiO-66 and Co-UiO-66, we expect only hydroxyl groups on the metals for Cu-UiO-66 and Cr-UiO-66, respectively. It should be noted in passing that the Cl and DMF concentrations in these materials are similar to those found for Ni-UiO-66. Thus, the $Co(OH)_3$-, $Cu(OH)_3$-, and $Cr(OH)_4$-Zr_6O_8 structures depicted in **Figure 3.6** for M-UiO-66 are concluded to prevail as the supported metal oxo complexes. TGA measurements suggest an earlier structure breakdown for Cu-UiO-66 and Cr-UiO-66 (occurring already at 350 °C, see **Figure 6.37b** and **c**, SI).

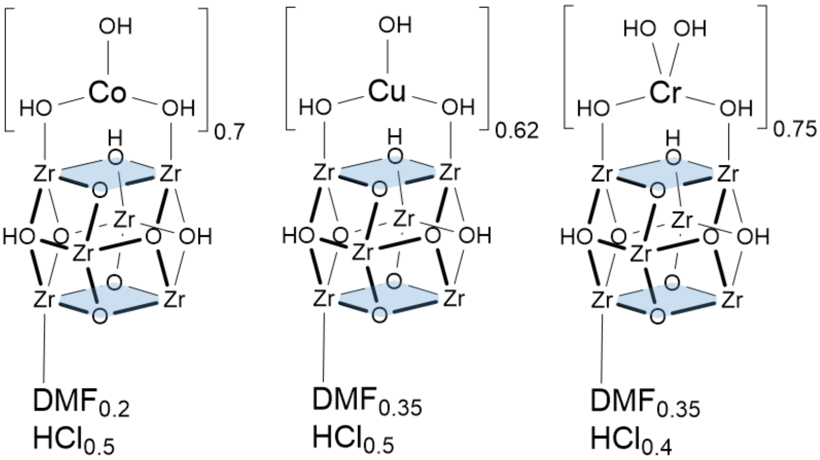

Figure 3.6: Proposed structures for M-UiO-66 (M = Co, Cu, Cr) upon activation at 300 °C.

3.2.3 Butene adsorption on p-UiO-66

Adsorption of 1-butene on the p-UiO-66 can be described by two Langmuir type isotherms (see **Figure 6.39**, SI) which shows the presence of strong and weak adsorption sites. The saturated uptake of 1-butene on the stronger site was calculated to be 0.8 $mol_{butene}·mol_{node}^{-1}$ with ΔH_{ads} of −46±1 $kJ·mol^{-1}$. The uptake at saturation level coincides with the concentration of free defect sites (0.78 $mol·mol_{node}^{-1}$). Thus, we conclude that free defect sites act as the strong binding sites for butene. The weaker site exhibits a 1-butene adsorption enthalpy ΔH_{ads} of −37±0.2 $kJ·mol^{-1}$, which is attributed to physisorbed butene in MOF pores.

DFT calculations for the 1-butene adsorption on the undercoordinated Zr of the free defect site (**Figure 3.1**) yield an adsorption enthalpy ΔH_{ads} of −48 $kJ·mol^{-1}$ in good agreement with the observed experimental values (see **Table 3.2**). The 1-butene molecule is adsorbed through asymmetric π-donation to the undercoordinated Zr center with its primary and secondary C atoms at distance of 2.84 Å and 3.24 Å respectively from Zr (**Figure 3.7**).

The effect of a pre-adsorbed butene on a neighboring free defect site on an adjacent node (adjacent free defect sites are formed, opposite of each other, upon removal of a BDC linker) was examined (see **Figure 6.42**, SI). Each 1-butene molecule is adsorbed through π-donation to the respective vacant Zr center on each adjacent free defect sites of the node. Computation of the adsorption enthalpies for the successive adsorption of a 1-butene molecule on these defect sites ($\Delta H_{\mathrm{ads},1} = -48\ \mathrm{kJ{\cdot}mol^{-1}}$ and $\Delta H_{\mathrm{ads},2} = -50\ \mathrm{kJ{\cdot}mol^{-1}}$) shows binding energies are similar with binding of the second butene benefitting from butene-butene interactions. Moreover, the computed adsorption enthalpies for the successive adsorption of the second 1-butene molecule on the same free defect site suggest that the second 1-butene molecule can be weakly adsorbed on the bridging μ_3-OH (**Figure 3.7**, B1, $\Delta H_{\mathrm{ads},2} = -29\ \mathrm{kJ{\cdot}mol^{-1}}$) or the terminal -OH groups (see **Figure 6.41**, B2, $\Delta H_{\mathrm{ads},2} = -19\ \mathrm{kJ{\cdot}mol^{-1}}$) of the free defect site (the first 1-butene molecule is adsorbed on the Zr center of this defect site). The 1-butene adsorption enthalpy ΔH_{ads} on the μ_3-OH group of the chlorine-containing defect site was computed to be $-25\ \mathrm{kJ{\cdot}mol^{-1}}$ (see **Figure 3.7**, C1) while that computed on the DMF-containing defect site (**Figure 3.7**, D1) is $-31\ \mathrm{kJ{\cdot}mol^{-1}}$. Similar 1-butene adsorption enthalpies were computed for 1-butene adsorption on the proton of the terminal hydroxyl groups of these respective defect sites (**Figure 6.41**, SI). Again, weaker adsorption enthalpies were computed for the successive adsorption of the second 1-butene molecule on the chlorine-containing defect sites (**Figure 6.41**, SI). Overall, this suggests that the bridging and terminal hydroxyl groups may correspond to the experimentally observed weak adsorption sites. An estimate of the mean enthalpy of 1-butene adsorption on the various hydroxyl groups, weighted by the experimentally known fractions of defect sites, was computed to be $-29\ \mathrm{kJ{\cdot}mol^{-1}}$, i.e., about $12\ \mathrm{kJ{\cdot}mol^{-1}}$ weaker than the experimental "weak" 1-butene adsorption. However, our IR and TGA analysis indicate that p-UiO-66 activation at 350 °C should result in complete removal of all hydroxyl groups from the node. Moreover, similar 1-butene adsorption enthalpies measured for the weak sites in p-UiO-66 activated at 300 °C as compared to the p-UiO-66 activated at 250 °C (see **Figure 6.39** and **Figure 6.40**, SI) suggest that the weak sites for adsorption were not completely lost upon activation. Therefore, we conclude that 1-butene physisorption in the pores of UiO-66 might also contribute to the weak site adsorption. The cluster models used for the DFT calculations are too small to capture physisorption within the pore and the long-range dispersion interactions of the periodic network that may also be present.

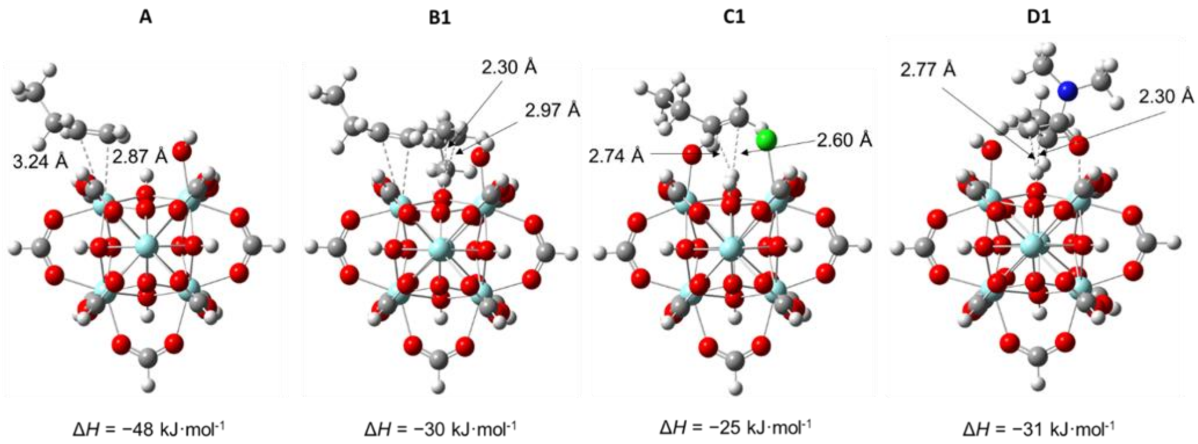

Figure 3.7: Adsorption of 1-butene on the (A) undercoordinated Zr Lewis acid center of the vacant defect site, (B1) the bridging μ_3-OH group of a free defect site with an adsorbed 1-butene, (C1) the bridging μ_3-OH group of a chlorine-containing defect site (UiO-66-Cl-dissociated), and (D1) the bridging μ_3-OH group of a DMF-containing defect site (UiO-66-DMF). The enthalpies and free energies of 1-butene adsorption at 40 °C are shown. The vacant defect site and isolated 1-butene molecule are chosen as the reference. Color code: Zr (cyan), Cl (green), O (red), N (blue), C (grey), H (white).

Table 3.2: Adsorption enthalpies for 1-butene on p-UiO-66 (activated at 250 °C) measured at 40 °C

Site in p-UiO-66 on which butene adsorbs	Computed ΔH_{ads} / kJ·mol^{-1}	Experimental ΔH_{ads} / kJ·mol^{-1}
Defect site – bare Zr (A)	−48	−46±1
Node – bridging OH (B1)	−30	
Node with Cl – bridging OH (C1)	−25	−37±1
Node with DMF – bridging OH (D1)	−31	

3.2.4 Butene adsorption on Ni-UiO-66 and other M-UiO-66 (M = Co, Cu, Cr)

The adsorption enthalpies of Ni-UiO-66, determined by isothermal calorimetry and thermogravimetric analysis after activation at different temperatures, are tabulated in **Table 3.3**. Nonlinear regression to the three-site Langmuir adsorption model (see **Figure 6.43**, **Figure 6.44**, **Figure 6.45**, SI) resulted in ΔH_{ads} of −54±3 kJ·mol^{-1} after activation at 250 °C, ΔH_{ads} of −66±6 kJ·mol^{-1} after activation at 300 °C, and ΔH_{ads} of −70±9 kJ·mol^{-1} after activation at 350 °C, respectively, for the Ni site. Similar to the experimental observations, the corresponding DFT-computed adsorption enthalpies on different Ni-UiO-66 models (**Figure 3.3**) increased from −49 kJ·mol^{-1} to −99 kJ·mol^{-1} for the cluster models corresponding to activation at 250 °C and 350 °C, respectively. Therefore, the uptake on the strong adsorption site observed experimentally is attributed to the Ni^{2+} on the UiO-66 node. The increasingly negative adsorption enthalpy with increasing activation temperature from 250 °C to 350 °C is attributed to the increasing under-coordination of the metal site upon removal of an aqua ligand and the generation of an undercoordinated Ni. The second site in this model corresponds to the free defect site on the parent site. Therefore, the number of butene molecules for this site was set to the number of remaining free defect sites (for exact calculations, see **Section 6.2.5**, SI) and the enthalpy was set to −46 kJ·mol^{-1} for consistency during the fitting process. Lastly, the experimentally observed weak site resembles the weak site in the p-UiO-66, based on which we propose that it again involves physisorption.

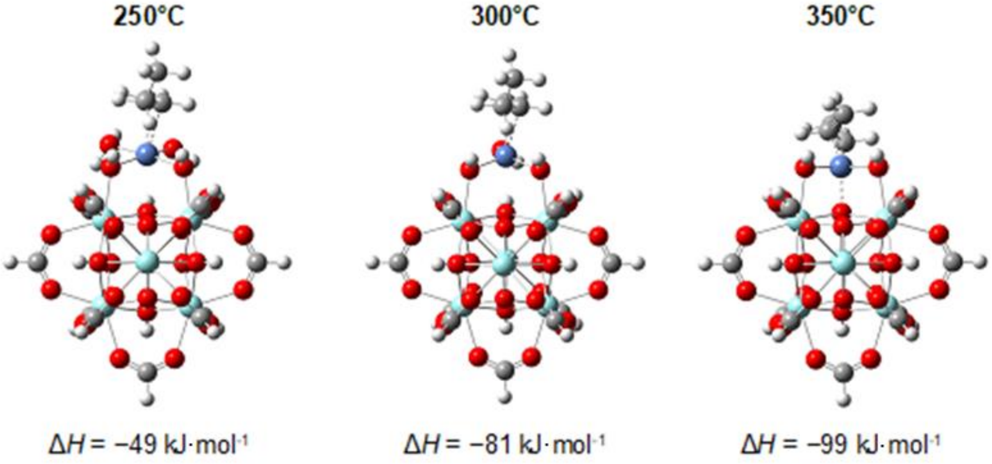

Figure 3.8: Adsorption of 1-butene on cluster models for Ni-UiO-66 activated at 250 °C, 300 °C, 350 °C. The standard enthalpies of 1-butene adsorption at 30 °C are shown. The respective Ni-UiO-66 model and isolated 1-butene molecule are chosen as the reference for all calculations. Color code: Zr (cyan), Ni (blue), O (red), C (grey), H (white).

Table 3.3: Adsorption enthalpies of 1-butene on the strong adsorption sites (attributed to the metal) in 2.5%Ni-UiO-66 after different activation temperatures measured at 40 °C. The computed values from the structures given in the following figure are opposed.

2.5% Ni-UiO-66 Activation temperature	**Computed ΔH_{ads} / kJ·mol^{-1}**	**Experimental ΔH_{ads} / kJ·mol^{-1}** Metal site
250 °C	−49	−54±3
300 °C	−81	−66±6
350 °C	−99	−86±9

The enthalpies for adsorption of butene on Co-, Cu- and Cr-UiO-66, determined from fitting butene adsorption isotherms to a Langmuir three-site adsorption model (i.e., for adsorption on accessible Zr and Ni cations and physisorption, see **Figure 6.46**, **Figure 6.47**, and **Figure 6.48**, in SI), are compared to the computed ΔH_{ads} in **Table 3.4**. The computed values are in satisfactory agreement with the experimental values (the mean absolute deviation is 13 kJ·mol^{-1} with an experimental uncertainty of about 5 kJ·mol^{-1}. Both, experiment and computation, indicate that the adsorption enthalpy is largest in magnitude for Ni-UiO-66. The experiments yield adsorption strength ordered as Ni > Cu > Cr > Co, whereas the computations yield Ni > Cu > Cr > Co. Furthermore, the experiments show that ΔH_{ads} of −49±7 kJ·mol^{-1} for Co-UiO-66 approaches the values for p-UiO-66. For the DFT calculations, ΔH_{ads} of −41 kJ·mol^{-1} for Cr-UiO-66 is weaker than on the bare Zr site of p-UiO-66.

Table 3.4: Adsorption of 1-butene on cluster models for M-UiO-66 (M = Ni, Co, Cu, Cr) activated at 300 °C. The standard enthalpies of 1-butene adsorption at 40 °C are shown.

M-UiO-66	**Computed ΔH_{ads} / kJ·mol^{-1}**	**Experimental ΔH_{ads} / kJ·mol^{-1}**
		Metal site
2.5%Ni-UiO-66	−81	−66±6
2.5%Co-UiO-66	−56	−49±7
2.5%Cu-UiO-66	−60	−59±4
2.5%Cr-UiO-66	−41	−55±2

3.2.5 Catalysis

The dimerization of 1-butene on Ni^{2+} produces primarily linear octenes as well as methylheptenes and dimethylhexenes (see **Scheme 3.1**). Ni-UiO-66 showed excellent catalytic activity for dimerization of butene with rates that were similar to ethene dimerization rates of a modified Ni-UiO-67 catalyst reported in literature.[224] The activation temperature strongly influenced the catalytic activity (**Figure 3.9**). The extrapolated initial activity resulted in TOFs of 2.9·10^{-3} mol$_{Butene}$·mol$_{Ni}$$^{-1}$·s^{-1}, 5.3·10^{-3} mol$_{Butene}$·mol$_{Ni}$$^{-1}$·s^{-1} and 5.9·10^{-3} mol$_{Butene}$·mol$_{Ni}$$^{-1}$·s^{-1} after activation at 250 °C, 300 °C and 350 °C, respectively. The low activity after activation at 250 °C indicates that the presence of hydroxyl and water ligands reduce the catalytic activity significantly, i.e., the presence of molecular water reduces the activity. The deactivation rate increased with increasing activation temperature. This deactivation is speculated to result from the loss of active sites due to site blocking, for example *via* isomerization of 1-butene leading to an accumulation in more branched products eventually leading to pore blocking.

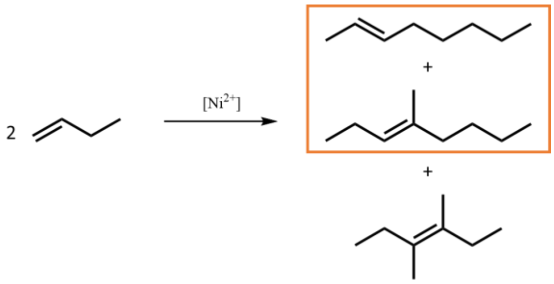

Scheme 3.1: Butene dimerization over a Ni^{2+} site reacts towards the desired dimerization products, n-octene and methylheptene, and the less desirable doubly branched product dimethylhexene.

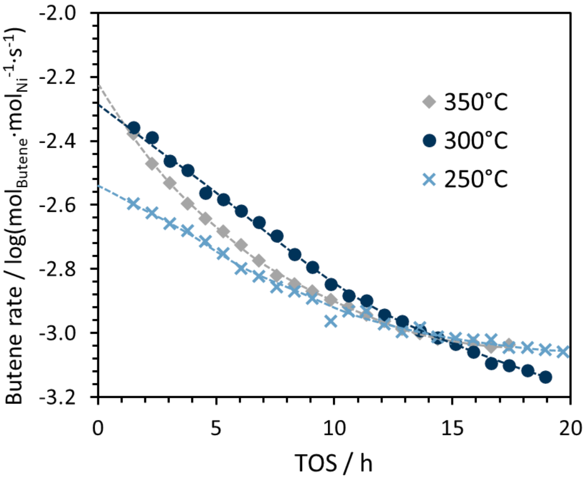

Figure 3.9: Conversion of 1-butene on the 2.5%Ni-UiO-66 at 50 bar, 250 °C and WHSV = 8.3 h^{-1} using catalyst materials activated at different temperatures (250 °C, 300 °C and 350 °C).

Figure 3.10 compares the 1-butene conversion on Ni-, Co-, Cu-, Cr- and the p-UiO-66. The Ni-UiO-66 shows the highest activity, with initial butene consumption rates of $5.3{\cdot}10^{-3}$ $mol_{C4,conv}{\cdot}mol_{Ni}^{-1}{\cdot}s^{-1}$ when extrapolated to zero time on stream (TOS). This rate is more than one order of magnitude higher than those for Co-UiO-66 and Cr-UiO-66 ($16.6{\cdot}10^{-5}$ $mol_{C4,conv.}{\cdot}mo_{Ni}^{-1}{\cdot}s^{-1}$ and $12.3{\cdot}10^{-5}$ $mol_{C4,conv.}$ ${\cdot}mol_{Ni}^{-1}{\cdot}s^{-1}$, respectively) and two to three orders of magnitude higher than those for Cu-UiO-66 and p-UiO-66

($4.7\cdot10^{-5}$ $mol_{C4,conv.}\cdot mol_{Ni}^{-1}\cdot s^{-1}$ and $0.6\cdot10^{-5}$ $mol_{C4,conv.}\cdot mol_{Ni}^{-1}\cdot s^{-1}$, respectively). Despite the activity difference, all catalysts showed high selectivity (>85%) towards n-octene and methylheptene (**Figure 6.49**, SI).

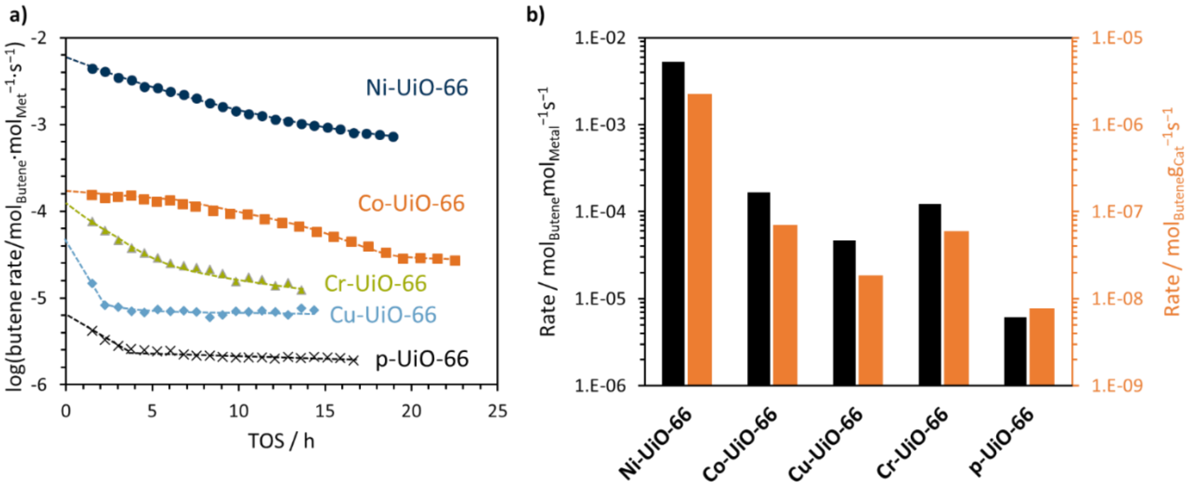

Figure 3.10: Performance in 1-butene dimerization of the p-UiO-66 and the M-UiO-66 (M = Ni, Co, Cu, Cr). Reaction conditions: 50 bar, 250 °C and WHSV = 8.3 h^{-1}, catalysts activated at 300 °C in N_2. a) Conversion of butene on the p-UiO-66 and the M-UiO-66 (M = Ni, Co, Cu, Cr) as a function of TOS. b) Extrapolated butene consumption rates for different catalysts.

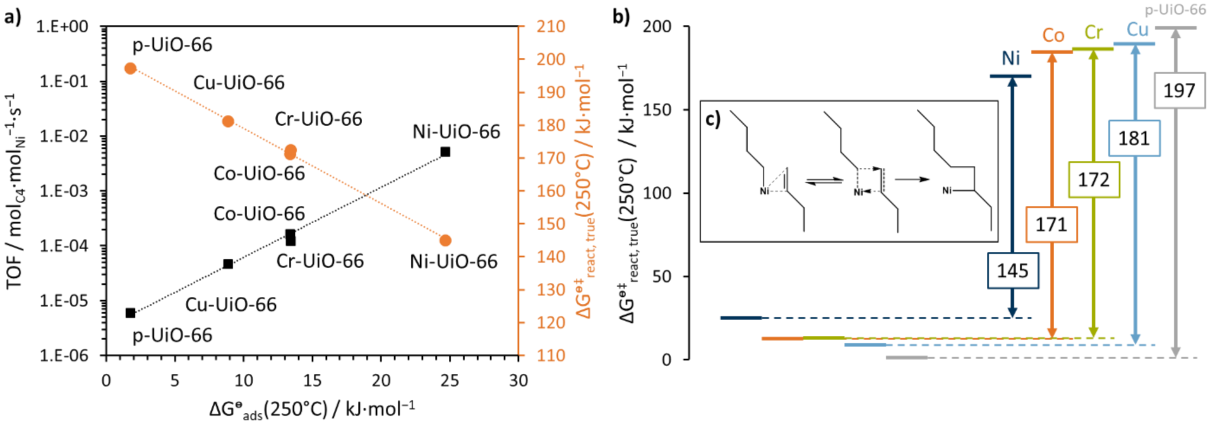

Figure 3.11: a) Correlation ($R^2 = 0.999$) of 1-butene consumption rates and true Gibbs free energies of activation with the extrapolated true free energies of 1-butene adsorption for the p-UiO-66 and the M-UiO-66 at reaction temperature. b) Free energy diagrams for the different catalysts. c) Transition state for C-C formation.

The Gibbs free energies of the adsorption were extrapolated from the measured ΔH_{ads} and adsorption constants K at 40 °C to the reaction temperature of 250 °C. As shown in **Figure 3.11a**, the logarithm of the turnover frequencies (TOFs) for the different materials for 1-butene dimerization correlate well with the Gibbs free energies of adsorption of 1-butene. Ni-UiO-66, being the most active catalyst, showed the highest Gibbs free energy of adsorption. Comparing the true Gibbs free energy of 1-butene activation, $\Delta G^{\circ\ddagger}$, (the reaction is first order in 1-butene) with the Gibbs free energies of 1-butene adsorption also shows a linear relationship (the calculations for all free energies are compiled in **Section 6.2.7** of the SI). The difference of nearly 36 kJ·mol^{-1} in $\Delta G^{\circ\ddagger}$ between Cu and Ni containing UiO-66 highlights the significant difference in catalytic activities (see **Figure 3.11b**). We speculate at present that the strong adsorption of the second 1-butene molecule weakens the metal-carbon bond to the first adsorbed butene, initiating the C-C formation. This facilitates the ′insertion′ of the second butene molecule in the M-C bond of the alkyl group (see **Figure 3.11c**). While we cannot rigorously rule out that the rate determining step is related with adsorption assisted desorption of the formed octene, DFT calculations suggest that the rate determining step is related to the C-C bond formation (at least for Ni and Co). Thus, for catalyst design it appears to be crucial to assure a strong π-bond of the alkene to the Lewis acidic metal cation to achieve high catalytic activity.

3.2.6 Catalysis pathway

The catalytic pathway for dimerization of 1-butene on the M-UiO-66 catalysts was investigated by DFT calculations on cluster models of the respective M-UiO-66 catalysts. The Cossee-Arlman mechanism (**Scheme 3.2**) has been widely established for Ni-based catalysts by theory and experiment.[21,131,134,157,170] Thus, we hypothesize it to be operative on all catalysts studied here.

The mechanism proceeds *via* the adsorption of 1-butene on a metal-hydride (intermediate A) to form intermediate B. The adsorbed 1-butene undergoes a hydride insertion into the metal-hydrogen bond to form the M-butyl intermediate C. This is followed by the adsorption of 1-butene to form intermediate D. The adsorbed 1-butene inserts into the metal-butyl species to form the metal-octyl intermediate E, which subsequently undergoes a β-hydride elimination step to form the adsorbed octene dimer (intermediate F). The 1-octene product desorbs to regenerate the active site and complete the catalytic cycle. This mechanism, however, requires the formation of a metal-hydride site. Previously in **Chapter 2**, we have shown the in-situ formation of the metal-hydride active site to occur on high-temperature activated catalysts starting from the metal-hydroxide (structure upon catalyst activation at 300 °C).

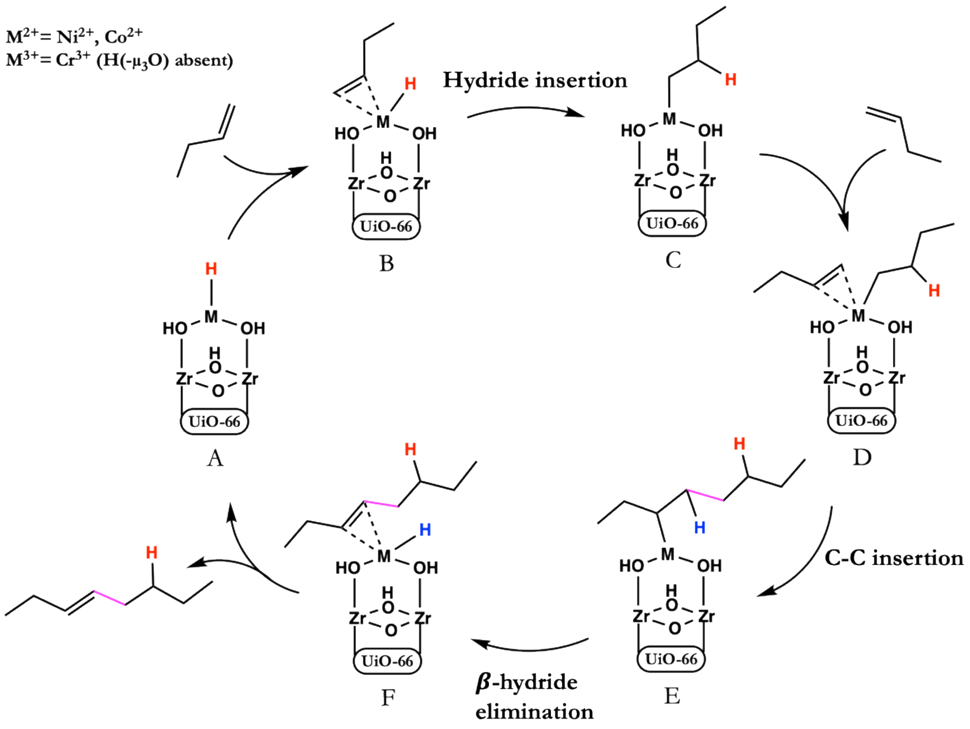

Scheme 3.2. The metal-hydride mediated Cossee-Arlman reaction mechanism investigated in M-UiO-66 catalysts.

The free energy diagrams for the formation of linear 3-octene dimer computed on cluster models of different M-UiO-66 (M = Ni^{2+}, Co^{2+}, Cu^{2+}, Cr^{3+}) catalysts at 250 °C are shown in Figure 3.12. The adsorption of butene is exergonic on low-spin Ni-UiO-66 (−5 kJ·mol^{-1}), while it is endergonic on high-spin Co-UiO-66, Cu-UiO-66, and Cr-UiO-66 catalysts (44 kJ·mol^{-1} to 60 kJ·mol^{-1}). In contrast to the other M-UiO-66 catalysts which exhibit lower hydride insertion free energy barriers ($\Delta G^{\circ\ddagger}$ = 14 kJ·mol^{-1} - 20 kJ·mol^{-1}), Co-UiO-66 and Cu-UiO-66 exhibit a larger hydride insertion free energy barrier ($\Delta G^{\circ\ddagger}$ = 54 kJ·mol^{-1} and 116 kJ·mol^{-1}, respectively). The intrinsic free energy barriers for C-C formation (for the coupling between butyl fragment and adsorbed butene) on the M-UiO-66 catalysts increase from $\Delta G^{\circ\ddagger}$ = 87 kJ·mol^{-1} on the Cr-UiO-66 catalyst to $\Delta G^{\circ\ddagger}$ = 167 kJ·mol^{-1} on the Cu-UiO-66 catalyst ($\Delta G^{\circ\ddagger}$ = 85 kJ·mol^{-1} and 114 kJ·mol^{-1} on Ni-UiO-66 and Co-UiO-66 catalysts, respectively). We note that the intrinsic activity of the M-UiO-66 catalysts for the C-C coupling step increases as the oxidation state of the catalytic metal increases from +1 (Cu-UiO-66) to +3 (Cr-UiO-66). The β-hydride elimination step for the formation of the octene dimer from the M-octyl intermediate occurs with a free energy barrier $\Delta G^{\circ\ddagger}$ = 57 kJ·mol^{-1} on the Ni-UiO-66 catalyst, 94 kJ·mol^{-1} on Co-UiO-66, 105 kJ·mol^{-1} on Cr-UiO-66, and 146 kJ·mol^{-1} on Cu-UiO-66. Note that while Cu was in +2 oxidation state in the precursor and in the activated catalyst, we hypothesize Cu^{2+} to auto-reduce under reaction conditions, as observed previously in zeolites,[228] following the lower computed free energy barriers for 1-butene dimerization on Cu^{2+}-UiO-66 as compared to Co-UiO-66 and Cr-UiO-66, thereby in contrast to its experimentally observed activity.

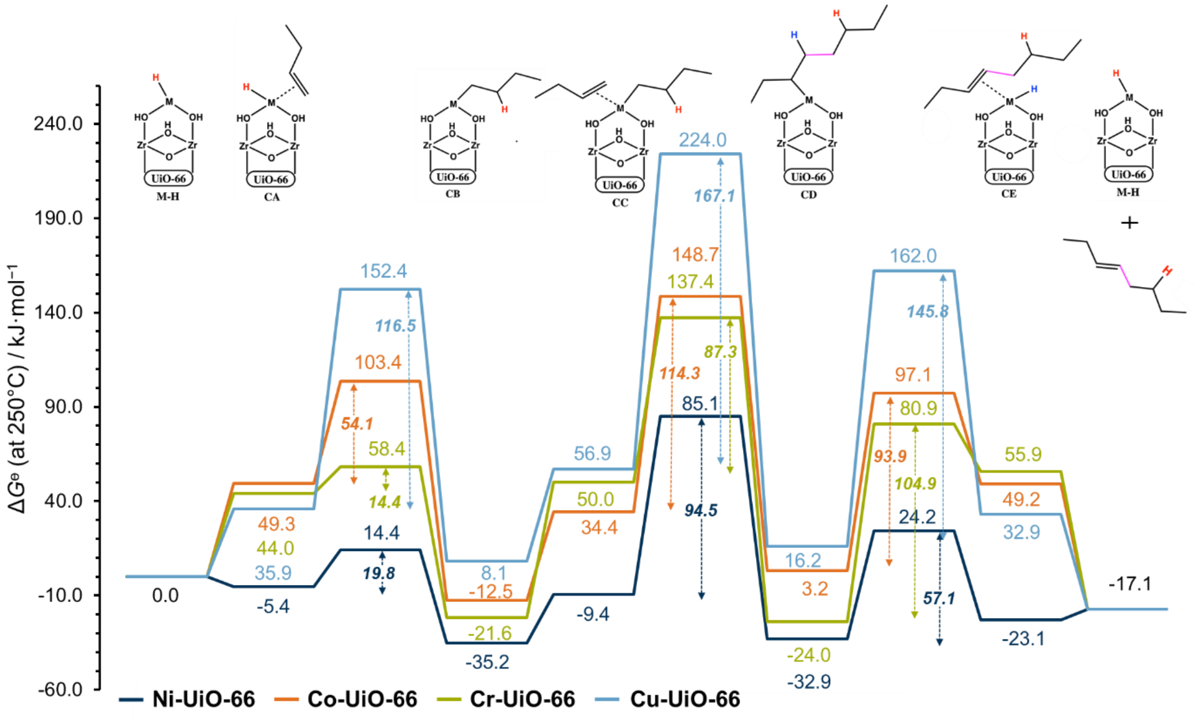

Figure 3.12: Standard free energy diagrams for the formation of linear oct-3-ene dimer on Ni-UiO-66 (magenta), Co-UiO-66 (red), Cr-UiO-66 (green), and Cu-UiO-66 (blue) catalysts at T = 250 °C and p = 1 bar.

Assuming the largest energy barrier as the rate-determining step, the C-C bond formation (alkyl insertion) is the rate-limiting step for the Ni-UiO-66 ($\Delta G^{\circ\ddagger}$ = 95 kJ·mol^{-1}), Co-UiO-66 ($\Delta G^{\circ\ddagger}$ = 114 kJ·mol^{-1}), and Cu-UiO-66 ($\Delta G^{\circ\ddagger}$ = 167 kJ·mol^{-1}) catalysts. In contrast, the β-hydride elimination step appears to be rate-limiting for Cr-UiO-66 ($\Delta G^{\circ\ddagger}$ = 105 kJ·mol^{-1}). Overall, the computed rate-limiting free energy barriers suggest Ni-UiO-66 catalyst to be the most active catalyst amongst those investigated and support the experimentally observed trend in activity: Ni > Co ≈ Cr > Cu.

Figure 3.13 shows the correlation of experimentally and theoretically determined $\Delta G^{\circ\ddagger}$ values. While the trend is the same, the exact ΔG° values differ (15 - 70 kJ·mol^{-1}). Uncertainties in the determination of the entropy contributions in theoretical predictions limiting the significance of the calculated $\Delta G^{\circ\ddagger}$ values could explain the differences between experiment and theory.

It should be mentioned that we assume the M-H active site to form in situ upon butene dimerization. However, the favorability of the formation of the M-H site across all the metals, specifically Cu, where theory predicts higher dimerization rates compared to Co and Cr, should be investigated in the future, as experiments suggest activity trends.

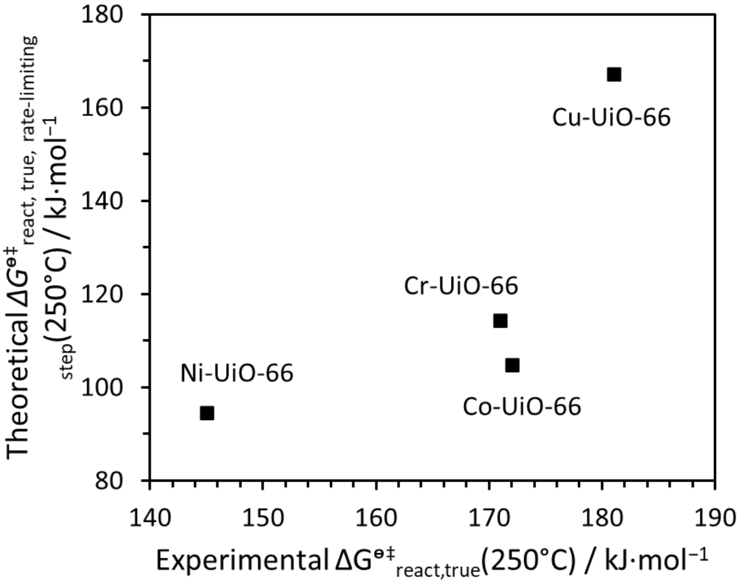

Figure 3.13: Correlation of computed 1-butene dimerization Gibbs free energy barriers of rate-limiting step (the step with the largest energy barrier) and true Gibbs free energies of activation determined from experiments.

The here presented combination of DFT calculations, adsorption and activity experiments suggest that the adsorption free energy of 1-butene on the M(OH)-UiO-66 catalysts is an important descriptor for designing active catalysts for 1-butene dimerization.

3.3 Conclusion

The present work shows that the two ´defect sites´ at the node of the p-UiO-66 can be grafted selectively with single metal cations of Ni, Co, Cu, and Cr. Molecular water and a hydroxyl group are associated with the metal cation after activation in flowing N_2 at 250 °C. IR spectra of these activated materials indicate additional Cl^- anions interacting with the hydroxyl groups.

The adsorbed water (ligand) desorbs at 300 °C, leading to a M-OH site. The absence of molecular water associated to the metal cation significantly increases the butene adsorption enthalpy. For Ni-UiO-66, differences between DFT calculations and the experimentally determined adsorption enthalpies suggest that mixtures of M-(H_2O)(OH) and M-OH sites may be present after activation at 300 °C. However, the good fit of the adsorption enthalpies of butene with the other samples suggest that with these samples water was fully desorbed after activation at 300 °C.

Ni-UiO-66 is by far the most active metal cation for 1-butene dimerization among the catalysts studied. The logarithm of the catalyzed rate of the reaction correlates linearly with the 1-butene adsorption enthalpies on the metal cations. We conclude that the higher adsorption strength of the second butene molecule weakens the metal-carbon bond of the alkyl species formed from adsorbed butene and the hydride residing on the activated metal cation. This in turn facilitates the formation of the C-C bond ("insertion of the second butene molecule") leading to the adsorbed octene. While we cannot fully exclude the role of an adsorption assisted desorption determining the rate of octene formation, we conclude on the basis of DFT calculations that this pathway is less likely, at least for the most active Ni-UiO-66.

The contribution shows a clear direction for future design of more complex dimerization catalysts, indicating that the most important parameter is the strength of interaction of butene with the metal cations catalyzing the dimerization.

3.4 Materials and Methods

3.4.1 Synthesis of the parent UiO-66 and M-UiO-66 (M = Ni, Co, Cu, Cr)

The synthesis of the parent UiO-66 MOF, as well as the procedure for producing the Ni-UiO-66 is described in **Section 2.4.1** and **2.4.2**. Co-UiO-66, Cu-UiO-66 and Cr-UiO-66 were produced *via* the exact same method.

3.4.2 Material characterization

The metal loading of the catalysts was determined by inductively coupled plasma-atomic emission spectroscopy (ICP-AES, Perkin Elmer 7300DV). Prior to the ICP-AES tests, the samples were digested in a mixture of HNO_3/HCl/HF/H_2O followed by H_3BO_3 addition for extra HF treatment. The organic composition of the material was analyzed based on the principle of spontaneous combustion and subsequent separation by gas chromatography of the evolving gases using an elemental analyzer (EuroEA 3000 Series, EuroVector CHNS-O). For the chlorine analysis, the material without prior treatment was weighed into a platinum boat and heated up to 1000 °C. The remainings of the sample were analyzed in terms of chlorine content *via* titration (904 Titrando; Metrohm; Tiamo 2.4).

The thermogravimetric analysis (TGA) to determine the concentration of missing BDC linkers was performed with a Mettler Toledo TGA. 10 mg of sample was loaded into the instrument and heated to 800 °C at a rate of 1 $°C·min^{-1}$ under a constant flow of 20 $mL·min^{-1}$ synthetic air.

Proton nuclear magnetic resonance (^1H NMR) spectroscopy was used to determine the residual DMF and/or formate species in the parent UiO-66. Typically, 20 mg of UiO-66 were digested in 1mL of 1 M NaOH solution in D_2O. The mixture was left to digest over a period of 24 hours. The organic portion of the MOF (linker, solvent, formate etc.) was dissolved, while the inorganic component sinks to the bottom in the form of ZrO_2. The 1H NMR of the organic part was recorded with a 400 MHz spectrometer. Each organic component was quantified by the integrated peak area of each portion.

The OH vibrations of the UiO-66 were analyzed *via* infrared spectroscopy (IR). The sample was pressed into self-supporting wafers of around 7 mg·cm^{-3} and activated at different temperatures (250-350 °C) under vacuum (p < 10^{-5} mbar). The spectra were recorded on a Vertex 70 spectrometer from Bruker Optics collecting 120 scans at 50 °C with a resolution of 4 cm^{-1}. The H-D exchange was performed by dosing 10 mbar of D_2O into the IR cell at temperatures between 50-350 °C (when no Zr-OH band at 3672 cm^{-1} could be observed) for 10 min followed by a subsequent vacuum treatment ($p < 10^{-5}$ mbar, 30min). The temperature as then cooled to 323K, at which the spectrum was taken.

Thermogravimetric analysis was carried on a microbalance in a Seteram TG-DSC 111 calorimeter connected to a high vacuum system. Prior to adsorption, about 25 mg of sample was pretreated at 250-350 °C for 1 h under vacuum ($p < 10^{-4}$ mbar), and then cooled to 40 °C. Afterwards, 1-butene was introduced into the system in small dosing steps from 0.1 to 500 mbar. The butene uptake was determined by the sample weight increase, and the released heat was monitored by the heat flux signal.

3.4.3 Computational details

DFT calculations were carried out using cluster models of the metal-oxo supported Zr_6O_8 nodes for UiO-66 and the Gaussian 16 software package.[229] The M06-L local density exchange-correlation functional[209] and a def2-SVP basis set for C, O, and H atoms and a def2-TZVPP basis set for the metal (Ni, Co, Cr, Cu, and Zr) atoms were used in all of the reported calculations.[210,211] The associated Stuttgart/Dresden (SDD) effective core potential[230] was employed for the core electrons in Zr. An ultrafine grid was employed for performing the numerical integrations. Vibrational frequencies were computed at the optimized geometries to calculate the enthalpic and entropic contributions to the Gibbs free energy and to determine the nature of the stationary point. The intermediates were checked to have only real vibrational frequencies while the transition states had only one imaginary vibrational frequency. Vibrational frequencies below 50 cm^{-1} were corrected to 50 cm^{-1} while computing free energies to account for anharmonicity. Multiple spin states were examined for all metals to determine the spin of the ground state structure. The computed frequencies were scaled by a factor of 0.956 to determine the IR spectrum for the different cluster models studied.[231] A cumulative IR spectrum representing the synthesized parent UiO-66 sample was obtained by weighting the IR spectrum for the proposed activated UiO-66 model, the UiO-66-HCl-dissociated model, and the UiO-66-DMF model with the corresponding number of free defect sites, Cl-containing sites, and DMF containing sites obtained experimentally from the ICP analysis. Similarly, a cumulative IR spectrum for the Ni-UiO-66 sample was obtained by weighting the IR spectra calculated using cluster models for different species present in the metalated sample with the number of corresponding sites determined experimentally.

Cluster models, with a single metal oxo complex bound to a Zr_6O_8 node of UiO-66, representing mono-nuclear, single-site, isolated catalysts were extracted from previously optimized periodic structures of UiO-66. The benzoate linkers of the MOF were replaced by formate linkers to reduce the cluster size for computations. The positions of the C atoms of the formate linkers were held fixed during all optimizations to mimic the structural constraints imposed by the periodic MOF structure. One of the formate linkers, coordinated to the Zr6O8 node of UiO-66, was replaced by -OH and -H2O ligands to represent the missing linker defect while maintaining overall charge neutrality of the cluster model.[232]

3.4.4 Catalytic testing

The catalytic tests were performed according to the procedures described in **Section 2.4.5**.

4 Impact of zeolite properties on the activity of single Ni cations for selective butene dimerization

This chapter is based on unpublished results. The project is a joint effort of Abelina Ellert, Mengjie Zhou, Dr. Ricardo Bermejo-Deval, Dr. Rachit Khare, Prof. Maricruz Sanchez-Sanchez, Prof. Johannes A. Lercher and me. I led the project and performed most of the catalyst characterization, catalytic experiments as well as kinetic studies.

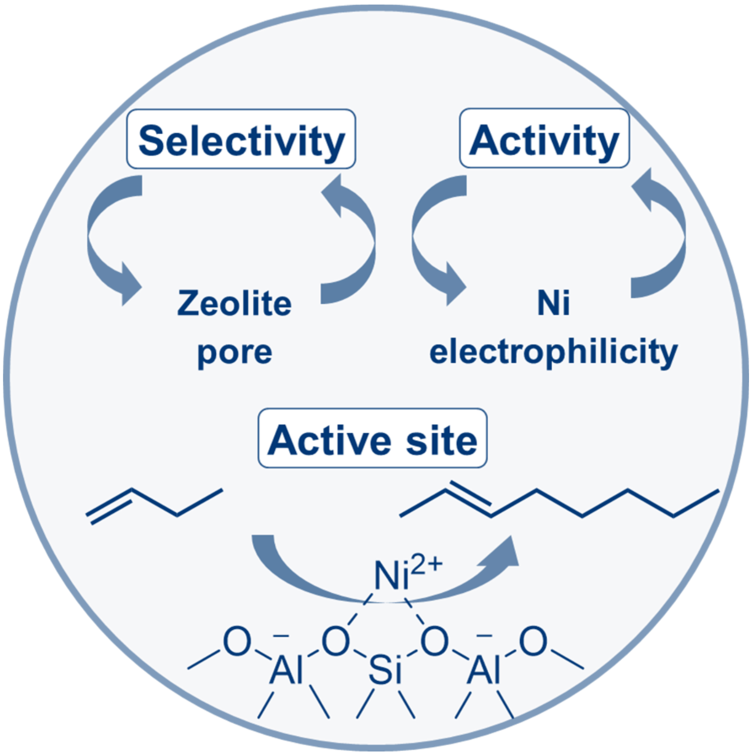

Dimerization of 1-butene is a well-known upgrading process to linear olefins and presents a typical example of C-C bond formation reactions. The industrially applied Ni catalysts supported by amorphous aluminosilicates are highly active but suffer from low selectivity to the linear dimers and rapid deactivation. The presence of Brønsted acid sites and numerous Ni species lead to an ambiguity with respect to the nature of the active site and the elementary steps in the dimerization mechanism. The defined pore architecture of zeolites promises to stabilize the Ni species for a larger homogeneity of the active site and to introduce shape selectivity to the reaction.

CO adsorption in combination with XAFS measurements presents an attractive technique to analyze the active Ni species. Comparing different zeolite constraints that feature the active single Ni^{2+} cation as the dominant Ni species reveals shape selectivity for zeolites with small pores. X-ray photoelectron spectroscopy determines Ni acidity as the main parameter affecting dimerization activity. This work presents, therefore, a precise study of the active Ni site and offers different possibilities in tuning dimerization activity and selectivity.

4.1 Introduction

The formation of new C-C bonds during alkene dimerization is an attractive method to upgrade n-butenes from naphtha cracking (steam and fluid catalytic) into highly valuable C8 hydrocarbons.[6,8] Branched dimer products, such as dimethylhexenes, are essential intermediates to produce gasoline additives. On the other hand, the linear dimers are used as solvents, lubricants, or co-monomers in the production of linear low-density polyethylene. Additionally, they are converted upon hydroformylation and hydrogenation into phthalic esters and further utilized as reactants for plasticizers.[3,11]

Nickel based materials have been described as the most promising catalysts because they exhibit high dimerization activity and outstanding selectivity towards linear dimers[61,69] and have been applied commercially in the homogeneous Dimersol process by the *Institut Français du Pétrole*[7] and the heterogeneous OCTOL process by *Evonik Industries*.[6] The heterogeneous process uses a bifunctional NiO catalyst supported on amorphous aluminosilicate (ASA) at 70-120 °C and 25-35 bar and offers the advantages of easy catalyst separation.[6,34] Remaining Brønsted acid sites (BAS) on the ASA support are detrimental for the linear dimer selectivity.[45] They catalyze branched dimer formation and other side reactions, e.g., skeletal and internal isomerization and cracking, all of them leading to a product composition that exclude linear dimers.[14,15,17] Additionally, these side reactions on BAS produce large hydrocarbons and coke, which causes pore blockage and promote, therefore, fast deactivation.[21]

Many different supports besides amorphous ASA have been tested in alkene dimerization and have shown strong influences on the activity, selectivity, and deactivation behavior of the Ni catalyst.[29] The choice of support is crucial to stabilize the active site during activation[60,67] or reaction.[44] *Mlinar et al.* have shown that an increased space around the active Ni cations in mesoporous aluminosilicates induces higher propene dimerization rates.[62,159] In addition, the pore and channel structure of the support have been reported to influence the product distribution of butene dimerization towards linear products.[64] The ordered micro- and mesoporous channel systems of zeolites make them, therefore, a suitable support to investigate the influence of the Ni environment on activity and selectivity in dimerization. In our previous work, we demonstrated that the Ni-LTA catalyzes butene dimerization at 50 bar and 160 °C and maintains exceptionally high linear product selectivities of 35-55% at up to 35% conversion, which increases those selectivities reported for ASA.[61,174]

Different active sites have been proposed in solid Ni-based catalysts ranging from Ni-hydride species in Ni-BEA,[21,49] single Ni^{2+} cations in different Ni-zeolites[60,61,174] and Ni^{+} ions in Ni-FAU[46,56,57] to $[Ni^{II}OH]^{+}$ in Al-MCM-41[2,68] and NiOH with a Ni^{+}/Ni^{2+} redox shuttle mechanism on ASA[44,69]. In some proposals, H^{+} from BAS are suggested to participate in the mechanism.[44,71,72] The ambiguity with respect for the nature of the active site and the influence of its chemical environment prevent a deeper understanding of the dimerization reaction mechanism.

This work, therefore, focuses on the identification of the active Ni sites in three different Ni-exchanged zeolites. We have studied CHA, MFI, and FAU, with different pore sizes and interconnectivities to determine the influence of spatial constraints and local environment on the activity and selectivity of Ni sites in butene dimerization. Similar Si/Al ratios of ~15 ensure similar acidities.

4.2 Results and discussion

4.2.1 Nature of active sites in butene dimerization in Ni-exchanged zeolites

First, we have studied butene dimerization of Ni exchanged in small-pore zeolite CHA. Two CHA zeolites with similar Al content (Si/Al = 11) but different Al pair concentrations were synthesized according to a modified recipe from literature (for exact procedure, see **Section 4.4.1**). The synthesis resulted in CHAs with 50% (280 μmol·g^{-1}) and 95% (690 μmol·g^{-1}) Al pairs. A third commercial CHA material was purchased (Si/Al = 15) and contains 30% (150 μmol·g^{-1}) paired Al. For the Ni ion exchange, the CHA zeolites were used in their Na-form to minimize the presence of BAS (see **Figure 6.52c**, **Figure 6.53c**, and **Figure 6.54c**, SI). Different Ni loadings were then introduced *via* ion exchange to each of the three CHA.

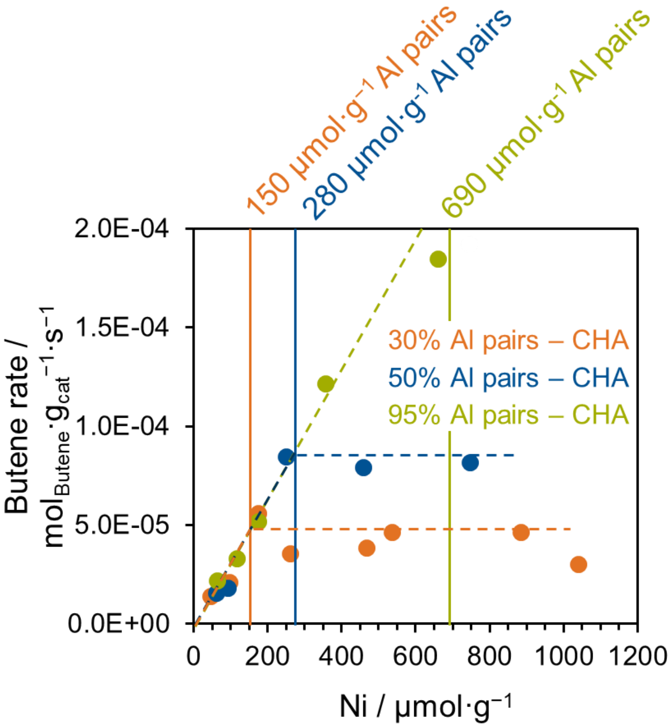

Figure 4.1: Butene consumption rates of Ni-Na-CHA samples with different Al pair concentrations and Ni loadings (T = 160 °C, p = 50 bar, WHSV = 50-500 h^{-1}, rates at differential conversion: 5%<X<10%).

These Ni-Na-CHA catalysts were tested in butene dimerization, and the reaction rates at differential conversions are shown in **Figure 4.1**. The butene consumption rate per gram increases linearly with Ni loading until the Ni concentration reaches the Al pair concentration for all three CHA. Once this Ni loading is exceeded, the rates level off. These results indicate that the activity is associated with single Ni^{2+} cations exchanged on Al pairs.

The influence of different Ni loadings on the dimerization activity was also investigated when exchanging Ni in a medium-pore size MFI (Si/Al = 15, 270 μmol·g⁻¹ Al pairs). The samples were first exchanged with Na to minimize the presence of BAS before introducing Ni. The Brønsted and Lewis acidity of the resulting Ni-Na-MFI samples were determined by pyridine adsorption and are listed in **Table 6.12**. It should be noted that despite using the Na-form, most of the samples show low concentrations of remaining BAS. Complete removal of BAS was found to be very difficult, even though a Ni-Na-co-exchange was applied. We observed that the introduction of Ni using $Ni(OAc)_2$ was usually accompanied by the reinstallation of small concentrations of BAS.

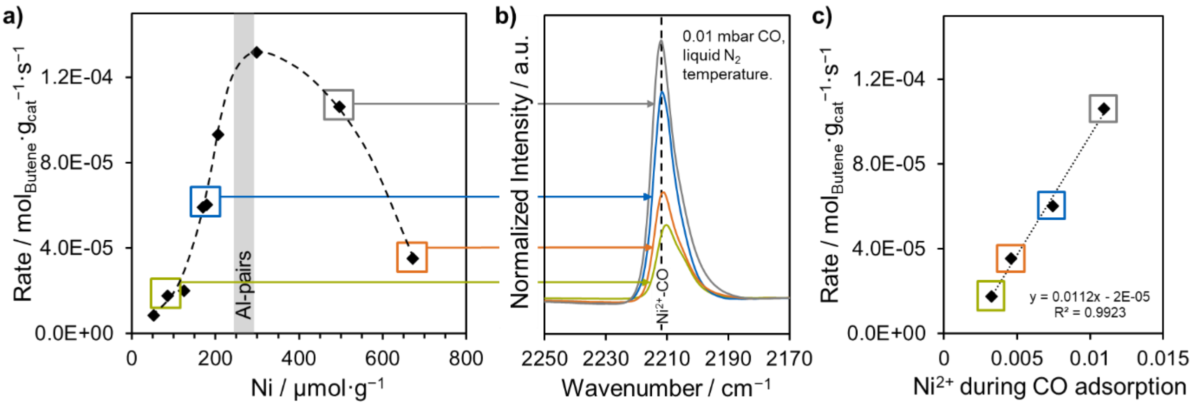

Figure 4.2: a) Butene rates for Ni-Na-MFI samples (T = 160 °C, p = 50 bar, WHSV = 50-500 h⁻¹, rates at differential conversion: 5%<X<10%), b) IR region of Ni^{2+}-CO vibration during CO adsorption (0.01 mbar CO), and c) the correlation of the two.

The butene consumption rates per gram of the Ni-Na-MFI samples increase with Ni concentration up to a Ni loading of ~300 μmol·g⁻¹ (**Figure 4.2a**). The sample with the highest activity features a Ni loading corresponding to the exchange of Ni^{2+} for the total concentration of Al pairs. This implies that the activity is associated with single Ni cations on Al pairs, which agrees well with the observations in CHA (**Figure 4.1**). Conversely, once the Ni loading has surpassed the concentration of Al pairs, the activity per gram of Ni-Na-MFI catalysts does not level off but decreases with increasing Ni loading. We examined the nature and location of Ni species exchanged in different Ni-MFI samples by CO adsorption at liquid nitrogen temperature using infrared spectroscopy (IR) to understand this effect. Full spectra can be found in the SI, **Figure 6.55**. The main vibration band for adsorbed CO is detected at 2212 cm^{-1}, which is attributed to the Ni^{2+}-monocarbonyl species adsorbed on isolated Ni^{2+} sites exchanged in zeolites (**Figure 4.2b**).[66,233,234] The shoulder at 2204 cm^{-1} has been described to stem from a Ni^{2+}-dicarbonyl species.[233] When increasing the CO pressure from $1\cdot10^{-2}$ to $5\cdot10^{-2}$ mbar, additional carbonyl species associated with Ni^{+}, Ni^{0}, Na^{+}, and BAS were observed (see **Figure 6.56**, SI). The band at 2179 cm^{-1} is assigned to CO interacting with Na cations or BAS,[66,233,235,236] as this feature also appeared in the spectrum for the CO adsorption on the parent H-MFI (SI, **Figure 6.57**). In addition, a shoulder at 2194 cm^{-1} arises for the two MFI samples with high Ni content (*496Ni116BAS*-MFI and *671Ni60BA*S-MFI), which is attributed to Ni^{2+} grafted onto a surface[237] or Ni^{2+} of NiO-nanoparticles.[66] This implies the formation of Ni clusters for the samples with Ni loading above the saturation limit of paired Al sites. It should be noted that at CO pressures above $5\cdot10^{-2}$ mbar, bands corresponding to Ni^{+}-monocarbonyl (2111 cm^{-1}), Ni^{+}-dicarbonyl, and Ni^{0} polycarbonyls species (2130 cm^{-1}) appeared.[66,234,238] The amount of these reduced Ni species, however, are similar in all samples and only appears when CO pressures are relatively high. Therefore, we attribute the formation of Ni^{+} and Ni^{0} to the CO-IR reducing conditions and conclude that the observed CO absorption band at 2212 cm^{-1} in the low-pressure range points to only Ni^{2+} species present in the Ni-Na-MFI samples.

We analyzed, therefore, the dependency of the catalyst activity of Ni-Na-MFI samples with this Ni^{2+} species by the integral of the Ni^{2+}-CO vibration band at 2212 cm^{-1} at low CO pressures (0.01 mbar). We chose this pressure as contributions from other cations, as discussed above, arose only at higher pressures. The contribution of the Ni-dicarbonyl species, however, was excluded by peak deconvolution. Details can be found in the SI (**Section 6.3.3**, **Figure 6.58** and **Table 6.14**). The linear correlation of the butene rates with the Ni^{2+} cation concentration (**Figure 4.3c**) provides evidence of Ni^{2+} cations functioning as the active species in butene dimerization.

The butene rate per gram in the MFI decreases at Ni loadings that exceed the paired Al concentration (**Figure 4.2**), while it remained constant in the Ni-CHA series past this concentration (**Figure 4.1**). We speculate that the cause for the activity decrease in Ni-MFI catalysts is the formation of inactive, positively charged Ni_xO_y nanoclusters exchanged on paired Al sites at high Ni loadings. These clusters would form at the expense of the previously exchanged single Ni^{2+} cations, decreasing the overall number of active sites and the rates per gram. In contrast, the constant rate per gram in CHA materials at Ni loadings is higher than the paired Al concentrations attributed to the precipitation of neutral NiO_x particles, probably on the external crystal surface, without affecting the concentration of single Ni^{2+} cations within the zeolite micropores.

Finally, the dependency of butene consumption rates on the Ni loading was additionally studied in a large-pore zeolite FAU (Si/Al = 15, 310 μmol·g^{-1} Al pairs). The Ni, Na, BAS, and LAS concentration are listed in **Table 6.15** for the Ni-Na-FAU. In contrast to the small- and medium-pore sized zeolites CHA and MFI, the activity per gram in FAU remains approximately constant with Ni loading in the range of 50-600 μmol$_{Ni}$·g^{-1} (see SI, **Figure 6.60**). This indicates that the activity per Ni or turnover frequency (TOF) decreases with increasing Ni loadings in FAU (see **Figure 4.3a**, black triangles). On the other hand, it should also be noted that the TOF reached in FAU at low Ni loadings is 1.5 orders of magnitude higher than in CHA and MFI. This difference in TOF will be discussed later in detail.

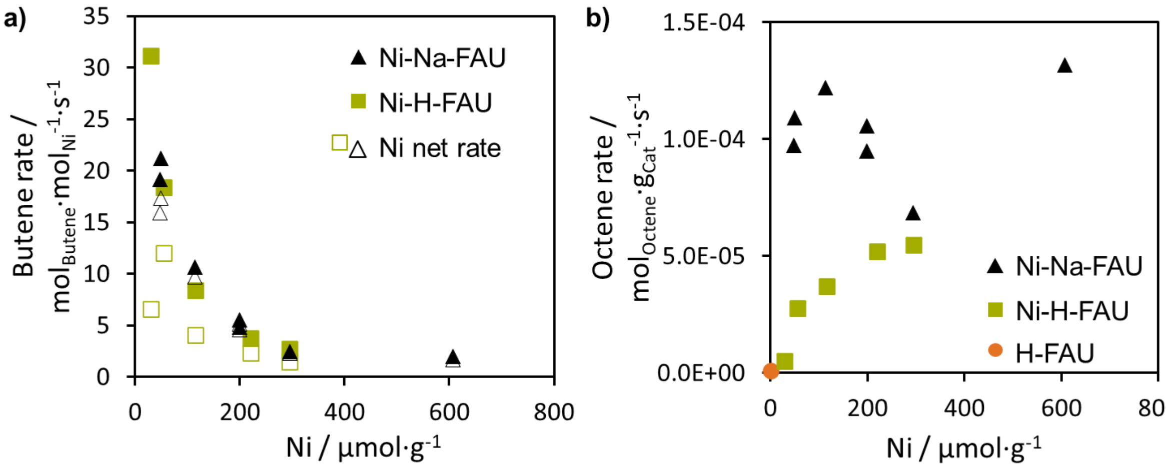

Figure 4.3: a) TOF and corrected TOF, as well as b) octene rates for Ni-Na-FAU in comparison to Ni-H-FAU samples (*T* = 160 °C, *p* = 50 bar, WHSV = 50-500 h^{-1}).

As observed from **Figure 4.3a**, the TOFs of a Ni-H-FAU series are nearly identical to those of the Ni-Na-FAU samples. Overall, a synergetic effect of having BAS and Ni in the materials can be ruled out (see **Figure 6.68**, SI). However, BAS activity in dimerization also contributes to the overall reaction rates, as can be inferred from the higher selectivities to branched dimers in the presence of BAS. Therefore, to establish a comparison between the Ni-H-FAU and Ni-Na-FAU materials, it is necessary to determine first the net contribution of Ni ions to the activity. For this purpose, we tested the activity of H-FAU in butene dimerization under the same conditions and obtained a TOF for BAS of 1.7 $\mathrm{mol_{Butene}{\cdot}mol_{BAS}^{-1}{\cdot}s^{-1}}$. With this value, the TOF per Ni can be corrected by subtracting the BAS contribution following **Equation 4.1**.

$$r_{\mathrm{net}}[\mathrm{mol}_{C4}{\cdot}mol_{Ni}^{-1}{\cdot}s^{-1}]=\frac{r[\mathrm{mol}_{C4}{\cdot}g_{Cat}^{-1}{\cdot}s^{-1}]\text{-}c_{\mathrm{BAS}}[\mathrm{mol}_{BAS}{\cdot}g^{-1}]{\cdot}r_{\mathrm{BAS}}[\mathrm{mol}_{C4}{\cdot}mol_{BAS}^{-1}{\cdot}s^{-1}]}{c_{Ni}[\mathrm{mol}_{Ni}{\cdot}g_{Cat}^{-1}]} \qquad \textbf{(Eq. 4.1)}$$

These net rates differ significantly in the presence and absence of Na^+ (**Figure 4.3a**, hollow symbols). While the TOF decreases exponentially for the Ni-Na-FAU with increasing Ni loading, the TOF of Ni-H-FAU reaches a maximum at Ni loadings of 50 $\mu mol{\cdot}g^{-1}$ and then decreases exponentially with higher loadings.

The Ni-Na-FAU catalysts with unusually high TOF were studied using X-ray absorption spectroscopy to determine the local coordination structure of the highly active Ni sites. **Figure 4.4b** shows the k^2-weighted phase-uncorrected Fourier-transformed extended X-ray absorption fine structure (FT-EXAFS) of Ni-Na-FAU samples. The FT-EXAFS for all Ni-Na-FAU samples features a signal at ~1.5-1.6 Å that corresponds to Ni-O interactions.[239] Ni-Na-FAU samples with Ni loadings ≥200 $\mu mol{\cdot}g^{-1}$ also show an intense signal for a second coordination shell that appears at ~2.7 Å (see **Figure 4.4**). This feature can be attributed to either Ni-Ni coordination in bulk NiO or NiOH or to Ni-Si coordination in the Ni^{2+} cations located in the S_I position in FAU (see **Figure 4.5**).[239]

The sample with the highest Ni activity, i.e., Ni-Na-FAU with the lowest Ni content (50 $\mu mol{\cdot}g^{-1}$) does not feature the signal for Ni-Ni interactions ~2.7 Å. This implies that this sample does not contain any bulk NiO or NiOH particles. The Ni-O coordination number of approximately 4.2 suggests that the Ni^{2+} cations in this sample are predominantly located in the S_{II} site in FAU (see **Figure 4.5**) and that these single Ni^{2+} cations are active for butene dimerization while those Ni^{2+} species incorporated in bulk NiO particles or present in the S_I sites are inactive.

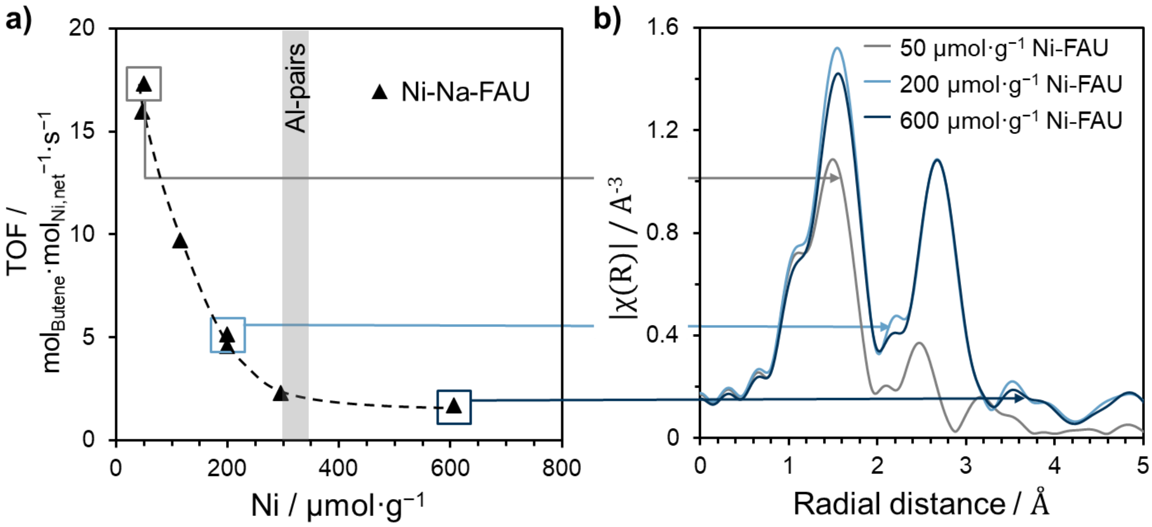

Figure 4.4: a) Turnover frequencies for Ni-Na-FAU catalysts in butene dimerization (T = 160 °C, p = 50 bar, WHSV = 50-500 h^{-1}) and b) FT-EXAFS three selected Ni-Na-FAU samples (*50Ni130BAS*-FAU, *199Ni28BAS*-FAU, and *607Ni89BAS*-FAU).

The fitted Ni-O coordination numbers increased from 4.2 to ~6 for samples with 200 and 600 μmol·g^{-1} of Ni (see **Figure 4.4b**). We speculate that this increase in the Ni-O coordination number stems from a shift of the Ni location. Ni-O coordination of 4.2 indicates of Ni^{2+} cations located within the 6-membered rings (6MR) between the sodalite cage and the supercage of the FAU framework.[240] In this location, also known as the S_{II} position (see **Figure 4.5**), the Ni is accessible to butene from the supercage and can therefore participate in the reaction. We hypothesize that, due to competition with Na^+ for the exchange sites, Ni exchanges the more accessible S_{II} position at low loadings in Na-FAU materials. Once Ni loading increases, a gradual exchange into the inaccessible S_I position leads to a decrease in Ni-based TOF.

This hypothesis is sustained by the butene reaction rates observed for Ni-H-FAU materials. The net activity of Ni in the absence of Na^+ first increases with Ni loading and then decreases (**Figure 4.3a**, hollow symbols). We propose that, in the absence of a monovalent competing ion like Na^+, Ni^{2+} first occupies the more stable but for butene inaccessible S_I positions in the hexagonal prisms, which leads to a significantly reduced Ni net dimerization activity. With increasing Ni loading, Ni^{2+} exchanges in the more accessible S_{II} positions up to the point where all S_{II} with Al pairs are occupied. Ni loadings exceeding that concentration are exchanged either in inaccessible positions or form NiO particles/nanoclusters.

In summary, the measured XAFS, together with the dramatic decrease in TOF observed with increasing Ni loadings, implies that FAU cannot stabilize the isolated Ni cations in accessible positions at high loadings, and most of the metal ions do not participate in the reaction. While for loadings under 200 $\mu mol \cdot g^{-1}$ an important fraction of Ni^{2+} ions exchange in inaccessible S_{II} positions, at Ni loadings above 300 $\mu mol \cdot g^{-1}$, the formation of NiO particles or Ni_xO_y nanocluster cannot be ruled out.

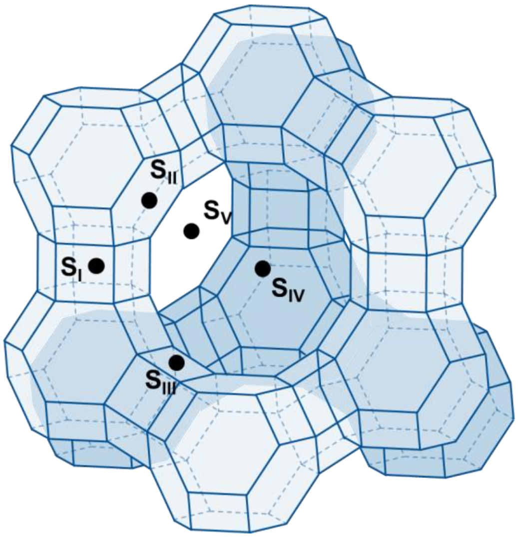

Figure 4.5: Different positions of cations in the FAU framework. S_I is sitting in the hexagonal prism, S_{II} is in the 6MR between sodalite cage and supercage, S_{III} in between hexagonal prism and supercage, S_{IV} in the middle of the supercage and S_V between two supercages.

The different positions of Ni in Ni-H-FAU and Ni-Na-FAU are also evidenced when examining the selectivities to different C_8 isomers and, in particular, the linear octene formation rates. The production of linear octenes can be used as a direct indicator for the Ni activity because BAS-catalyzed dimerization does not form linear products. This was verified by reference tests on H-FAU material, where $<1 \cdot 10^{-7}$ $mol_{Octene} \cdot mol_{BAS}^{-1} \cdot s^{-1}$ was detected (**Figure 6.68**, SI). As visible from **Figure 4.3b**, the octene rate for the Ni-H-FAU with 25 $\mu mol \cdot g^{-1}$ of Ni is nearly zero, indicating that most of the activity in that sample is related to BAS. Conversely, the same concentration of Ni in Ni-Na-FAU material shows a high octene selectivity, and therefore an essential contribution of Ni to the overall activity, with the TOF for Ni-Na-FAU in this Ni loading range is almost one order of magnitude higher than Ni-H-FAU (**Figure 4.3a**).

4.2.2 Influences of activation procedure on active sites in Ni-Na-MFI

To gain more insight into the generation and activation of the active site, we investigated the influence of different activation procedures on the catalyst´s performance. We chose an MFI sample that, based on our characterization results, contains single Ni^{2+} cations as the predominant Ni species. In this zeolite, the Ni species are accessible to butene at any position (unlike FAU) and are less likely to suffer pore diffusion limitations than in CHA. The *179Ni89BAS*-MFI sample was activated under different oxidizing, inert, and reducing conditions and tested according to their performances in butene dimerization. **Figure 4.6** depicts the conversion and the selectivity to linear octene after activation in flowing synthetic air (synair), nitrogen, hydrogen, and a sequential procedure of first hydrogen and then synair.

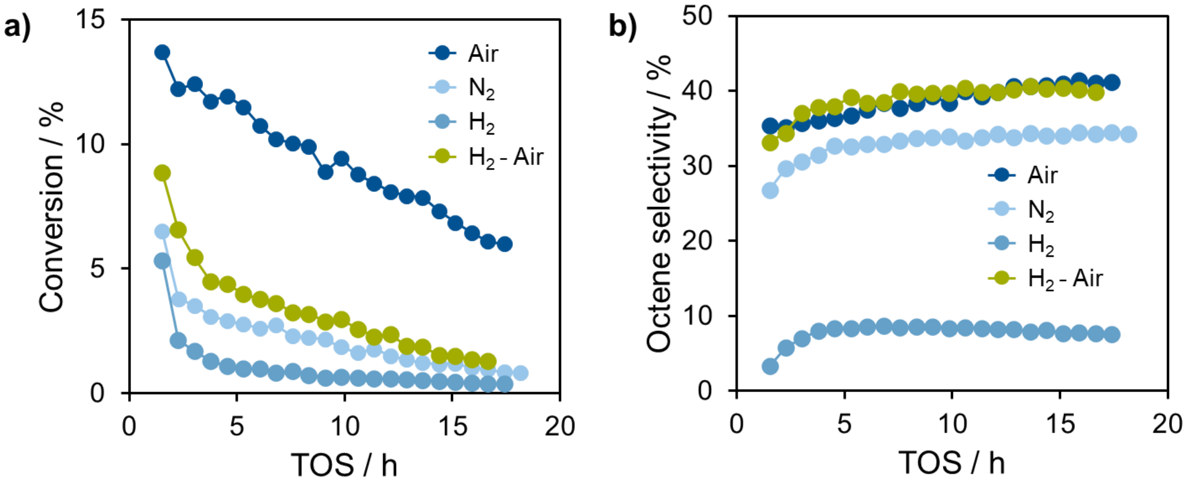

Figure 4.6: Different activation procedures on *179Ni89BAS*-MFI sample (activation conditions: T = 450 °C, 2 h, 100-120 mL·min^{-1}; reaction conditions: T = 160 °C, p = 50 bar, WHSV = 50 h^{-1}).

The procedure of activating in synair yielded the highest butene conversions and the highest linear octene selectivity. The activations in nitrogen or hydrogen resulted in less than 50% activity and a reduced octene selectivity. It is interesting to notice that the catalyst treated in hydrogen and subsequent synthetic air restores full selectivity while yielding ~60% activity compared to the air-treated sample.

IR spectra of the sample under flowing conditions were taken to investigate the present species on the sample after different activation procedures. **Figure 4.7** shows no significant differences for the activation in nitrogen and synair. In contrast, the sample treated in hydrogen shows higher intensities for the OH vibrations at 3610 cm^{-1}, assigned to BAS, and at 3660 cm^{-1}, which can be either the OH species on extra-framework alumina (EFAl) or a Ni-OH species.[241] The intensity of the vibration at 3660 cm^{-1} diminishes already when the H_2 stream is stopped, suggesting low stability for this species. Therefore, we exclude the formation of EFAl as the reason for the increase in this vibration because partial destruction of the framework would not be reversible. The vibration at 3660 cm^{-1} is attributed to the reversible formation of a Ni-OH species, which converts back to the single Ni^{2+} cations after subsequent air treatment.

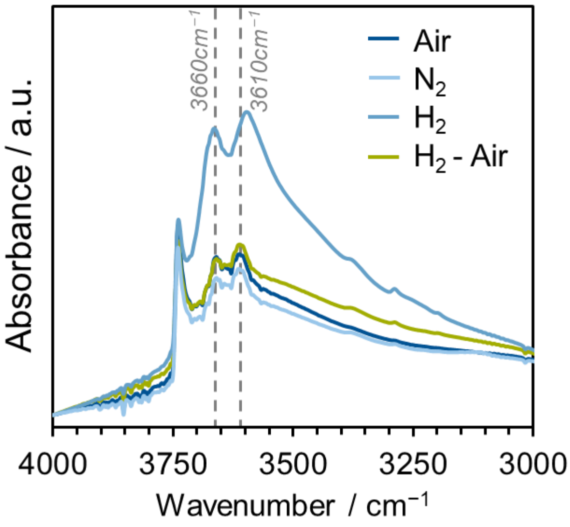

Figure 4.7: IR spectra of activated 17989BAS-MFI upon different activation treatments at 30 mL·min^{-1} gas flow and 450 °C for 1 h. Spectra were recorded after cooling down to 150 °C.

To further elucidate the structure of the Ni species, low-temperature CO-IR was performed after different activation treatments and compared to the activity in butene dimerization in **Figure 4.8**. The spectra at $1\cdot10^{-2}$ mbar of CO were analyzed analogous to the investigation of MFI samples with different Ni loadings (see section before). As depicted in **Figure 4.8b**, the rates for different treatments correlate well with the area of the Ni^{2+}-CO vibration except for the hydrogen treatment.

The activated sample in air shows the highest amount of isolated Ni^{2+}-sites, which explains the increased activity for this procedure. It appears that the treatment in air generates a higher concentration of the active species (that is, single Ni^{2+} cations) than the activation in nitrogen because the CO-IR did not reveal any differences in the nature of the Ni species present in both samples. The higher Ni^{2+} concentration could be related to activation by oxidation of the Ni or a superior stabilization of the single Ni^{2+} cations during the oxidation treatment. In contrast, the treatment in nitrogen might not prevent the migration of Ni. In addition, a more considerable BAS-CO contribution was observed (see **Figure 6.69**, SI) during CO adsorption, but only subtle differences could be noticed under flowing conditions (see **Figure 4.7**). This indicates that the emerging BAS reduce the octene selectivity while affecting the activity slightly positively.

The sample activated in hydrogen features the smallest amount of single Ni^{2+} species, as deduced from the CO interaction (**Figure 4.8a**). Additionally, the broad vibration for Ni^0 between 2060 and 2085 cm^{-1} arises,[234] indicating that the treatment in hydrogen reduces the Ni. As Ni^0 particles have been suggested before to be inactive in dimerization reactions,[33,41,42] we assume this to be the reason for the significantly reduced activity. Additionally, the largest amount of BAS was observed in the CO-IR for the hydrogen-treated sample (see **Figure 6.69**, SI). Together with the observations from IR under flowing conditions, this leads us to conclude that the increased BAS amount and the concomitant activity are why the rate for the hydrogen treated sample is too high to match the correlation of the Ni activity in **Figure 4.8b**. In addition, the BAS produce more branched products leading to a low linear octene selectivity (**Figure 4.6b**). However, we are not able to strictly rule out contributions of other Ni species such as NiOH.

When applying a subsequential activation procedure with hydrogen and synthetic air, the amount of Ni^{2+} species can be almost fully restored and correlates well with the butene consumption rate (**Figure 4.8**). This indicates that the initial hydrogen treatment reduces the Ni^{2+} to Ni^0, but the agglomeration to larger Ni^0 particles has not been initiated to a large extent. Instead, the reduced particles are probably still located near the ion exchange positions and can be mostly reoxidized after exposure to air. This explains the completely restored octene selectivity and the reduced BAS contribution after exposure to hydrogen and air under flowing conditions.

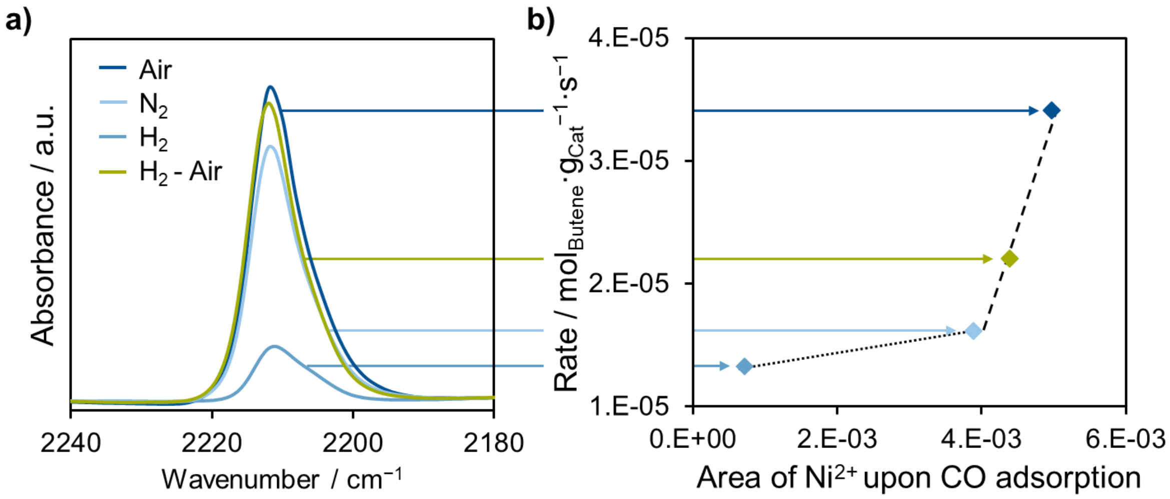

Figure 4.8: a) Areas of Ni^{2+}-CO vibration at $p = 1 \cdot 10^{-2}$ mbar and b) their correlation with butene consumption rates as well as linear octene formation rates (reaction conditions: $T = 160$ °C, $p = 50$ bar, WHSV = 50 h^{-1}).

4.2.3 Effect of local environment of Ni^{2+} sites on their activity in dimerization

The different zeolite frameworks are compared according to their selectivity and activity in butene dimerization in **Figure 4.9** and **Figure 4.10**. For this purpose, we have chosen CHA, MFI, and FAU samples with single Ni^{2+} cations as the dominant Ni species (*174Ni-*CHA(30%Al-pairs), *179Ni89BAS*-MFI and *47Ni89BAS*-FAU). The Ni-CHA catalyst yields linear octene selectivities of 30-50% for conversions up to 30%. This is among the highest reported linear octene selectivities so far and comparable to the performance of an earlier published Ni-Ca-LTA catalyst.[61] CHA and LTA are both small-pore zeolites. Therefore, we conclude that small pores prevent the formation or diffusion of branched products. Compared to FAU and MFI, the selectivity towards linear octene decreases with increasing channel size, indicating the principle of shape selectivity.

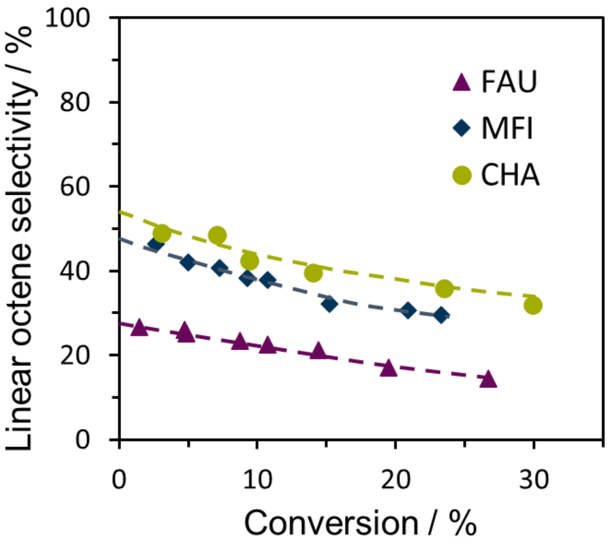

Figure 4.9: Selectivity of different zeolite frameworks with single Ni^{2+} cations (*174Ni*-CHA(30%Al-pairs), *179Ni89BAS*-MFI and *47Ni89BAS*-FAU).

The activity of Ni exchanged on different zeolites is compared in **Figure 4.10**. The TOF in butene dimerization is the highest for FAU (21 $mol_{Butene}\cdot mol_{Ni}^{-1}\cdot s^{-1}$), with values 1.5 orders of magnitude higher than those for MFI and CHA ($5\cdot10^{-1}$-$6\cdot10^{-1}$ $mol_{Butene}\cdot mol_{Ni}^{-1}\cdot s^{-1}$). The characterization and activity study shows that the active site is the same in all three zeolite frameworks, namely single Ni^{2+} ions. Thus, the difference in Ni activity must be caused by the environment of Ni ions in the different zeolite frameworks. In comparison, single Ni^{2+} cations supported on a metal-organic framework (2.5%Ni-UiO-66) lead to butene consumption rates of $3\cdot10^{-3}$ $mol_{Butene}\cdot mol_{Ni}^{-1}\cdot s^{-1}$, (see **Section 2.2.1**, **Figure 2.2**) which is at least two orders of magnitude lower than the rates for CHA and MFI (see **Figure 4.10**). In addition, the linear octene formation rates in **Figure 4.10** exhibit a similar trend as described for the butene consumption rates, showing that the selectivity changes do not affect the octene rates as drastically as the activity differences. In view of this, we conclude that the environment of Ni^{2+} in the different supports dramatically influences the activity. Changes in the electronegativity of Ni ions could be the cause of activity differences. For further investigation, we analyzed the different Ni-catalysts *via* X-ray photoelectron spectroscopy (XPS) (see **Figure 6.72**, SI).

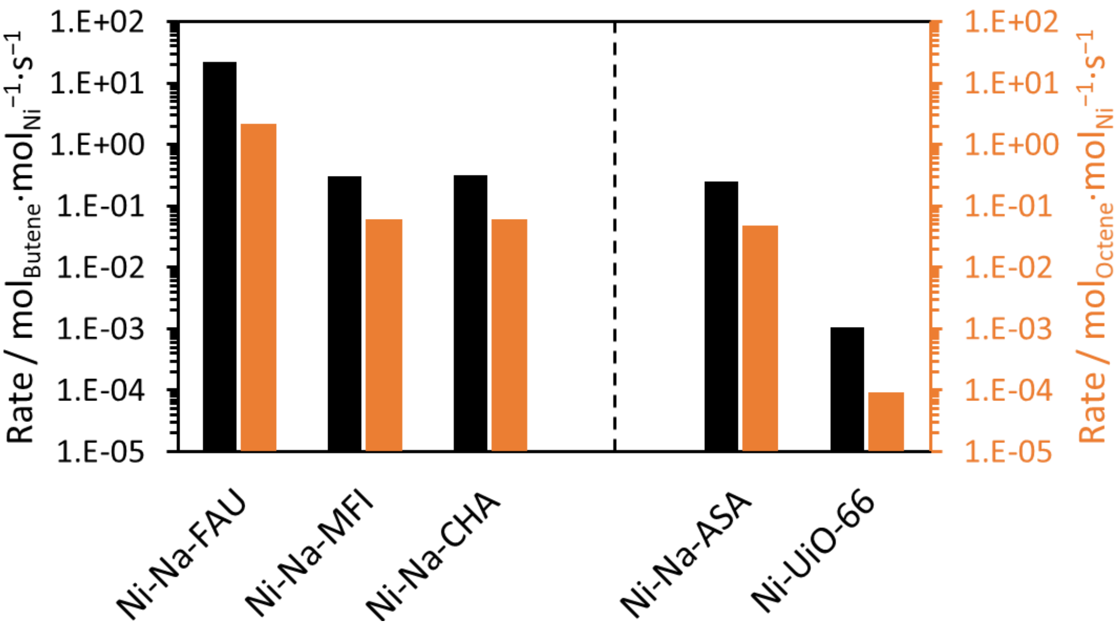

Figure 4.10: Butene consumption rates and octene formation rates of Ni based catalysts (*174Ni*-CHA(30%Al-pairs), *179Ni89BAS*-MFI, *47Ni89BAS*-FAU and 2.5%Ni-UiO-66 samples) at differential conversion (5-10%) in butene dimerization (activation conditions (zeolites): T = 450 °C, 2 h, 100 mL·min^{-1} synair; activation conditions (MOF): T = 300 °C, 1 h, 100 mL·min^{-1} nitrogen; reaction conditions (zeolites): T = 160 °C, p = 5 bar; reaction conditions (MOF): T = 250 °C, p = 50 bar, rates calculated at T = 160 °C and p = 50 bar by extrapolating Arrhenius plots).

Table 4.1 summarizes the binding energies and associated data of the XPS analysis of Ni-based catalysts. It is important to mention that the FAU samples we chose here are the *114Ni62BAS*- and *199Ni28BAS*-FAU samples, as lower Ni loadings resulted in poor signal-to-noise ratios. All four samples show a $2p_{3/2}$ contribution at around ~856 eV, assigned to Ni^{2+} cations exchanged into the zeolite framework.[242–244] The binding energy is shifted to higher values in the order Ni-UiO-66 < Ni-Na-MFI ≤ Ni-Na-CHA < Ni-Na-FAU. Higher binding energies indicate that Ni ions are in an environment that renders them more acidic (lower electron density). The TOFs increase with increasing Ni binding energies resulting in a strong correlation of the two parameters (**Figure 4.11**). The low activity of the MOF can be explained by a more electron-rich Ni caused by the Ni-O-Zr units of the MOF. Zr has a lower electronegativity than Al and therefore withdraws fewer electrons from the Ni framework leading to a less acidic Ni when supported by a MOF.

It should be noted that we cannot rigorously rule out charging effects during the XPS measurements, which is why the data should be treated with caution. Based on the strong correlation found between rates and binding energy (**Figure 4.11**), we still conclude that a more acidic character of Ni facilitates the butene adsorption, the first step during the dimerization reaction and yields higher dimerization activities. Tuning the acidity of the Ni with the help of the support can be, therefore, a strategy to increase dimerization activity.

Table 4.1: XPS Binding energies (eV) of Ni^{2+} species in different Ni based catalysts (*114Ni62BAS*-FAU, *199Ni28BAS*-FAU, *179Ni89BAS*-MFI, *174Ni*-CHA(30%Al-pairs) and 2.5%Ni-UiO-66)

Sample	Ni $2p_{3/2}$	FWHM[a]	ΔE_{sat}[b]	Ni $2p_{1/2}$	FWHM[a]	ΔE_{sat}[b]
114Ni62BAS-FAU	856.80	2.47	5.26	874.46	3.09	5.96
199Ni28BAS-FAU	856.63	2.69	5.53	874.32	2.94	5.91
179Ni89BAS-MFI	856.44	3.38	5.77	874.22	3.66	6.10
174Ni-CHA	856.47	3.38	5.76	874.22	3.66	6.10
Ni-UiO-66	856.06	2.63	5.43	873.86	3.16	6.27

[a] Full line width at half-maximum intensity.
[b] Energy difference between the satellite and main transitions.

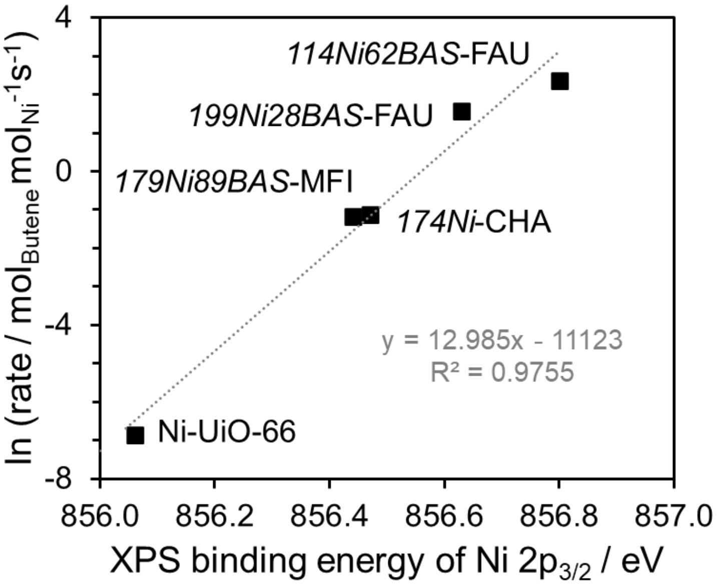

Figure 4.11: Correlation of the dimerization rate and the XPS binding energy of Ni $2p_{3/2}$ for different catalysts (*114Ni62BAS*-FAU, *199Ni28BAS*-FAU, *179Ni89BAS*-MFI, *174Ni*-CHA(30%Al-pairs) and 2.5%Ni-UiO-66). For the Ni-UiO-66, the extrapolated rate at $T = 160$ °C was used to ensure comparable reaction conditions for all catalysts.

Activation energies and reaction orders were measured for the Ni-based zeolite (**Figure 4.12**) to gain further insight into the activity of the three zeolites. The reaction orders are between one and two, which can be expected for a bimolecular reaction such as dimerization.[2,35,60,61,171] It is interesting to notice that reaction order for Ni-MFI is lower than for Ni-CHA and Ni-FAU. This could be due to higher butene coverage in MFI at similar butene partial pressures. For all three catalysts, the activity increases with lowering the temperature leading to negative apparent activation energies ($E_{a,\mathrm{app}}$). This suggests a strongly exothermic step prior to the rate-determining step (RDS). The Ni-UiO-66 features a positive $E_{a,\mathrm{app}}$ of 58 kJ·mol^{-1} (see **Section 2.2.1**, **Figure 2.1**), indicating a different mechanism and/or a large intrinsic barrier.

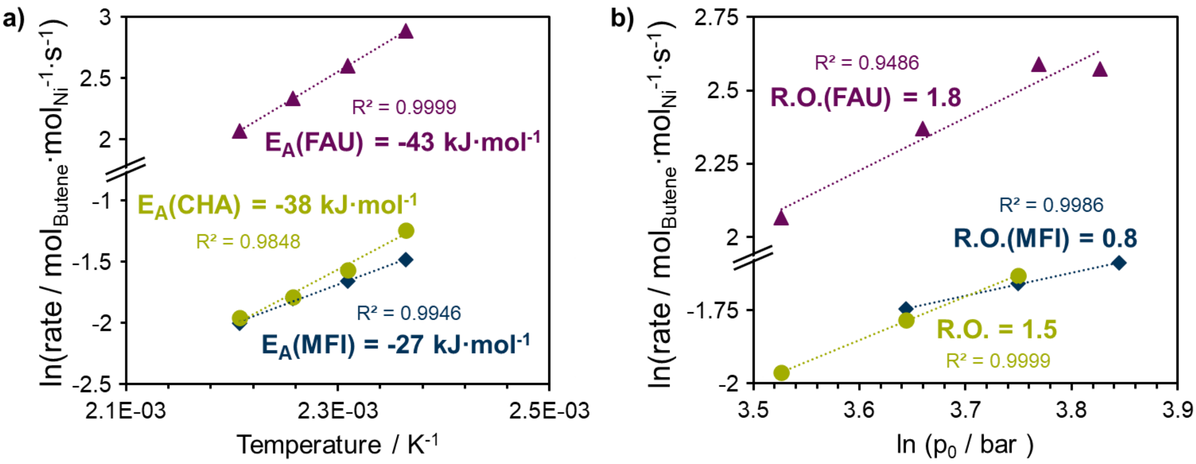

Figure 4.12: Activation energies and reaction order for *174Ni*-CHA(30%Al-pairs), *179Ni89BAS*-MFI and *47Ni89BAS*-FAU samples to compare the performance of the different frameworks (T = 150-180 °C, p = 40-55 bar, WHSV = 50 h^{-1} for CHA and MFI and 1000 h^{-1} for FAU).

The intrinsic activation barriers depend on the coordination and adsorption of butene. As mentioned before, the negative $E_{a,\mathrm{app}}$ suggests a large adsorption enthalpy ΔH_{ads} as the strongly exothermic step prior to C-C formation. TGA measurements indicate an ΔH_{ads} of 68-72 kJ·mol^{-1} for Ni-Na-MFI (see SI, **Figure 6.74**). However, determining ΔH_{ads} precisely for the Ni species without falsely taking contributions from other cations into account is quite challenging as butene also adsorbs on Na and the remaining BAS (see SI, **Figure 6.73**). In any case, the RDS (assumingly the C-C formation) is expected to have an intrinsic barrier of 33 to 69 kJ·mol^{-1} for the three zeolites in good agreement with the literature.[33,170]

The prevailing mechanism in dimerization reactions is still under debate, as various cycles have been proposed (Cossee-Arlman mechanism, the metallacycle mechanism, the proton-transfer mechanism, or a Ni^{+}/Ni^{2+} redox shuttle mechanism, see **Section 1.3**). We have demonstrated here that single Ni^{2+} cations serve as the active site and the importance of its acidity for high dimerization activities. As partially reduced Ni sites would be beneficial for oxidation of the metal during the C-C formation step in the metallacycle or during the butene adsorption of the redox-shuttle mechanism, both catalytic cycles were excluded here. This could indicate a Cossee-Arlman-type mechanism as depicted in **Scheme 4.1**. The Cossee-Arlman mechanism proposes that the formation of the Ni-alkyl active sites requires the interaction of the Ni^{2+} ion with the π-bond of an alkene. Therefore, a higher electrophilicity of Ni ions would favor the initiation of the cycle, explaining the higher rates observed in FAU with respect to CHA and MFI and the low reaction rates of Ni-UiO-66.

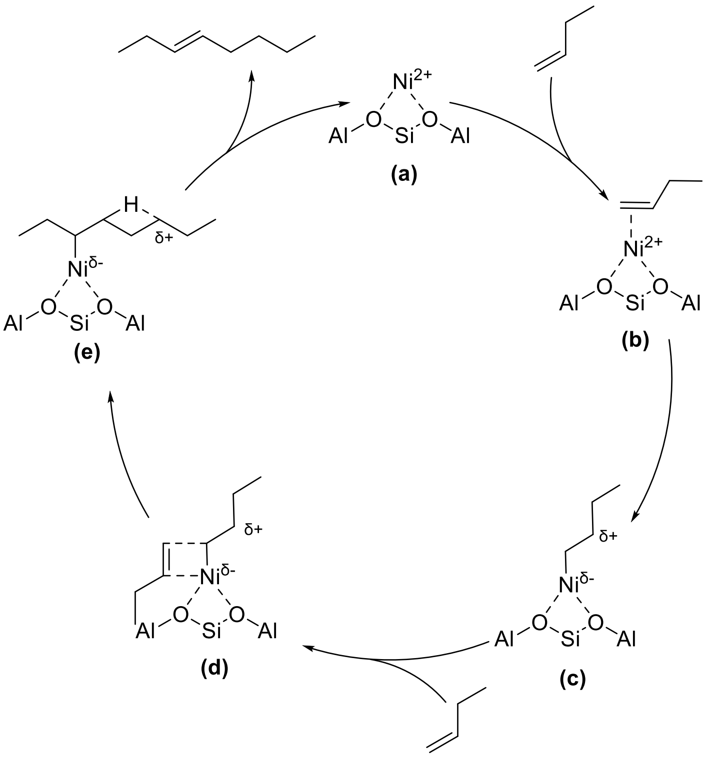

Scheme 4.1: Proposed reaction cycle following a Cossee-Arlman-type mechanism for butene dimerization over Ni based zeolites.

As described in **Section 2.2.3** we propose for Ni-UiO-66 a Cossee-Arlman mechanism on a nickel-hydride species as active site, which was based on the agreement of experimentally and theoretically determined activation energies. In the case of the zeolites, the bare Ni cation is displayed as active site instead of a metal-hydride species, as the significantly lower activation energies could hint towards a bare nickel as active site. However, the Cossee-Arlman mechanism could also take place on a nickel-hydride species as depicted in **Figure 2.5b** and **Scheme 3.2** as no direct evidence was found to exclude the hydride species.

We measured XAFS on the *179Ni89BAS*-MFI sample during the butene reaction to gain further insights into the mechanism. The in-situ measurements were performed under conditions of 1 bar and 160 °C, at which the catalyst still shows activity for butene dimerization (**Figure 6.75**, SI). The spectra in the near-edge region are given in **Figure 4.13**, and the changes upon reaction are displayed from light to dark blue.

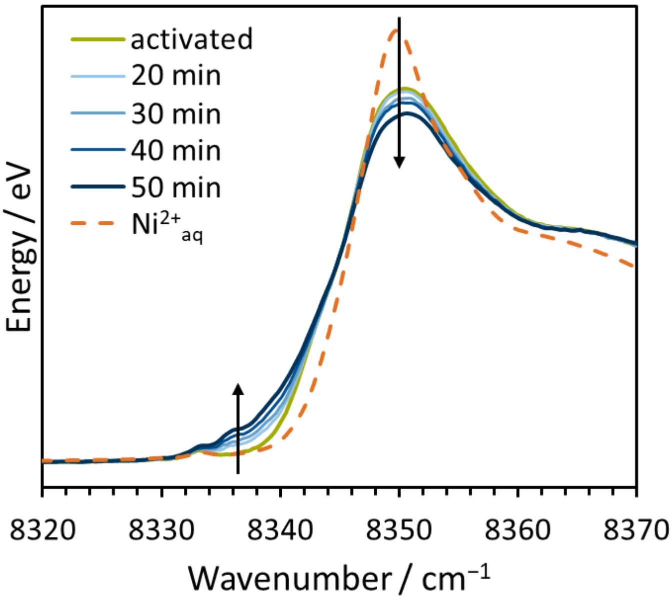

Figure 4.13: XANES spectra of *179Ni89BAS*-MFI after activation in 10% O_2 in helium for 1 h at 450 °C and 10 °C·min^{-1} (green graph), during and after reaction of 1-butene at 1 bar and 160 °C (light to dark blue lines) and aqueous Ni^{2+} reference (red dashed line).

After activation in the oxidative atmosphere, the decrease in the Ni-K-edge intensity at 8350 eV demonstrates the dehydration of Ni^{2+}. Changes in the pre-edge region (8336 eV) as well as in the intensity of the K-edge (8359 eV) upon butene admission onto the catalyst (blue lines) are caused by a reduction of the Ni^{2+} to lower-valent Ni-species (Ni^{+} or Ni^{0}).[44,245,246] Especially the increasing feature at 8336 eV hints at monovalent Ni^{+}.[247] This could indicate that the active Ni^{2+} species is reduced to Ni^{+} upon butene adsorption, which participates then in the catalytic cycle.

Similar observations were made by *Metzger et al.* in a Ni-based MOF, who, however, attributed the reduction of the Ni species to deactivation.[123] *Rabeah et al.* observed a reduction of the active single Ni cations during low-pressure (2 bar) admission of butene, whereas this behavior was not observed at 12.5 bar. The authors suggested that higher pressures stabilize the single Ni cations on the support, while at low pressures, the reduction and agglomeration to Ni^0 particles induce rapid deactivation.[44] This study highlights the importance of closing the pressure gap between characterization methods and reaction conditions and questions the conclusion of other studies on Ni-based zeolites that did not observe any changes of the proposed active Ni^{2+} site during the reaction by XAS. The difference in conditions during XAS measurements (atmospheric pressures) and reaction conditions (elevated pressures) might overlook changes in the active site and the mechanism at elevated pressures.

Being aware of the limited significance of the XAS measurements at atmospheric pressures, it is still interesting to notice that the Ni species in the MFI samples is reduced, which could hint to a reduced stability of the active sites in MFI. Further experiments should include the investigation in the other zeolite supports as well as in the MOF to allow meaningful conclusions about differences in the active sites.

4.3 Conclusion

In this work, we have identified single Ni^{2+} cations as the catalytically active sites in butene dimerization *via* the combination of different characterization techniques and activity measurements at increasing Ni loadings. While a certain shape selectivity is observed for small-pore zeolite CHA favoring linear octene dimerization, the highest rates per Ni are obtained for Ni-exchanged FAU. CO adsorption monitored by IR reveals that different activation procedures influences the nature and concentration of the active Ni site and causes therefore differences in activity and selectivity. Comparing the active single Ni^{2+} sites supported by zeolites to Ni ions in a MOF support, XPS revealed a linear dependency of the Ni acidity and the catalytic activity, with FAU zeolite stabilizing Ni ions with the highest acidity. These results suggest that an increased electrophilicity of Ni^{2+} caused by the zeolite support effectively enhances dimerization activities, facilitating the butene adsorption step in the Cossee-Arlman mechanism. On the other hand, FAU can only stabilize a limited concentration of these highly active Ni^{2+} ions in accessible positions. XAFS measurements in combination with a series of Ni-Na- and Ni-H-FAU indicate that Ni activity becomes significantly high for those materials where Ni sits predominantly on accessible S_I positions.

We show the importance of the support for obtaining higher linear dimer selectivity and significantly higher dimerization rates by tuning the acidity of the active Ni^{2+} species. This work provides, therefore, a deeper insight into the active site and the mechanistic cycle, especially the importance of the Ni´s electrophilicity on the butene adsorption.

4.4 Experimental

4.4.1 Catalyst synthesis

CHA synthesis

The CHA zeolites were synthesized according to a modified recipe from literature.[86,248]

In a typical synthesis of the CHA with 50% Al pairs, 28.1 g of an aqueous *N,N,N*-trimethyl-1-adamantyl-ammonium hydroxide (TMAdaOH) solution (26.6 mmol, 20 wt% Sachem) were mixed with 25.7 g of doubly deionized water (18.2 MΩ, 1425 mmol) and stirred for 15 min at room temperature. Then, 0.354 g of aluminum hydroxide hydrate ($Al(OH)_3{\cdot}xH_2O$, ~3.69 mmol, 98 wt%, Sigma Aldrich) was added and the mixture was thoroughly stirred for another 15 min. After adding 10.0 g of silica (Ludox, 66.6 mmol, 40 wt%, Sigma Aldrich) the contents were homogenized under ambient conditions for 2 h. The synthesis gel resulted in a molar ratio of 6.67 SiO_2 / 0.369 $Al(OH)_3$ / 2.66 TMAdaOH / 3007 H_2O_{total}. The gel was transferred to a 100 mL Teflon-lined stainless-steel autoclave (Toption Instruments) and heated in a forced convection oven at 160 °C for 6 days under rotation of 30 rpm.

In a typical synthesis of the CHA with 95% Al pairs, 26.6 g of an aqueous TMAdaOH solution (25.1 mmol, 20 wt% Sachem) were mixed with 24.3 g of doubly deionized water (18.2 MΩ, 1347 mmol) and stirred for 15 min under ambient conditions. Then, 0.327 g of aluminum hydroxide hydrate ($Al(OH)_3{\cdot}xH_2O$, ~3.41 mmol, 98 wt%, Sigma Aldrich) and 3.85 g of an aqueous 5 M sodium hydroxide solution (16.1 mmol, ≥ 98%, Sigma-Aldrich) were added. After each addition, the mixture was thoroughly stirred for 15 min. 9.45 g of silica (Ludox, 62.9 mmol, 40 wt%, Sigma Aldrich) were added and the contents were homogenized under ambient conditions for 2 h. The synthesis gel resulted in a molar ratio of 6.29 SiO_2 / 0.341 $Al(OH)_3$ / 2.51 TMAdaOH / 3021 H_2O_{total}. The gel was transferred to a 100 mL Teflon-lined stainless-steel autoclave (Toption Instruments) and heated in a forced convection oven at 160 °C for 6 days under rotation of 30 rpm.

The resulting solid CHA products were washed thoroughly with doubly deionized water and acetone in alternating steps until the pH-values stayed constant at around 6. After the final washing step with water, the product was fully dried in the oven at 80 °C and then calcined in flowing synthetic air (100 $mL{\cdot}min^{-1}$) at 580 °C for 10 h (ramping rate 1 $°C{\cdot}min^{-1}$).

Introducing metals into zeolites

NH_4-ZSM-5 zeolite (Si/Al = 15, Zeolyst) and H-FAU zeolite (Zeolyst International CBV 720, Si/Al = 15) were calcined in flowing synthetic air (100 $mL\cdot min^{-1}$) for 6 h at 550 °C (3 $°C\cdot min^{-1}$) to obtain the clean H-form.

Na-forms of the zeolites were prepared by three ion exchanges of the H-form with 0.06 M aqueous NaOAc (20 $g_{solution}\cdot g_{zeolite}^{-1}$, ≥99%, Sigma Aldrich) overnight at 80 °C. After each ion exchange, the solid was washed thoroughly with doubly deionized water (20 $g_{water}\cdot g_{zeolite}^{-1}$) and dried at 80 °C for several hours. After the last ion exchange and a calcination procedure in flowing synthetic air (100 $mL\cdot min^{-1}$) for 6 h at 500 °C (3 $°C\cdot min^{-1}$), the zeolite was washed twice with 0.1 M NaOAc (20 $g_{solution}\cdot g_{zeolite}^{-1}$) by centrifugation (3 min, 4000 rpm). The zeolite was calcined in flowing synthetic air (100 $mL\cdot min^{-1}$) for 6 h at 500 °C (3 $°C\cdot min^{-1}$) resulting in the Na-form.

The Ni^{2+} introduction was carried out as a Ni/Na co-exchange with varying concentrations of exchange solutions (20 $g_{solution}\cdot g_{zeolite}^{-1}$) overnight at 80 °C. The molarity of the solutions varied between 0.002-0.06 M $NiOAc_2$ (≥99%, Sigma Aldrich) and 0.001-0.6 M NaOAc to obtain loadings of 25-1100 $\mu mol\cdot g^{-1}$ Ni. The pH value was 6-7 during the total time of the ion exchange. The solid was washed thoroughly with doubly deionized water (20 $g_{water}\cdot g_{zeolite}^{-1}$), dried at 80 °C for several hours and calcined in flowing synthetic air (100 $mL\cdot min^{-1}$) for 6 h at 500 °C (3 $°C\cdot min^{-1}$). This resulted in the here described Ni-Na-form of the zeolites.

For the Ni-H-FAU, this procedure was carried out in the same way except for using the H-form instead of the Na-form and the Ni was introduced by a Ni^{2+} ion exchange instead of the co-exchange with Na.

Determination of Al pairs

The Al pair concentration was determined according to the ion exchange procedure of Dědeček et al.[87] The Na-form of the zeolites was stirred in an aqueous 0.05 M $Co(NO_3)_2$ (150 $mL_{solution}\cdot g_{zeolite}^{-1}$, ≥98%, Sigma Aldrich) under ambient conditions overnight. The sample was washed with water (3x 20 $mL_{solution}\cdot g_{zeolite}^{-1}$) and dried in an oven at 80 °C for several hours. This exchange was performed three times in total. The solid was then calcined in flowing synthetic air (100 mL·min^{-1}) at 500 °C for 6 h (ramping rate 3 °C·min^{-1}). The Co content was subsequently determined by AAS to reveal the amount of Al pairs.

4.4.2 Catalyst characterization

The Si-, Al-, Na-, Ni- and Co-contents were determined by atomic absorption spectroscopy (AAS) conducted using a *Solar M5 Dual Flame* graphite furnace atomic absorption spectrometer by *Thermo Fisher*. After drying the samples 250 °C for 24 h, they were dissolved in a mixture of hydrofluoric and nitric acid and injected into the graphite furnace. The concentration of each element was determined *via* previous calibration. The error was estimated to be approx. 3 μmol·g^{-1}.

Brønsted acid site (BAS) and Lewis acid site (LAS) concentrations were determined *via* pyridine adsorption monitored by infrared (IR) spectroscopy. The samples were pressed into self-supporting wafers of ~10 mg·cm^{-2}, which were inserted into the measuring cell of a *Nicolet 5700* FT-IR spectrometer by *Thermo Electron Corporation* equipped with a liquid nitrogen cooled detector. The sample was activated for 1 h at 450 °C in vacuum (<1·10^{-5} mbar, heating rate 10 °C·min^{-1}). After cooling to 150 °C, pyridine was equilibrated at 5·10^{-1} mbar for 1 h. The system was evacuated for 1 h before measurements. The spectra were taken after activation and after outgassing in the range from 400 to 4000 cm^{-1} (120 scans, resolution 2 cm^{-1}). The difference spectra of these two measurements were analyzed according to the characteristic bands for Brønsted acidity at 1540 cm^{-1} and Lewis acidity at 1450 cm^{-1}. The respective concentrations were calculated applying **Equation 4.2** with acid site concentration c_{acid}, integrated peak area A_{int}, wafer area A_{wafer}, wafer mass m_{wafer} and the respective extinction coefficient (0.73 cm·mol^{-1} for BAS and 0.96 cm·mol^{-1} for LAS[249]).

$$c_{acid}\left[\frac{\mathrm{mol}}{\mathrm{g}}\right] = \frac{A_{int}[\mathrm{cm}^{-1}] \cdot A_{wafer}[\mathrm{cm}^{2}] \cdot 1000}{m_{wafer}[\mathrm{mg}] \cdot \epsilon\left[\frac{\mathrm{cm}}{\mathrm{mol}}\right]} \qquad \textbf{(Eq. 4.2)}$$

Low-temperature CO-adsorption was conducted on a *Vertex 70 spectrometer* by *Bruker Optics* equipped with a liquid nitrogen cooled detector. A self-supporting wafer was prepared as described above and activated in the measurement cell for 1 h at 450 °C in vacuum (<1·10^{-5} mbar, heating rate 10 °C·min^{-1}). Synthetic air (25 mbar) was dosed into the cell for another hour. The temperature was then cooled to 100 °C in gas atmosphere. Then, the cell was evacuated ($p<1\cdot10^{-6}$ mbar) and further cooled to liquid nitrogen temperature. The adsorption of CO was performed by dosing increasing pressure steps from $1\cdot10^{-4}$ mbar to 1 mbar. The next step was only initiated after stabilization of spectral features. Scans were regularly taken in the range from 1250 to 4000 cm^{-1} (120 scans, resolution 2 cm^{-1}).

IR spectra of one pellet were recorded after different subsequent activation treatments in flowing gas. Spectra were collected on a Nicolet iS50 AEM by Thermo Electron Corporation featuring a liquid nitrogen cooled detector. The sample was pressed into a self-supporting wafer with an approximate density of 10 $mg\cdot cm^{-2}$, which was inserted into the measurement cell. The waver was heated upon flow of the respective gas (30 $mL\cdot min^{-1}$) to 450 °C and kept at this temperature for 1 h. Thereafter, the measurement cell was cooled to 150 °C to take spectra (resolution 0.5 cm^{-1}) with appropriate signal intensity before heating up again in the subsequent gas atmosphere. The order of gas admission into the cell was N_2, synthetic air, H_2 and synthetic air.

In the following described XAFS measurements were performed similarly as reported by *Khare et al.* in the literature.[250] Ni K-edge X-ray absorption spectra were obtained at the P65 beamline of the German electron synchrotron (DESY) in Hamburg, Germany. The PETRA III storage ring was operated at 6 GeV energy and 100 mA beam-current in top-up mode. A water-cooled Si111 double crystal monochromator (DCM) was used for obtaining monochromatic X-rays. Two Si mirrors were installed in front of the DCM to reject higher harmonics. The DCM was calibrated for Ni K-edge by measuring a Ni-foil and defining the first major inflection point as 8333 eV. A Ni-foil was also placed between the second and third ionization chamber for the energy calibration of each measured spectrum. The energy resolution of the beamline is estimated to be ~1.2 eV at the Ni K-edge. The XAS spectra were measured in both transmission mode and in fluorescence mode using a passivated implanted planar silicon (PIPS) detector. The spot-size of X-ray beam at the sample was 1.6 mm (horizontal) × 200 μm (vertical). Spectra for X-ray absorption near edge structure (XANES) analyses were measured between −100 eV and +200 eV around the Ni K-edge while the spectra for extended X-ray absorption fine structure (EXAFS) analyses were obtained between −150 eV and +600 eV around the Ni K-edge. For XANES analyses, E_0 was fixed at 8333 eV and the spectra were normalized and flattened. For EXAFS analyses, spectra were background subtracted, normalized, k^2-weighted, and Fourier-transformed in the k range of 3-11 $Å^{-1}$. The EXAFS fitting was performed in k-space between 3 and 11 $Å^{-1}$ on the k^1-, k^2-, and k^3-weighted data. E_0 was set such that energy-shift (ΔE_0) obtained during the fit was less than 2 eV. A Ni-foil was first fitted to obtain the amplitude reduction factor, $S_0^2 = 0.8$, which was then used in the subsequent fits. XANES and EXAFS data analyses were performed using Athena and Artemis software packages.[206] The data were monitored for any signs of X-ray beam damage. Several successive scans were averaged to reduce signal-to-noise ratio and improve the data quality.

In situ measurements were performed using a quartz capillary micro-reactor setup. In a typical experiment, the catalyst was placed in a quartz capillary (1 mm o.d., 20 μm thickness) supported between two quartz wool plugs. The capillary was heated from below with a hot-air gas-blower (Oxford FMB). Gas flow rates were maintained using Bronkhorst electronic mass flow controllers and the pressure was continuously monitored using a pressure gauge (Omega). The catalyst sample was first activated under 5 mL·min^{-1} O_2 (10% in He) at 160 °C (10 °C·min^{-1}) for 1 h. After activation, the sample was cooled down to 160 °C for XAS measurements on the activated sample. Spectra were also measured on the activated sample under a flow of 5 mL·min^{-1} 1-butene at 160 °C and ambient pressure.

X-ray photoelectron spectroscopy (XPS) data were acquired with a Kratos Axis Supra spectrometer at a base pressure of $<10^{-8}$ torr using monochromatic Al K_α radiation (E = 1486.6 eV), a charge neutralizer, and pass energies of 160 eV (survey spectra) and 80 eV (region spectra). All binding energy values were calibrated using the 1s photoemission peak for adventitious carbon at 284.8 eV. Data analysis and modelling was performed with CasaXPS using a Shirley background and Kratos relative sensitivity factors as implemented in this software.[251]

The adsorption of 1-butene was measured gravimetrically on a microbalance in a Seteram TG-DSC 111 calorimeter connected to a high vacuum system. About 25 mg of sample was pretreated at 450 °C for 1 h under vacuum ($p < 10^{-4}$ mbar), and then cooled to 40 °C. 1-Butene was introduced into the system in small dosing steps from $3 \cdot 10^{-3}$ to 500 mbar. The butene uptake was calculated from the sample weight increase. The released heat was monitored by the heat flux signal.

X-ray diffraction (XRD) patterns were recorded on a *PANalytical Empyreal System* diffractometer with a Cu-K_α radiation source (1.54 Å, 45 kV, 40 mA). A sample spinner was utilized to record patterns in the range of 5 to 50 °2θ with a step size of 0.0131303 °2θ at ambient conditions.

N_2-physisorption was performed at liquid nitrogen temperature on a *PMI Automatic Sorptometer 1990*. Samples were heated in vacuum at 250 °C for 2 h (heating rate 5 $°C \cdot min^{-1}$) before the measurement. BET surface area S_{BET}, micropore volume V_{micro} and mesopore surface area S_{meso} were determined according to BET theory[252] applying a linear regression for p/p_0 = 0.05-0.3 and t-values between 6 and 8 Å.

4.4.3 Catalytic tests

The catalytic tests were performed according to the procedures described in **Section 2.4.5**.

Standard measurements were performed at 160 °C and 50 bar with a feed flow rate of 0.04 $mL \cdot min^{-1}$. Catalyst loading varied between 10-200 mg with WHSV of 6-2200 $g \cdot g^{-1} \cdot h^{-1}$. Especially active catalysts, as the FAU catalysts, were diluted with SiO_2 in a 1:10 ratio and tested with higher flow rates.

5 Conclusion

Dimerization of 1-butene is a well-known industrial process to transform butene into linear olefins. Identifying the nature of the active site as well as the mechanistic steps in the dimerization cycle are key for designing highly active and selective catalysts for butene dimerization. Metal-organic frameworks (MOFs) present excellent model catalysts due to their ability to stabilize single Ni cations while excluding strong Brønsted acid sites. Zeolites consist of the same primary building units as the industrially applied amorphous catalysts and promise high activity. Their well-ordered microporous structure additionally pledges to control the selectivity towards the linear dimers. The comparison of different zeolite constraints allows more profound insights into the influence of Ni´s immediate environment.

UiO-66 based catalysts with single Ni and few Ni cation metal oxo clusters at undercoordinated zirconia nodes of UiO-66 were catalytically active for butene dimerization without a cocatalyst. The activity trend of UiO-66 catalysts with various Ni loadings suggests that the single Ni cations are active, while the clusters do not participate in the reaction. Upon activation at 300 °C in an inert atmosphere, X-ray absorption spectroscopy predicts partial dehydration leading to single [$Ni^{2+}(OH)^-$] sites attached to the Zr_6 node of UiO-66 *via* two μ-OH groups. DFT studies for the 1-butene dimerization mechanism suggest the Cossee-Arlman reaction mechanism to be energetically favored over the metallacycle or the proton-transfer mechanism. The observed induction period during dimerization is attributed to the transition of the [$Ni^{2+}(OH)^-$] site to a Ni^{2+}-H^- site for 1-butene dimerization.

Single Ni and other metal (Co, Cr, and Cu) cations supported by UiO-66 were investigated according to their dimerization activity, product selectivity, and butene adsorption properties. Ni-UiO-66 is by far the most active metal cation for 1-butene dimerization among the catalysts studied. The logarithm of the catalyzed rate of the reaction correlates linearly with the 1-butene adsorption enthalpies on the metal cations, which is supported by DFT calculations. We conclude that the higher adsorption strength of the second butene molecule weakens the metal-carbon bond of the alkyl species formed from adsorbed butene and the hydride residing on the activated metal cation. This, in turn, facilitates the formation of the C-C bond (′insertion of the second butene molecule′), leading to the adsorbed octene.

The catalytically active sites in zeolites were identified as single Ni^{2+} cations *via* the combination of different characterization techniques (synthesis of different paired Al concentrations, CO adsorption in IR, X-ray absorption spectroscopy) and activity measurements at increasing Ni loadings. While shape selectivity towards the linear dimers is observed for the small-pore zeolite CHA, the highest rates per Ni are obtained for Ni-exchanged FAU. CO adsorption reveals that different activation procedures influence the nature and concentration of the active Ni site and cause differences in activity and selectivity. Comparing the active single Ni^{2+} sites supported by zeolites to Ni ions in a MOF support, XPS revealed a linear dependency of the catalytic activity on the Ni electrophilicity with FAU zeolite stabilizing Ni ions with the highest electrophilicity. These results suggest that an increased electrophilicity of Ni^{2+} cations caused by the support effectively enhances butene adsorption in the Cossee-Arlman mechanism. The dimerization activity is thereby promoted, explaining the higher rates observed in FAU compared to CHA and MFI and the low reaction rates of Ni-UiO-66.

This work, therefore, offers a comprehensive insight into the possibilities of MOFs and microporous zeolites as supports for Ni-catalyzed butene dimerization. The here-reported mechanistic studies allow more profound insights into the catalytic cycle for heterogeneous Ni-based butene dimerization and pave the way for custom-tailoring Ni performances for industrial applications.

6 Supporting Information

6.1 Supporting information: Metal-organic framework supported single-site Ni catalysts for butene dimerization

6.1.1 Catalyst characterization

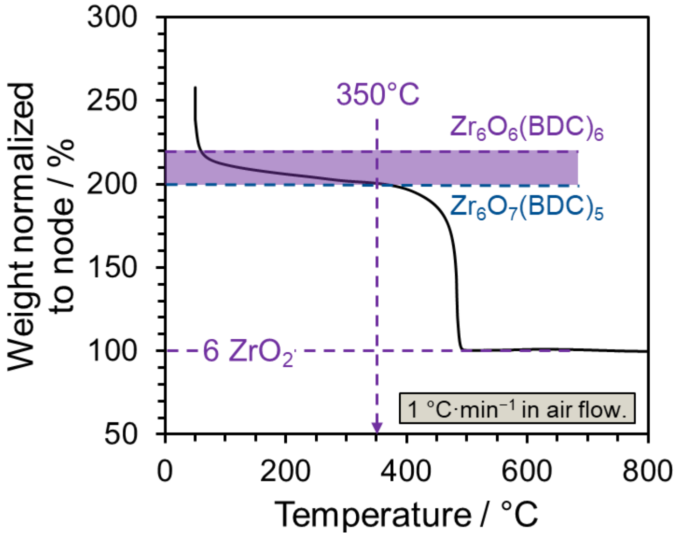

Figure 6.1: TGA curve of parent UiO-66. The sample was heated in air flow to 800 °C (ramp rate of 1 °C·min^{-1}).

Weight loss at the temperature <100 °C is assigned to the removal of physically adsorbed impurities (mostly H_2O). Weight loss at 200-350 °C can be assigned to the dehydroxylation of the Zr_6 cornerstone and the oxidation of monocarboxylate ligands (formate). At 350 °C, only zirconium oxide and benzene dicarboxylate (BDC) linkers remain. The oxidation of coordinated BDC linkers (decomposition of the framework) starts at >350 °C. This step is completed when the temperature reaches 500 °C. Thus, the end residue is pure ZrO_2. If the final ZrO_2 is normalized to 100%, the normalized weight for a non-defect UiO-66 ($Zr_6O_{6+x}(BDC)_{6-x}$) is 220% at 350 °C.[112] We determined that x=1, suggesting 1 BDC linker missing per Zr_6 cluster in the MOF (**Table 6.1**).

Table 6.1: Quantification of missing linker in the MOF

$Zr_6O_{6+x}(BDC)_{6-x}$	
6-x	x
BDC linkers / mol·mol$_{node}^{-1}$	Missing BDC linkers / mol·mol$_{node}^{-1}$
5.00	1.00

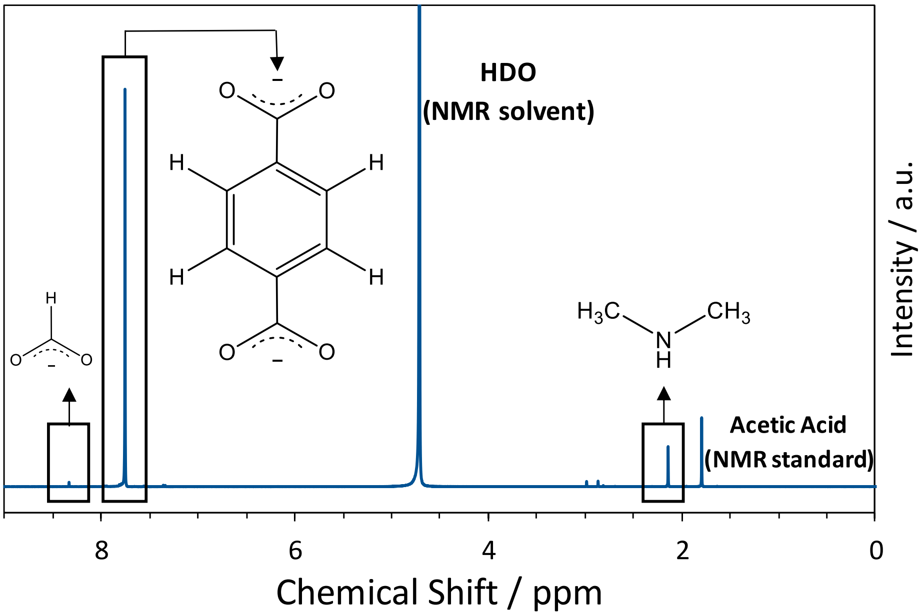

Figure 6.2: ^{1}H NMR spectrum of the UiO-66 dissolved in NaOH/D_2O solution.

The nuclear magnetic resonance (NMR) spectrum shows the important components of the MOF structure. The BDC linkers appear at ~7.8 ppm, the formate groups at ~8.3 ppm, and dimethylamine (DMA) at ~2.1 ppm. It has been reported that missing linker defects lead to either -OH/-H_2O groups or formate species on the node.[195] Formate groups are considered to originate from solvent (DMF) decomposition during the MOF synthesis.[120] Quantification of the peaks of formate and BDC linkers (~7.8 ppm) results in the molar ratio of 0.01, indicating a small portion of formate still being present on the node after extensive washing. We also observed small amounts of DMA groups from the residual DMF solvent (**Table 6.2**).

Table 6.2: Quantification of organic groups in the MOF

Formate / BDC	Formate / $mol \cdot mol_{node}^{-1}$	BDC / $mol \cdot mol_{node}^{-1}$	DMA / BDC
0.01	0.05	5.00	1/10.6

Table 6.3: Samples used in this work and the corresponding metal loadings

Sample	Ni loadings / wt.%	Ni/Zr (molar)	Ni/Zr_6 node (molar)
Parent UiO-66	-	-	-
1.3%Ni-UiO-66	1.3	0.06	0.34
2.5%Ni-UiO-66	2.5	0.11	0.67
5%Ni-UiO-66	5.0	0.23	1.37
10%Ni-UiO-66	10.0	0.48	2.90
3.4%Ni-ZrO_2	3.4	0.07	0.44 *

* For calculation, 6 ZrO_2 units are considered as one Zr_6 node.

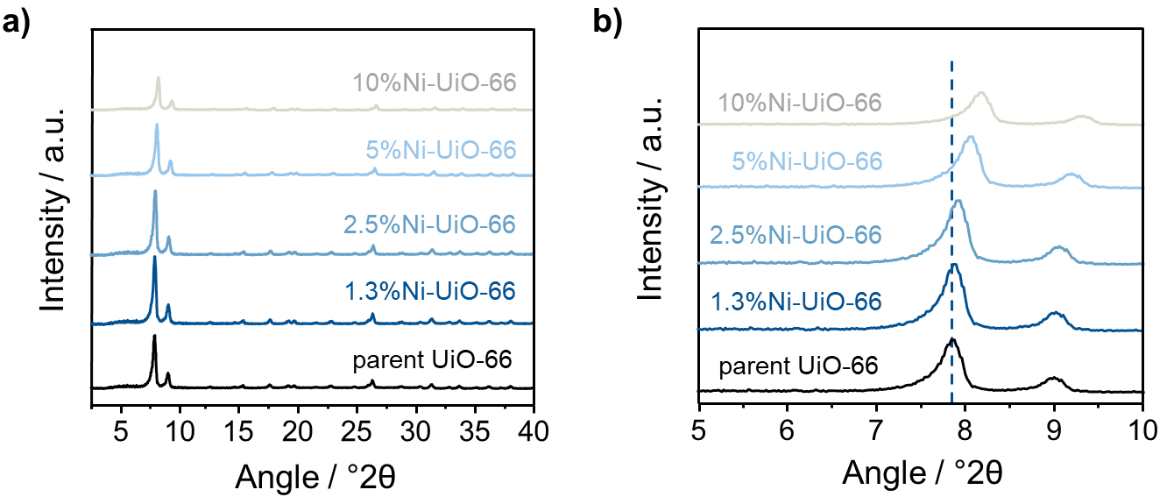

Figure 6.3: a) XRD patterns of parent UiO-66 and Ni-UiO-66 with different Ni loadings. b) Close-up of the low-angle region.

These results demonstrate that the crystallinity of UiO-66 is retained after Ni deposition. The diffraction peak intensity is slightly lower in the high Ni loaded samples 5%Ni-UiO-66 and 10%Ni-UiO-66. In addition, a shift to the high angle side was observed after Ni deposition. It is hypothesized that Ni species deposited in the pores of the MOF decreased the interplanar spacing of the crystal faces.

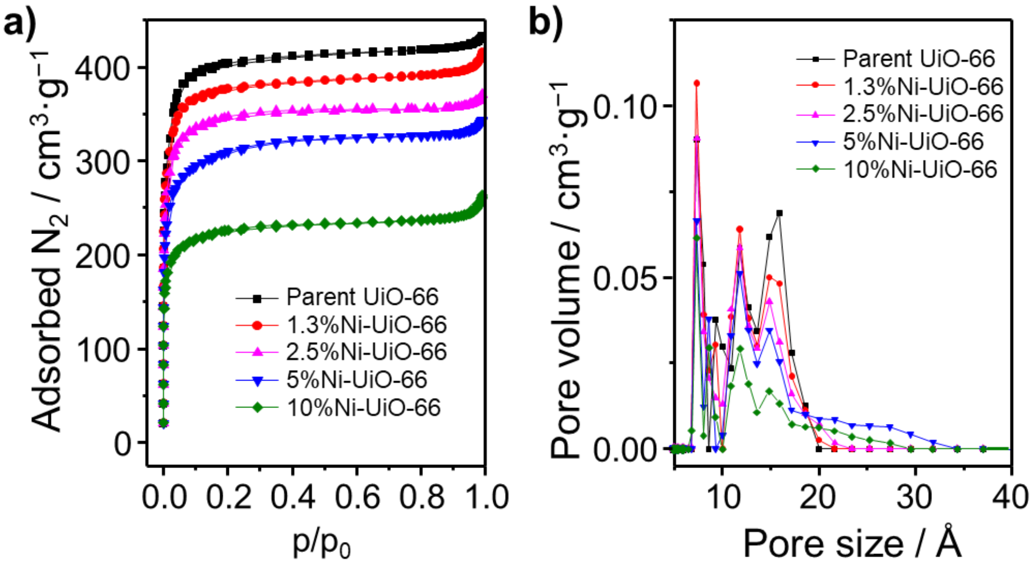

Figure 6.4: a) N_2 adsorption isotherms and b) pore size distribution of parent UiO-66 and Ni-UiO-66 samples.

Table 6.4: Texture properties determined based on the N_2 adsorption isotherms

Sample	**BET surface area / $m^2 \cdot g^{-1}$**	**Pore volume / $cm^3 \cdot g^{-1}$**
Parent UiO-66	1560	0.67
1.3%Ni-UiO-66	1455	0.64
2.5%Ni-UiO-66	1327	0.57
5.0%Ni-UiO-66	1207	0.55
10%Ni-UiO-66	857	0.40

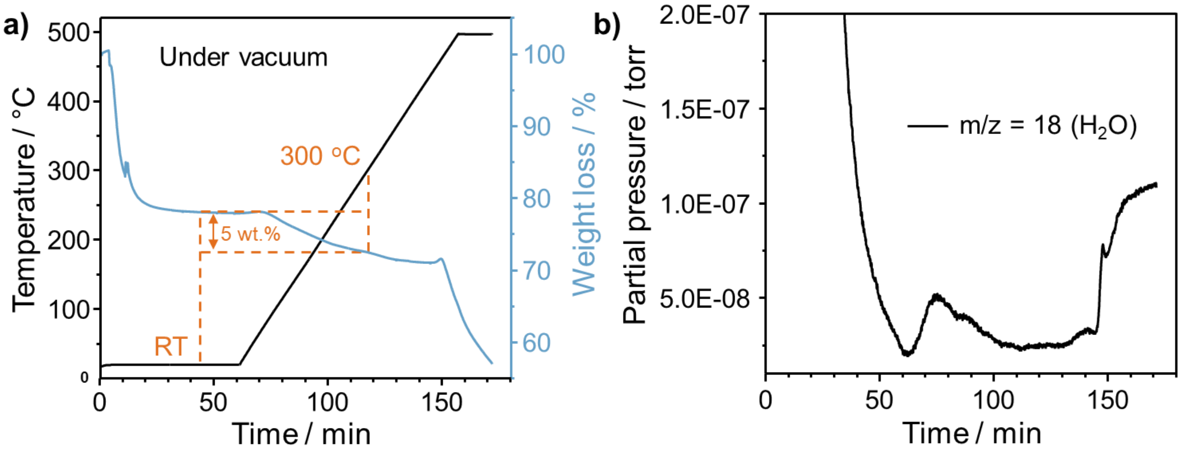

Figure 6.5: a) Vacuum-TGA curve of parent 2.5%Ni-UiO-66. b) Corresponding mass spectrum of water.

Sample was first placed in the vacuum chamber at room temperature (RT). Then it was heated at the ramp rate of 5 °C·min^{-1} up to 500 °C. ~22 wt.% water (~ 20 H_2O molecules) was removed at the temperature <100 °C. Extra ~5 wt.% of water, corresponding to 4-5 H_2O molecules, was desorbed form the MOF by heating it to 300 °C.

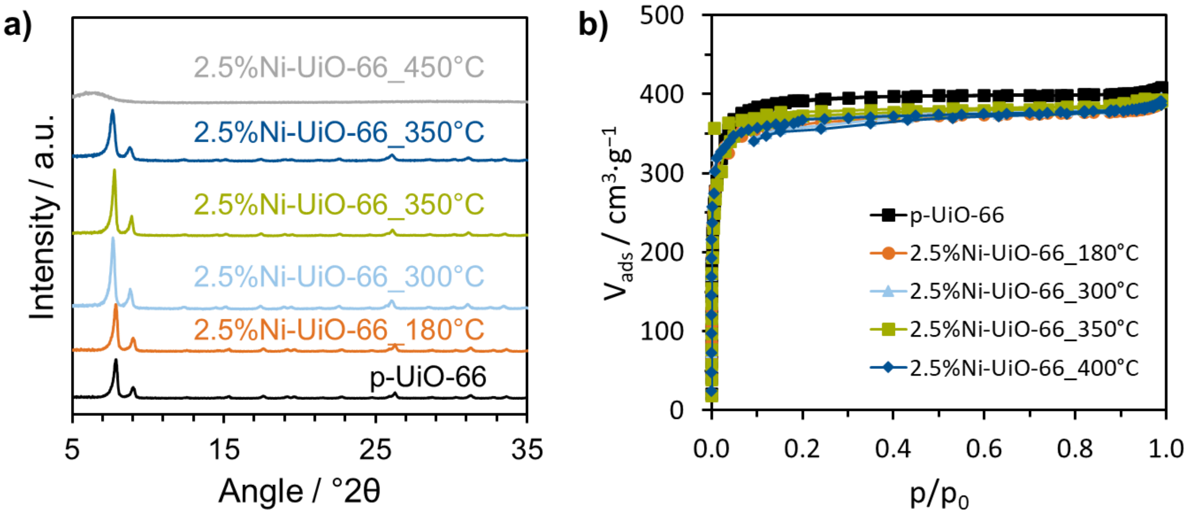

Figure 6.6: a) XRD patterns and b) N_2 adsorption isotherms for 2.5%Ni-UiO-66 degassed in vacuum at different temperatures, e.g., 180, 300, 350, 400, and 450 °C, for 4 h, respectively.

Only minor changes in the porosity and crystallinity for 2.5%Ni-UiO-66 were observed. It indicates that the material is stable up to 400 °C. Further increasing the temperature leads to collapsing of the MOF structure.

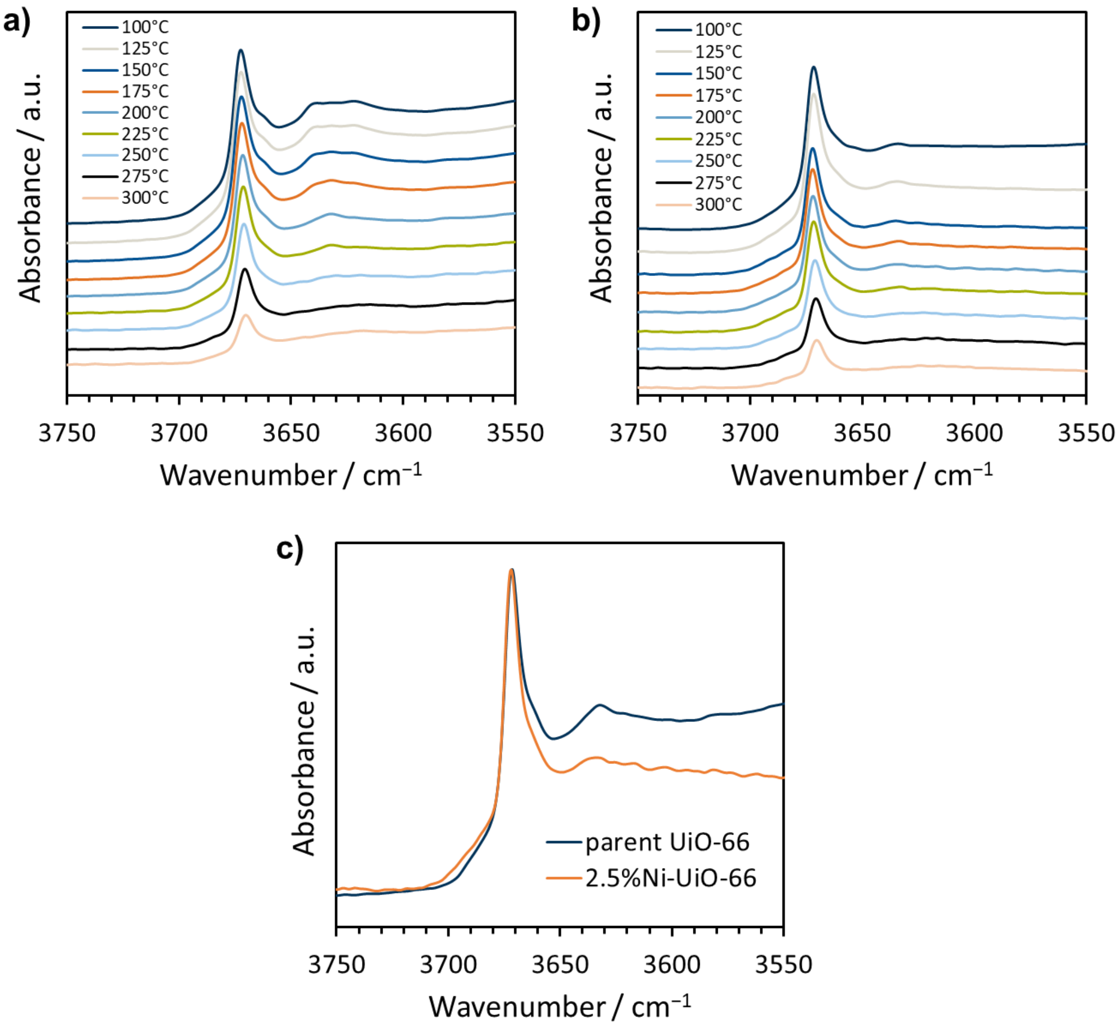

Figure 6.7: In-situ FTIR spectra of a) the parent UiO-66 and b) 2.5%Ni-UiO-66 collected during heat treatment of the sample under vacuum (10^{-3} mbar); c) a direct comparison of IR spectra collected at 250 °C for both samples.

6.1.2 Catalytic tests in butene dimerization

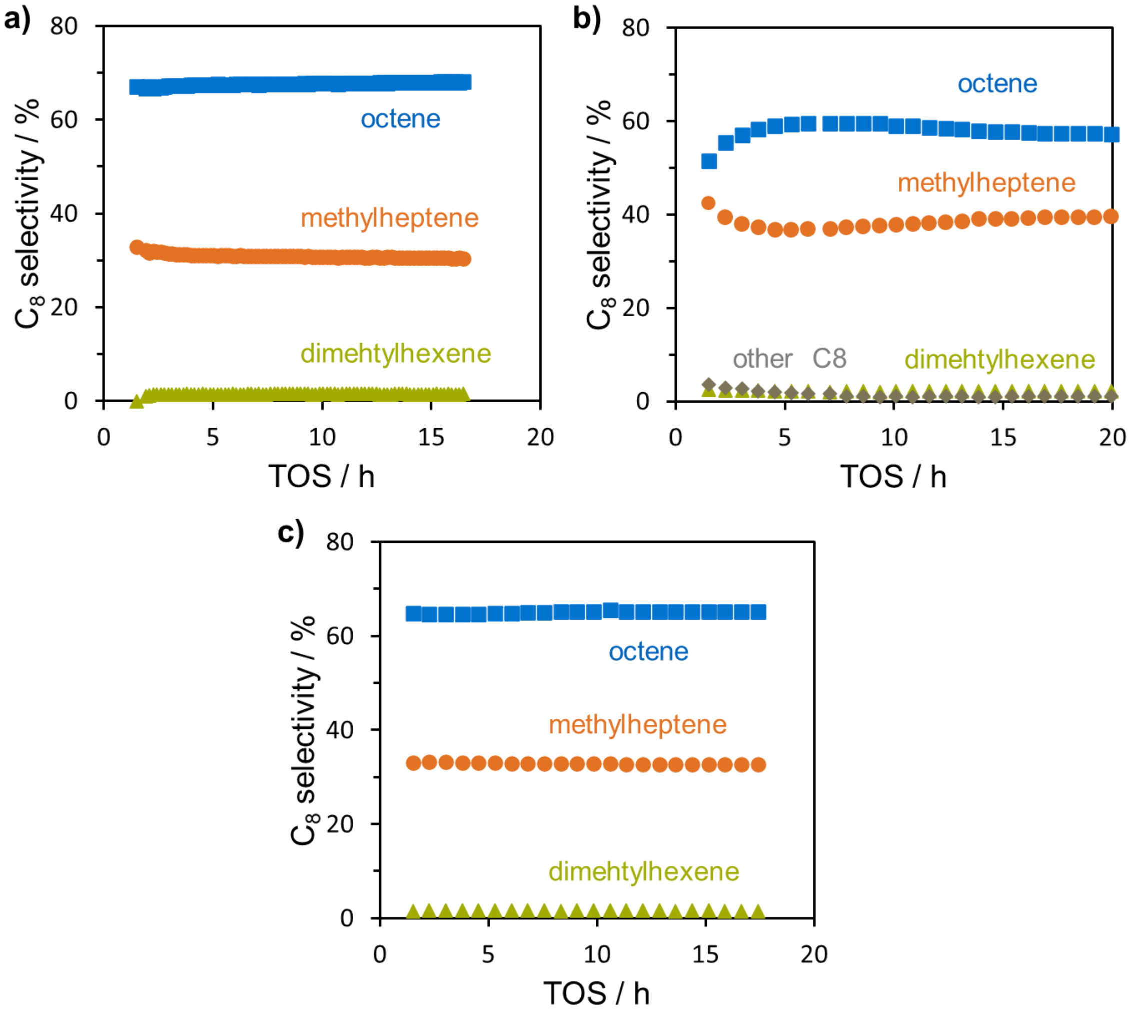

Figure 6.8: Product selectivity during 1-butene conversion on 2.5%Ni-UiO-66 at a) 200 °C, b) 230 °C, and c) 250 °C vs. time-on-stream (TOS).

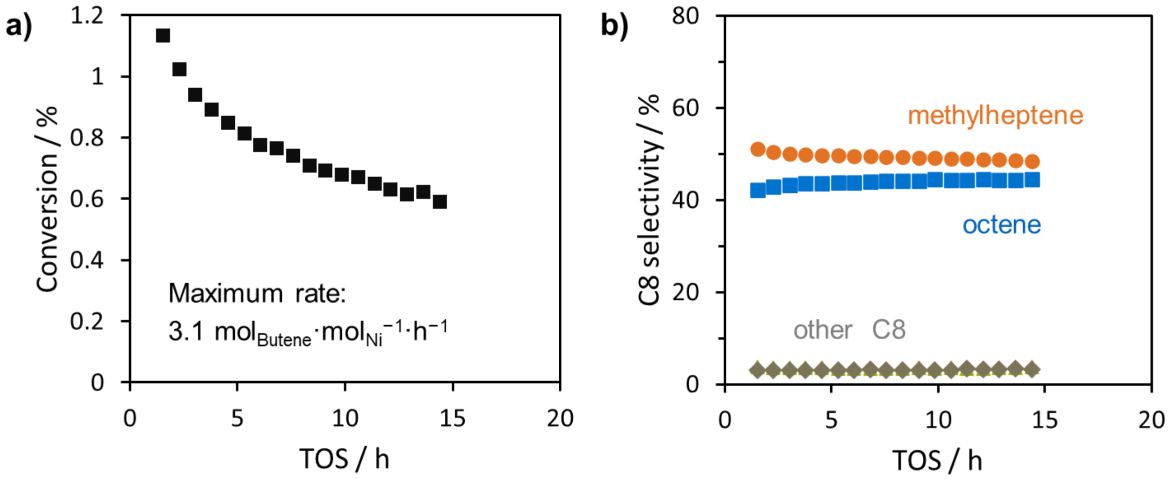

Figure 6.9: a) 1-Butene conversion and b) C_8 isomer selectivity on Ni-ZrO_2 measured at 250 °C vs TOS. The inset shows the maximum rate for 1-butene conversion (reaction conditions: $T = 250$ °C, $p = 50$ bar, WHSV = 8.4 h^{-1}).

The results show that both reaction rate (3.1 vs. 12.4 $mol_{butene} \cdot mol_{Ni}^{-1} \cdot h^{-1}$) and linear octene selectivity (~60% vs. ~50%) of Ni-ZrO_2 are lower than that of 2.5%Ni-UiO-66, which has a similar Ni loading.

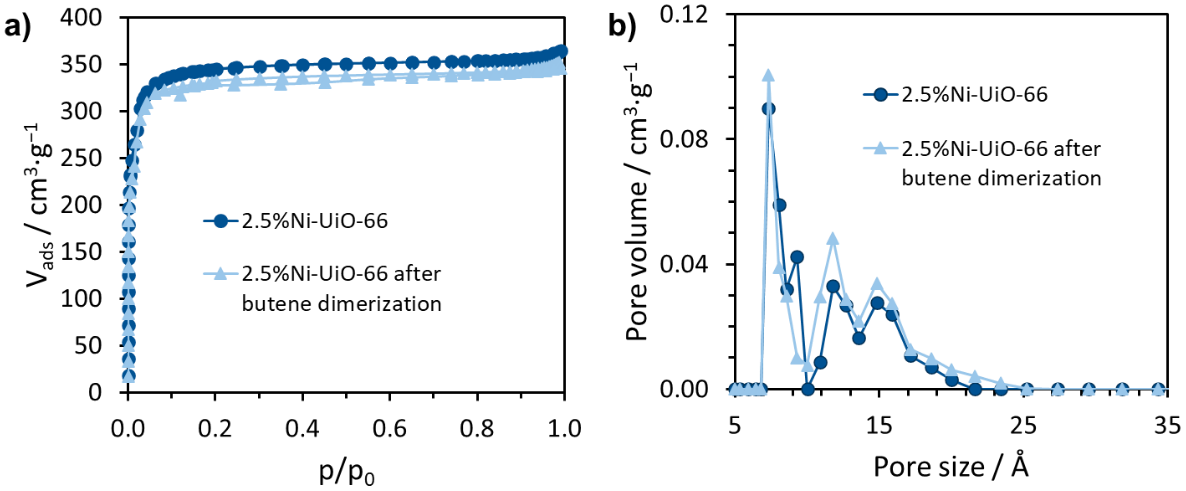

Figure 6.10: a) N_2-sorption isotherms and b) pore size distribution of fresh 2.5%Ni-UiO-66 and spent fresh 2.5%Ni-UiO-66 catalyst after butene dimerization.

Overall, the porosity of the material is mainly unchanged before and after participation in butene dimerization. A slight decrease in the pore volume is observed, which might be due to the formed dimerization products remaining in the pores.

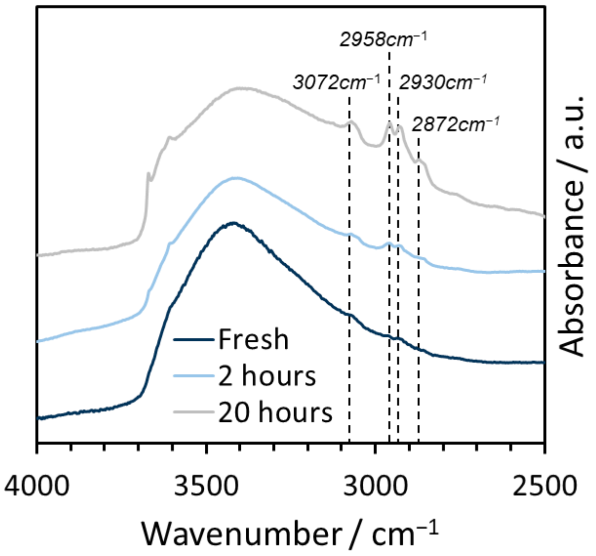

Figure 6.11: FTIR spectra of fresh 2.5%Ni-UiO-66 and spent fresh 2.5%Ni-UiO-66 catalyst after dimerization for 2 h and 20 h.

A pellet with a mass ratio of MOF to KBr of 1/100 was prepared and activated as described above. The spectra were collected at room temperature in transmission mode. The broad band at ~3200-3600 cm^{-1} for all three spectra is assigned to the O-H vibration from water molecules in the pores. The peak at 3072 cm^{-1} corresponds to the C-H vibration in =C-H. The peak at 2930 cm^{-1} is attributed to C-H vibration in $-CH_2$, and the peaks at 2872 and 2958 cm^{-1} are assigned to the C-H vibration in $-CH_3$. The observation proves that there are hydrocarbons adsorbed on Ni-UiO-66 after the dimerization reaction. It also suggests that the amount of adsorbed species was accumulating with reaction time.

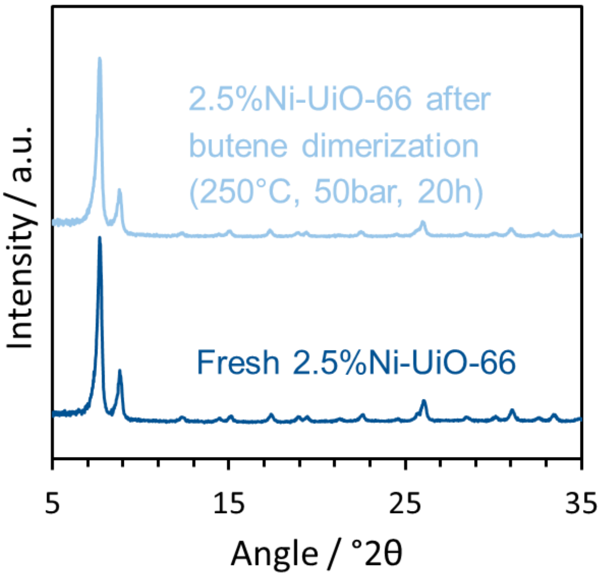

Figure 6.12: XRD patterns of fresh 2.5%Ni-UiO-66 and spent fresh 2.5%Ni-UiO-66 catalyst after butene dimerization.

XRD patterns demonstrate that the crystallinity of the material is retained after reaction performed at 250 °C and 50 bar of butene for 20 h.

6.1.3 XAFS measurements and simulations

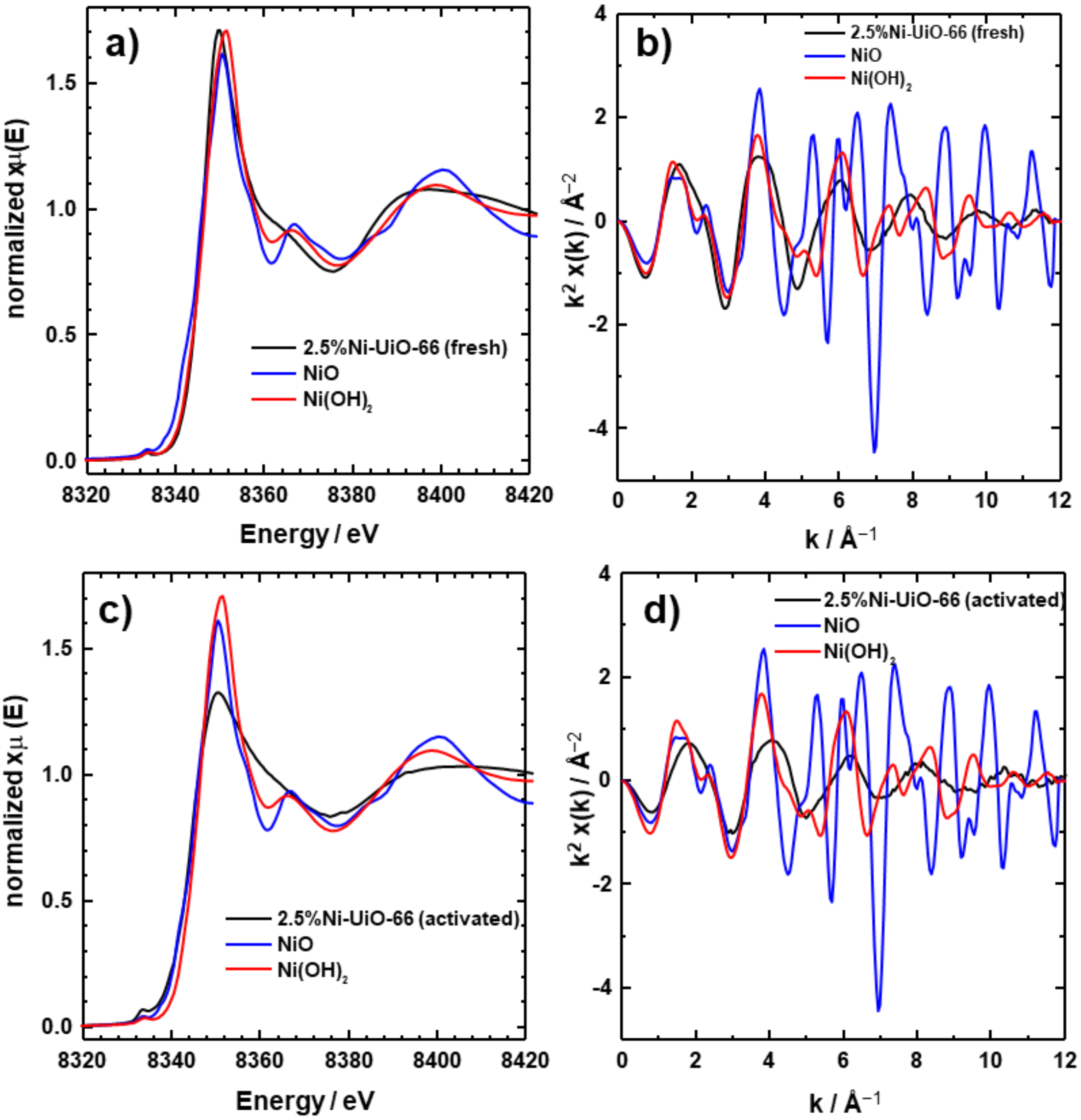

Figure 6.13: Comparison of k^2-weighted Ni K-edge normalized XANES spectra and $\chi(k)$ plots of fresh and activated 2.5%Ni-UiO-66. Spectra of reference materials are also shown.

The spectra show that Ni in the fresh sample is similar to $Ni(OH)_2$. The structure of Ni exhibit features in between NiO and $Ni(OH)_2$ after activation in helium at 300 °C.

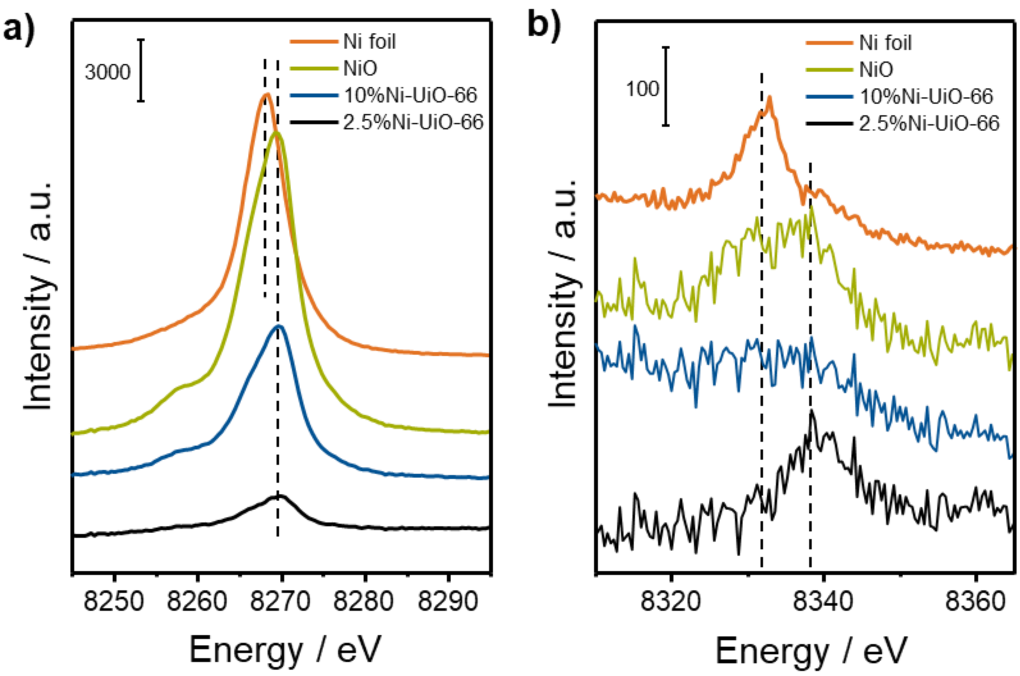

Figure 6.14: a) Ni core-to-core *Kβ* XES spectra and b) valence-to-core *Kβ* XES spectra of the Ni-UiO-66 samples. The XES spectra of metallic Ni and NiO are also included.

The position of core-to-core *Kβ* peaks (also named as $K\beta_{1,3}$ lines) can be related to the number of unpaired spins at the absorbing atom, which was used to determine the oxidation state. In particular, changes in the oxidation state were analyzed by the shift of the $K\beta_{1,3}$ peak. Compared to XANES, the shifts are more linearly correlated with the oxidation state and depend less on the structure.[253] Thus, the XES spectra confirm that Ni species in the MOF are divalent, as they have the same peak position at ~8269 eV as NiO. The valence-to-core *Kβ* lines (known and $K\beta_{2,5}$) are sensitive to the local structure, e.g., the distance and type of coordinated ligands. Although the $K\beta_{2,5}$ lines for the samples are weak (~8338 eV), we can still conclude that the high Ni loaded 10%Ni-UiO-66 has the same type of ligand (O) as that of 2.5%Ni-UiO-66. There might also be extra Ni atoms around the central Ni atom in the 10%Ni-UiO-66, as there is a weak signal at 8332 eV, which is also shown in NiO and Ni foil.

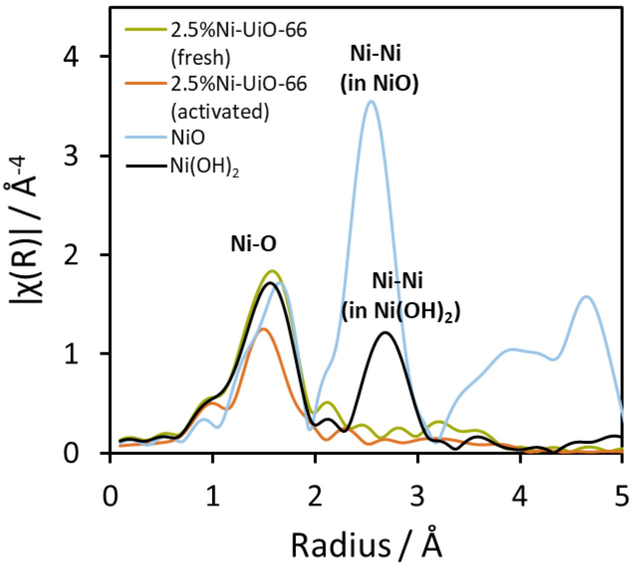

Figure 6.15: k^2-weighted Ni-EXAFS $\chi(R)$ spectra of the freshly prepared and activated 2.5%Ni-UiO-66 (300 °C, helium) and reference compounds.

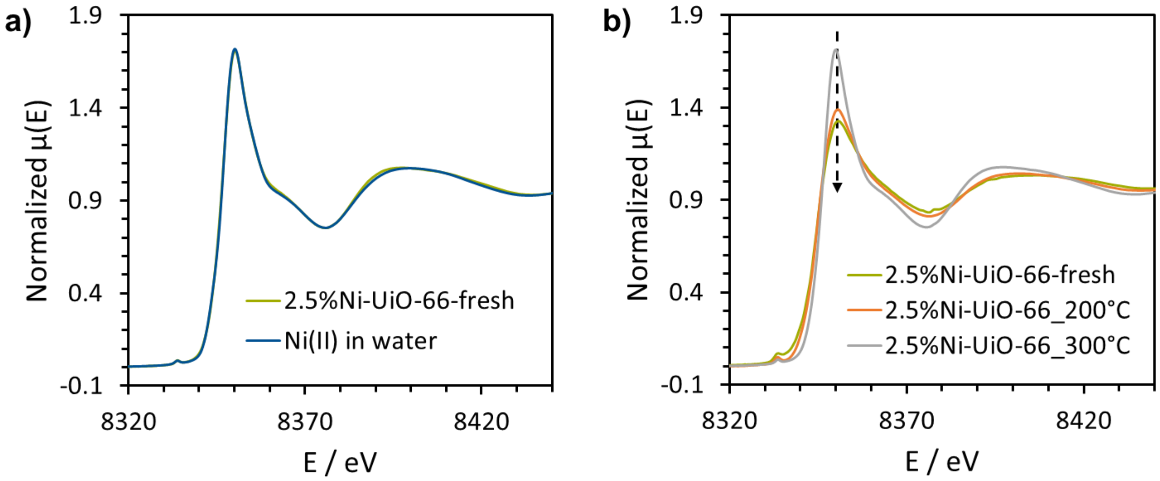

Figure 6.16: a) XANES curves of freshly prepared 2.5%Ni-UiO-66 and Ni^{II} ions in water. These two spectra are nearly identical. b) XANES curves for freshly prepared 2.5%Ni-UiO-66 and after treatment in helium at 200 °C and 300 °C.

The two spectra of freshly prepared 2.5%Ni-UiO-66 and Ni^{II} ions in water are nearly identical. The decrease in the white line upon activation is due to less ligands in the first shell, e.g., dehydration here.

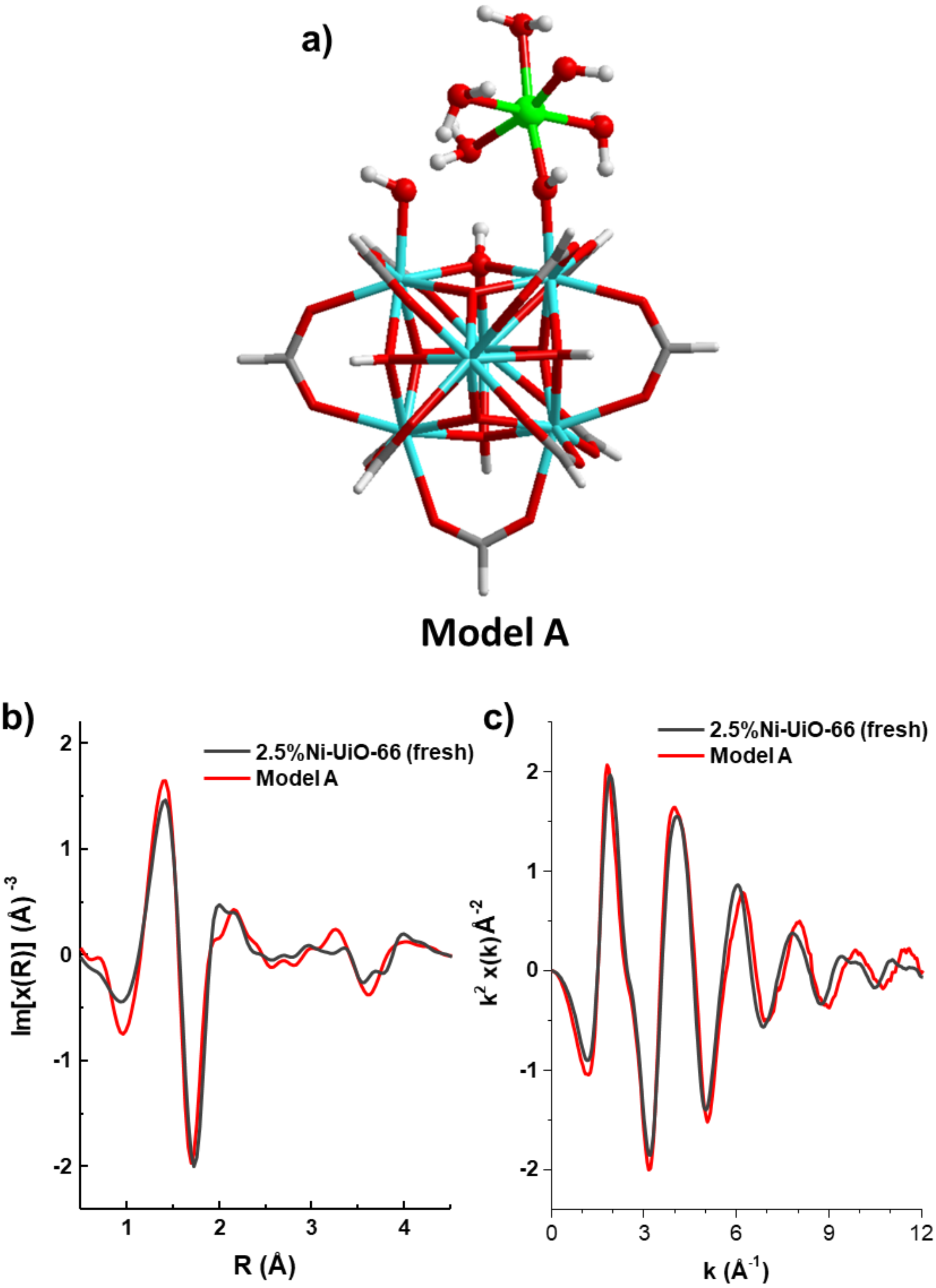

Figure 6.17: a) Proposed DFT optimized model (Model A) for Ni species in the fresh 2.5%Ni-UiO-66. The k^2-weighted Ni-EXAFS, b) Img[$\chi(R)$] and c) $\chi(k)$ spectra of experimentally measured freshly prepared 2.5%Ni-UiO-66 (black curve) and the FEFF simulated EXAFS spectra of Model A (red graph).

The simulated spectra match nearly perfect with the experimental measured results.

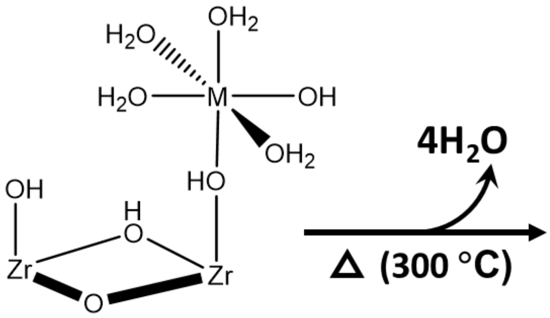

Figure 6.18: Possible dehydration reaction during the heat treatment of Ni-UiO-66 in helium at 300 °C.

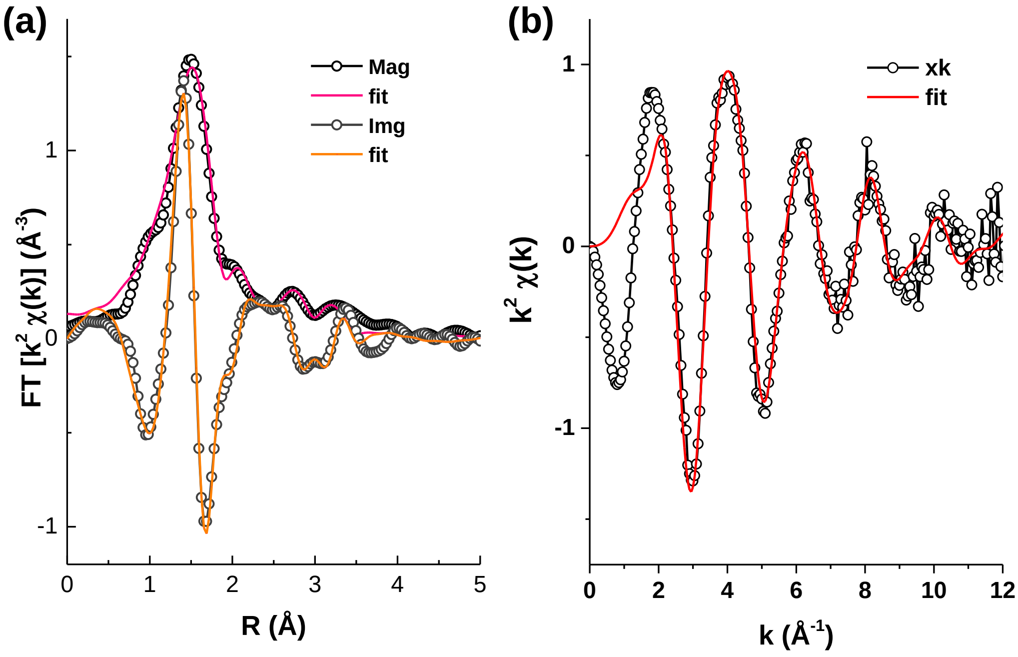

Figure 6.19: k^2-weighted Ni K-edge a) Mag[$\chi(R)$] and Img[$\chi(R)$] spectra, and b) $\chi(k)$ plots of activated 1.3%Ni-UiO-66, and the corresponding FEFF fits.

Table 6.5: EXAFS fitting results of activated 1.3%Ni-UiO-66

Back scatters	**Coordination number**	**Interatomic distances / Å**	**Debye-Waller factor / $\Delta\sigma^2$, Å^2**
Ni-O	3.2 ± 0.3	1.912 ± 0.021	0.0059 ± 0.0013
Ni-Ni	-	-	-

Ni-Zr	1.4 ± 0.7	3.592 ± 0.020	0.0139 ± 0.0027

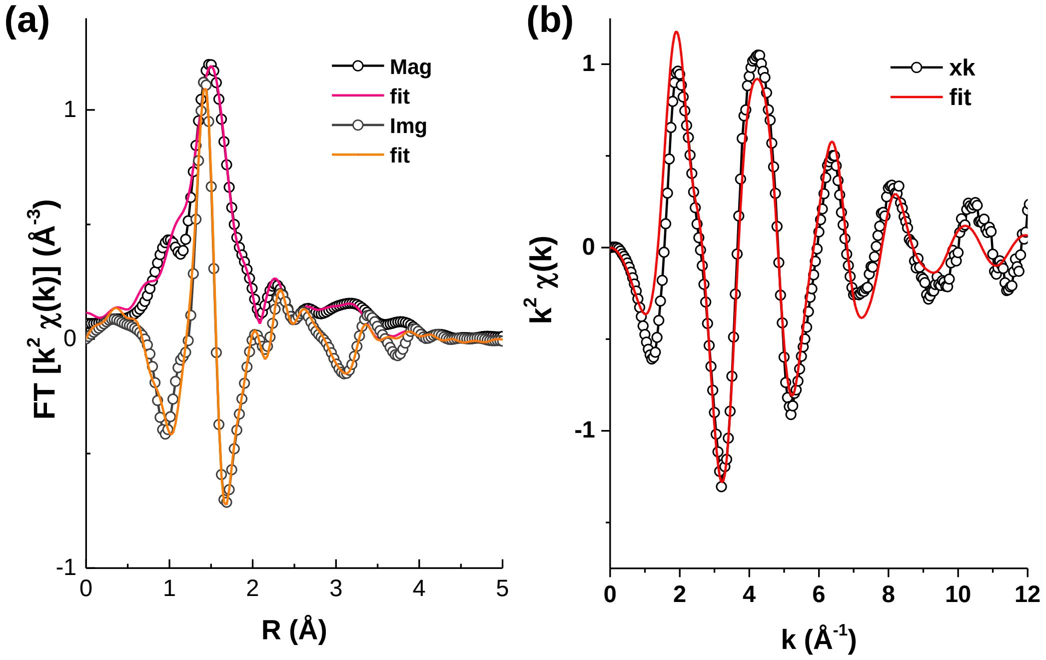

Figure 6.20: k^2-weighted Ni K-edge a) Mag[$\chi(R)$] and Img[$\chi(R)$] spectra, and b) $\chi(k)$ plots of activated 2.5%Ni-UiO-66, and the corresponding FEFF fits.

Table 6.6: EXAFS fitting results of activated 2.5%Ni-UiO-66

Back scatters	**Coordination number**	**Interatomic distances / Å**	**Debye-Waller factor / $\Delta\sigma^2$, Å^2**
Ni-O	3.0 ± 0.4	1.908 ± 0.015	0.0077 ± 0.0011
Ni-Ni	-	-	-
Ni-Zr	1.1 ± 0.5	3.601 ± 0.022	0.0166 ± 0.0029

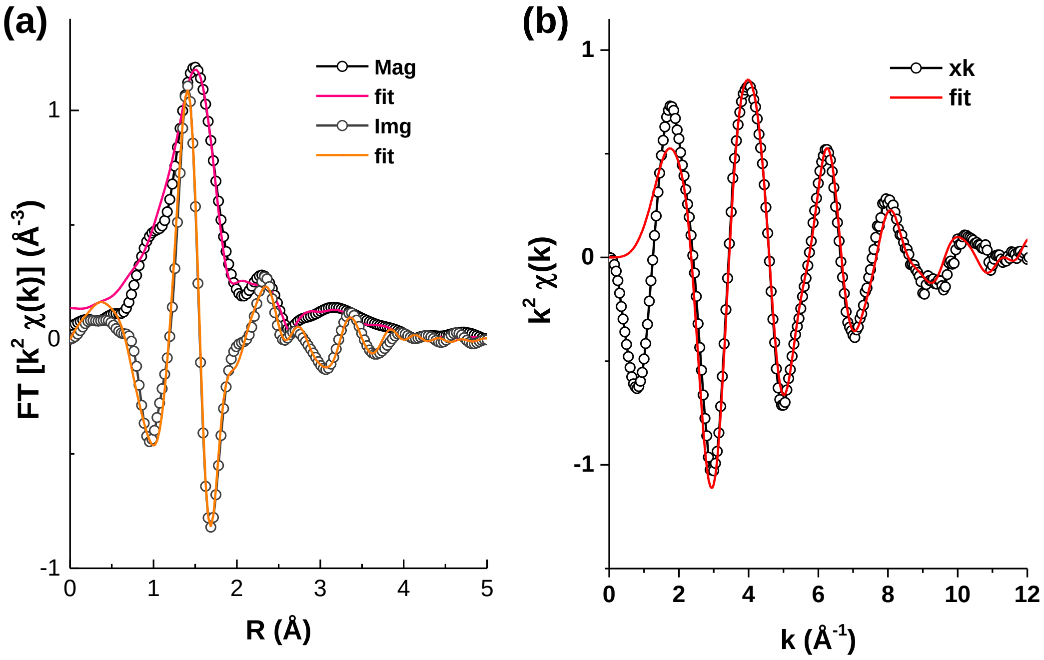

Figure 6.21: k^2-weighted Ni K-edge a) Mag[$\chi(R)$] and Img[$\chi(R)$] spectra, and b) $\chi(k)$ plots of activated 5%Ni-UiO-66, and the corresponding FEFF fits.

Table 6.7: EXAFS fitting results of activated 5%Ni-UiO-66

Back scatters	**Coordination number**	**Interatomic distances / Å**	**Debye-Waller factor / $\Delta\sigma^2$, Å^2**
Ni-O	3.4 ± 0.4	1.912 ± 0.036	0.0063 ± 0.0019
Ni-Ni	0.3 ± 0.2	2.972 ± 0.029	0.0106 ± 0.0020
Ni-Zr	0.8 ± 0.5	3.603 ± 0.031	0.0179 ± 0.0037

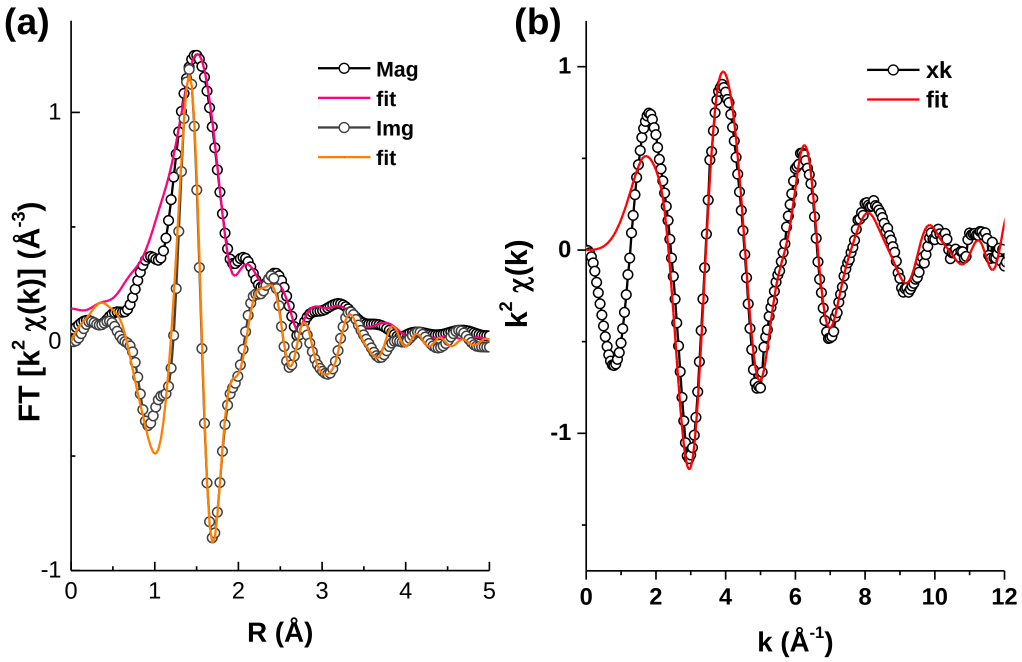

Figure 6.22: k^2-weighted Ni K-edge a) Mag[$\chi(R)$] and Img[$\chi(R)$] spectra, and b) $\chi(k)$ plots of activated 10%Ni-UiO-66, and the corresponding FEFF fits.

Table 6.8: EXAFS fitting results of activated 10%Ni-UiO-66

Back scatters	Coordination number	Interatomic distances / Å	Debye-Waller factor / $\Delta\sigma^2$, Å^2
Ni-O	3.6 ± 0.5	1.917 ± 0.036	0.0094 ± 0.0011
Ni-Ni	0.9 ± 0.5	2.979 ± 0.014	0.0121 ± 0.0029
Ni-Zr	-	-	-

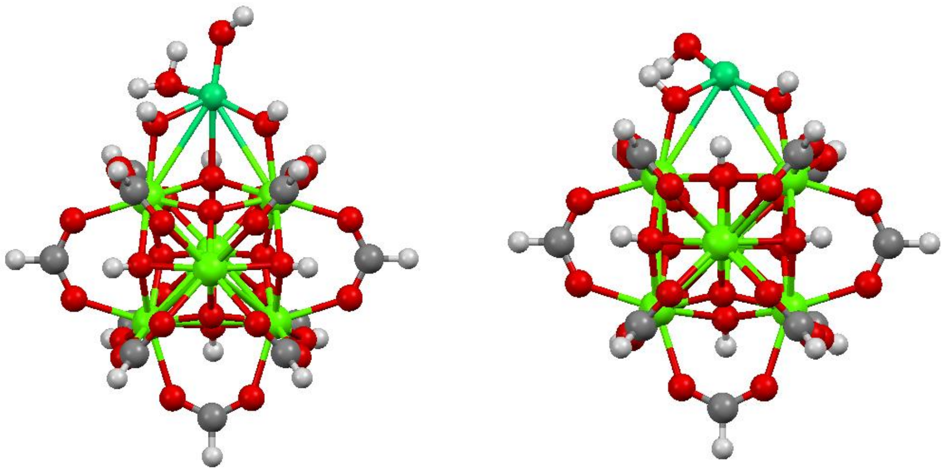

Model B (-OH/-H$_2$O) **Model C (-OH)**

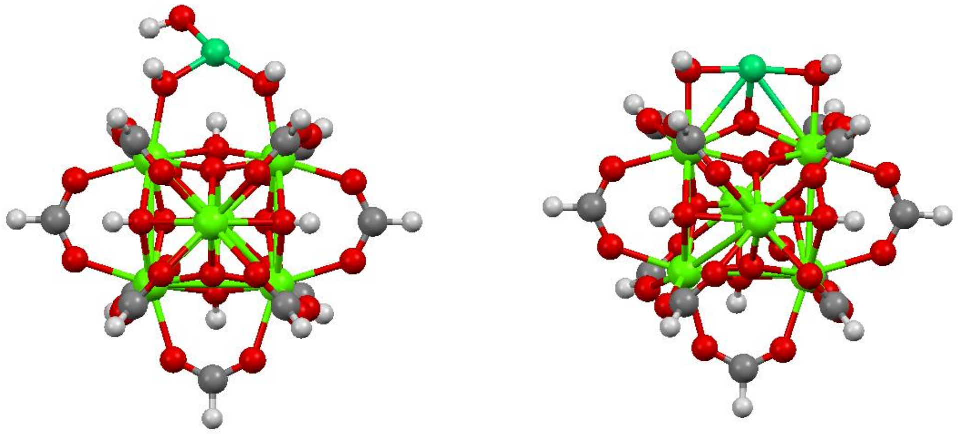

Model D (-OH) **Model E (bare Ni)**

Figure 6.23: DFT-optimized structures of monomeric Ni-UiO-66 cluster models. (Color code: Zr (light green), Ni (dark green), H (light grey), C (dark grey), O (red)).

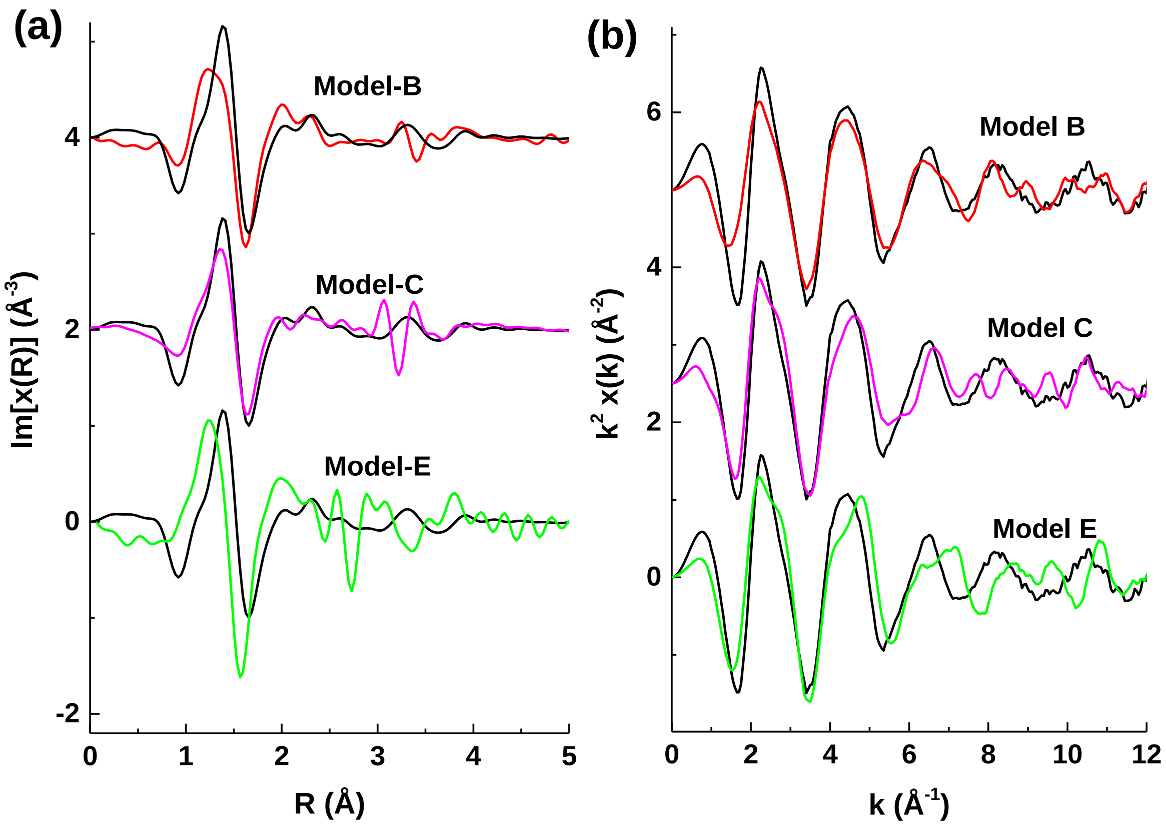

Figure 6.24: The k^2-weighted Ni-EXAFS a) Img[$\chi(R)$] and b) $\chi(k)$ spectra of experimentally measured 2.5%Ni-UiO-66 (black curve) and the calculated EXAFS spectra of DFT optimized models from **Figure 6.23**.

6.1.4 Mechanistic calculations

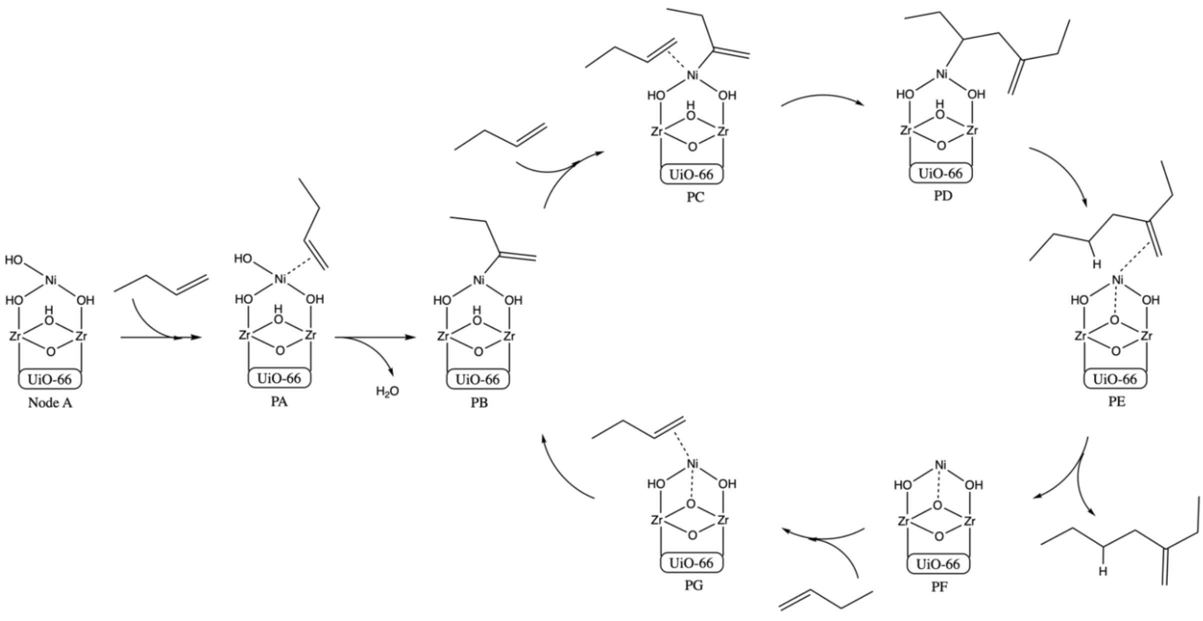

Scheme 6.1: Proton-transfer (Cycle I) mechanism for dimerization of 1-butene starting from M-OH active site.

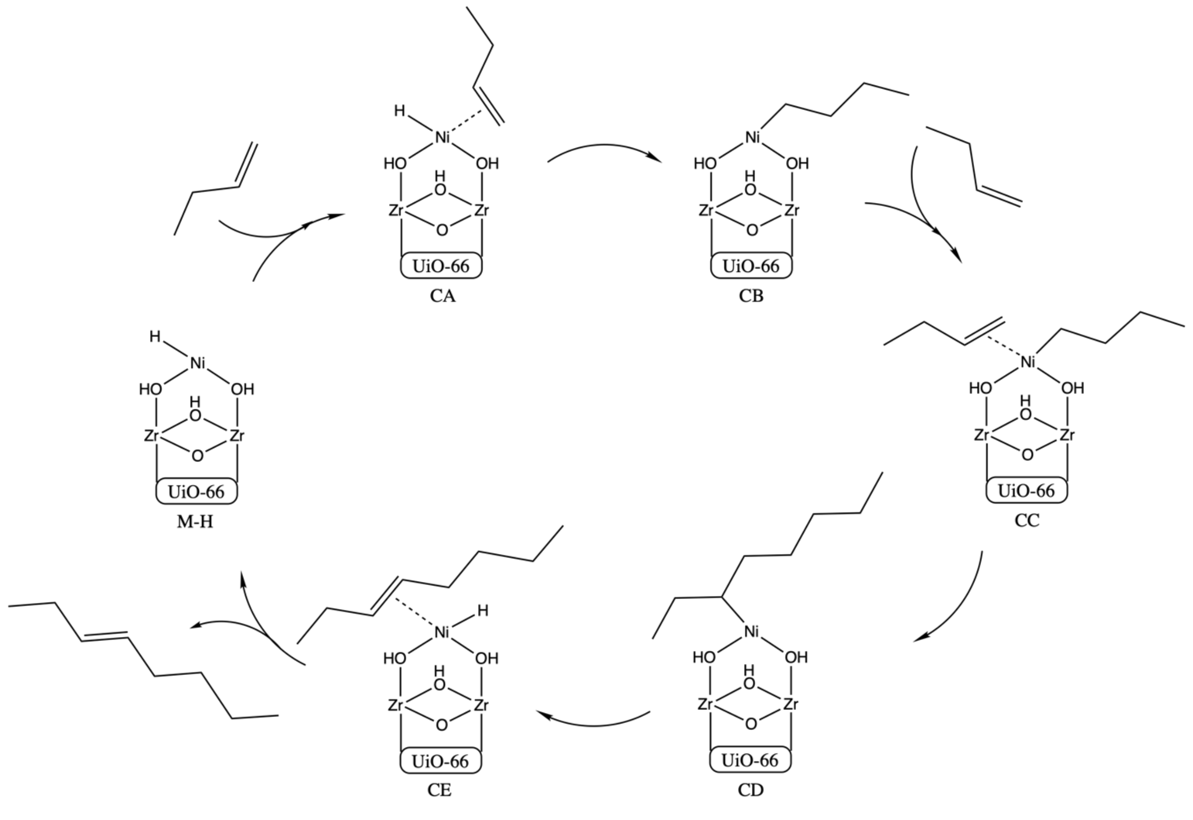

Scheme 6.2: Cossee-Arlman (Cycle II) mechanism for dimerization of 1-butene in the absence of a physisorbed 1-butene molecule.

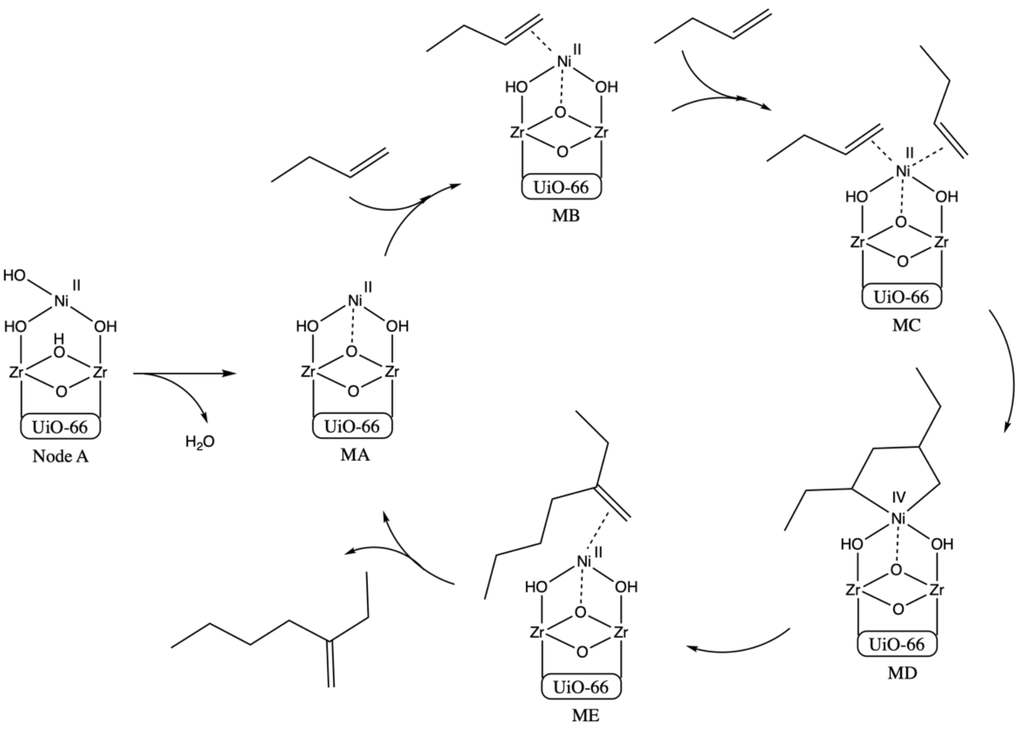

Scheme 6.3: Metallacycle (Cycle III) mechanism for dimerization of 1-butene.

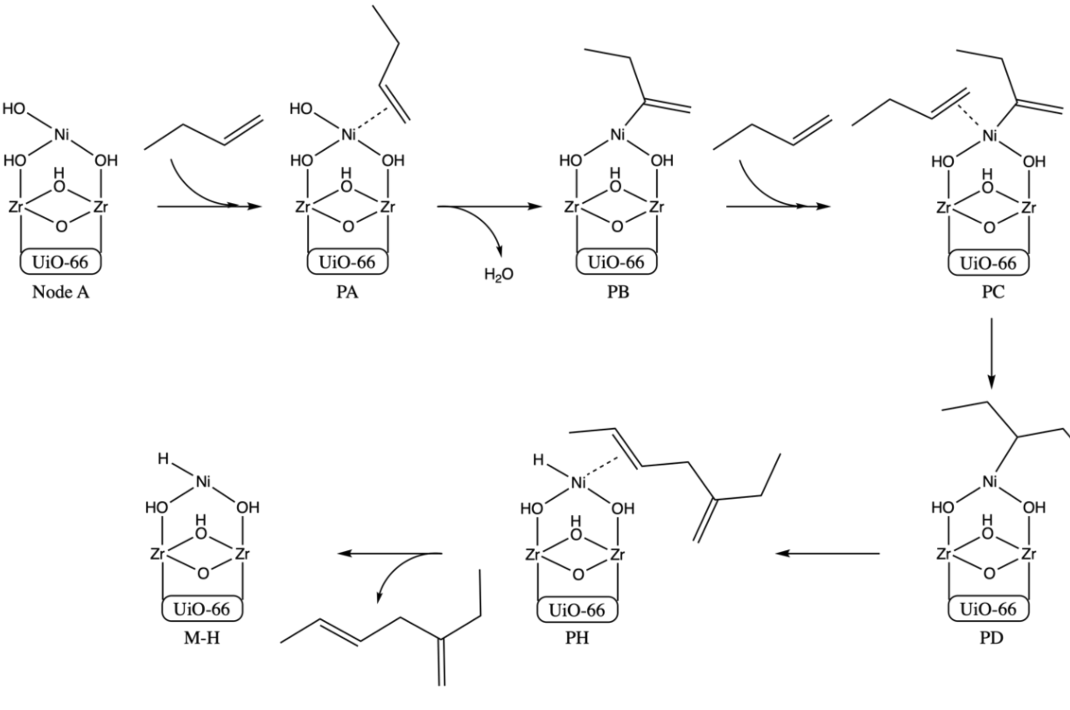

Scheme 6.4: Reaction mechanism for the generation of Ni-H active site for the Cossee-Arlman dimerization mechanism.

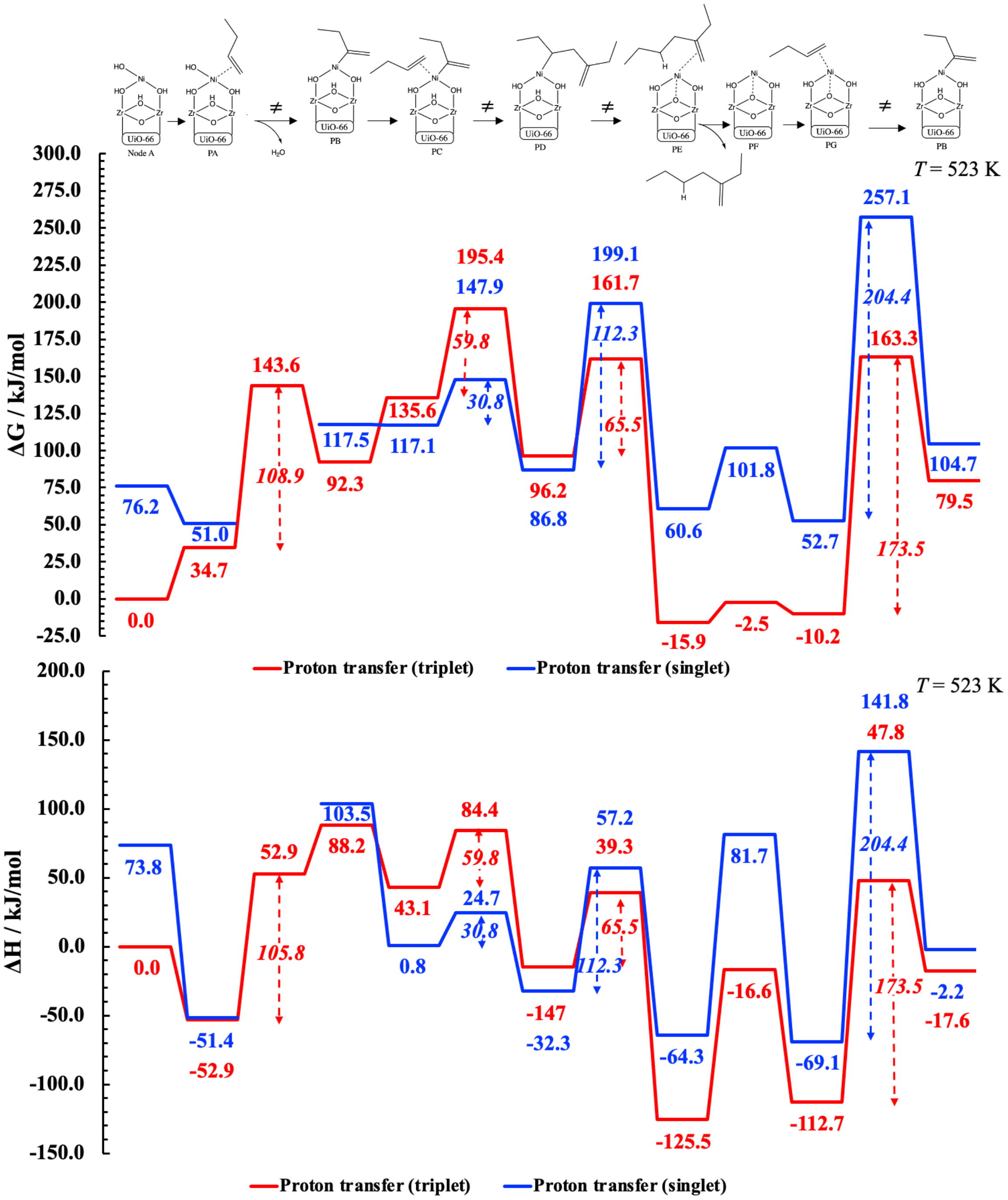

Figure 6.25: Standard free energy diagram (top) and enthalpy diagram (bottom) for the dimerization of 1-butene following the proton transfer mechanism on Ni-UiO-66 in triplet (red) and singlet (blue) spin state at $T = 250$ °C and $p = 1$ bar.

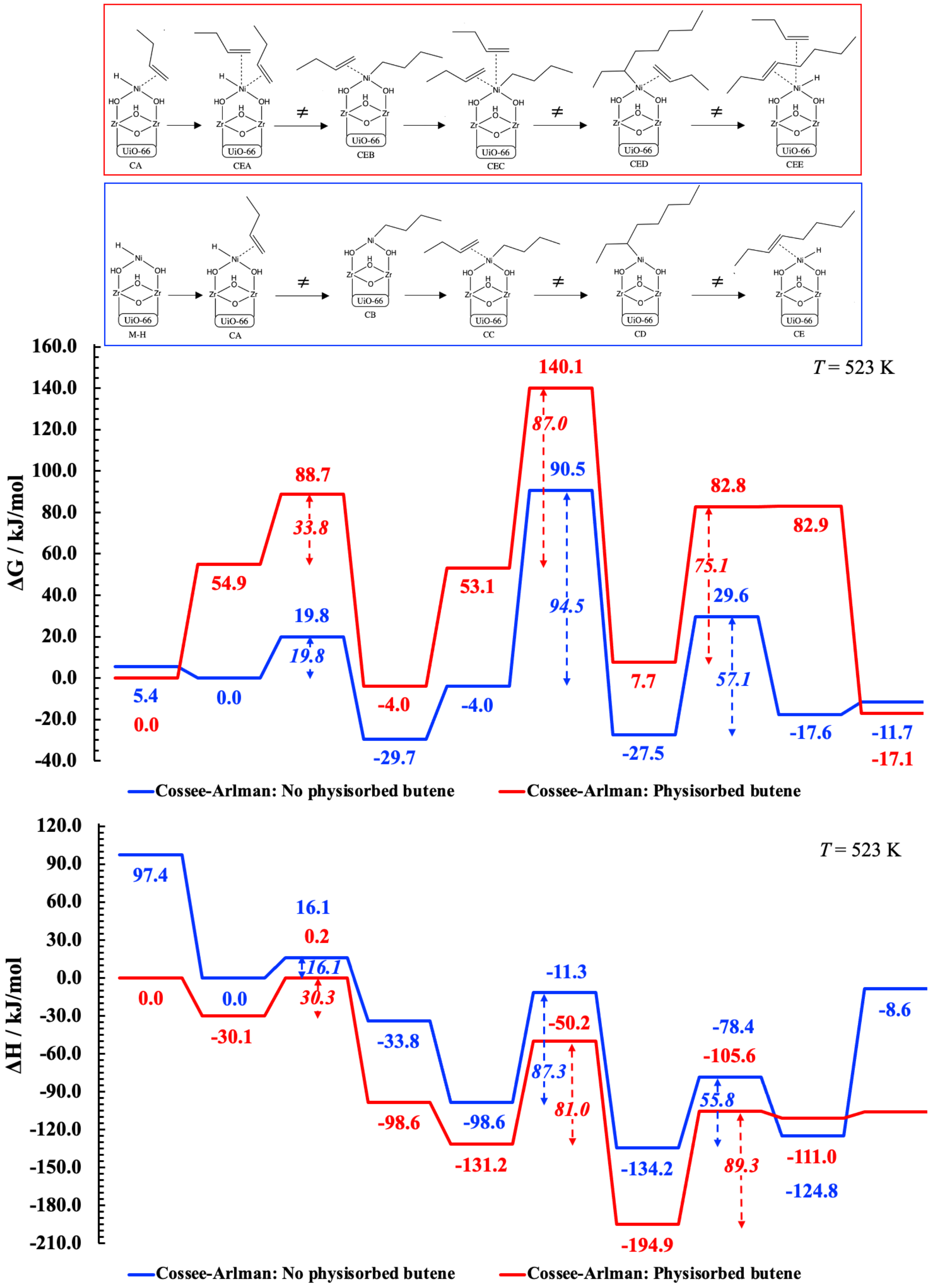

Figure 6.26: Standard free energy diagram (top) and enthalpy diagram (bottom) for generation of Ni-H active site following the Cossee-Arlman reaction mechanism on Ni-UiO-66 in the presence (red) and absence (blue) of a physisorbed 1-butene molecule at T = 250 °C and p = 1 bar.

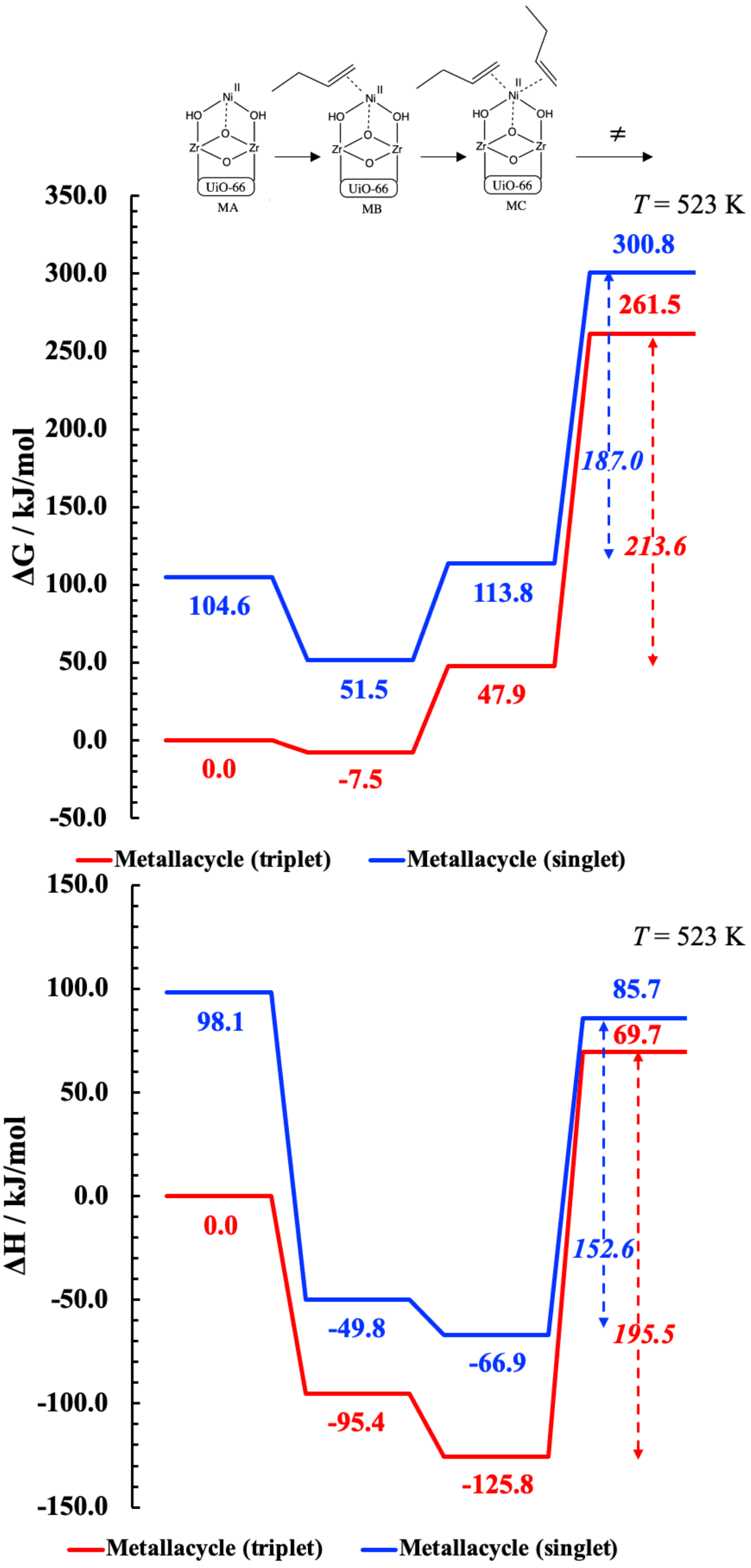

Figure 6.27: Standard free energy diagram (top) and enthalpy diagram (bottom) for dimerization of 1-butene following the metallacycle mechanism on Ni-UiO-66 in triplet (red) and singlet (blue) spin states at $T = 250$ °C and $p = 1$ bar.

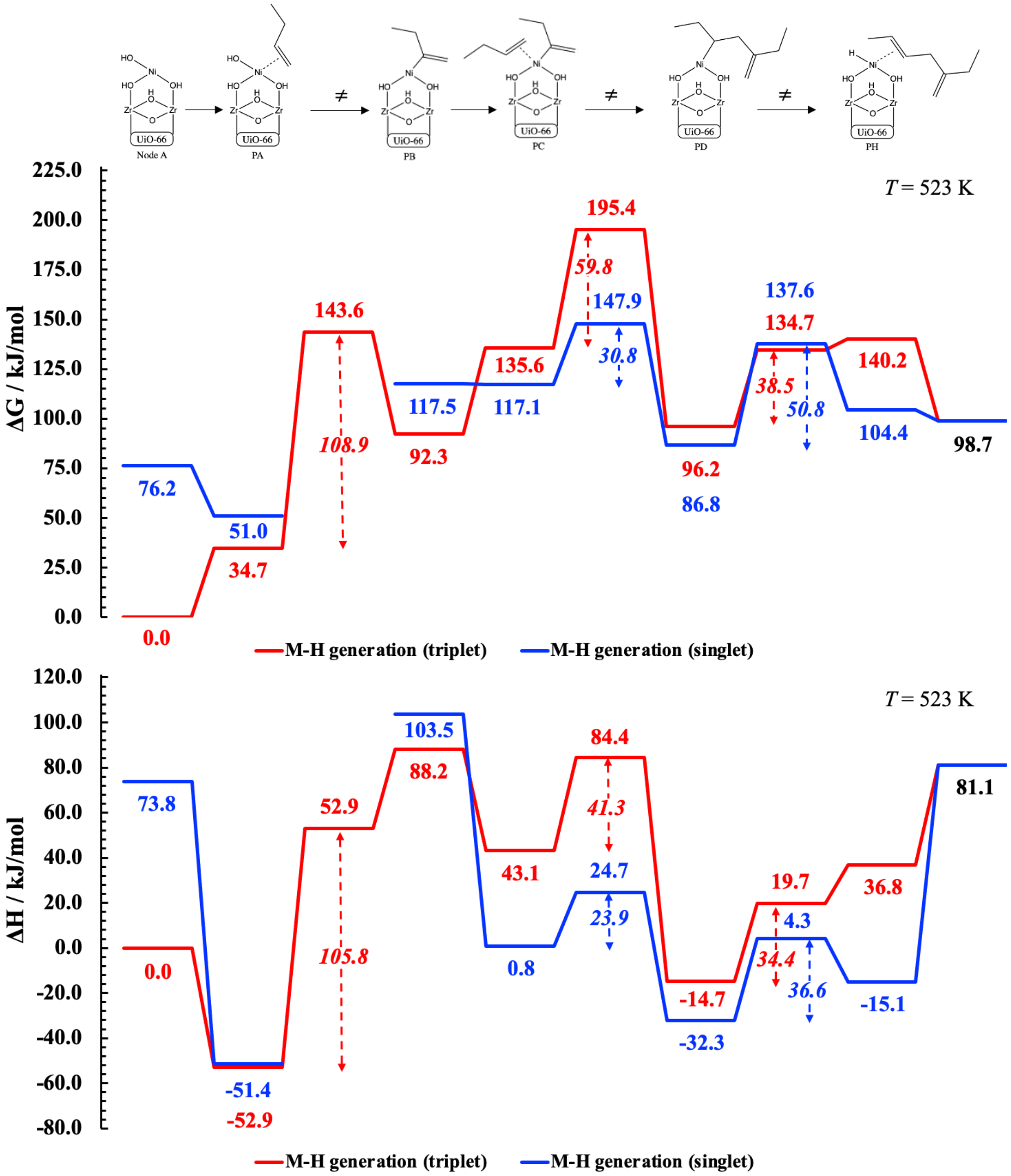

Figure 6.28: Standard free energy diagram (top) and enthalpy diagram (bottom) for generation of Ni-H active site following the proton transfer mechanism on Ni-UiO-66 in triplet (red) and singlet (blue) spin state at $T = 250$ °C and $p = 1$ bar.

6.2 Supporting information: Influence of adsorption on butene dimerization activity of single metal cations on UiO-66 nodes

6.2.1 Structure elucidation of parent UiO-66

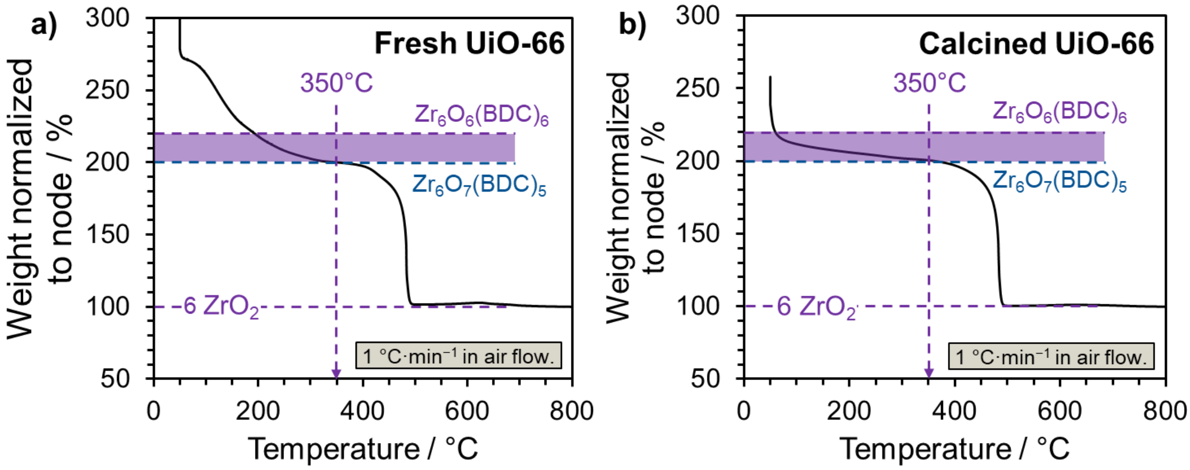

Figure 6.29: Thermogravimetric analysis (TGA) of a) the fresh parent UiO-66 and b) the calcined UiO-66 (for 4 h at 250 °C in nitrogen), showing for both materials a normalized wight of 200% at 350 °C. The weight was normalized to the end weight.

The organic composition of the material was analyzed based on the principle of spontaneous combustion and subsequent separation by gas chromatography of the evolving gases using an elemental analyzer. For the chlorine analysis, the material without prior treatment was weighed into a platinum boat and heated up to 1000 °C. The remainings were analyzed in terms of chlorine content *via* titration. The resulting amounts in $\mathrm{mol{\cdot}g_{cat}^{-1}}$ were then normalized to the amount of carbon, as for each sample 40 $\mathrm{mol_C{\cdot}mol_{node}^{-1}}$ from the BDC linkers can be assumed. As the amount of dimethylformamide (DMF) is very little, the number of carbon atoms from the DMF can be neglected.

Table 6.9: Elemental analysis of p-UiO-66 (the molar mass was calculated from the TGA measurements)

	p-UiO-66		
Temperature	**250 °C**	**300 °C**	**350 °C**
Defect sites / mol·mol$_{node}^{-1}$	2.0	2.0	2.0
Cl / mol·mol$_{node}^{-1}$	0.60	0.50	0.35
C / mol·mol$_{node}^{-1}$	40.0	40.0	40.0
H / mol·mol$_{node}^{-1}$	72.0	56.7	54.7
N / mol·mol$_{node}^{-1}$	0.62	0.59	0.35
Free Defect sites / mol·mol$_{node}^{-1}$	**0.78**	**0.91**	**1.09**

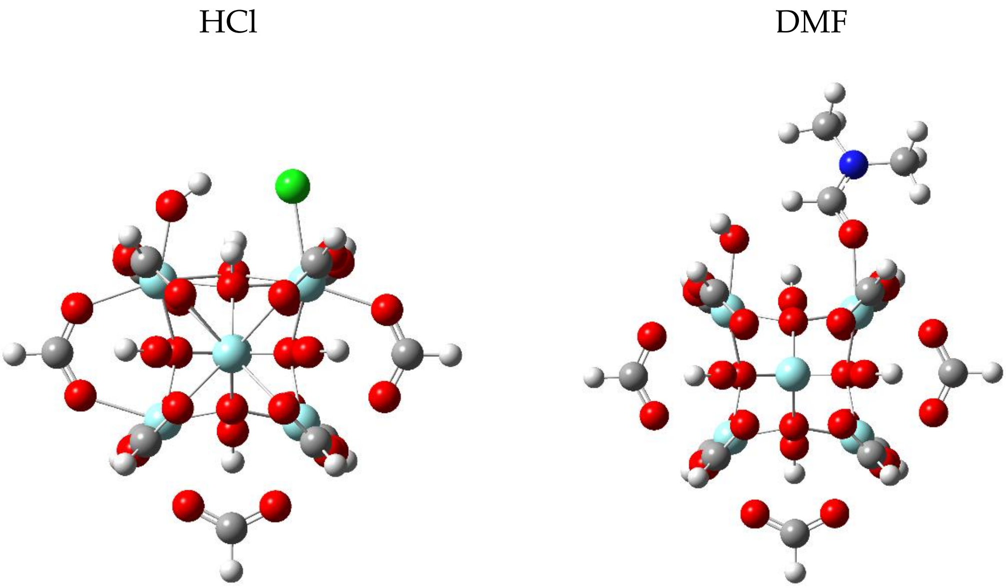

HCl

DMF

$\Delta H = -98.0\ kJ\cdot mol^{-1}$

$\Delta G = -53.2\ kJ\cdot mol^{-1}$

$\Delta H = -125.8\ kJ\cdot mol^{-1}$

$\Delta G = -72.0\ kJ\cdot mol^{-1}$

Figure 6.30: Computed binding enthalpies and free energies for dissociated HCl and DMF on a defect site in UiO-66.

D_2O adsorption on p-UiO-66

The parent sample was monitored by IR spectroscopy in the transmission absorption mode (sample were pressed into self-supporting wafers). Once the wafer was in place, the temperature was raised to 250 °C and maintained for 2 h under vacuum ($p < 10^{-5}$ mbar). The spectra were recorded on a Vertex 70 spectrometer from Bruker Optics at a resolution of 4 cm^{-1} collecting 120 scans at 50 °C.

The H-D exchange was performed by dosing D_2O into the IR cell at 250 °C until no Zr-OH band (3672 cm^{-1}) existed on the IR spectra, following with an activation treatment (250 °C for 2 h under vacuum).

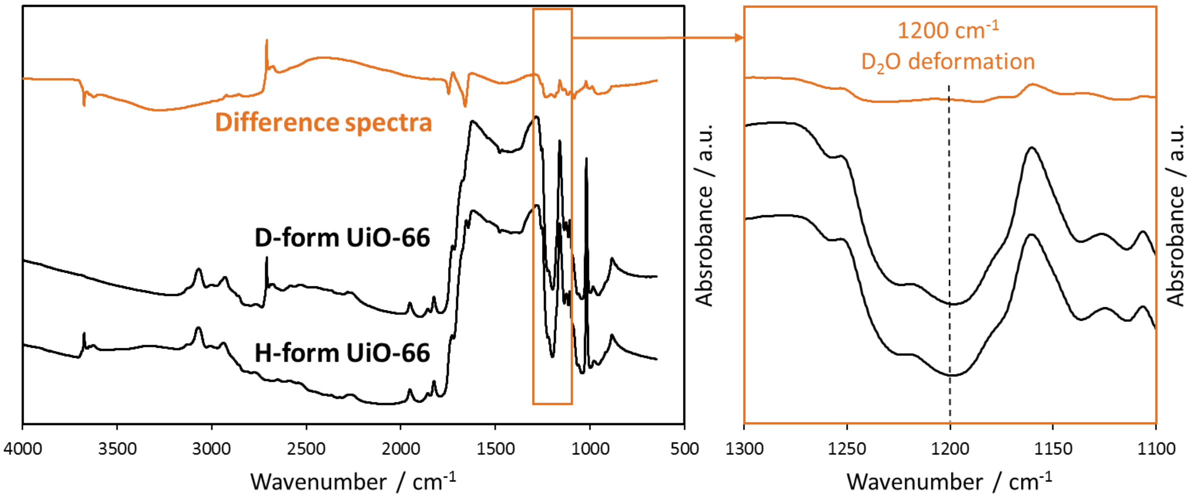

Figure 6.31: IR spectra of H-form and D-form of the UiO-66 and the difference spectra (D-form subtracting H-form). Spectra were collected at 50 °C under vacuum ($p < 10^{-5}$ mbar). Samples were pretreated at 250 °C for 2 h before collecting the IR spectra.

6.2.2 Simulated IR spectra for different UiO-66 models

The cluster models used to denote the vacant defect sites (activated UiO-66), chlorine-containing defect sites (UiO-66-HCl), and DMF-containing defect sites (UiO-66-DMF) and the corresponding individual peak assignments in the -OH stretching region (3600-3800 cm^{-1}) are shown in sub-**Sections 2.6.1**, **2.6.2**, and **2.6.3** respectively. Cumulative IR spectra (**Figure 3.2** and **Error! Reference source not found.b**, bottom) representing the synthesized defective p-UiO-66 sample and Ni-UiO-66 sample was further obtained as a combination of the simulated spectra of the different defect sites, weighted by the experimentally determined number of each defect site. The simulated cumulative IR spectra for the p-UiO-66 sample and Ni-UiO-66 sample show good agreement with the experimental IR spectra (within 30 cm^{-1}). The simulated IR spectra exhibit an additional peak at 3605 cm^{-1} which corresponds to the dissociated proton, (μ_3-O)H, on the chlorine-containing defect site. A possible reason for this might be a lower intensity of this peak in the experimental IR spectra which makes it difficult to separate from the background noise. Moreover, this proton can be delocalized on the different faces of the UiO-66-Cl defect-containing node at available μ_3-O groups leading to the absence (or lowered intensity) of this peak in the experimental IR spectra.

Simulated IR spectrum for activated UiO-66

The cluster model for activated UiO-66 and the corresponding simulated IR spectrum are shown below in **Figure 6.32**.

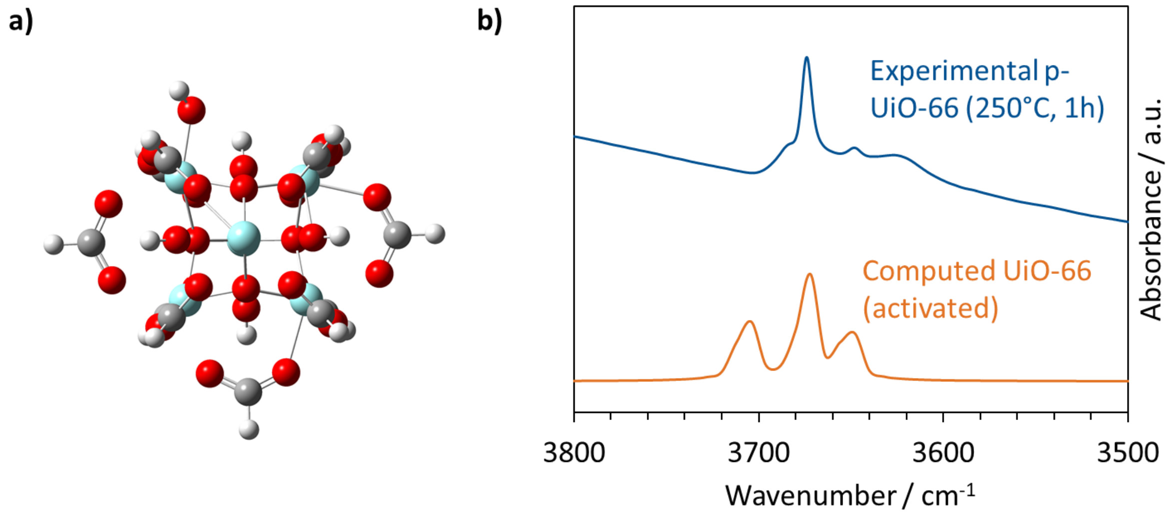

Figure 6.32: a) Cluster model for activated UiO-66. Color code: Zr (cyan), O (red), C (gray), H (white). b) Simulated IR spectrum for activated UiO-66 model using M06-L functional and scaled by a factor of 0.943.

Three peaks were obtained at 3648 cm^{-1}, 3673 cm^{-1}, and 3704 cm^{-1} corresponding to the μ_3-OH stretch in the defect plane, μ_3-OH stretches in the other plane, and terminal -OH stretch, respectively.

Simulated IR spectrum for UiO-66-HCl

The cluster model for UiO-66-HCl and the corresponding simulated IR spectrum are shown below in **Figure 6.33**. The HCl is dissociated, meaning the Cl is located on the Zr of the defect site, while the proton is on the bridging μ_3-O.

The μ_3-OH stretch due to the dissociated proton on the μ_3-O (top and front in the model above) occurs at 3560 cm^{-1}. The asymmetric and symmetric stretches due to the terminal -OH and the μ_3-OH (top and behind in the model above) occur at 3632-3640 cm^{-1}. Lastly, the -OH vibrations due to the remaining μ_3-OH groups are obtained at 3664-3672 cm^{-1}.

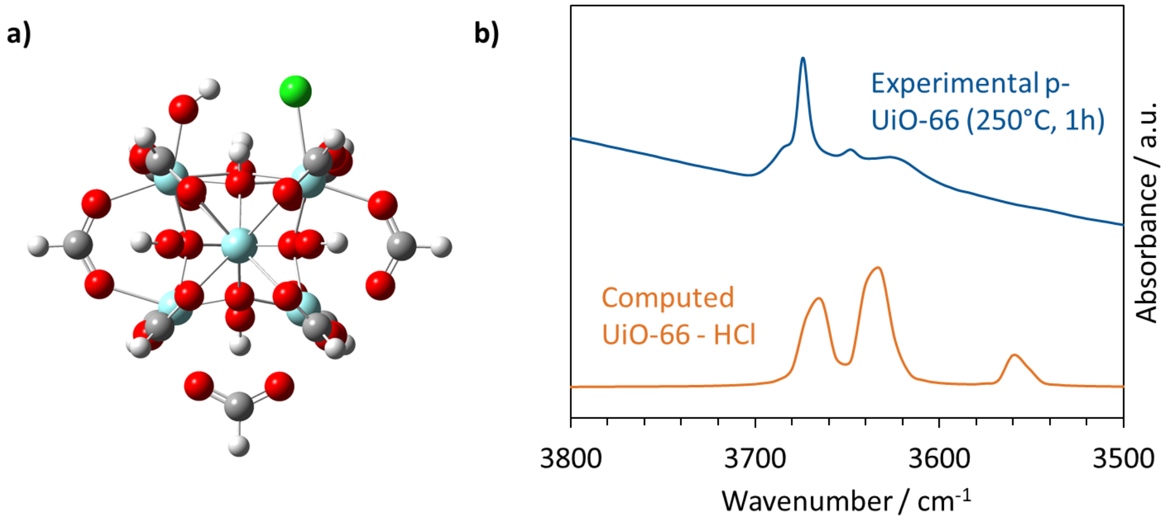

Figure 6.33: a) Cluster model for UiO-66-HCl. Color code: Zr (cyan), Cl (green), O (red), C (gray), H (white). b) Simulated IR spectrum for UiO-66-HCl model using M06-L functional and scaled by a factor of 0.943.

Simulated IR spectrum for UiO-66-DMF

The cluster model for UiO-66-DMF and the corresponding simulated IR spectrum are shown below in **Figure 6.34**.

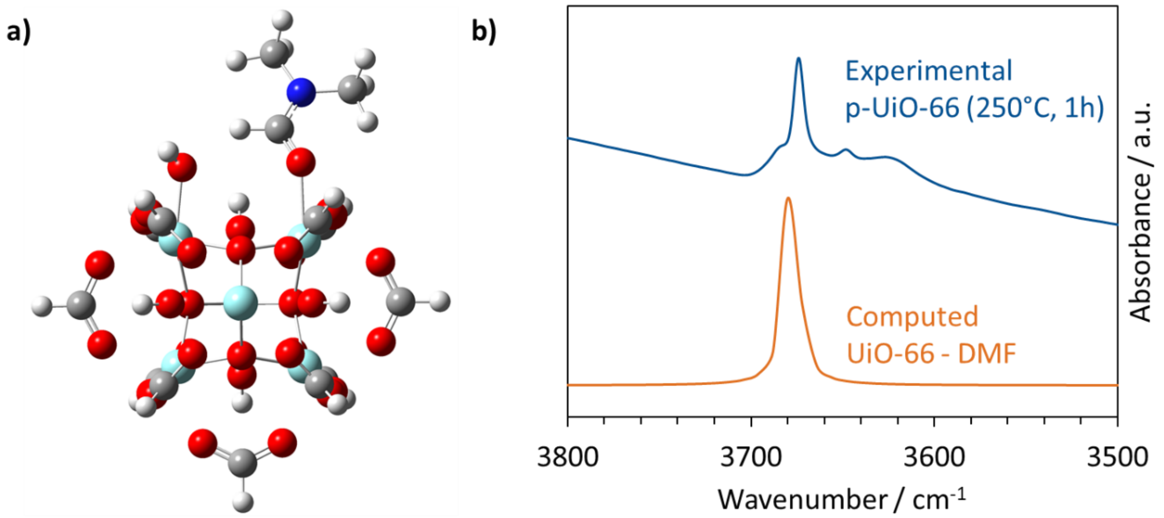

Figure 6.34: a) Cluster model for UiO-66-DMF. Color code: Zr (cyan), O (red), N (blue), C (gray), H (white). b) Simulated IR spectrum for UiO-66-DMF model using M06-L functional and scaled by a factor of 0.943.

The peak observed at 3680 cm^{-1} corresponds to the terminal -OH and μ_3-OH stretches.

Simulated IR spectrum for Ni-UiO-66

The cluster model for activated Ni-UiO-66 and its corresponding simulated IR spectra are shown below.

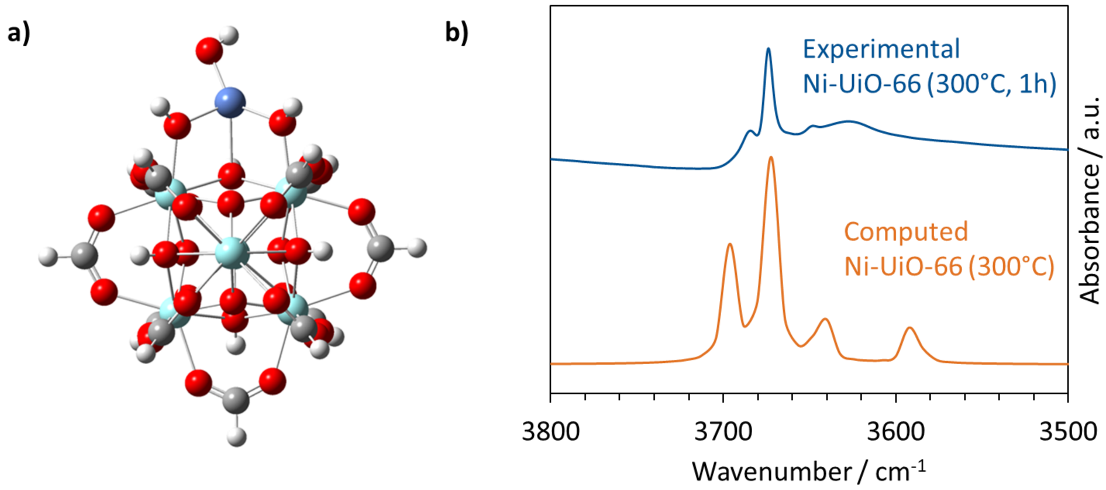

Figure 6.35: a) Cluster model for Ni-UiO-66. Color code: Zr (cyan), Ni (blue), O (red), C (gray), H (white). b) Simulated IR spectrum for Ni-UiO-66 model using M06-L functional and scaled by a factor of 0.943.

The peak observed at 3592 cm^{-1} corresponds to the OH stretch of the μ_3-OH group in the defect plane (below Ni) while the peaks at 3640 cm^{-1}, 3672 cm^{-1}, and 3696 cm^{-1} correspond to -OH stretches of the Ni-OH, remaining μ_3-OH, and bridging Ni-OH-Zr groups.

6.2.3 Structure elucidation of Ni-UiO-66 and other M-UiO-66 (M = Co, Cu, Cr)

XAFS measurements of Ni-UiO-66

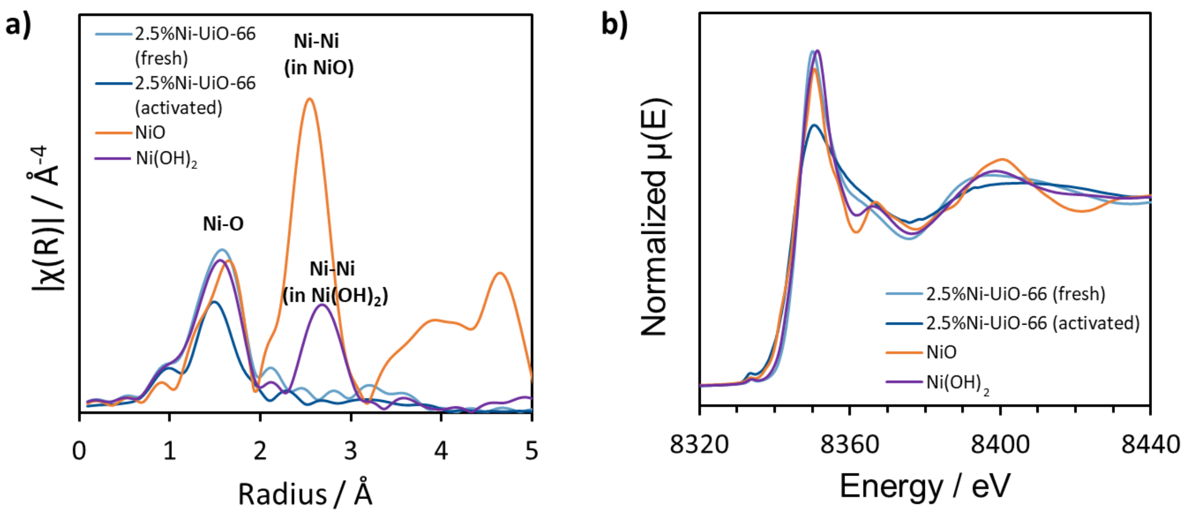

Figure 6.36: XAFS measurements of the freshly prepared and activated (300 °C, helium) 2.5%Ni-UiO-66 and reference compounds: a) k^2-weighted Ni-EXAFS $\chi(R)$ spectra and b) normalized μ(E).

The XAFS measurements confirm single Ni^{2+} cations for the 2.5%Ni-UiO-66.

Elemental analysis of Ni-UiO-66

The organic composition of the material was analyzed based on the principle of spontaneous combustion and subsequent separation by gas chromatography of the evolving gases using an elemental analyzer. For the chlorine analysis, the material without prior treatment was weighed into a platinum boat and heated up to 1000 °C. The remainings were analyzed in terms of chlorine content *via* titration. The resulting amounts in $mol \cdot g_{cat}^{-1}$ were then normalized to the amount of carbon, as for each sample 40 $mol_C \cdot mol_{node}^{-1}$ from the BDC linkers can be assumed. As the amount of DMF is very little, the number of carbon atoms from the DMF.

The metal loading of the catalysts was determined by separate measurement *via* inductively coupled plasma-atomic emission spectroscopy (ICP-AES). Prior to the ICP-AES tests, the samples were activated at 250 °C, weighed and then digested in a mixture of HNO_3/HCl/HF/H_2O followed by H_3BO_3 addition for extra HF treatment.

Table 6.10: Elemental analysis of 2.5%Ni-UiO-66 after activation at different temperatures

	2.5%Ni-UiO-66		
	250 °C	**300 °C**	**350 °C**
Molar Mass of M-UiO-66 at 250 °C / g·mol^{-1}	1621	1603	1590
Nodes at 250 °C / mmol·g^{-1}	0.617	0.624	0.629
Defect sites / mol·mol$_{node}^{-1}$	2.0	2.0	2.0
Cl / mol·mol$_{node}^{-1}$	0.46	0.47	0.58
C / mol·mol$_{node}^{-1}$	40.0	40.0	40.0
H / mol·mol$_{node}^{-1}$	58.2	24.4	34.0
N / mol·mol$_{node}^{-1}$	0.58	0.37	0
Metal / mol·mol$_{node}^{-1}$	0.69	0.69	0.69
Free Defect sites / mol·mol$_{node}^{-1}$	**0.25**	**0.47**	**0.73**

Thermogravimetric analysis of 2.5%M-UiO-66

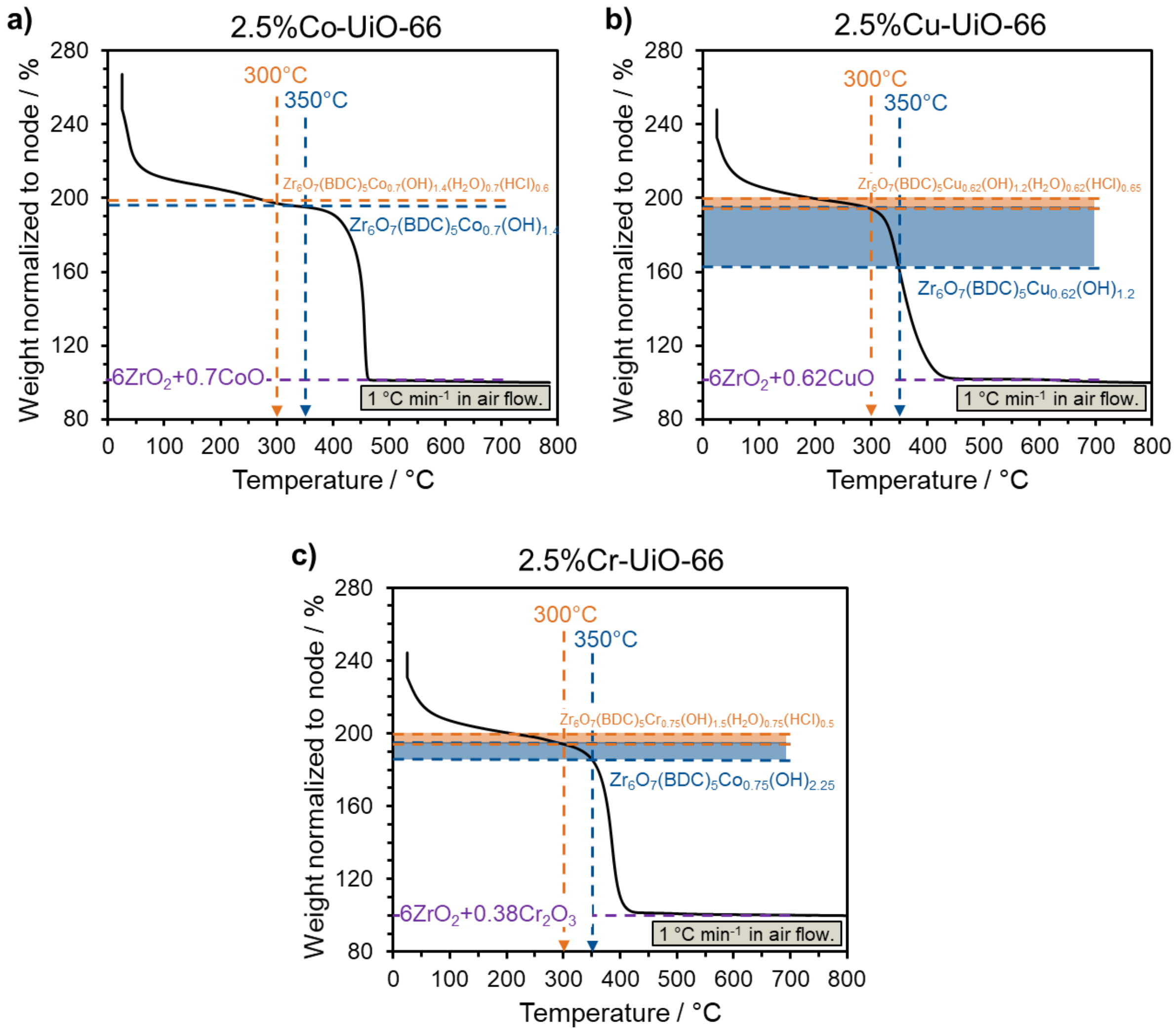

Figure 6.37: TGA curves of a) 2.5%Co-UiO-66 b) 2.5%-Cu-UiO-66 and c) 2.5%Cr-UiO-66. The weight was normalized to the end weight at 800 °C, reflecting 6 ZrO_2 and the corresponding metal oxide.

Elemental analysis of 2.5%M-UiO-66

The organic composition of the material was analyzed based on the principle of spontaneous combustion and subsequent separation by gas chromatography of the evolving gases using an elemental analyzer. For the chlorine analysis, the material without prior treatment was weighed into a platinum boat and heated up to 1000 °C. The remainings were analyzed in terms of chlorine content *via* titration. The resulting amounts in $mol\cdot g_{cat}^{-1}$ were then normalized to the amount of carbon, as for each sample 40 $mol_C\cdot mol_{node}^{-1}$ from the BDC linkers can be assumed. As the amount of DMF is very little, the number of carbon atoms from the DMF can be neglected.

The metal loading of the catalysts was determined by separate measurement *via* ICP-AES. Prior to the ICP-AES tests, the samples were activated at 250 °C, weighed and then digested in a mixture of HNO_3/HCl/HF/H_2O followed by H_3BO_3 addition for extra HF treatment.

Table 6.11: Elemental analysis of 2.5%M-UiO-66 (M = Ni, Co, Cu, Cr) per node after activation at 300 °C. The obtained amounts from elemental analyses were normalized to the amount of carbon.

Elemental Analysis	**2.5%Ni-UiO-66**	**2.5%Co-UiO-66**	**2.5%Cu-UiO-66**	**2.5%Cr-UiO-66**
Molar Mass of M-UiO-66 at 250 °C / g·mol^{-1}	1621	1589	1581	1600
Nodes at 250 °C / mmol·g^{-1}	0.617	0.629	0.632	0.642
Defect sites / mol·mol$_{node}^{-1}$	2.0	2.0	2.0	2.0
Cl / mol·mol$_{node}^{-1}$	0.547	0.47	0.52	0.36
C / mol·mol$_{node}^{-1}$	40.0	40.0	40.0	40.0
H / mol·mol$_{node}^{-1}$	24.4	32.0	33.2	31.1
N / mol·mol$_{node}^{-1}$	0.37	0.20	0.34	0.36
Metal / mol·mol$_{node}^{-1}$	0.69	0.69	0.62	0.75
Free Defect sites / mol·mol$_{node}^{-1}$	**0.47**	**0.64**	**0.52**	**0.53**

D_2O adsorption on Co-UiO-66

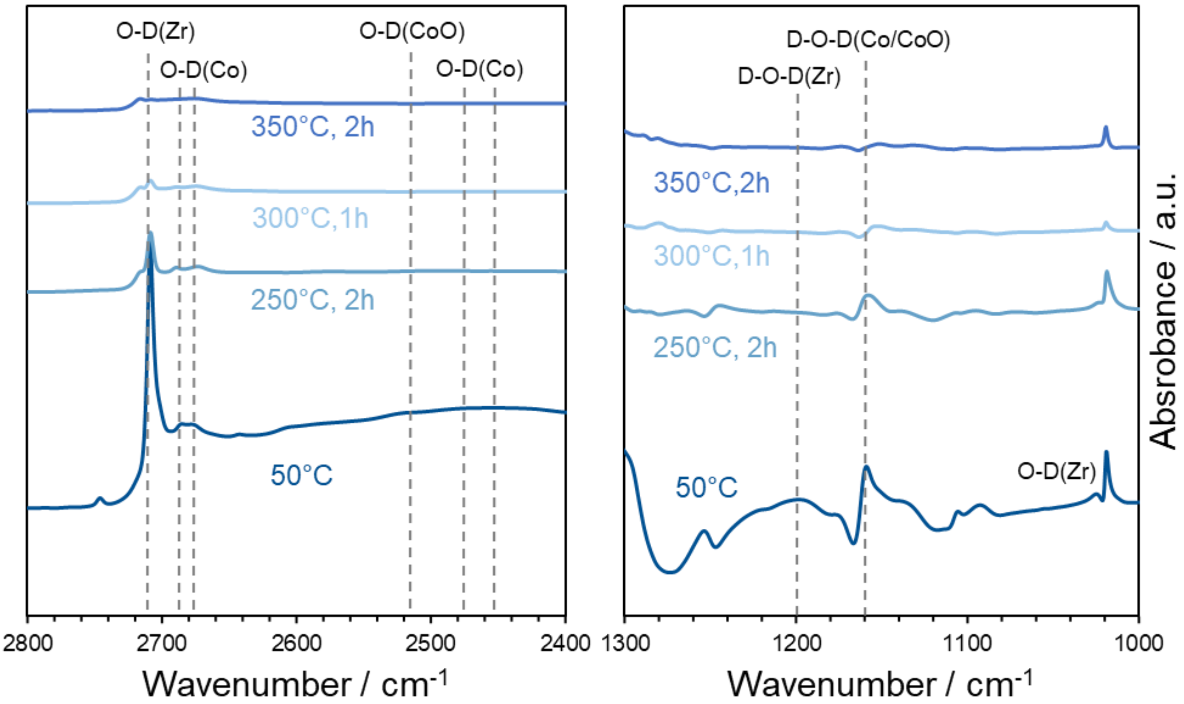

Figure 6.38: D_2O adsorption, monitored by IR, reveals O-D and D-O-D vibration on the cobalt. This leads to the assumption that the degree of hydration changes upon activation resulting in the given structures.

6.2.4 Butene adsorption on p-UiO-66

Thermogravimetric butene adsorption on p-UiO-66

The butene adsorption was measured after activating the sample at 250 °C. This activation temperature was chosen, as this was the activation temperature that was used for the p-UiO-66 before the introduction of the metals. Therefore, the structure at this stage was important to evaluate.

The uptake was fitted according to **Equation 6.1**. The results for S, K_s, W and K_w were used to fit the adsorption enthalpies $\Delta H_{ads,S}$ and $\Delta H_{ads,W}$ with **Equation 6.2**.

$$Uptake = \frac{S * K_S * x}{1 + K_S * x} + \frac{W * K_W * x}{1 + K_W * x} \qquad \textbf{(Eq. 6.1)}$$

$$Integral\ Heat = \Delta H_{ads,S} * \frac{S * K_S * x}{1 + K_S * x} + \Delta H_{ads,W} * \frac{W * K_W * x}{1 + K_W * x} \qquad \textbf{(Eq. 6.2)}$$

With S = strong site uptake, W = weak site uptake, K_S = adsorption constant on strong sites, K_W = adsorption constant on weak sites and $\Delta H_{ads,S}$ = adsorption enthalpy on strong site and $\Delta H_{ads,W}$ = adsorption enthalpy on weak site.

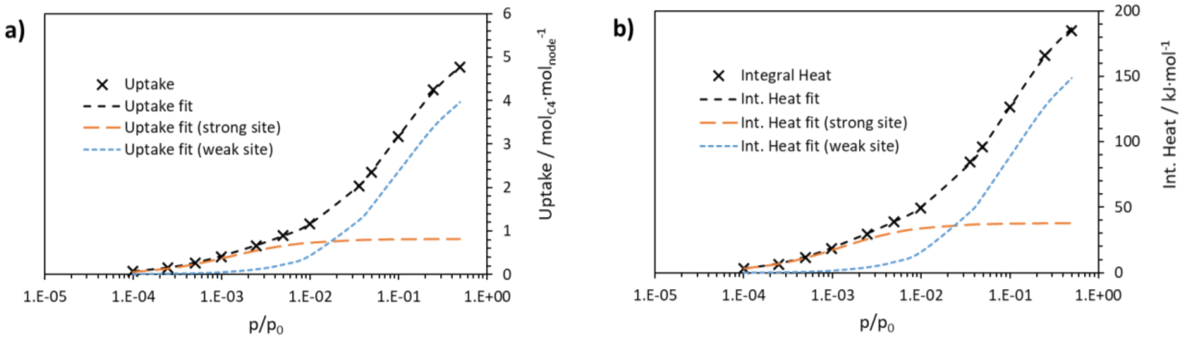

c)

	p-UiO-66 (activated at 250°C)
Strong site uptake S / mol$_{C4}$·mol$_{node}$$^{-1}$	0.82±0.04
Weak site uptake W / mol$_{C4}$·mol$_{node}$$^{-1}$	4.79±0.04
Adsorption Konstant K_S (strong)	838±93
Adsorption Konstant K_W (weak)	9.85±0.34
ΔH_{ads} (strong sites) / kJ·mol^{-1}	46.4±0.7
ΔH_{ads} (strong sites) / kJ·mol^{-1}	37.4±0.3

Figure 6.39: Butene adsorption on p-UiO-66 (activated at 250 °C, 1 h, $p < 10^{-5}$ mbar) at 40 °C. a) Isotherm of the measured butene adsorption. Uptake and fitted uptake in black. b) Integral heat and fitted integral heat. c) Parameters that resulted from the fit.

Butene adsorption was also investigated after activation at 300 °C. The corresponding fits are displayed below.

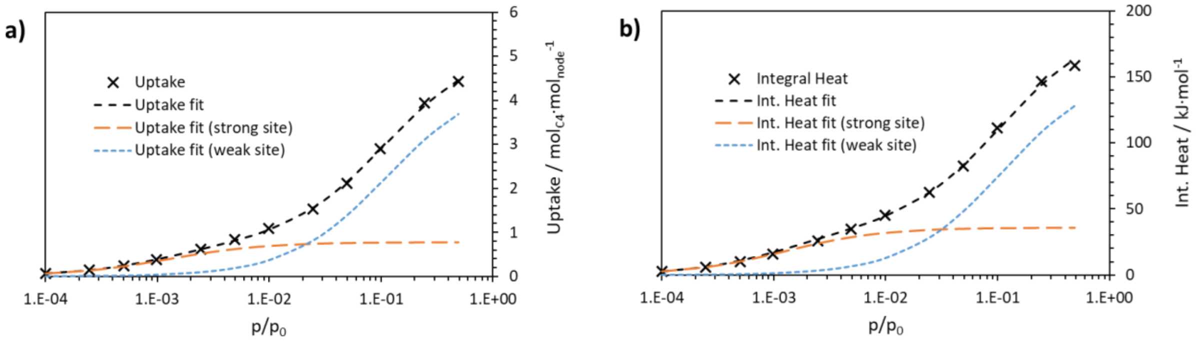

c)

	p-UiO-66 (activated at 300°C)
Strong site uptake S / mol$_{C4}$·mol$_{node}^{-1}$	0.78±0.05
Weak site uptake W / mol$_{C4}$·mol$_{node}^{-1}$	4.53±0.05
Adsorption Konstant K_S (strong)	798±124
Adsorption Konstant K_W (weak)	8.9±0.5
ΔH_{ads} (strong sites) / kJ·mol^{-1}	46.2±1.7
ΔH_{ads} (strong sites) / kJ·mol^{-1}	34.7±0.6

Figure 6.40: Butene adsorption on p-UiO-66 (activated at 300 °C, 1 h, $p < 10^{-5}$ mbar) at 40 °C. a) Isotherm of the measured butene adsorption. Uptake and fitted uptake in black. b) Integral heat and fitted integral heat. c) Parameters that resulted from the fit.

Calculated adsorption of 1-butene on the vacant UiO-66, UiO-66-Cl, and UiO-66-DMF

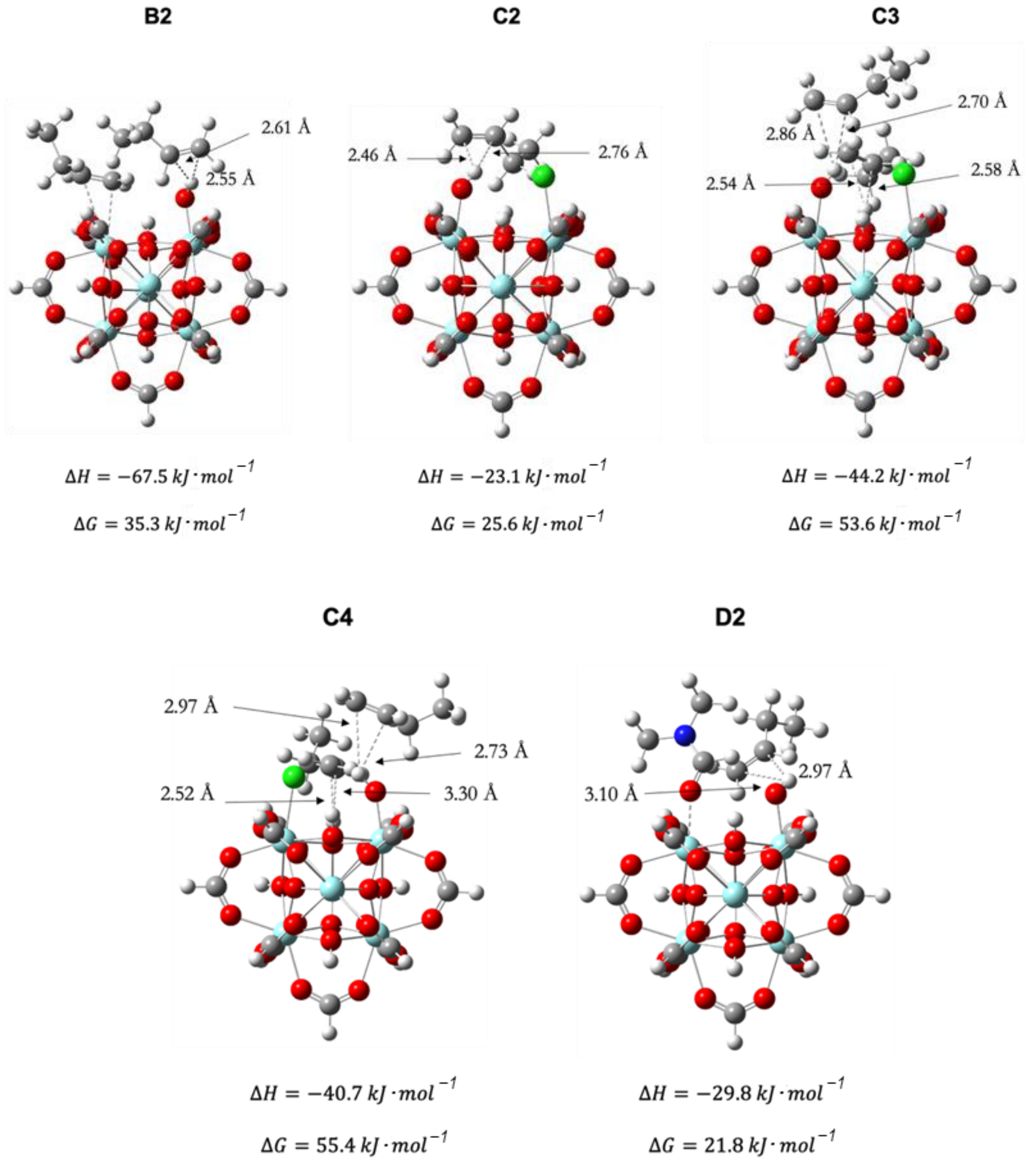

Figure 6.41: Adsorption of 1-butene on the (B2) terminal -OH of a vacant defect site in presence of a co-adsorbed 1-butene molecule, (C2) terminal -OH of chlorine-containing defect site (UiO-66-Cl), (C3) terminal -OH of UiO-66-Cl with another 1-butene co-adsorbed on μ_3-OH, (C4) terminal -OH of UiO-66-Cl with another 1-butene co-adsorbed on the chemically different μ_3-OH, (D2) terminal -OH of DMF-containing defect site (UiO-66-DMF). The enthalpies and free energies of 1-butene adsorption at 25 °C are shown. The respective defect sites and isolated 1-butene molecule are chosen as the reference for respective calculations. Color code: Zr (cyan), Cl (green), O (red), N (blue), C (grey), H (white).

Successive butene adsorption on p-UiO-66

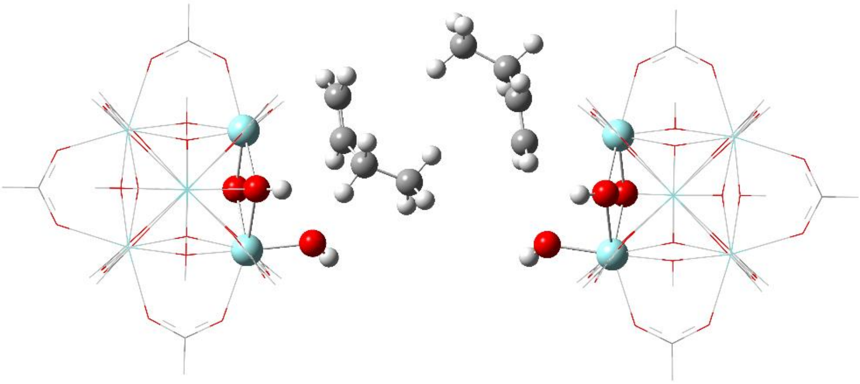

Figure 6.42: Successive adsorption of two 1-butene molecules on neighboring defect sites created on adjacent nodes. The pre-adsorption of 1-butene on one defect site was not found to influence the adsorption of 1-butene on the other defect site. Color code: Zr (cyan), O (red), C (grey), H (white). The atoms in the defect plane of the two nodes and the adsorbed butene molecules are shown in ball-and-stick representation while the remaining node is shown in wireframe representation for clarity.

6.2.5 Butene adsorption on Ni-UiO-66 and other M-UiO-66 (M = Co, Cu, Cr)

The butene adsorption was measured at 40 °C after activating the sample at 250 °C, 300 °C and 350 °C (1 h, $p<10^{-5}$ mbar).

The uptake was fitted according to **Equation 6.3**. Instead of dual Langmuir, a triple site model was used. The results for M, K_M, S, K_s, W and K_w were used to fit the adsorption enthalpies $\Delta H_{ads,S}$ and $\Delta H_{ads,W}$ with **Equation 6.4**.

$$Uptake = \frac{M * K_M * x}{1 + K_M * x} + \frac{S * K_S * x}{1 + K_S * x} + \frac{W * K_W * x}{1 + K_W * x} \qquad \textbf{(Eq. 6.3)}$$

$$Integral\ Heat = \Delta H_{ads,M} * \frac{S * K_M * x}{1 + K_M * x} + \Delta H_{ads,S} * \frac{S * K_S * x}{1 + K_S * x} + \Delta H_{ads,W} * \frac{W * K_W * x}{1 + K_W * x} \qquad \textbf{(Eq. 6.4)}$$

With M = metal site uptake, S = strong site uptake, W = weak site uptake, K_M = adsorption constant on metal sites, K_S = adsorption constant on strong sites, K_W = adsorption constant on weak sites and $\Delta H_{ads,S}$ = adsorption enthalpy on strong site and $\Delta H_{ads,W}$ = adsorption enthalpy on weak site.

Thermogravimetric analysis of butene adsorption on Ni-UiO-66 after different activation temperatures

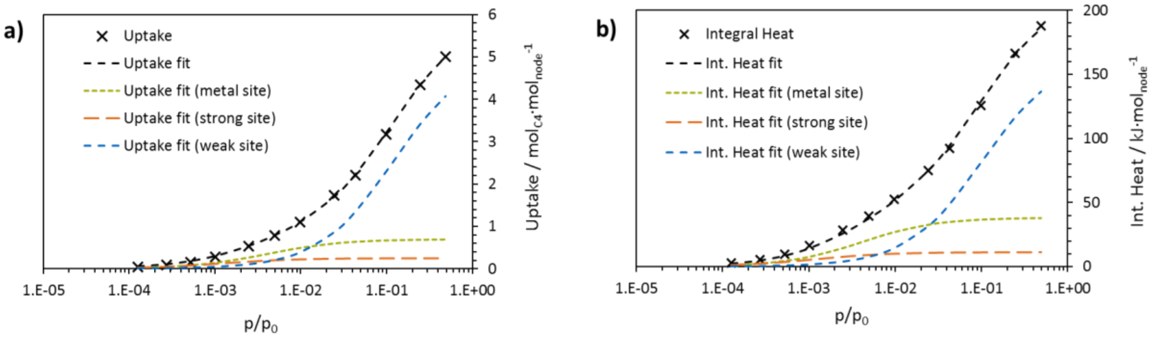

c)

	Ni-UiO-66 (activated at 250°C)
Metal site uptake M / mol$_{C4}$·mol$_{node}^{-1}$	0.69*
Strong site uptake S / mol$_{C4}$·mol$_{node}^{-1}$	0.25*
Weak site uptake W / mol$_{C4}$·mol$_{node}^{-1}$	4.46±0.09
Adsorption Konstant K_M (strong)	242.5±17.6
Adsorption Konstant K_S (free defect site)	839*
Adsorption Konstant K_W (weak)	9.8*
$\Delta H_{ads,S}$ (strong sites) / kJ·mol^{-1}	54.3±2.7
$\Delta H_{ads,F}$ (free defect sites) / kJ·mol^{-1}	46*
$\Delta H_{ads,W}$ (weak sites) / kJ·mol^{-1}	37*

Figure 6.43: Butene adsorption on Ni-UiO-66 (activated at 250 °C, 1 h, $p < 10^{-5}$ mbar) at 40 °C. a) Isotherm of the measured butene adsorption. Uptake and fitted uptake in black. b) Integral heat and fitted integral heat. c) Parameters that resulted from the fit. Numbers with a star were set.

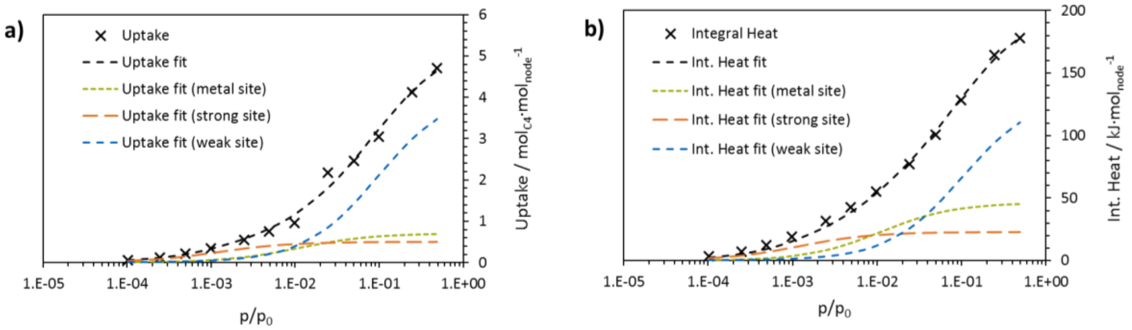

c)

	Ni-UiO-66 (activated at 300°C)
Metal site uptake M / mol$_{C4}$·mol$_{node}$$^{-1}$	0.69*
Strong site uptake S / mol$_{C4}$·mol$_{node}$$^{-1}$	0.50*
Weak site uptake W / mol$_{C4}$·mol$_{node}$$^{-1}$	3.60±0.18
Adsorption Konstant K_M (strong)	89.3±64.0
Adsorption Konstant K_S (free defect site)	839*
Adsorption Konstant K_W (weak)	9.8*
$\Delta H_{ads,S}$ (strong sites) / kJ·mol^{-1}	65.9±5.9
$\Delta H_{ads,F}$ (free defect sites) / kJ·mol^{-1}	46*
$\Delta H_{ads,W}$ (weak sites) / kJ·mol^{-1}	37*

Figure 6.44: Butene adsorption on Ni-UiO-66 (activated at 300 °C, 1 h, $p < 10^{-5}$ mbar) at 40 °C. a) Isotherm of the measured butene adsorption. Uptake and fitted uptake in black. b) Integral heat and fitted integral heat. c) Parameters that resulted from the fit. Numbers with a star were set.

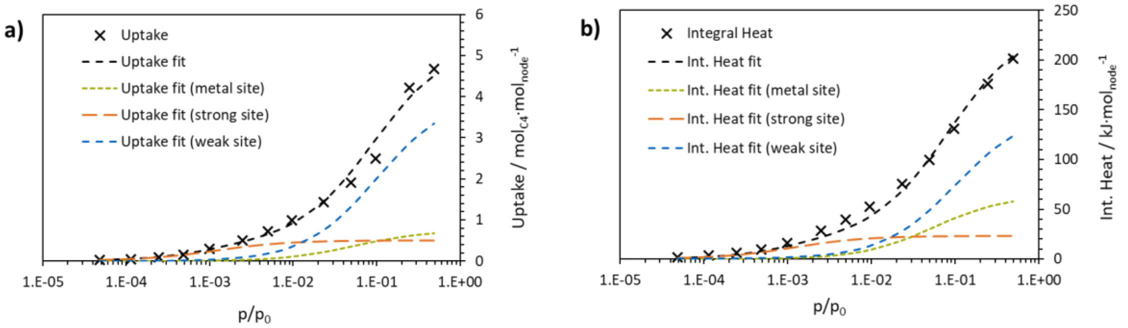

c)

	Ni-UiO-66 (activated at 350°C)
Metal site uptake M / mol$_{C4}$·mol$_{node}$$^{-1}$	0.75*
Strong site uptake S / mol$_{C4}$·mol$_{node}$$^{-1}$	0.50*
Weak site uptake W / mol$_{C4}$·mol$_{node}$$^{-1}$	4.03±0.13
Adsorption Konstant K_M (strong)	18.0±5.8
Adsorption Konstant K_S (free defect site)	839*
Adsorption Konstant K_W (weak)	9.9*
$\Delta H_{ads,S}$ (strong sites) / kJ·mol^{-1}	85.6±9.0
$\Delta H_{ads,F}$ (free defect sites) / kJ·mol^{-1}	46*
$\Delta H_{ads,W}$ (weak sites) / kJ·mol^{-1}	37*

Figure 6.45: Butene adsorption on Ni-UiO-66 (activated at 350 °C, 1 h, $p < 10^{-5}$ mbar) at 40 °C. a) Isotherm of the measured butene adsorption. Uptake and fitted uptake in black. b) Integral heat and fitted integral heat. c) Parameters that resulted from the fit. Numbers with a star were set.

Thermogravimetric analysis of butene adsorption on other M-UiO-66 (M = Co, Cu, Cr)

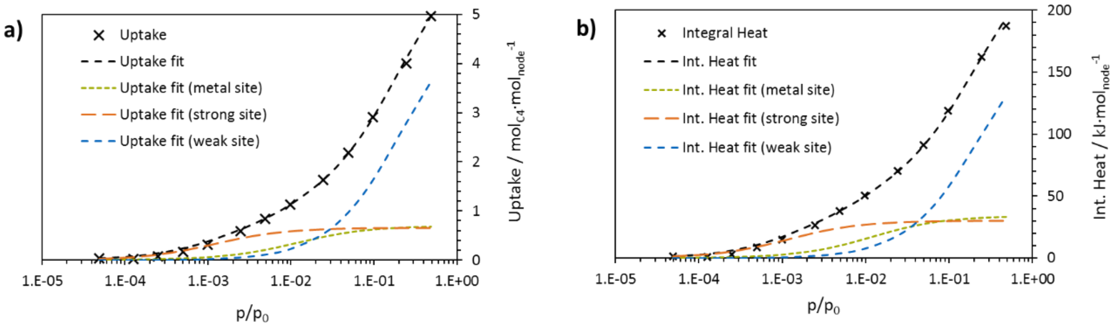

c)

	Co-UiO-66 (activated at 300°C)
Metal site uptake M / mol$_{C4}$·mol$_{node}$$^{-1}$	0.69*
Strong site uptake S / mol$_{C4}$·mol$_{node}$$^{-1}$	0.65*
Weak site uptake W / mol$_{C4}$·mol$_{node}$$^{-1}$	5.24±0.16
Adsorption Konstant K_M (strong)	83.6±16.1
Adsorption Konstant K_S (free defect site)	839*
Adsorption Konstant K_W (weak)	4.6±0.4
$\Delta H_{ads,S}$ (strong sites) / kJ·mol^{-1}	48.6±7.1
$\Delta H_{ads,F}$ (free defect sites) / kJ·mol^{-1}	46*
$\Delta H_{ads,W}$ (weak sites) / kJ·mol^{-1}	37*

Figure 6.46: Butene adsorption on Co-UiO-66 (activated at 300 °C, 1 h, $p < 10^{-5}$ mbar) at 40 °C. a) Isotherm of the measured butene adsorption. Uptake and fitted uptake in black. b) Integral heat and fitted integral heat. c) Parameters that resulted from the fit. Numbers with a star were set.

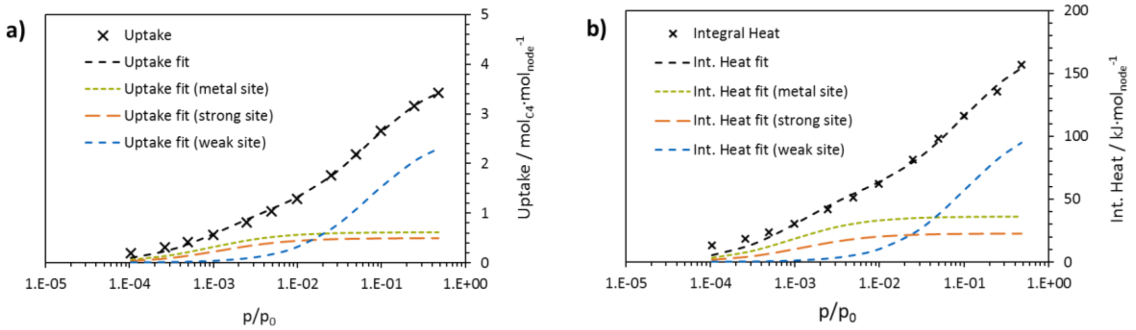

c)

	Cu-UiO-66 (activated at 300°C)
Metal site uptake M / mol$_{C4}$·mol$_{node}$$^{-1}$	0.62*
Strong site uptake S / mol$_{C4}$·mol$_{node}$$^{-1}$	0.50*
Weak site uptake W / mol$_{C4}$·mol$_{node}$$^{-1}$	3.12±0.14
Adsorption Konstant K_M (strong)	1086±201
Adsorption Konstant K_S (free defect site)	839*
Adsorption Konstant K_W (weak)	9.8*
$\Delta H_{ads,S}$ (strong sites) / kJ·mol^{-1}	58.6±3.9
$\Delta H_{ads,F}$ (free defect sites) / kJ·mol^{-1}	46*
$\Delta H_{ads,W}$ (weak sites) / kJ·mol^{-1}	37*

Figure 6.47: Butene adsorption on Cr-UiO-66 (activated at 300 °C, 1 h, $p < 10^{-5}$ mbar) at 40 °C. a) Isotherm of the measured butene adsorption. Uptake and fitted uptake in black. b) Integral heat and fitted integral heat. c) Parameters that resulted from the fit. Numbers with a star were set.

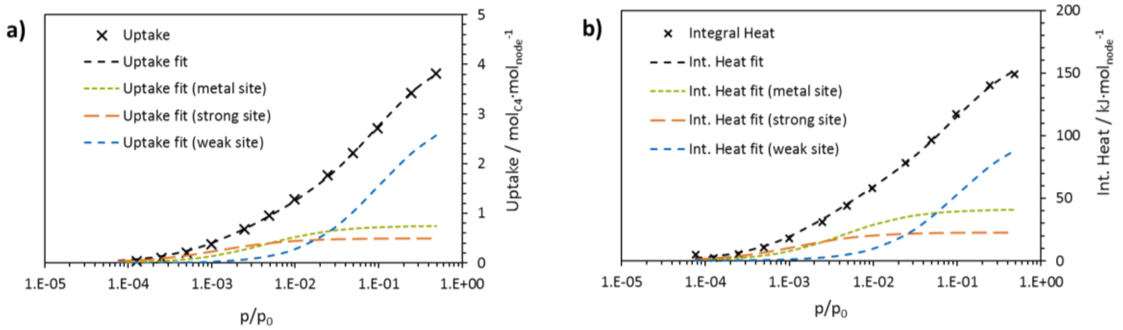

c)

	Cr-UiO-66 (activated at 300°C)
Metal site uptake M / mol$_{C4}$·mol$_{node}$$^{-1}$	0.75*
Strong site uptake S / mol$_{C4}$·mol$_{node}$$^{-1}$	0.50*
Weak site uptake W / mol$_{C4}$·mol$_{node}$$^{-1}$	2.88±0.08
Adsorption Konstant K_M (strong)	230±22
Adsorption Konstant K_S (free defect site)	839*
Adsorption Konstant K_W (weak)	9.8*
$\Delta H_{ads,S}$ (strong sites) / kJ·mol^{-1}	55.3±2.2
$\Delta H_{ads,F}$ (free defect sites) / kJ·mol^{-1}	46*
$\Delta H_{ads,W}$ (weak sites) / kJ·mol^{-1}	37*

Figure 6.48: Butene adsorption on Cr-UiO-66 (activated at 300 °C, 1 h, $p < 10^{-5}$ mbar) at 40 °C. a) Isotherm of the measured butene adsorption. Uptake and fitted uptake in black. b) Integral heat and fitted integral heat. c) Parameters that resulted from the fit. Numbers with a star were set.

6.2.6 Catalytic tests in butene dimerization

Selectivity of p-UiO-66 and M-UiO-66 (M = Ni, Co, Cu, Cr)

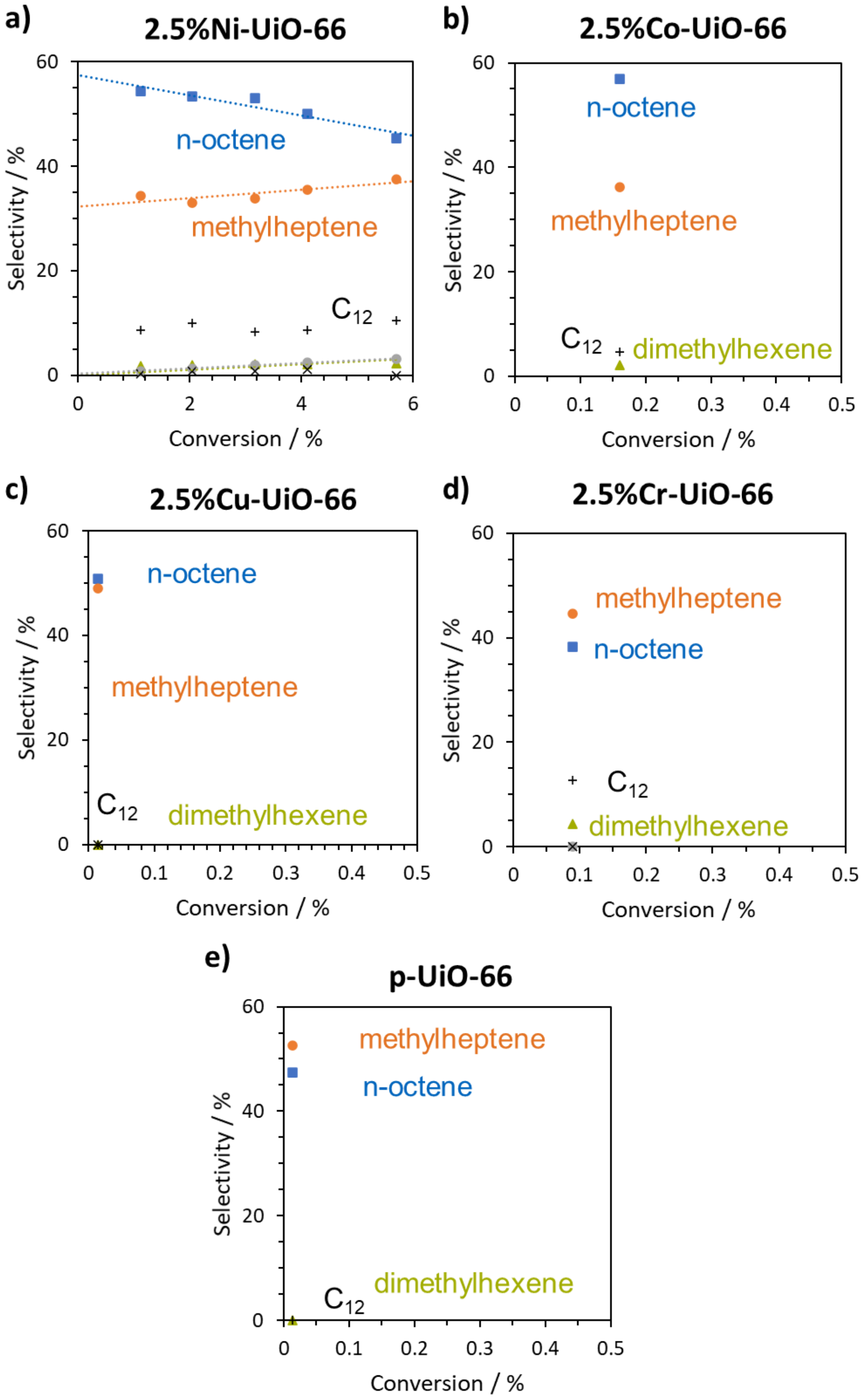

Figure 6.49: Selectivity of the different M-UiO-66 (M = Ni, Co, Cu, Cr) compared to the p-UiO-66 in butene dimerization (reaction conditions: 50 bar, 250 °C and WHSV = 8.3 h^{-1}).

6.2.7 Calculation of free energies

We describe here the calculation of the free adsorption energies and the free energies of the transition state.

1) Determine K_M and $\Delta H_{ads,M}$

   The adsorption konstants K_M and the heat of adsorption $\Delta H_{ads,M}$ for the metals were determined following **Equation 6.3** and **6.4** as described in **Section 6.2.5**. For the p-UiO-66, the adsorption constant K_S and the heat of adsorption $\Delta H_{ads,S}$ were calculated using **Equation 6.1** and **6.2** in **Section 6.2.4** and are treated the same as K_M and $\Delta H_{ads,M}$ in the following.

2) Calculate $\Delta G^{\mathrm{e}}_{ads}(40\ °C)$

   The free adsorption energy at a temperature of 40 °C was calculated according to **Equation 6.5**.

$$\Delta G^{\ominus}_{ads}(40\ °\mathrm{C}) = -RT_1 * \ln\,(K_\mathrm{M}) \qquad \textbf{(Eq. 6.5)}$$

   With R = universal gas constant and T_1 = 40 °C.

3) Calculate $\Delta G^{\mathrm{e}}_{ads}(250\ °C)$

   Using the Van´t Hoff equation (**Equation 6.6**), the adsorption constant was determined at reaction temperature, which was then transferred into the adsorption free energy $\Delta G^{\mathrm{e}}_{ads}(250\ °C)$ at 250 °C with the help of **Equation 6.7**.

$$K_{\mathrm{M},250°\mathrm{C}} = \exp\left[\frac{\Delta H_{\mathrm{ads,M}}}{R} * \left(\frac{1}{T_1} - \frac{1}{T_2}\right) + \ln(K_\mathrm{M})\right] \qquad \textbf{(Eq. 6.6)}$$

$$\Delta G_{\mathrm{ads}}(250\ °\mathrm{C}) = -RT_2 * \ln\,(K_{\mathrm{M},250°\mathrm{C}}) \qquad \textbf{(Eq. 6.7)}$$

   With T_2 = 250 °C.

4) Determine $k_{measured}$

   The reaction constant was determined from the turnover frequency (TOF) following a first order (**Equation 6.8**).

$$k_{\mathrm{measured}}(250\ °\mathrm{C}) = \frac{\mathrm{TOF}}{p_0} \qquad \textbf{(Eq. 6.8)}$$

With p_0 = partial pressure of butene = 0.85·50bar.

5) Calculate $\Delta^{\ddagger}G^{\ominus}_{app}$(250 °C)

The apparent free energy of the transition state $\Delta^{\ddagger}G^{\ominus}_{app}$ was calculated from the Eyring equation (**Equation 6.9**).

$$\Delta^{\ddagger}G^{\ominus}_{app} = \ln\left(k_{measured} * \frac{h}{k_B T}\right) * (-RT_2) \qquad \textbf{(Eq. 6.9)}$$

With h = Planck´s constant and k_B = Boltzmann constant.

6) Calculate $\Delta^{\ddagger}G^{\ominus}_{true}$(250 °C)

The true free energy of the transition state $\Delta^{\ddagger}G^{\ominus}_{true}$(250 °C) composes of the apparent free energy of the transition state $\Delta^{\ddagger}G^{\ominus}_{app}$ and the adsorption free energy $\Delta G^{\ominus}_{ads}$(250 °C).

$$\Delta^{\ddagger}G^{\ominus}_{true} = \Delta^{\ddagger}G^{\ominus}_{app} - \Delta G^{\ominus}_{ads}(250\ °C) \qquad \textbf{(Eq. 6.10)}$$

6.2.8 DFT Calculation of enthalpy diagram for M-UiO-66 catalysts

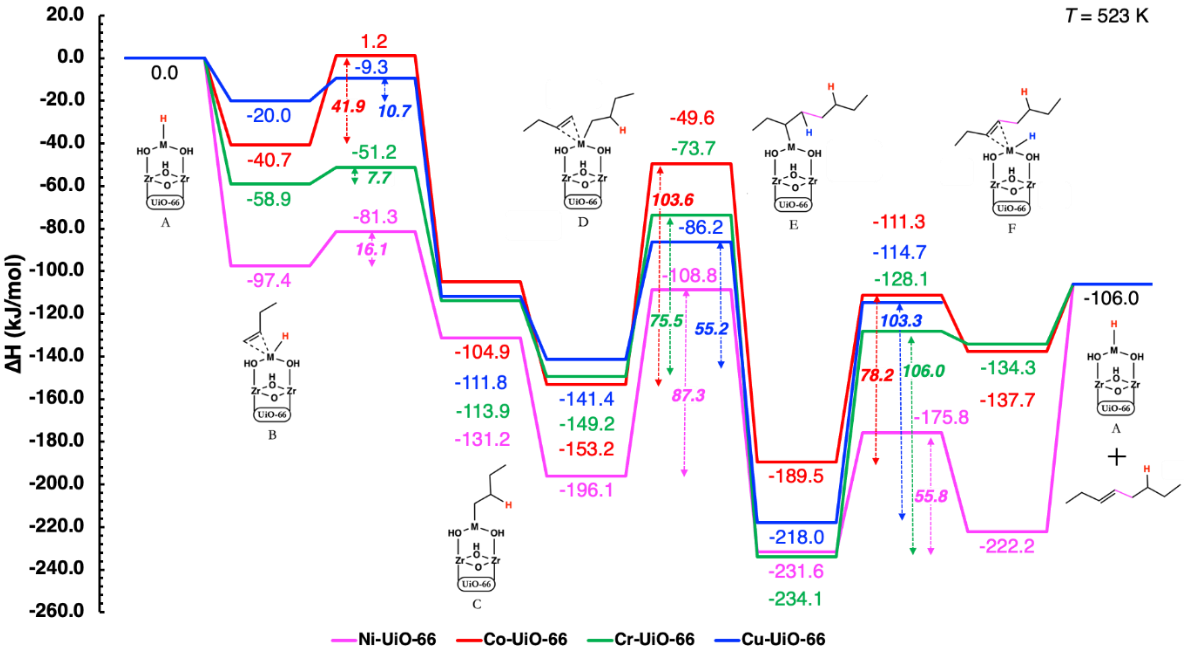

Figure 6.50: Enthalpy diagrams for the formation of linear oct-3-ene dimer on different Ni-UiO-66 (magenta), Co-UiO-66 (red), Cr-UiO-66 (green), and Cu-UiO-66 (blue) catalysts at T = 250 °C and p = 1 bar.

6.3 Supporting information: Impact of zeolite properties on the activity of single Ni sites for selective butene dimerization

6.3.1 CHA

X-ray diffraction (XRD) and N_2 sorption experiments revealed the preservation of the zeolite framework throughout the ion exchanges (see **Figure 6.51a** and **b**, **Figure 6.52a** and **b**, and **Figure 6.53a** and **b**) for all three CHA materials. The introduction of cations did not reduce the crystallinity, the micropore volume or the BET surface area significantly. Only the sample with 95% Al pair showed minor reduction in the inner surface area.

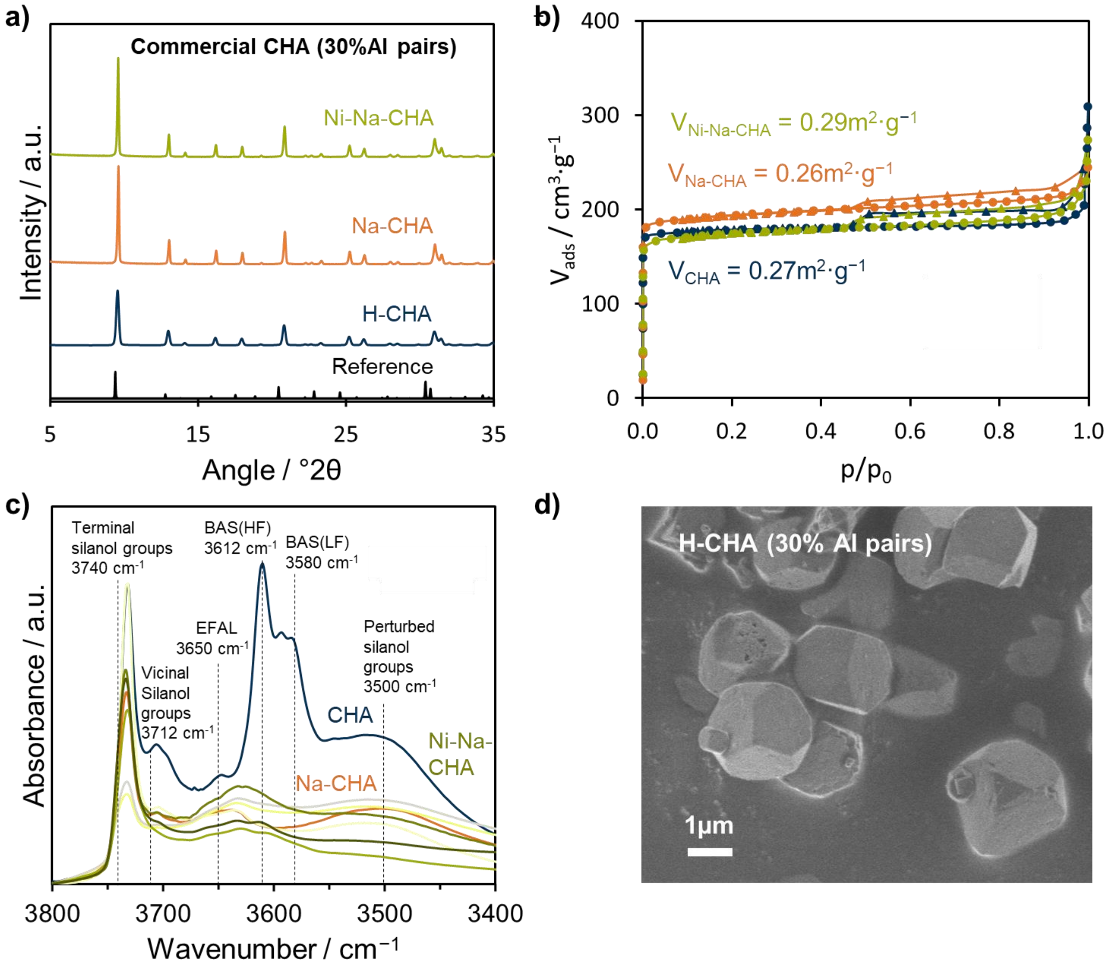

Figure 6.51:Structural characterization of the commercial CHA catalyst with 30% Al pairs. a) XRD reflexes of the H-CHA, Na-CHA and one exemplary Ni-Na-CHA material. b) N_2 sorption isotherms of the same samples. c) IR spectra of H-CHA (blue), Na-CHA (orange) and Ni-Na-CHA (green) samples. d) SEM image of H-CHA.

The acidity of the CHA catalysts was analyzed by IR. As pyridine is too large to penetrate the small 8MR channels of the CHA, it was not possible to determine the BAS concentrations quantitatively. The IR spectra in **Figure 6.51c**, **Figure 6.52c**, and **Figure 6.53c**, show the reduction of BAS by the decrease of the 3612 cm^{-1} vibration upon cation introduction. It can be observed that the OH vibration of BAS slightly increases again after Ni introduction. The cointroduction of BAS during the Ni exchange was observed for all here reported zeolites and can be easily monitored in the IR spectra of the synthesized CHA (**Figure 6.52c**, and **Figure 6.53c**). Small remaining BAS concentration in the Ni-Na-CHA samples can therefore not be excluded.

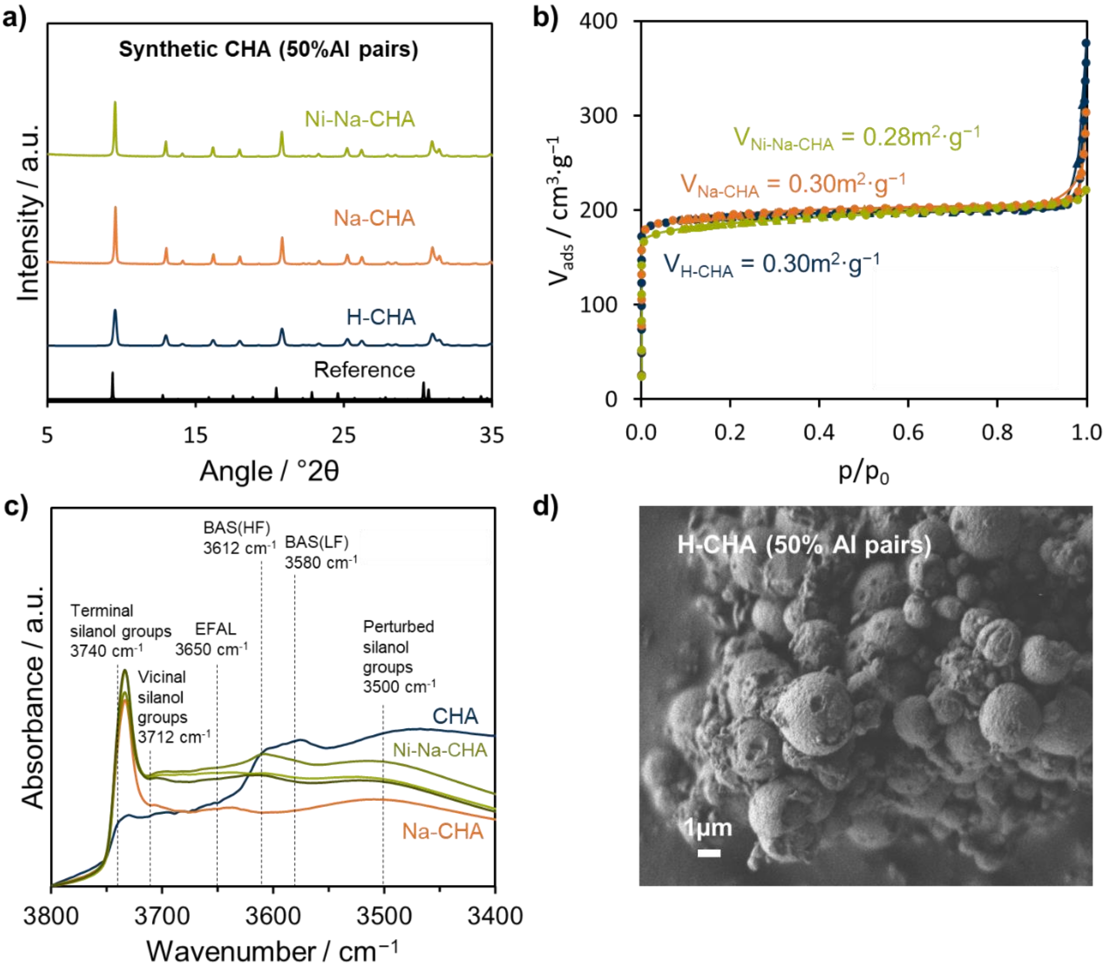

Figure 6.52: Structural characterization of the snthesized CHA catalyst with 50% Al pairs. a) XRD reflexes of the H-CHA, Na-CHA and one exemplary Ni-Na-CHA material. b) N_2 sorption isotherms of the same samples. c) IR spectra of H-CHA (blue), Na-CHA (orange) and Ni-Na-CHA (green) samples. d) SEM image of H-CHA.

The structure of the CHA samples was investigated by SEM (**Figure 6.51d**, **Figure 6.52d**, and **Figure 6.53d**). The crystals of the CHA with 30% Al pairs and the CHA with 95% Al pairs are shaped in form of cubes while the CHA with 50% Al pairs rather features sphere-shaped crystals. The crystal size for all three CHA materials is about 1-2 µm in length.

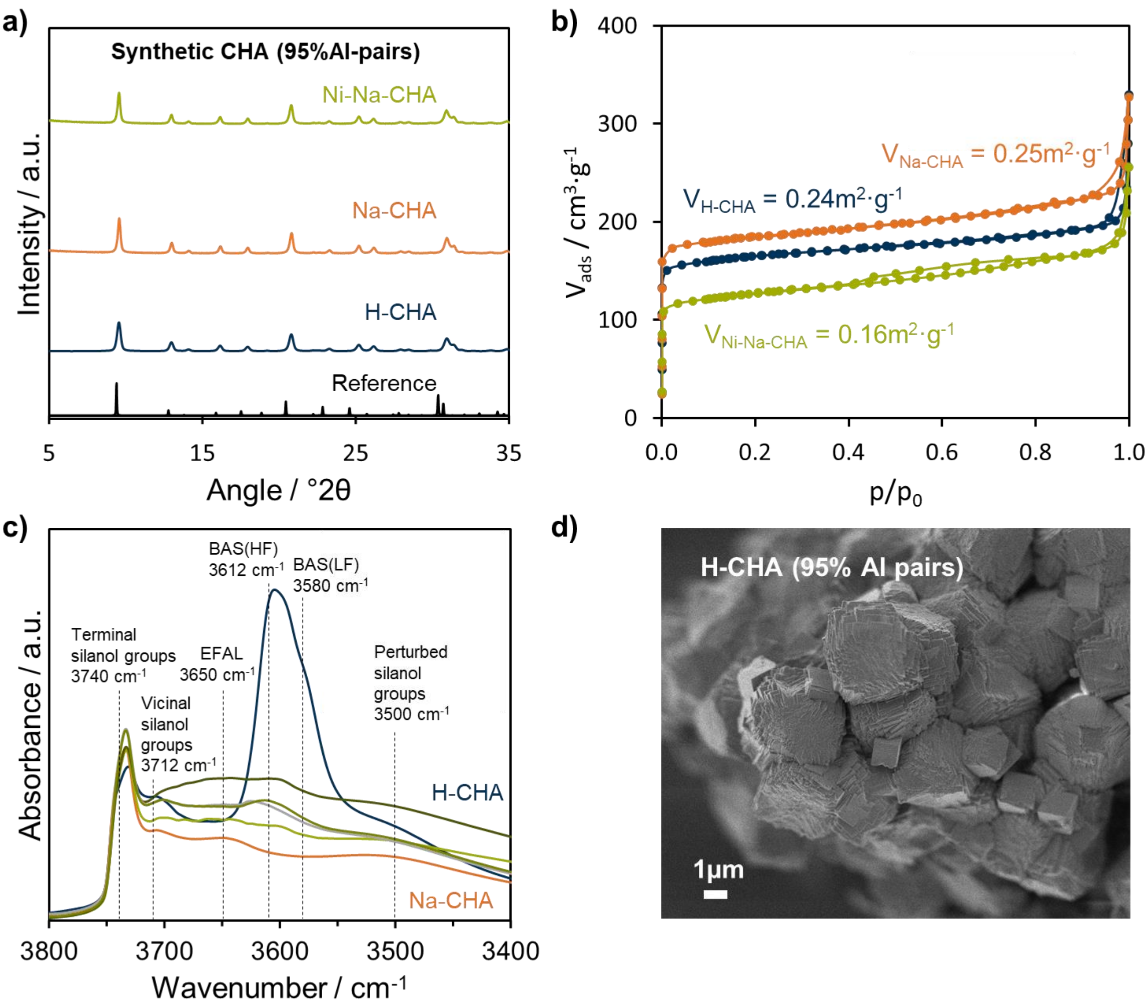

Figure 6.53: Structural characterization of the snthesized CHA catalyst with 95% Al pairs. a) XRD reflexes of the H-CHA, Na-CHA and one exemplary Ni-Na-CHA material. b) N_2 sorption isotherms of the same samples. c) IR spectra of H-CHA (blue), Na-CHA (orange) and Ni-Na-CHA (green) samples. c) SEM image of H-CHA.

6.3.2 MFI

Structural analysis was performed for the MFI samples similarly to the CHA characterization. XRD, N_2 sorption experiments, and SEM revealed the preservation of the zeolite framework throughout the ion exchanges (see **Figure 6.54**a, b, and d).

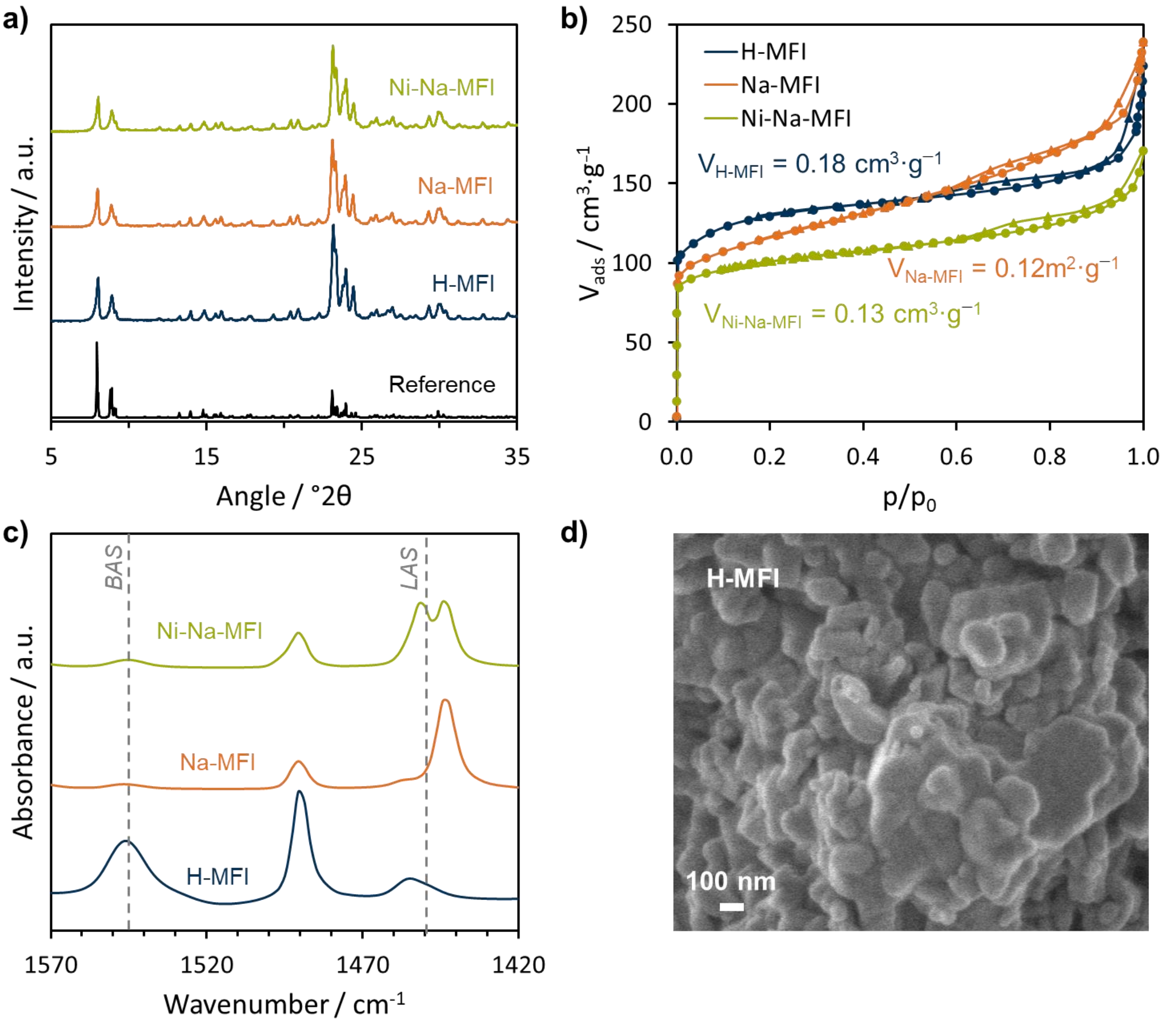

Figure 6.54: Structural characterization of the commcercial MFI catalyst. a) XRD reflexes of the H-MFI, Na-MFI and one exemplary Ni-Na-MFI material. b) N_2 sorption isotherms of the same samples. c) Pyridin-IR spectra of H-MFI, Na-MFI (orange) and Ni-Na-MFI (green) sample. d) SEM image of H-MFI.

The acidity of each sample was checked by pyridine adsorption monitored *via* IR spectroscopy and analyzed according to the characteristic bands for Brønsted acidity at 1540 cm⁻¹ and Lewis acidity at 1450 cm⁻¹ (see **Figure 6.54c**). In **Table 6.12**, the different BAS and LAS concentrations are listed for the MFI samples.

Table 6.12: Na and Ni content (determined by EA) as well as BAS and LAS concentration (determined by pyridine adsorption) for H-MFI, Na-MFI and Ni-Na-MFI samples.

Sample	**Na / µmol·g⁻¹**	**Ni / µmol·g⁻¹**	**BAS / µmol·g⁻¹**	**LAS / µmol·g⁻¹**
H-MFI	-	-	957	153
Na-MFI	970	0	8	810
52Ni134BAS	718	52	134	998
85Ni21BAS	713	85	21	181
126Ni13BAS	696	126	13	154
170Ni44BAS	705	170	44	447
179Ni89BAS	613	179	89	923
206Ni43BAS	626	206	43	373
298Ni58BAS	622	298	58	468
496Ni116BAS	692	496	116	428
671Ni60BAS	713	671	60	983

Table 6.13: BET surface areas, micropore volumes and mesoporous surface areas determined by N_2 sorption experiments for different MFI samples.

Sample	**BET surface area / m²·g⁻¹**	**Micropore volume / cm³·g⁻¹**	**Mesoporous surface Area / m²·g⁻¹**	**Charge Balance**
H-MFI	402	0.18	49.1	-
Na-MFI$_{Na}$	375	0.12	140	0.99
85Ni21BAS	338	0.13	65.8	0.95
179Ni89BAS	337	0.14	55.6	1.14

496Ni116BAS	313	0.12	74.2	1.85
671Ni60BAS	330	0.10	132	2.35

N_2 sorption experiments show a decrease of the BET surface area as well as the micropore volume with increasing Ni loadings (see leading to the assumption that particles form within the pores of MFI.

CO adsorption experiments were monitored by IR spectroscopy to monitor the Ni species in different Ni-Na-MFI samples. In the following, the different species are analyzed and the details of the deconvolution of the Ni^{2+}-CO vibration are shown.

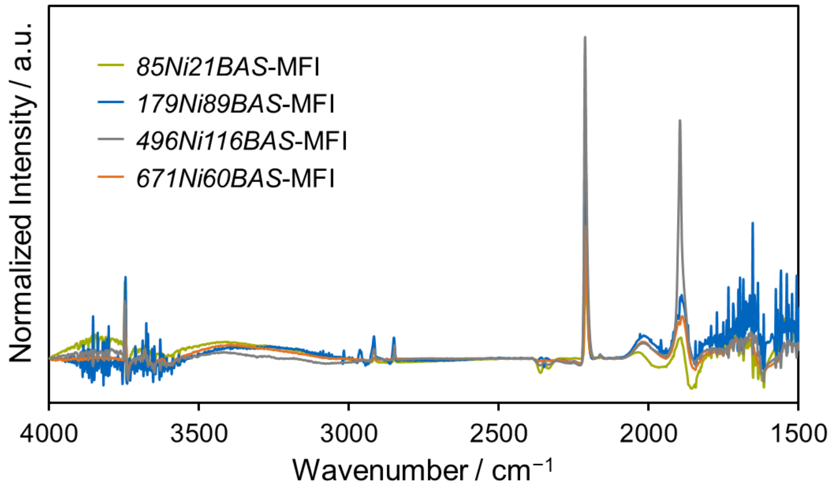

Figure 6.55: Full IR difference spectra of four Ni-Na-MFI samples during CO adsorption (0.01 mbar CO).

Other species, then the single Ni^{2+}-cations, interacting with CO were observed when increasing the pressure above $5 \cdot 10^{-2}$ mbar. All samples exhibit a broad band at 2030 cm^{-1}, which is associated with Ni^0 polycarbonyls. Additionally, the features for the mono- and dicarbonyl species of Ni^+ (2111 and 2130 cm^{-1})[66,234,238] were similar for all four MFI samples and do not show any correlation with the activity in butene dimerization. We therefore assume these species to form upon in-situ reduction by CO at higher pressures. The signal at 2130 cm^{-1} could be assigned to physisorbed CO, which will shift with increasing pressures to 2139 cm^{-1}.[233,235,236] It has also been reported that this vibration originates from CO, which is polarized by surface-oxygen-species from the zeolite framework.[237]

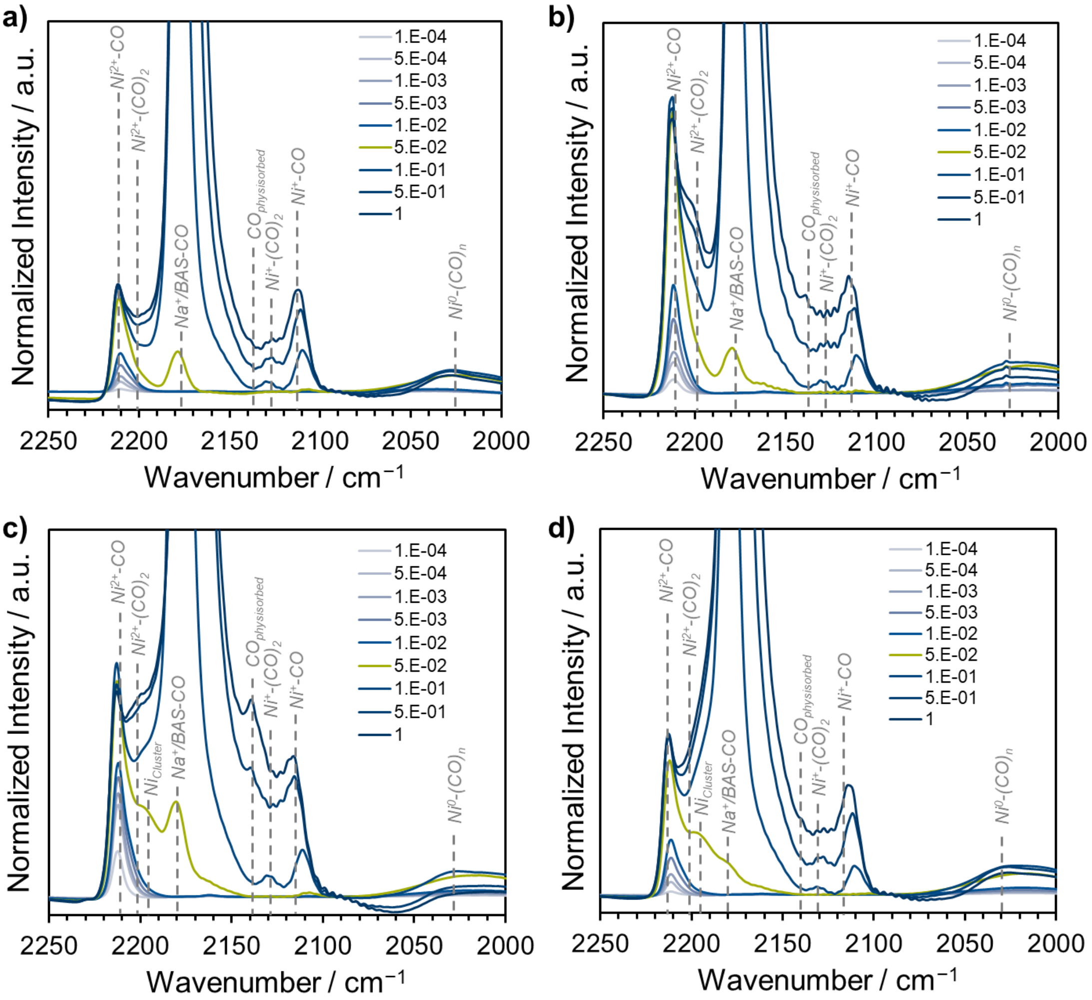

Figure 6.56: Normalized IR difference spectra of a) *85Ni21BAS*-, b) *179Ni89BAS*-, c) *496Ni116BAS*- and d) *671Ni60BAS*-MFI upon low-temperature dosing of CO-dosing. Pressure during dosing steps from $1\cdot10^{-4}$ mbar (light blue) to 1 mbar (dark blue) levels are given in mbar. Spectra at $5\cdot10^{-2}$ mbar are highlighted in green. Dosing of CO was performed at liquid nitrogen temperature. The spectra are normalized to zeolite lattice vibrations (approx. 2100 cm^{-1} to 1700 cm^{-1}).

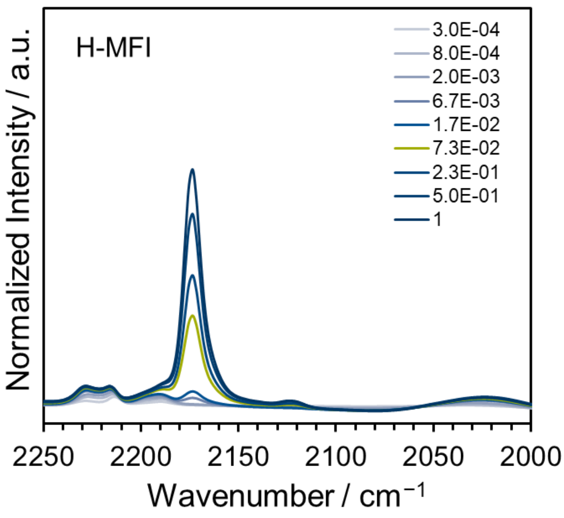

Figure 6.57: Difference IR spectra of H-MFI upon low-temperature dosing of CO. Pressure during dosing steps from $1{\cdot}10^{-4}$ mbar (light blue) to 1 mbar (dark blue) levels are given in mbar. Spectra at $5{\cdot}10^{-2}$ mbar are highlighted in green. Dosing of CO was performed at liquid nitrogen temperature.

The CO-IR spectra of the MFI samples with different Ni loadings were fitted with two Gaussian peaks for the Ni^{2+}-CO and Ni^{2+}-$(CO)_2$ vibration. The fits are depicted in **Figure 6.58** and the corresponding values are summarized in **Table 6.14**. The areas of the Ni^{2+}-CO vibration (dashed green) were used for the correlation with the rates in **Figure 4.2**. We also tried using the complete peak areas from 2180-2230 cm^{-1} without deconvoluting and subtracting the Ni^{2+}-$(CO)_2$ contribution. The comparison of these peak areas with the butene consumption rates also resulted in a strong correlation.

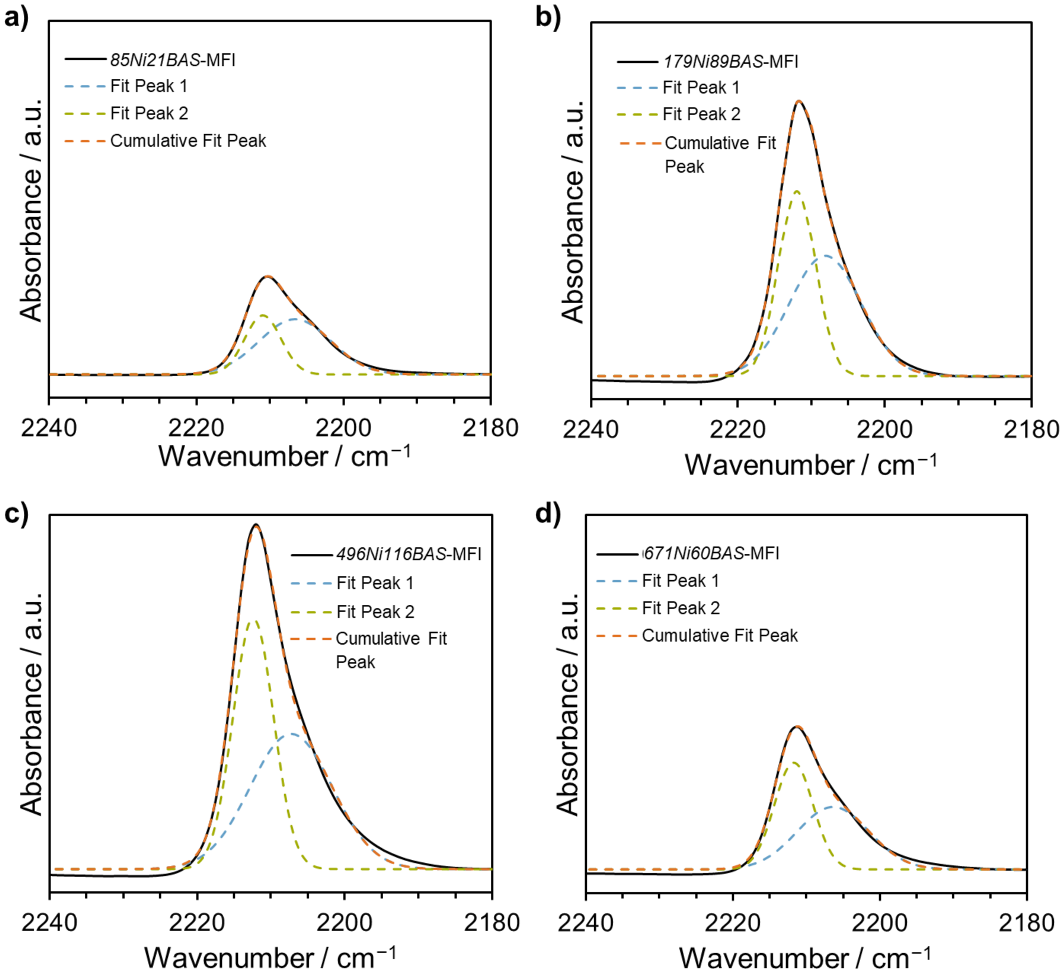

Figure 6.58: Deconvoluted and normalized IR difference spectra upon low-temperature CO-adsorption ($1 \cdot 10^{-2}$ mbar) on different Ni-Na-MFI samples (*85Ni21BAS*-, *179Ni89BAS*-, *496Ni116BAS*-, and *671Ni60BAS*-MFI). CO-dosing was performed at liquid nitrogen temperature. Two Gaussian peaks were fitted with a fixed baseline at zero applying Levenberg-Marquardt iteration mechanism. Fitted peaks of Ni^{2+}-CO (dashed green), Ni^{2+}-$(CO)_2$ (dashed blue), cumulative fit (dashed orange) and experimental spectra (solid black) are given. Spectra were normalized to lattice vibrations (approx. 2100 cm^{-1} to 1700 cm^{-1}) for fair comparison between samples.

Table 6.14: Results of peak deconvolution of normalized IR difference spectra upon low-temperature CO-adsorption ($1\cdot10^{-2}$ mbar) on *85Ni21BAS*-, *179Ni89BAS*-, *496Ni116BAS*-, and *671Ni60BAS*-MFI. CO-dosing was performed at liquid nitrogen temperature. Deconvolution was performed with two Gaussian peaks and fixed baseline at zero applying Levenberg-Marquardt iteration mechanism. Peak center, area, full width at half maximum (FWHM) and their respective standard deviation σ are given for each peak.

Sample	**Peak**	**Center / cm^{-1}**	**σ_{center} / cm^{-1}**	**Area / cm^{-1}**	**σ_{area} / cm^{-1}**	**FWHM / cm^{-1}**	**σ_{FWHM} / cm^{-1}**
85Ni21BAS	1	2206.60	2.39	$2.86\cdot10^{-3}$	$1.37\cdot10^{-3}$	11.44	2.25
	2	2210.97	0.49	$1.55\cdot10^{-3}$	$1.29\cdot10^{-3}$	5.79	1.95
179Ni89BAS	1	2208.12	2.15	$6.24\cdot10^{-3}$	$2.90\cdot10^{-3}$	11.47	1.86
	2	2211.96	0.37	$4.98\cdot10^{-3}$	$2.76\cdot10^{-3}$	5.96	1.34
496Ni116BAS	1	2207.25	1.50	$8.00\cdot10^{-3}$	$2.04\cdot10^{-3}$	13.13	1.47
	2	2212.39	0.18	$7.34\cdot10^{-3}$	$1.90\cdot10^{-3}$	6.47	0.70
671Ni60BAS	1	2206.37	2.46	$3.24\cdot10^{-3}$	$1.52\cdot10^{-3}$	11.53	2.64
	2	2211.72	0.22	$2.98\cdot10^{-3}$	$1.44\cdot10^{-3}$	6.19	1.03

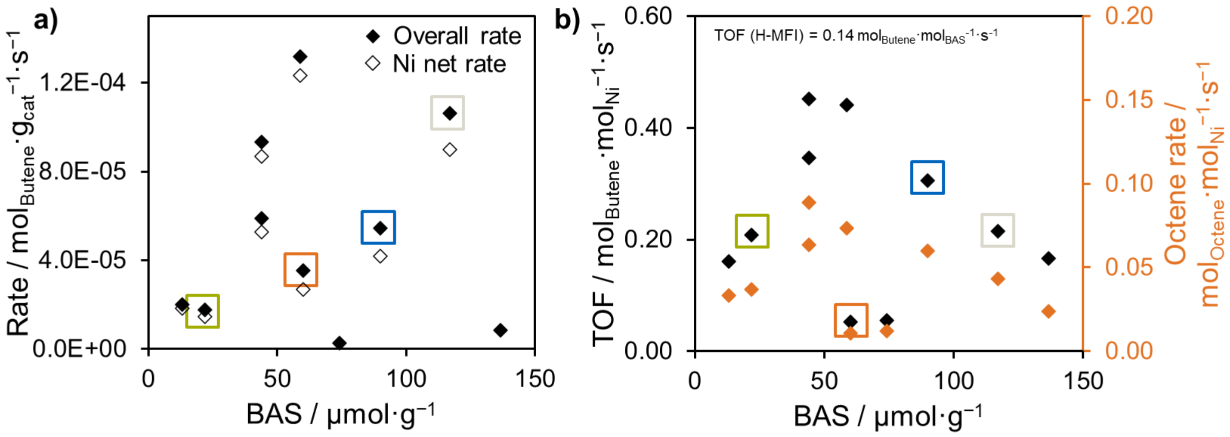

Figure 6.59: BAS contribution in Ni-Na-MFI samples. a) Butene consumption rates per gram (filled symbols) and after subtracting the BAS contribution per gram (´Ni net rate´, hollow symbols). b) TOFs (black symbols) and linear octene formation rates (orange symbols) are shown against the BAS concentration.

6.3.3 FAU

The acidity of each FAU sample was checked by pyridine adsorption monitored *via* IR spectroscopy and analyzed according to the characteristic bands for Brønsted acidity at 1540 cm^{-1} and Lewis acidity at 1450 cm^{-1} (similar to the MFI samples). In **Table 6.15** and **Table 6.16**, the different BAS and LAS concentrations are listed for the FAU samples.

Table 6.15: Na, Ni, BAS, and LAS concentration for H-FAU, Na-FAU and Ni-Na-FAU samples.

Sample	**Na / µmol·g^{-1}**	**Ni / µmol·g^{-1}**	**BAS / µmol·g^{-1}**	**LAS / µmol·g^{-1}**
H-FAU	-	-	436	168
Na-FAU$_{Na}$	1217	-	8	810
47Ni89BAS	700	47	89	190
50Ni130BAS	800	50	130	219
114Ni62BAS	731	114	62	116
199Ni28BAS	735	199	28	20
199Ni42BAS	809	199	42	200
295Ni24BAS	766	295	24	26
607Ni89BAS	770	607	89	118

Table 6.16: Na, Ni, BAS, and LAS concentration for H-FAU and Ni-H-FAU samples.

Sample	**Na / µmol·g^{-1}**	**Ni / µmol·g^{-1}**	**BAS / µmol·g^{-1}**	**LAS / µmol·g^{-1}**
H-FAU	-	-	430	168
29Ni419BAS	8	29	419	295

55Ni151BAS	10	55	204	151
116Ni295BAS	10	116	295	275
220Ni186BAS	8	220	186	497
295Ni207BAS	10	295	207	446

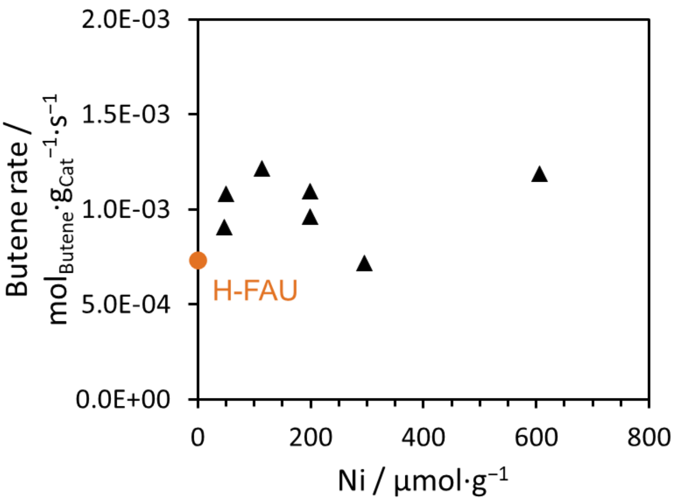

Figure 6.60: Butene rates per gram of Ni-Na-FAU catalysts (black triangles) and H-FAU (orange circle).

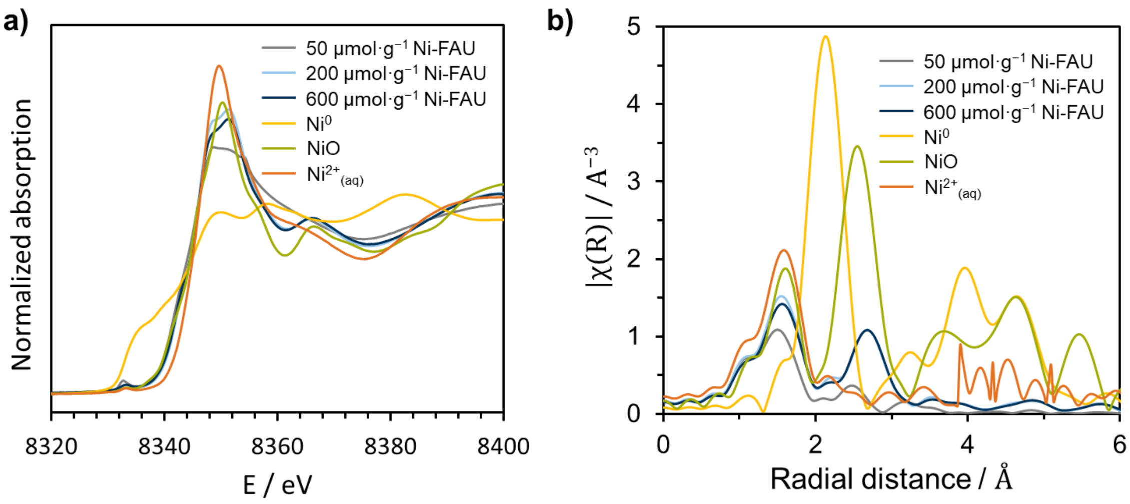

Figure 6.61: XAFS measurements of the activated (450 °C, synair) Ni-Na-FAU catalysts (*50Ni130BAS*-FAU, *199Ni28BAS*-FAU, and *607Ni89BAS*-FAU and reference compounds: a) normalized µ(E) and b) k^2-weighted Ni-EXAFS $\chi(R)$ spectra.

Table 6.17: EXAFS fitting parameters: coordination numbers (CNs), interatomic distances (d), ΔE_0, and Debye-Waller factors (σ^2) for Ni-O and Ni-Si paths in *50Ni130BAS*-FAU, *199Ni28BAS*-FAU, and *607Ni89BAS*-FAU catalysts.

Sample	**Path**	**CN**	**d / Å**	**ΔE_0 / eV**	**$\sigma^2 \cdot 1000$ / Å^2**	**R-factor**
50Ni130BAS	Ni-O	3.6±1.2	2.000±0.021	-1.67±3.12	10.4±3.6	0.082
	Ni-Si	2.1±2.4	3.221±0.049		11.4±11.8	
199Ni28BAS	Ni-O	5.1±1.6	2.033±0.016	-0.73±2.04	9.4±3.3	0.063
	Ni-Si	5.1±1.9	3.240±0.017		5.2±2.7	
607Ni89BAS	Ni-O	4.7±1.5	2.037±0.016	-0.45±1.99	9.2±3.3	0.067
	Ni-Si	5.6±2.0	3.248±0.017		6.0±2.7	

Table 6.18: EXAFS fitting parameters: coordination numbers (CNs), interatomic distances (d), ΔE_0, and Debye-Waller factors (σ^2) for Ni-O and Ni-Ni paths in *199Ni28BAS*-FAU and *607Ni89BAS*-FAU catalysts.

Sample	**Path**	**CN**	**d / Å**	**ΔE_0 / eV**	**$\sigma^2 \cdot 1000$ / Å^2**	**R-factor**
199Ni28BAS	Ni-O	5.2±1.8	2.059±0.023	2.76±3.02	9.9±4.0	0.093
	Ni-Ni	5.5±2.9	3.053±0.023		11.7±4.1	
607Ni89BAS	Ni-O	4.9±1.6	2.063±0.021	2.98±2.75	10.0±3.8	0.082
	Ni-Ni	6.64±3.1	3.059±0.022		13.3±3.9	

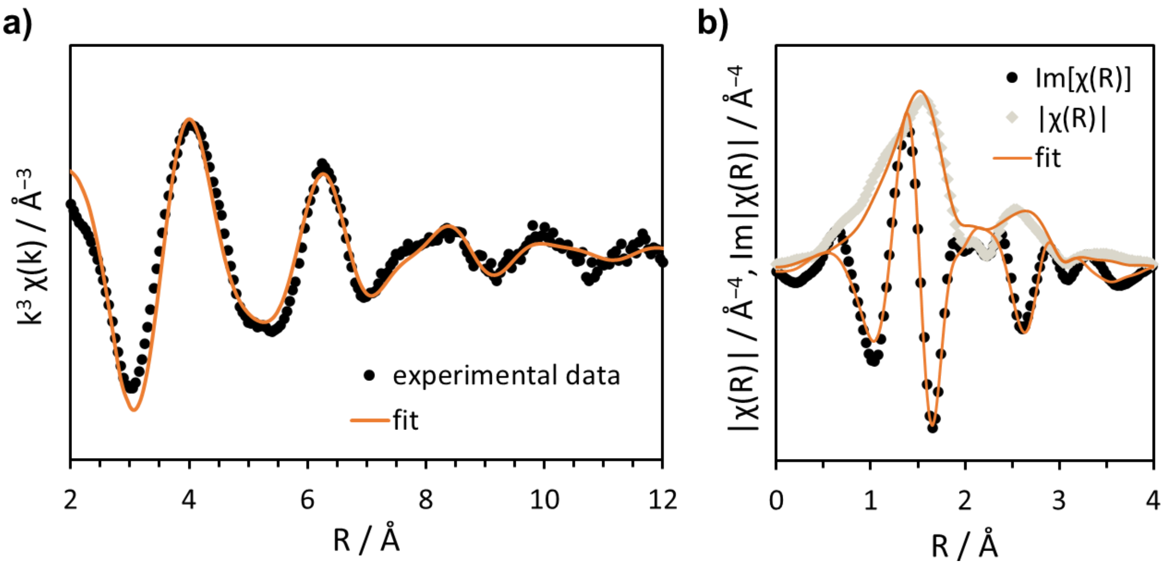

Figure 6.62: a) k^3-weighted EXAFS $\chi(k)$ spectra and fits of *50Ni130BAS*-FAU. b) EXAFS χ(R) spectra and fits of *50Ni130BAS*-FAU.

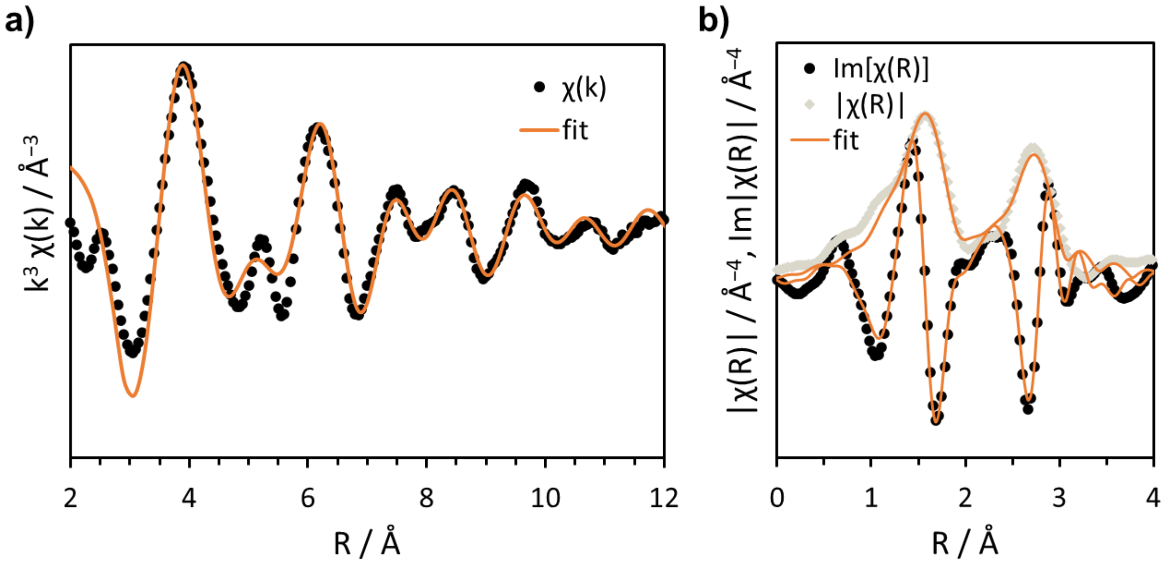

Figure 6.63: a) k^3-weighted EXAFS $\chi(k)$ spectra and fits of *199Ni42BAS*-FAU. b) EXAFS χ(R) spectra and fits of *199Ni42BAS*-FAU. (Ni-Si interactions are considered for the second shell signals).

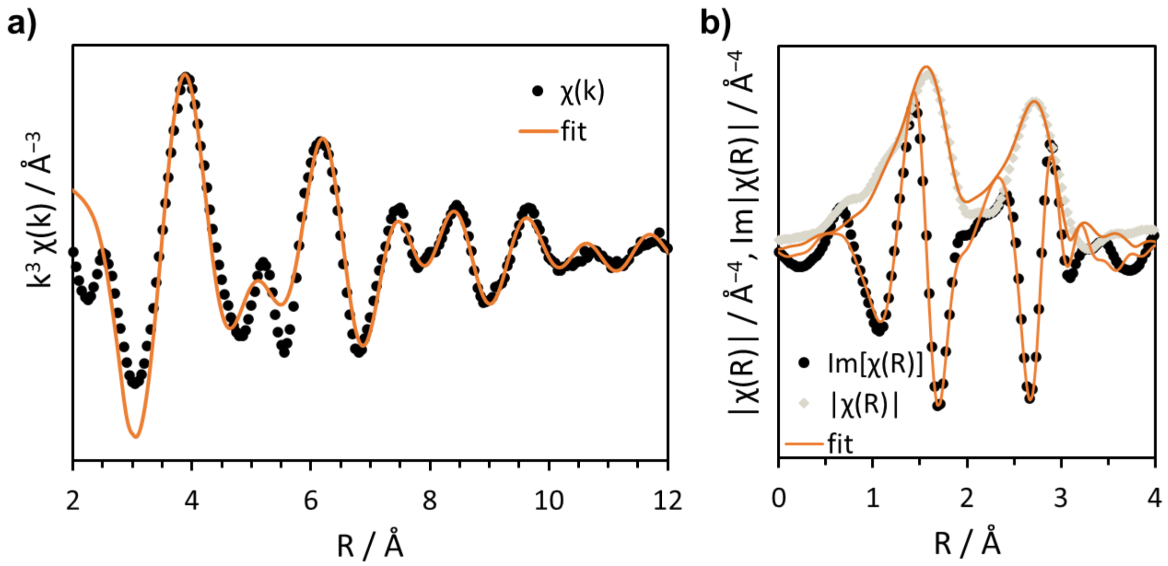

Figure 6.64: a) k^3-weighted EXAFS $\chi(k)$ spectra and fits of *607Ni89BAS*-FAU. b) EXAFS χ(R) spectra and fits of *607Ni89BAS*-FAU. (Ni-Si interactions are considered for the second shell signals).

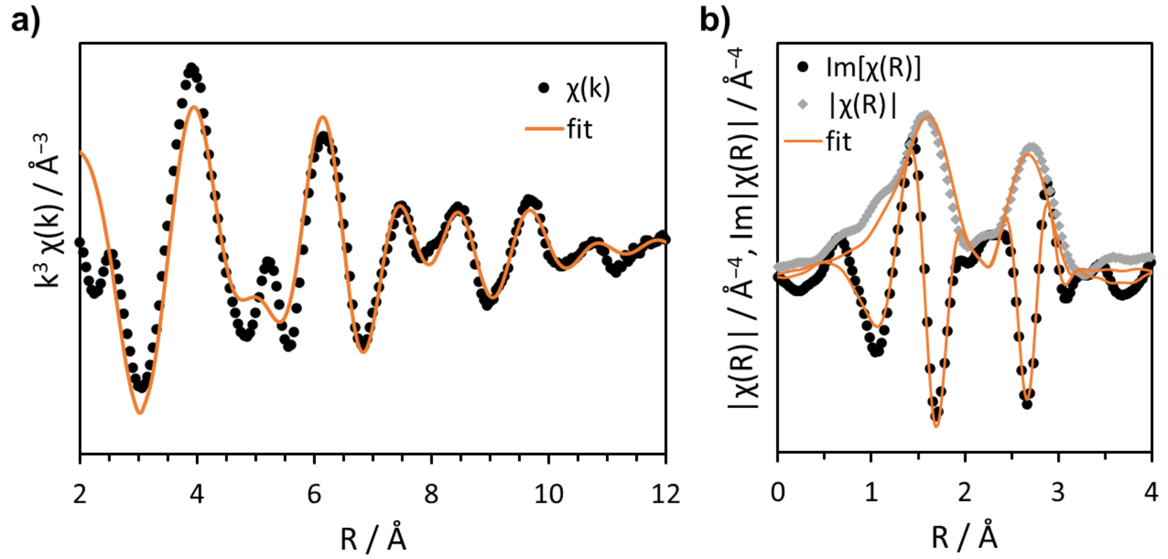

Figure 6.65: a) k^3-weighted EXAFS $\chi(k)$ spectra and fits of *199Ni42BAS*-FAU. b) EXAFS χ(R) spectra and fits of *199Ni42BAS*-FAU. (Ni-Ni interactions are considered for the second shell signals).

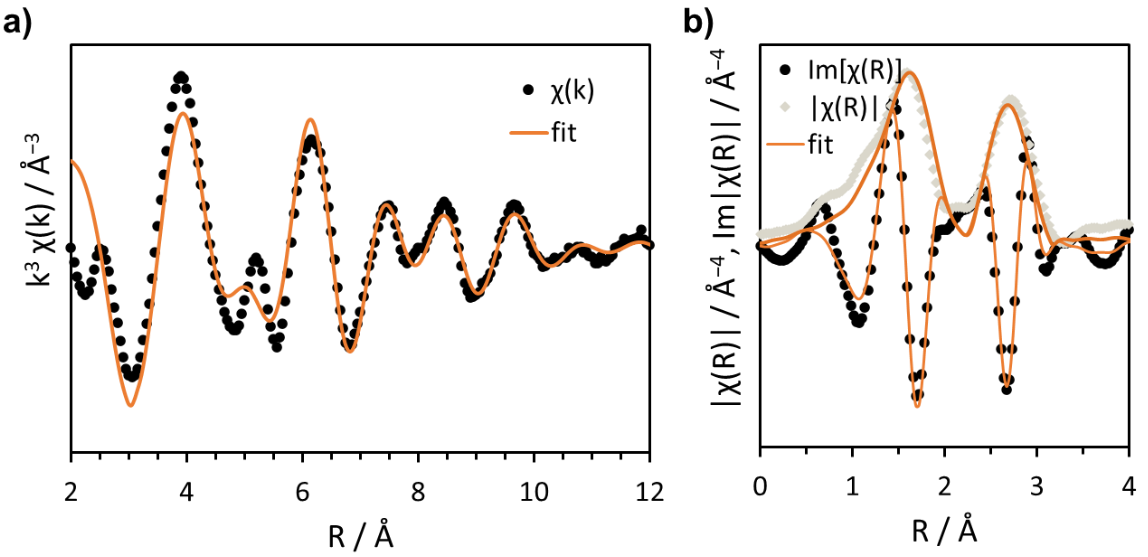

Figure 6.66: a) k^3-weighted EXAFS EXAFS $\chi(k)$ spectra and fits of *607Ni89BAS*-FAU. b) EXAFS χ(R) spectra and fits of *607Ni89BAS*-FAU. (Ni-Ni interactions are considered for the second shell signals).

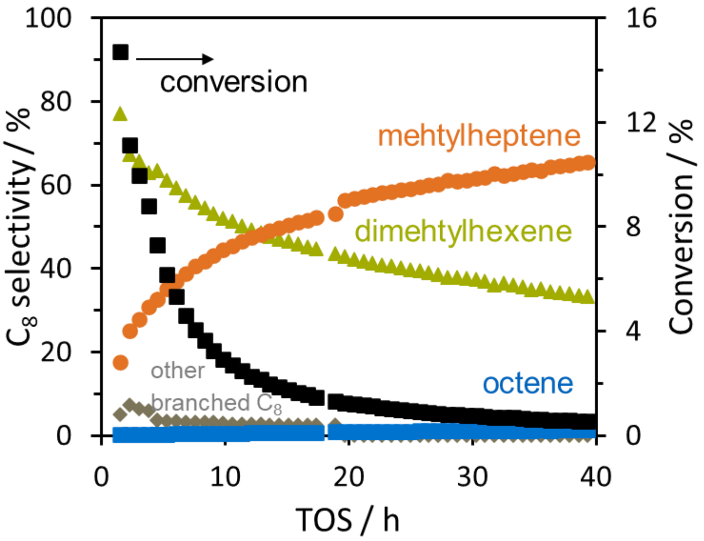

Figure 6.67: Conversion and C_8 selectivities for H-FAU (reaction conditions: T = 160 °C, p = 50 bar, WHSV = 500 h^{-1}).

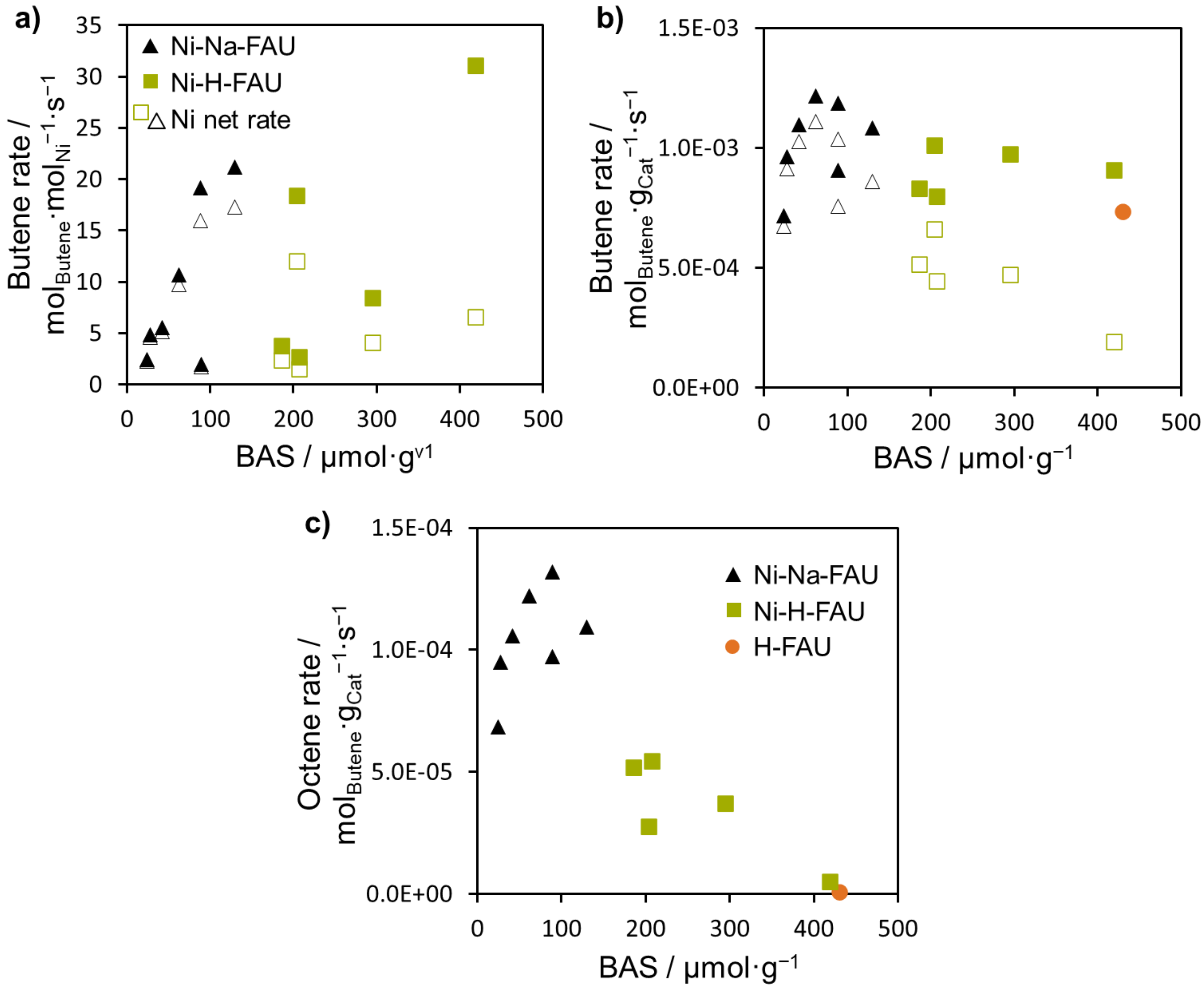

Figure 6.68: Butene consumption rates a) per Ni, b) per gram and c) octene formation rates for Ni-Na-FAU and Ni-H-FAU samples at different BAS concentrations.

6.3.4 Activation procedure

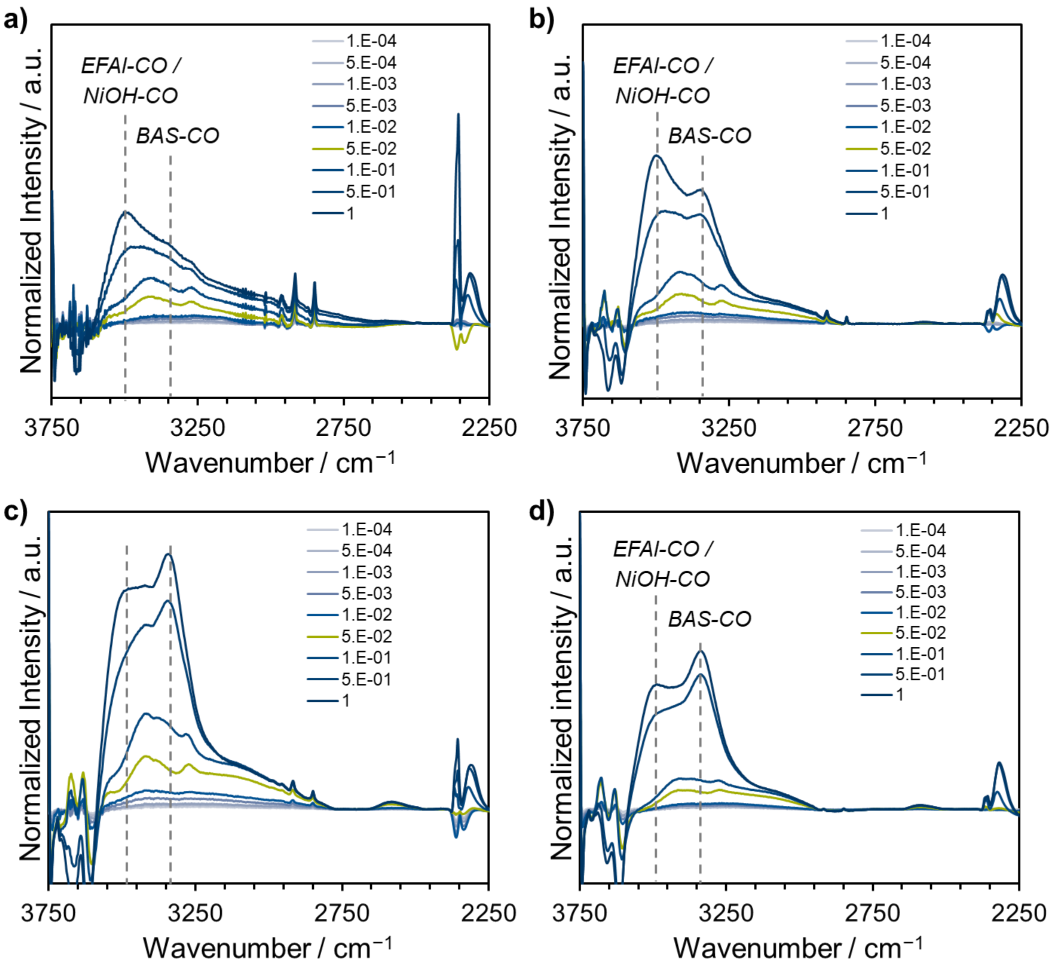

Figure 6.69: Region of EFAl and BAS contribution of normalized IR difference spectra of *179Ni89BAS*-MFI upon low-temperature dosing of CO-dosing after activation treatment in a) synthetic air, b) nitrogen, c) hydrogen, and d) hydrogen and then synthetic air.

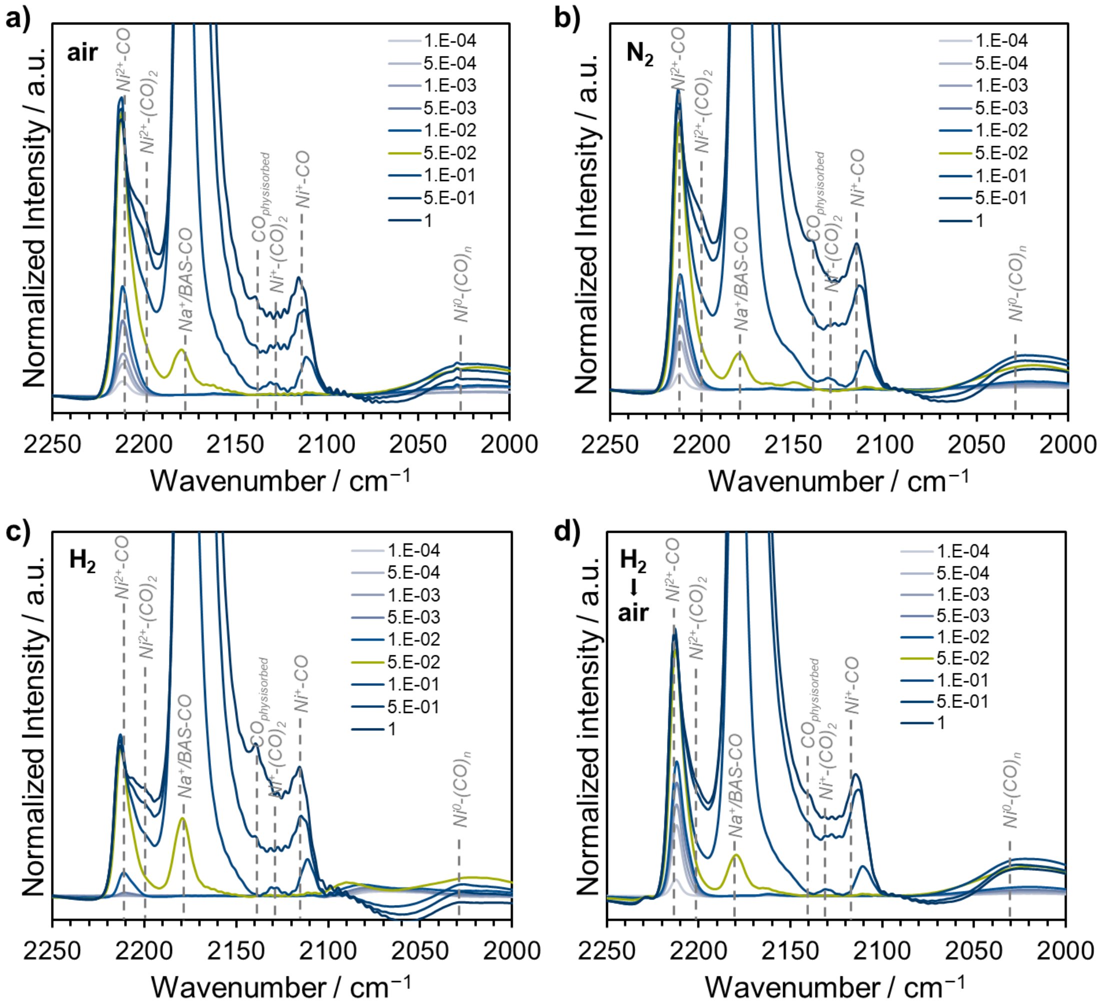

Figure 6.70: Normalized IR difference spectra of *179Ni89BAS*-MFI upon low-temperature dosing of CO-dosing after activation treatment in a) synthetic air, b) nitrogen, c) hydrogen, and d) hydrogen and then synthetic air. Pressure during dosing steps from $1{\cdot}10^{-4}$ mbar (light blue) to 1 mbar (dark blue) levels are given in mbar. Spectra at $5{\cdot}10^{-2}$ mbar are highlighted in green. Dosing of CO was performed at liquid nitrogen temperature. The spectra are normalized to zeolite lattice vibrations (approx. 2100 cm^{-1} to 1700 cm^{-1}).

Table 6.19: Results of peak deconvolution of normalized IR difference spectra upon low-temperature CO-adsorption ($1\cdot10^{-2}$ mbar) on *179Ni89BAS*-MFI upon different activation procedures (Activation: vacuum, 450 °C, 10 $°C\cdot min^{-1}$, 1 h → 25 mbar gas, 450 °C, 1 h). CO-dosing was performed at liquid nitrogen temperature. Deconvolution was performed with two Gaussian peaks and fixed baseline at zero applying Levenberg-Marquardt iteration mechanism. Peak center, area, full width at half maximum (FWHM) and their respective standard deviation σ are given for each peak.

Sample	**Peak**	**Center / cm^{-1}**	**σ_{center} / cm^{-1}**	**Area / cm^{-1}**	**σ_{area} / cm^{-1}**	**FWHM / cm^{-1}**	**σ_{FWHM} / cm^{-1}**
synair	1	2208.12	2.15	$6.24\cdot10^{-3}$	$2.90\cdot10^{-3}$	11.47	1.86
	2	2211.96	0.37	$4.98\cdot10^{-3}$	$2.76\cdot10^{-3}$	5.96	1.34
N_2	1	2208.35	1.06	$5.09\cdot10^{-3}$	$1.21\cdot10^{-3}$	11.11	0.89
	2	2212.13	0.19	$3.89\cdot10^{-3}$	$1.16\cdot10^{-3}$	5.89	0.68
H_2	1	2207.79	13.92	$9.86\cdot10^{-4}$	$3.71\cdot10^{-3}$	8.19	15.34
	2	2212.14	2.67	$7.12\cdot10^{-4}$	$3.62\cdot10^{-3}$	5.10	6.92
H_2→synair	1	2209.12	0.84	$5.93\cdot10^{-3}$	$1.22\cdot10^{-3}$	11.03	0.70
	2	2212.43	0.18	$4.39\cdot10^{-3}$	$1.18\cdot10^{-3}$	5.91	0.62

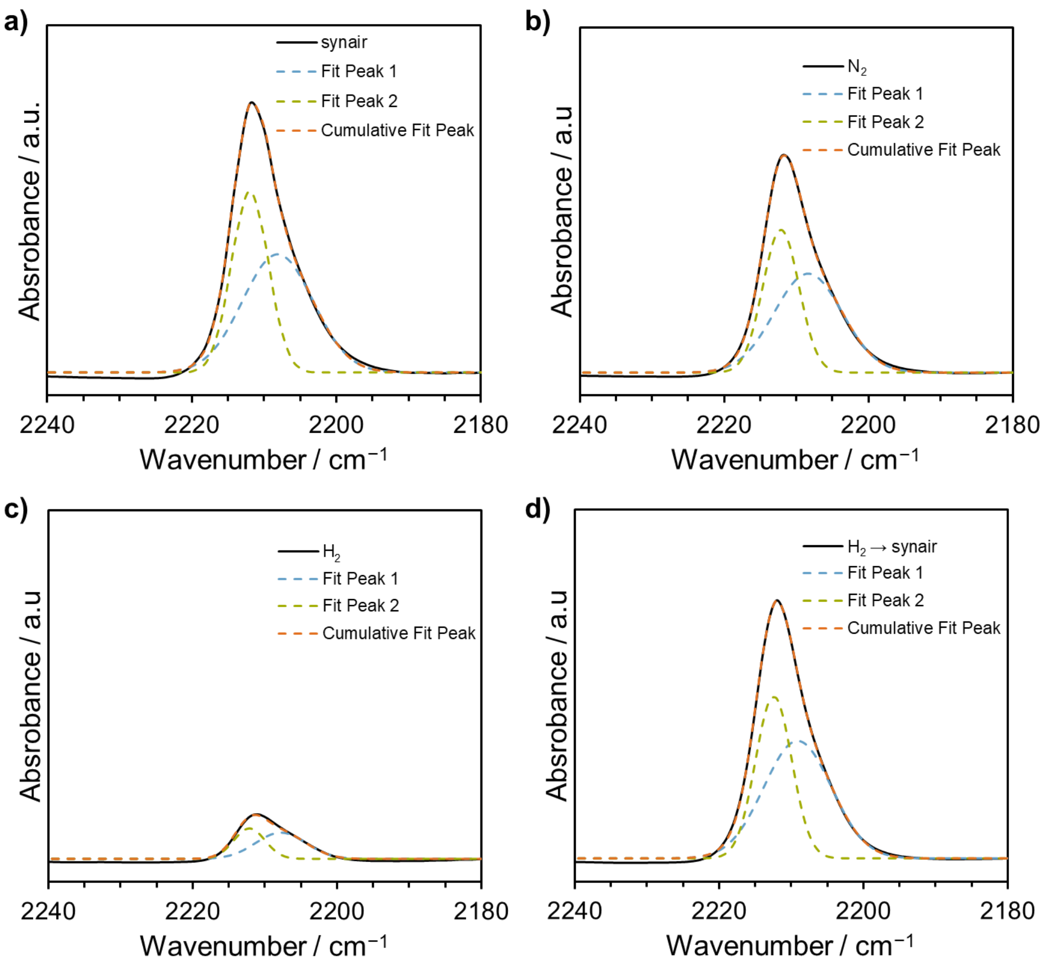

Figure 6.71: Deconvoluted and normalized IR difference spectra upon low-temperature CO-adsorption (1·10−2 mbar) on different Ni-Na-MFI samples (85Ni21BAS-, 179Ni89BAS-, 496Ni116BAS-, and 671Ni60BAS-MFI). CO-dosing was performed at liquid nitrogen temperature. Two Gaussian peaks were fitted with a fixed baseline at zero applying Levenberg-Marquardt iteration mechanism. Fitted peaks of Ni2+-CO (dashed orange), Ni2+-(CO)2 (dashed blue), cumulative fit (dashed green) and experimental spectra (solid black) are given. Spectra were normalized to lattice vibrations (approx. 2100 cm−1 to 1700 cm−1) for fair comparison between samples.

6.3.5 Selectivity and activity differences

a) *174Ni*-CHA **b)** *179Ni89BAS*-MFI

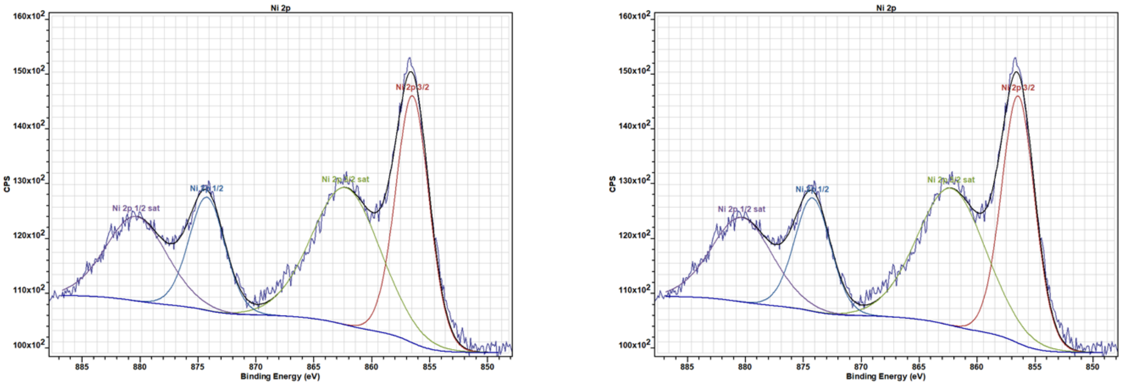

c) *114Ni62BAS*-FAU **d)** *199Ni28BAS*-FAU

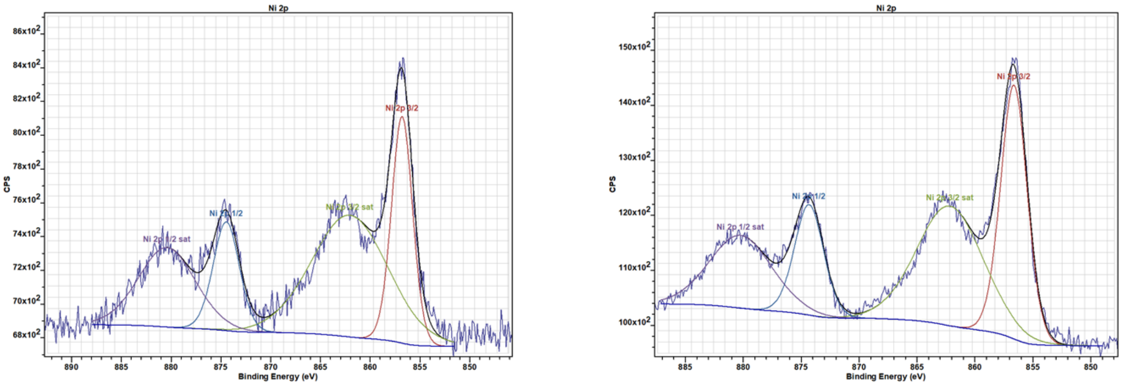

e) 2.5%Ni-UiO-66

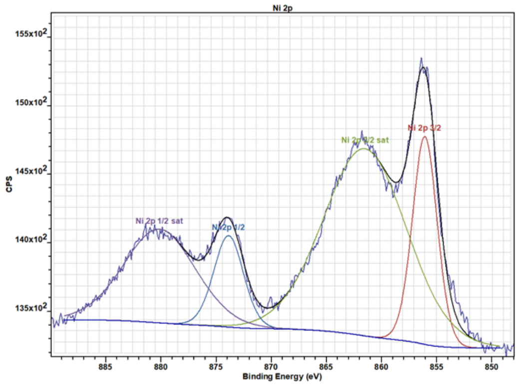

Figure 6.72: Deconvolution of the 2p transition and associated satellite for the XPS spectra of a) Ni-Na-CHA (*174N*i-CHA), b) Ni-Na-MFI (*179Ni89BAS*-MFI), c) Ni-Na-FAU (*114Ni62BAS*-FAU), d) Ni-Na-FAU (*199Ni28BAS*-FAU) and e) 2.5%Ni-UiO-66.

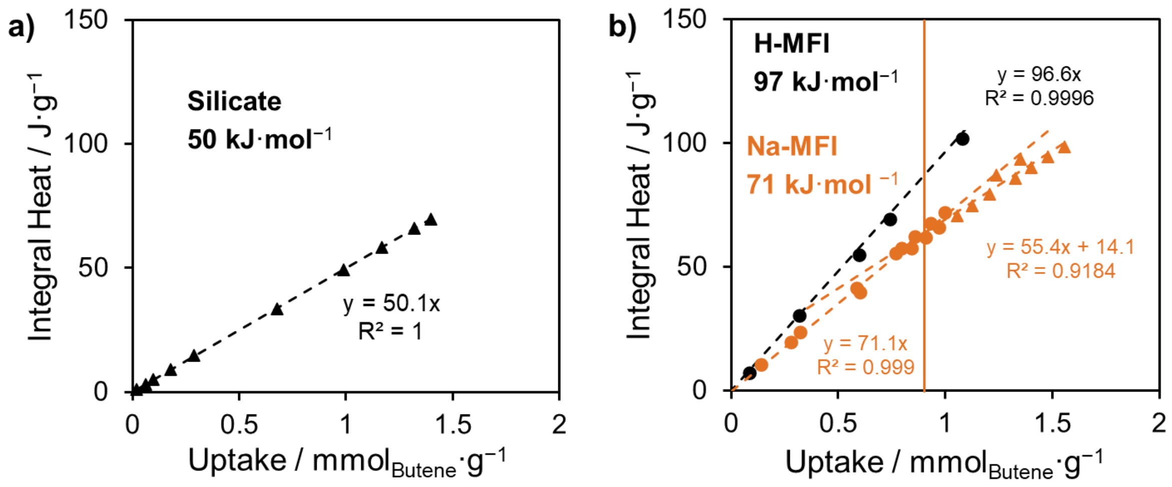

Figure 6.73: Adsorption enthalpies against butene uptakes on a) silicate and b) H-MFI and Na-MFI. The integral heat of Na-MFI shows two contributions: the adsorption on Na (circles) and the physisorption within the zeolites pores resembling the interaction on a silicate (triangles).

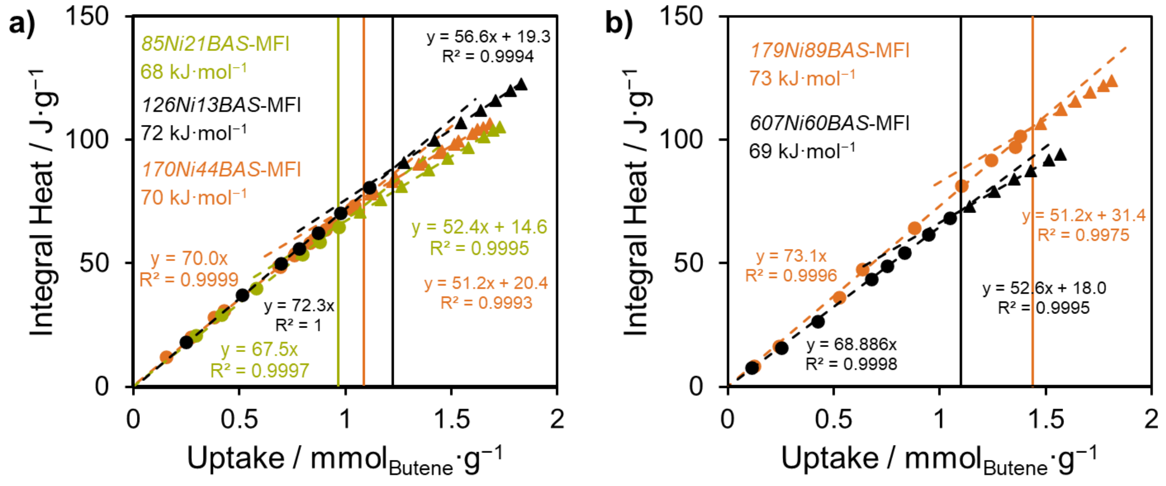

Figure 6.74: Adsorption enthalpies and butene uptakes on Ni-Na-MFI samples with different Ni loadings. The integral heat of each sample shows two contributions: the adsorption on Na and Ni (circles) and the physisorption within the zeolites pores resembling the interaction on a silicate (triangles).

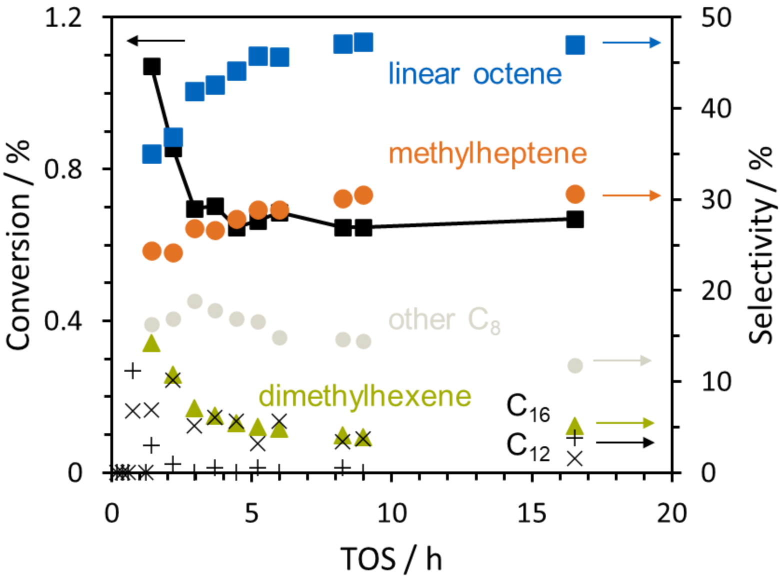

Figure 6.75: Conversion and selectivities of *179Ni89BAS*-MFI over time on stream (TOS) at low-pressure reaction conditions (T = 160 °C, p = 1 bar, 5 mL·min^{-1} of butene feed).

7 References

[1] J. Skupińska, *Chem. Rev.* **1991**, *91*, 613–648.

[2] I. Agirrezabal-Telleria, E. Iglesia, *J. Catal.* **2020**, *389*, 690–705.

[3] K. Weissermel, H. Arpe, *Industrial Organic Chemistry*, Wiley, **2003**.

[4] G. Chauvel, A; Lefebre, *Petrochemical Processes: Technical and Econimic Characteristics*, Houston, Tex. : Gulf Pub. Co. ; Paris : Éditions Technip, **1989**.

[5] A. Forestière, F. Favre, in *Multiph. Homog. Catal.*, John Wiley & Sons, Ltd, **2005**, pp. 547–587.

[6] S. Albrecht, D. Kießling, D. Maschmeyer, F. Nierlich, G. Wendt, *Chemie-Ingenieur-Technik* **2005**, *77*, 695–709.

[7] A. Forestière, H. Olivier-Bourbigou, L. Saussine, *Oil Gas Sci. Technol.* **2009**, *64*, 649–667.

[8] B. Nkosi, F. T. T. Ng, G. L. Rempel, *Appl. Catal. A Gen.* **1997**, *161*, 153–166.

[9] J. Schulze, M. Homann, *C4-Hydrocarbons and Derivatives: Resources, Production, Marketing*, Springer, Berlin, Heidelberg, **1989**.

[10] C. Yves, C. Dominique, G. Jean, L. Gerard, P. N. Hung, **1981**.

[11] A. Behr, Z. Bayrak, S. Peitz, G. Stochniol, D. Maschmeyer, *RSC Adv.* **2015**, *5*, 41372–41376.

[12] A. Finiels, F. Fajula, V. Hulea, *Cite this Catal. Sci. Technol* **2014**, *4*, 2412.

[13] C. T. O'Connor, M. Kojima, *Catal. Today* **1990**, *6*, 329–349.

[14] R. J. Quann, L. A. Green, S. A. Tabak, F. J. Krambeck, *Ind. Eng. Chem. Res.* **1988**, *27*, 565–570.

[15] M. L. Sarazen, E. Doskocil, E. Iglesia, *J. Catal.* **2016**, *344*, 553–569.

[16] Y. T. Kim, J. P. Chada, Z. Xu, Y. J. Pagan-Torres, D. C. Rosenfeld, W. L. Winniford, E. Schmidt, G. W. Huber, *J. Catal.* **2015**, *323*, 33–44.

[17] N. Kumar, P. Mäki-Arvela, T. Yläsalmi, J. Villegas, T. Heikkilä, A. R. Leino, K. Kordás, T. Salmi, D. Yu Murzin, *Microporous Mesoporous Mater.* **2012**, *147*, 127–134.

[18] M. L. Occelli, J. T. Hsu, L. G. Galaya, *J. Mol. Catal.* **1985**, *32*, 377–390.

[19] L. G. Galya, M. L. Occelli, J. T. Hsu, D. C. Young, *J. Mol. Catal.* **1985**, *32*, 391–403.

[20] M. Bjørgen, K. P. Lillerud, U. Olsbye, S. Bordiga, A. Zecchina, *J. Phys. Chem. B* **2004**, *108*, 7862–7870.

[21] R. Joshi, G. Zhang, J. T. Miller, R. Gounder, *ACS Catal.* **2018**, *8*, 11407–11422.

[22] N. Tsuda, T. Mori, N. Kosaka, Y. Sakai, *J. Mol. Catal.* **1985**, *28*, 183–190.

[23] S. M. Hassan, G. M. Panchenkov, O. I. Kuznetsov, *Bull. Chem. Soc. Jpn.* **1977**, *50*, 2597–2601.

[24] M. F. Delley, F. Núñez-Zarur, M. P. Conley, A. Comas-Vives, G. Siddiqi, S. Norsic, V. Monteil, O. V. Safonova, C. Copéret, *Proc. Natl. Acad. Sci. U. S. A.* **2014**, *111*, 11624–11629.

[25] B. M. Weckhuysen, I. E. Wachs, R. A. Schoonheydt, *Chem. Rev.* **1996**, *96*, 3327–3349.

[26] Z. Xu, J. P. Chada, D. Zhao, C. A. Carrero, Y. T. Kim, D. C. Rosenfeld, J. L. Rogers, S. J. Rozeveld, I. Hermans, G. W. Huber, *ACS Catal.* **2016**, *6*, 3815–3825.

[27] R. G. Schultz, J. M. Schuck, B. S. Wildi, *J. Catal.* **1966**, *6*, 385–396.

[28] R. G. Schultz, R. M. Engelbrecht, R. N. Moore, L. T. Wolford, *Olefin Dimerization over Cobalt-Oxide-on-Carbon Catalysts II. Butene and, Hexene Dimerization*, **1966**.

[29] H. Olivier-Bourbigou, P. A. R. Breuil, L. Magna, T. Michel, M. F. Espada Pastor, D. Delcroix, *Chem. Rev.* **2020**, *120*, 7919–7983.

[30] M. Sanati, C. Hörnell, S. G. Järäs, *The Oligomerization of Alkenes by Heterogeneous Catalysts*, **2007**.

[31] K. Ziegler, E. Holzkamp, H. Breil, H. Martin, *Angew. Chemie* **1955**, *67*, 541–547.

[32] K. Fischer, K. Jonas, P. Misbach, R. Stabba, G. Wilke, *Angew. Chemie Int. Ed. English* **1973**, *12*, 943–953.

[33] R. Y. Brogaard, U. Olsbye, *ACS Catal.* **2016**, *6*, 1205–1214.

[34] A. Brückner, U. Bentrup, H. Zanthoff, D. Maschmeyer, *J. Catal.* **2009**, *266*, 120–128.

[35] R. Henry, M. Komurcu, Y. Ganjkhanlou, R. Y. Brogaard, L. Lu, K. J. Jens, G. Berlier, U. Olsbye, *Catal. Today* **2018**, *299*, 154–163.

[36] G. Garbarino, P. Riani, A. Infantes-Molina, E. Rodríguez-Castellón, G. Busca, *Appl. Catal. A Gen.* **2016**, *525*, 180–189.

[37] T. Yashima, Y. Ushida, M. Ebisawa, N. Hara, *J. Catal.* **1975**, *36*, 320–326.

[38] T. Matsuda, H. Miura, K. Sugiyama, N. Qhno, *Selectivity in Ethylene Dimerization over Supported Nickel Oxide Catalysts*, **1978**.

[39] H. Imai, H. Uchida, *] Study of Nickel Oxide-Silica-Alumina Catalysts for Ethylene Polymerization. Study of Nickel Oxide-Silica-Alumina Catalysts for Ethylene Polymerization. III. The Performance of the Catalysts in Ethylene Polymerization and Butene Isomer Formation and Its Dependence on the Nickel Oxide Content*, **1965**.

[40] J. P. HOGAN, R. L. BANKS, W. C. LANNING, A. CLARK, *Ind. Eng. Chem. Res.* **1955**, *47*, 752.

[41] A. L. Lapidus, Y. I. Isakov, A. A. Slinkin, R. V. Avetisyan, K. M. Minachev, Y. T. Éidus, *Bull. Acad. Sci. USSR Div. Chem. Sci.* **1971**, *20*, 1797–1801.

[42] H. Choo, L. Kevan, *J. Phys. Chem. B* **2001**, *105*, 6353–6360.

[43] R. Spinicci, A. Tofanari, *Mater. Chem. Phys.* **1990**, *25*, 375–383.

[44] J. Rabeah, J. Radnik, V. Briois, D. Maschmeyer, G. Stochniol, S. Peitz, H. Reeker, C. La Fontaine, A. Brückner, *ACS Catal.* **2016**, *6*, 8224–8228.

[45] A. Ehrmaier, L. Löbbert, M. Sanchez-Sanchez, R. Bermejo-Deval, J. Lercher, *ChemCatChem* **2020**, *12*, DOI 10.1002/cctc.202000349.

[46] A. K. Ghosh, L. Kevan, *J. Phys. Chem.* **1990**, *94*, 3117–3121.

[47] P.-A. R. Breuil, L. Magna, H. Olivier-Bourbigou, *Catal. Letters* **2015**, *145*, 173–192.

[48] S. Forget, H. Olivier-Bourbigou, D. Delcroix, *ChemCatChem* **2017**, *9*, 2408–2417.

[49] S. Moussa, P. Concepción, M. A. Arribas, A. Martínez, *ACS Catal.* **2018**, *8*, 3903–3912.

[50] K. Toch, J. W. Thybaut, G. B. Marin, *Appl. Catal. A Gen.* **2015**, *489*, 292–304.

[51] J. R. Sohn, W. C. Park, S. E. Park, *Catal. Letters* **2002**, *81*, 259–264.

[52] T. Cai, D. Cao, Z. Song, L. Li, *Appl. Catal. A, Gen.* **1993**, *95*, L1–L7.

[53] A. A. Davydov, M. Kantcheva, M. L. Chepotko, *Catal. Letters* **2002**, *83*, 97–108.

[54] T. Cai, *Catal. Today* **1999**, *51*, 153–160.

[55] M. Hartmann, A. Pöppl, L. Kevan, *J. Phys. Chem.* **1996**, *100*, 9906–9910.

[56] L. Bonneviot, D. Olivier, M. Che, *J. Mol. Catal.* **1983**, *21*, 415–430.

[57] I. V. Elev, B. N. Shelimov, V. B. Kazansky, *J. Catal.* **1984**, *89*, 470–477.

[58] F. X. Cai, C. Lepetit, M. Kermarec, D. Olivier, *J. Mol. Catal.* **1987**, *43*, 93–116.

[59] A. Martínez, M. A. Arribas, P. Concepción, S. Moussa, *Appl. Catal. A Gen.* **2013**, *467*, 509–518.

[60] A. N. Mlinar, G. B. Baur, G. G. Bong, A. Getsoian, A. T. Bell, *J. Catal.* **2012**, *296*, 156–164.

[61] A. Ehrmaier, Y. Liu, S. Peitz, A. Jentys, Y. H. C. Chin, M. Sanchez-Sanchez, R. Bermejo-Deval, J. Lercher, *ACS Catal.* **2019**, *9*, 315–324.

[62] A. N. Mlinar, S. Shylesh, O. C. Ho, A. T. Bell, *ACS Catal.* **2014**, *4*, 337–343.

[63] M. Tanaka, A. Itadani, Y. Kuroda, M. Iwamoto, *J. Phys. Chem. C* **2012**, *116*, 5664–5672.

[64] G. Wendt, K. Hagenau, R. Dimitrova, Z. Popova, C. Dimitrov, *React. Kinet. Catal. Lett.* **1986**, *31*, 383–388.

[65] G. Wendt, J. Finster, R. Schöllner, H. Siegel, *Stud. Surf. Sci. Catal.* **1981**, *7*, 978–992.

[66] S. Moussa, M. A. Arribas, P. Concepción, A. Martínez, *Catal. Today* **2016**, *277*, 78–88.

[67] M. Lallemand, A. Finiels, F. Fajula, V. Hulea, *J. Phys. Chem. C* **2009**, *113*, 20360–20364.

[68] I. Agirrezabal-Telleria, E. Iglesia, *J. Catal.* **2017**, *352*, 505–514.

[69] T. H. Vuong, N. Rockstroh, U. Bentrup, J. Rabeah, J. Knossalla, S. Peitz, R. Franke, A. Brückner, *ACS Catal.* **2021**, *11*, 3541–3552.

[70] K. Kimura, H. A-I, A. Ozaki, *J. Catal.* **1970**, *18*, 271–280.

[71] F. T. T. Ng, D. C. Creaser, *Appl. Catal. A, Gen.* **1994**, *119*, 327–339.

[72] V. Hulea, F. Fajula, *J. Catal.* **2004**, *225*, 213–222.

[73] H. Hartati, A. Purwaningsih, T. S. Tjahjandarie, N. H. Saputri, I. S. Puspitasari, C. N. Lamanele, A. A. Sa’adah, A. S. Haque, D. Z. Mardho, *Open Chem.* **2020**, *18*, 295–302.

[74] W. K. W. Lee, J. S. J. Van Deventer, *Langmuir* **2003**, *19*, 8726–8734.

[75] J. Davidovits, *J. Therm. Anal.* **1991**, *37*, 1633–1656.

[76] J. G. S. Van Jaarsveld, J. S. J. Van Deventer, A. Schwartzman, *Miner. Eng.* **1999**, *12*, 75–91.

[77] F. Alscher, F. Nadolny, H. Frenzel, J. Knossalla, S. Peitz, E. Borovinskaya, C. Breitkopf, R. Franke, W. Reschetilowski, *Catal. Sci. Technol.* **2019**, *9*, 2456–2468.

[78] F. Nadolny, U. Bentrup, N. Rockstroh, F. Alscher, W. Reschetilowski, S. Peitz, R. Franke, A. Brückner, *Catal. Sci. Technol.* **2021**, *11*, 4732–4740.

[79] M. R. Agliullin, I. G. Danilova, A. V. Faizullin, S. V. Amarantov, S. V. Bubennov, T. R. Prosochkina, N. G. Grigor'Eva, E. A. Paukshtis, B. I. Kutepov, *Microporous Mesoporous Mater.* **2016**, *230*, 118–127.

[80] V. Blay, L. F. Bobadilla, A. Cabrera-García, *Zeolites and Metal-Organic Frameworks*, Amsterdam University Press, **2019**.

[81] M. Niwa, N. Katada, K. Okumura, *Characterization and Design of Zeolite Catalysts*, Springer Berlin Heidelberg, Berlin, Heidelberg, **2010**.

[82] A. W. Chester, E. G. Derouane, *Zeolite Characterization and Catalysis: A Tutorial*, Springer Netherlands, **2010**.

[83] W. M. Meier, H. J. Moeck, *J. Solid State Chem.* **1979**, *27*, 349–355.

[84] J. Weitkamp, *Solid State Ionics* **2000**, *131*, 175–188.

[85] J. Čejka, A. Corma, S. Zones, *Zeolites and Catalysis*, Wiley, **2010**.

[86] J. R. Di Iorio, R. Gounder, *Chem. Mater.* **2016**, *28*, 2236–2247.

[87] J. Dědeček, D. Kaucký, B. Wichterlová, O. Gonsiorová, *Phys. Chem. Chem. Phys.* **2002**, *4*, 5406–5413.

[88] M. Dusselier, M. E. Davis, *Chem. Rev.* **2018**, *118*, 5265–5329.

[89] C. Baerlocher, L. B. McCusker, "Database of Zeolite Structures," can be found under http://www.iza-structure.org/databases/, **n.d.**

[90] Y. Li, L. Li, J. Yu, *Chem* **2017**, *3*, 928–949.

[91] J. Pérez-Ramírez, C. H. Christensen, K. Egeblad, C. H. Christensen, J. C. Groen, *Chem. Soc. Rev.* **2008**, *37*, 2530–2542.

[92] L. Jiao, Y. Wang, H. L. Jiang, Q. Xu, *Adv. Mater.* **2018**, *30*, DOI 10.1002/adma.201703663.

[93] N. Stock, S. Biswas, *Chem. Rev.* **2012**, *112*, 933–969.

[94] B. F. Hoskins, R. Robson, *J. Am. Chem. Soc.* **1989**, *111*, 5962–5964.

[95] H. C. Zhou, J. R. Long, O. M. Yaghi, *Chem. Rev.* **2012**, *112*, 673–674.

[96] O. K. Farha, I. Eryazici, N. C. Jeong, B. G. Hauser, C. E. Wilmer, A. A. Sarjeant, R. Q. Snurr, S. T. Nguyen, A. Ö. Yazaydin, J. T. Hupp, *J. Am. Chem. Soc.* **2012**, *134*, 15016–15021.

[97] H. Furukawa, K. E. Cordova, M. O'Keeffe, O. M. Yaghi, *Science (80-.).* **2013**, *341*, DOI 10.1126/science.1230444.

[98] O. M. Yaghi, M. O'Keeffe, N. W. Ockwig, H. K. Chae, M. Eddaoudi, J. Kim, *Nature*

2003, *423*, 705–714.

[99] C. Wang, D. Liu, W. Lin, *J. Am. Chem. Soc.* **2013**, *135*, 13222–13234.

[100] W. Lu, Z. Wei, Z.-Y. Gu, T.-F. Liu, J. Park, J. Park, J. Tian, M. Zhang, Q. Zhang, T. Gentle III, et al., *Chem. Soc. Rev.* **2014**, *43*, 5561–5593.

[101] S. Yuan, L. Feng, K. Wang, J. Pang, M. Bosch, C. Lollar, Y. Sun, J. Qin, X. Yang, P. Zhang, et al., *Adv. Mater.* **2018**, *30*, 1704303.

[102] J. H. Cavka, S. Jakobsen, U. Olsbye, N. Guillou, C. Lamberti, S. Bordiga, K. P. Lillerud, *J. Am. Chem. Soc.* **2008**, DOI 10.1021/ja8057953.

[103] M. Kandiah, M. H. Nilsen, S. Usseglio, S. Jakobsen, U. Olsbye, M. Tilset, C. Larabi, E. A. Quadrelli, F. Bonino, K. P. Lillerud, *Chem. Mater.* **2010**, *22*, 6632–6640.

[104] G. C. Shearer, S. Chavan, J. Ethiraj, J. G. Vitillo, S. Svelle, U. Olsbye, C. Lamberti, S. Bordiga, K. P. Lillerud, *Chem. Mater.* **2014**, *26*, 4068–4071.

[105] H. Wu, Y. S. Chua, V. Krungleviciute, M. Tyagi, P. Chen, T. Yildirim, W. Zhou, *J. Am. Chem. Soc.* **2013**, *135*, 10525–10532.

[106] Y. Zhang, X. Zhang, J. Lyu, K. I. Otake, X. Wang, L. R. Redfern, C. D. Malliakas, Z. Li, T. Islamoglu, B. Wang, et al., *J. Am. Chem. Soc.* **2018**, *140*, 11179–11183.

[107] D. Yang, C. A. Gaggioli, D. Ray, M. Babucci, L. Gagliardi, B. C. Gates, *J. Am. Chem. Soc.* **2020**, *142*, 8044–8056.

[108] L. Valenzano, B. Civalleri, S. Chavan, S. Bordiga, M. H. Nilsen, S. Jakobsen, K. P. Lillerud, C. Lamberti, *Chem. Mater.* **2011**, *23*, 1700–1718.

[109] R. Wei, C. A. Gaggioli, G. Li, T. Islamoglu, Z. Zhang, P. Yu, O. K. Farha, C. J. Cramer, L. Gagliardi, D. Yang, et al., *Chem. Mater.* **2019**, *31*, 1655–1663.

[110] F. G. Cirujano, F. X. Llabrés I Xamena, *J. Phys. Chem. Lett.* **2020**, *11*, 4879–4890.

[111] M. R. DeStefano, T. Islamoglu, S. J. Garibay, J. T. Hupp, O. K. Farha, *Chem. Mater.* **2017**, *29*, 1357–1361.

[112] G. C. Shearer, S. Chavan, S. Bordiga, S. Svelle, U. Olsbye, K. P. Lillerud, *Chem. Mater.* **2016**, *28*, 3749–3761.

[113] Y. Liu, R. C. Klet, J. T. Hupp, O. Farha, *Chem. Commun.* **2016**, *52*, 7806–7809.

[114] D. M. Driscoll, D. Troya, P. M. Usov, A. J. Maynes, A. J. Morris, J. R. Morris, *J. Phys. Chem. C* **2018**, *122*, 14582–14589.

[115] S. Øien, D. Wragg, H. Reinsch, S. Svelle, S. Bordiga, C. Lamberti, K. P. Lillerud, *Cryst. Growth Des.* **2014**, *14*, 5370–5372.

[116] F. Vermoortele, B. Bueken, G. Le Bars, B. Van De Voorde, M. Vandichel, K. Houthoofd, A. Vimont, M. Daturi, M. Waroquier, V. Van Speybroeck, et al., *J. Am. Chem. Soc.* **2013**, *135*, 11465–11468.

[117] S. Dissegna, R. Hardian, K. Epp, G. Kieslich, M.-V. Coulet, P. Llewellyn, R. A. Fischer, *CrystEngComm* **2017**, *19*, 4137–4141.

[118] F. G. Cirujano, A. Corma, F. X. Llabrés i Xamena, *Chem. Eng. Sci.* **2015**, *124*, 52–60.

[119] C. Caratelli, J. Hajek, F. G. Cirujano, M. Waroquier, F. X. Llabrés i Xamena, V. Van

Speybroeck, *J. Catal.* **2017**, *352*, 401–414.

[120] D. Yang, M. A. Ortuño, V. Bernales, C. J. Cramer, L. Gagliardi, B. C. Gates, *J. Am. Chem. Soc.* **2018**, *140*, 3751–3759.

[121] A. N. Mlinar, B. K. Keitz, D. Gygi, E. D. Bloch, J. R. Long, A. T. Bell, *ACS Catal.* **2014**, *4*, 717–721.

[122] U. S. F. Arrozi, V. Bon, C. Kutzscher, I. Senkovska, S. Kaskel, *Dalt. Trans.* **2019**, *48*, 3415–3421.

[123] E. D. Metzger, R. J. Comito, Z. Wu, G. Zhang, R. C. Dubey, W. Xu, J. T. Miller, M. Dinca, *ACS Sustain. Chem. Eng.* **2019**, *7*, 6654–6661.

[124] E. D. Metzger, C. K. Brozek, R. J. Comito, M. Dinca, *ACS Cent. Sci.* **2016**, *2*, 148–153.

[125] R. J. Comito, E. D. Metzger, Z. Wu, G. Zhang, C. H. Hendon, J. T. Miller, M. Dincă, *Organometallics* **2017**, *36*, 1681–1683.

[126] J. Canivet, S. Aguado, Y. Schuurman, D. Farrusseng, *J. Am. Chem. Soc.* **2013**, *135*, 4195–4198.

[127] B. Liu, S. Jie, Z. Bu, B. G. Li, *RSC Adv.* **2014**, *4*, 62343–62346.

[128] S. T. Madrahimov, J. R. Gallagher, G. Zhang, Z. Meinhart, S. J. Garibay, M. Delferro, J. T. Miller, O. K. Farha, J. T. Hupp, S. T. Nguyen, *ACS Catal.* **2015**, *5*, 6713–6718.

[129] J. Liu, J. Ye, Z. Li, K. I. Otake, Y. Liao, A. W. Peters, H. Noh, D. G. Truhlar, L. Gagliardi, C. J. Cramer, et al., *J. Am. Chem. Soc.* **2018**, *140*, 11174–11178.

[130] Z. Li, A. W. Peters, J. Liu, X. Zhang, N. M. Schweitzer, J. T. Hupp, O. K. Farha, *Inorg. Chem. Front.* **2017**, *4*, 820–824.

[131] V. Bernales, A. B. League, Z. Li, N. M. Schweitzer, A. W. Peters, R. K. Carlson, J. T. Hupp, C. J. Cramer, O. K. Farha, L. Gagliardi, *J. Phys. Chem. C* **2016**, *120*, 23576–23583.

[132] Z. Li, N. M. Schweitzer, A. B. League, V. Bernales, A. W. Peters, A. B. Getsoian, T. C. Wang, J. T. Miller, A. Vjunov, J. L. Fulton, et al., *J. Am. Chem. Soc.* **2016**, *138*, 1977–1982.

[133] I. S. Kim, J. Borycz, A. E. Platero-Prats, S. Tussupbayev, T. C. Wang, O. K. Farha, J. T. Hupp, L. Gagliardi, K. W. Chapman, C. J. Cramer, et al., *Chem. Mater.* **2015**, *27*, 4772–4778.

[134] E. D. Metzger, R. J. Comito, C. H. Hendon, M. Dincă, *J. Am. Chem. Soc.* **2017**, *139*, 757–762.

[135] T. A. Goetjen, X. Zhang, J. Liu, J. T. Hupp, O. K. Farha, *ACS Sustain. Chem. Eng.* **2019**, *7*, 2553–2557.

[136] E. Roduner, *Chem. Soc. Rev.* **2006**, *35*, 583–592.

[137] L. Jiao, H. L. Jiang, *Chem* **2019**, *5*, 786–804.

[138] L. Zhu, X. Q. Liu, H. L. Jiang, L. B. Sun, *Chem. Rev.* **2017**, *117*, 8129–8176.

[139] M. Liu, J. Wu, H. Hou, *Chem. - A Eur. J.* **2019**, *25*, 2935–2948.

[140] R. C. Klet, S. Tussupbayev, J. Borycz, J. R. Gallagher, M. M. Stalzer, J. T. Miller, L. Gagliardi, J. T. Hupp, T. J. Marks, C. J. Cramer, et al., *J. Am. Chem. Soc.* **2015**, *137*, 15680–15683.

[141] D. Yang, S. O. Odoh, T. C. Wang, O. K. Farha, J. T. Hupp, C. J. Cramer, L. Gagliardi, B. C. Gates, *J. Am. Chem. Soc.* **2015**, *137*, 7391–7396.

[142] H. G. T. Nguyen, N. M. Schweitzer, C. Y. Chang, T. L. Drake, M. C. So, P. C. Stair, O. K. Farha, J. T. Hupp, S. T. Nguyen, *ACS Catal.* **2014**, *4*, 2496–2500.

[143] S. Yuan, Y. P. Chen, J. Qin, W. Lu, X. Wang, Q. Zhang, M. Bosch, T. F. Liu, X. Lian, H. C. Zhou, *Angew. Chemie - Int. Ed.* **2015**, *54*, 14696–14700.

[144] Z. Li, A. W. Peters, V. Bernales, M. A. Ortuño, N. M. Schweitzer, M. R. Destefano, L. C. Gallington, A. E. Platero-Prats, K. W. Chapman, C. J. Cramer, et al., *ACS Cent. Sci.* **2017**, *3*, 31–38.

[145] J. N. Cardenas, K. F. O'Driscoll, *J. Polym. Sci. Polym. Chem. Ed.* **1976**, *14*, 883–897.

[146] B. J. Burger, M. E. Thompson, W. D. Cotter, J. E. Bercaw, *J. Am. Chem. Soc* **1990**, *112*, 1566–1577.

[147] A. M. Al-Jarallah, J. A. Anabtawi, M. A. B. Siddiqui, A. M. Aitani, A. W. Al-Sa'Doun, *Catal. Today* **1992**, *14*, 1–121.

[148] F. Speiser, P. Braunstein, L. Saussine, **2005**, DOI 10.1021/ar050040d.

[149] A. Ehrmaier, *Dimerization of 1-Butene on Ni Based Solid Catalysts*, **2019**.

[150] M. L. Sarazen, E. Iglesia, *Proc. Natl. Acad. Sci. U. S. A.* **2017**, *114*, E3900–E3908.

[151] S. Schallmoser, G. L. Haller, M. Sanchez-Sanchez, J. A. Lercher, *J. Am. Chem. Soc.* **2017**, *139*, 8646–8652.

[152] M. L. Sarazen, E. Iglesia, *J. Catal.* **2017**, *354*, 287–298.

[153] P. Cossee, *J. Catal.* **1964**, *3*, 80–88.

[154] E. J. Arlman, P. Cossee, *J. Catal.* **1964**, *3*, 99–104.

[155] Y. Chauvin, H. Olivier, C. N. Wyrvalski, L. C. Simon, R. F. De Souzat, *J. Catal.* **1997**, *165*, 275–278.

[156] L. C. Simon, J. Dupont, R. F. De Souza, *Appl. Catal. A Gen.* **1998**, *175*, 215–220.

[157] W. Keim, *Angew. Chemie Int. Ed.* **2013**, *52*, 12492–12496.

[158] K. P. Bryliakov, A. A. Antonov, *J. Organomet. Chem.* **2018**, *867*, 55–61.

[159] A. N. Mlinar, O. C. Ho, G. G. Bong, A. T. Bell, *ChemCatChem* **2013**, *5*, 3139–3147.

[160] D. S. McGuinness, *Chem. Rev.* **2011**, *111*, 2321–2341.

[161] R. H. Grubbs, A. Miyashita, *J. Am. Chem. Soc.* **1978**, *100*, 7416–7418.

[162] S. Datta, M. B. Fischer, S. S. Wreford, *J. Organomet. Chem.* **1980**, *188*, 353–366.

[163] A. K. Tomov, V. C. Gibson, G. J. P. Britovsek, R. J. Long, M. Van Meurs, D. J. Jones, K. P. Tellmann, J. J. Chirinos, *Organometallics* **2009**, *28*, 7033.

[164] J. T. Dixon, M. J. Green, F. M. Hess, D. H. Morgan, *J. Organomet. Chem.* **2004**, *689*, 3641–3668.

[165] R. D. Köhn, *Angew. Chemie - Int. Ed.* **2008**, *47*, 245–247.

[166] D. F. Wass, *Dalt. Trans.* **2007**, *0*, 816–819.

[167] M. P. Conley, M. F. Delley, G. Siddiqi, G. Lapadula, S. Norsic, V. Monteil, O. V. Safonova, C. Copéret, *Angew. Chemie Int. Ed.* **2014**, *53*, 1872–1876.

[168] A. Fong, Y. Yuan, S. L. Ivry, S. L. Scott, B. Peters, **2015**, DOI 10.1021/acscatal.5b00016.

[169] C. P. Nicolaides, M. S. Scurrell, P. M. Semano, *Appl. Catal. A Gen.* **2003**, *245*, 43–53.

[170] R. Y. Brogaard, M. Kømurcu, M. M. Dyballa, A. Botan, V. Van Speybroeck, U. Olsbye, K. De Wispelaere, *ACS Catal.* **2019**, *9*, 5645–5650.

[171] F. T. T. Ng, D. C. Creaser, *Stud. Surf. Sci. Catal.* **1992**, *73*, 123–131.

[172] B. Nkosi, F. T. T. Ng, G. L. Rempel, *Appl. Catal. A Gen.* **1997**, *158*, 225–241.

[173] Y. Chauvin, D. Commereuc, F. Hugues, J. Thivolle-cazat, *Appl. Catal.* **1988**, *42*, 205–216.

[174] A. Ehrmaier, S. Peitz, M. Sanchez-Sanchez, R. Bermejo-Deval, J. Lercher, *Microporous Mesoporous Mater.* **2019**, *284*, 241–246.

[175] M. Lallemand, O. A. Rusu, E. Dumitriu, A. Finiels, F. Fajula, V. Hulea, *Stud. Surf. Sci. Catal.* **2008**, *174*, 1139–1142.

[176] M. Lallemand, O. A. Rusu, E. Dumitriu, A. Finiels, F. Fajula, V. Hulea, *Appl. Catal. A Gen.* **2008**, *338*, 37–43.

[177] M. L. Sarazen, E. Doskocil, E. Iglesia, *ACS Catal.* **2016**, *6*, 7059–7070.

[178] M. Yamamura, K. Chaki, T. Wakatsuki, H. Okado, K. Fujimoto, *Zeolites* **1994**, *14*, 643–649.

[179] R. J. Madon, M. Boudart, *Ind. Eng. Chem. Fundam.* **1982**, *21*, 438–447.

[180] Y. Ganjkhanlou, G. Berlier, E. Groppo, E. Borfecchia, S. Bordiga, *Top. Catal.* **2017**, *60*, 1664–1672.

[181] J. H. Lehr, J. Keeley, T. B. Kingery, Eds. , *Alternative Energy and Shale Gas Encyclopedia*, John Wiley & Sons, Inc., Hoboken, NJ, USA, **2016**.

[182] N. Rahimi, R. Karimzadeh, *Appl. Catal. A Gen.* **2011**, *398*, 1–17.

[183] S. A. Treese, P. R. Pujadó, D. S. J. Jones, *Handbook of Petroleum Processing*, Springer Netherlands, **2006**.

[184] E. Rozhko, A. Bavykina, D. Osadchii, M. Makkee, J. Gascon, *J. Catal.* **2017**, *345*, 270–280.

[185] Y. Shaikh, K. Albahily, M. Sutcliffe, V. Fomitcheva, S. Gambarotta, I. Korobkov, R. Duchateau, *Angew. Chemie Int. Ed.* **2012**, *51*, 1366–1369.

[186] A. M. Messinis, W. R. H. Wright, A. S. Batsanov, J. A. K. Howard, M. J. Hanton, P. W. Dyer, *ACS Catal.* **2018**, *8*, 11235–11248.

[187] P. Liu, E. Redekop, X. Gao, W. C. Liu, U. Olsbye, G. A. Somorjai, *J. Am. Chem. Soc.* **2019**, *141*, 11557–11564.

[188] J. A. Martens, R. Ravishankar, I. E. Mishin, P. A. Jacobs, *Angew. Chemie* **2000**, *39*, 4376–4379.

[189] Z. Xu, D. Zhao, J. P. Chada, D. C. Rosenfeld, J. L. Rogers, I. Hermans, G. W. Huber, *J.*

Catal. **2017**, *354*, 213–222.

[190] N. R. Jaegers, K. Khivantsev, L. Kovarik, D. W. Klas, J. Z. Hu, Y. Wang, J. Szanyi, *Catal. Sci. Technol.* **2019**, *9*, 6570–6576.

[191] I. S. Kim, Z. Li, J. Zheng, A. E. Platero-Prats, A. Mavrandonakis, S. Pellizzeri, M. Ferrandon, A. Vjunov, L. C. Gallington, T. E. Webber, et al., *Angew. Chemie* **2018**, *130*, 921–925.

[192] T. Ikuno, J. Zheng, A. Vjunov, M. Sanchez-Sanchez, M. A. Ortuño, D. R. Pahls, J. L. Fulton, D. M. Camaioni, Z. Li, D. Ray, et al., *J. Am. Chem. Soc.* **2017**, *139*, 10294–10301.

[193] S. P. Desai, J. Ye, J. Zheng, M. S. Ferrandon, T. E. Webber, A. E. Platero-Prats, J. Duan, P. Garcia-Holley, D. M. Camaioni, K. W. Chapman, et al., *J. Am. Chem. Soc.* **2018**, *140*, 15309–15318.

[194] M. A. Deimund, J. Labinger, M. E. Davis, *ACS Catal.* **2014**, *4*, 4189–4195.

[195] A. M. Abdel-Mageed, B. Rungtaweevoranit, M. Parlinska-Wojtan, X. Pei, O. M. Yaghi, R. Jürgen Behm, *J. Am. Chem. Soc.* **2019**, *141*, 5201–5210.

[196] M. J. Katz, Z. J. Brown, Y. J. Colón, P. W. Siu, K. A. Scheidt, R. Q. Snurr, J. T. Hupp, O. K. Farha, *Chem. Commun.* **2013**, *49*, 9449–9451.

[197] G. C. Shearer, S. Chavan, S. Bordiga, S. Svelle, U. Olsbye, K. P. Lillerud, *Chem. Mater.* **2016**, *28*, 3749–3761.

[198] N. Planas, J. E. Mondloch, S. Tussupbayev, J. Borycz, L. Gagliardi, J. T. Hupp, O. K. Farha, C. J. Cramer, *J. Phys. Chem. Lett.* **2014**, *5*, 3716–3723.

[199] M. J. Wulfers, R. F. Lobo, *Appl. Catal. A Gen.* **2015**, *505*, 394–401.

[200] A. Sarkar, D. Seth, F. T. T. Ng, G. L. Rempel, *Ind. Eng. Chem. Res.* **2014**, *53*, 18982–18992.

[201] E. J. Arlman, *J. Catal.* **1964**, *3*, 89–98.

[202] A. E. Platero-Prats, A. B. League, V. Bernales, J. Ye, L. C. Gallington, A. Vjunov, N. M. Schweitzer, Z. Li, J. Zheng, B. L. Mehdi, et al., *J. Am. Chem. Soc.* **2017**, *139*, 10410–10418.

[203] C. A. Angell, D. M. Gruen, *J. Am. Chem. Soc.* **1966**, *88*, 5192–5198.

[204] S. D. Ittel, L. K. Johnson, M. Brookhart, *Chem. Rev.* **2000**, *100*, 1169–1203.

[205] Y. Zhu, J. Zheng, J. Ye, Y. Cui, K. Koh, L. Kovarik, D. M. Camaioni, J. L. Fulton, D. G. Truhlar, M. Neurock, et al., *Nat. Commun.* **2020**, *11*, DOI 10.1038/s41467-020-19438-w.

[206] B. Ravel, M. Newville, in *J. Synchrotron Radiat.*, J Synchrotron Radiat, **2005**, pp. 537–541.

[207] J. Zheng, J. Ye, M. A. Ortuño, J. L. Fulton, O. Y. Gutiérrez, D. M. Camaioni, R. K. Motkuri, Z. Li, T. E. Webber, B. L. Mehdi, et al., *J. Am. Chem. Soc.* **2019**, *141*, 9292–9304.

[208] M. J. Frisch, G. Trucks, H. B. schlegel, G. E. Scuseria, M. A. Robb, al et, **2009**.

[209] Y. Zhao, D. G. Truhlar, *J. Chem. Phys.* **2006**, *125*, DOI 10.1063/1.2370993.

[210] F. Weigend, *Phys. Chem. Chem. Phys.* **2006**, *8*, 1057–1065.

[211] F. Weigend, R. Ahlrichs, *Phys. Chem. Chem. Phys.* **2005**, *7*, 3297–3305.

[212] J. Ye, L. Gagliardi, C. J. Cramer, D. G. Truhlar, *J. Catal.* **2017**, *354*, 278–286.

[213] J. R. Li, J. Sculley, H. C. Zhou, *Chem. Rev.* **2012**, *112*, 869–932.

[214] I. Stassen, B. Bueken, H. Reinsch, J. F. M. Oudenhoven, D. Wouters, J. Hajek, V. Van Speybroeck, N. Stock, P. M. Vereecken, R. Van Schaijk, et al., *Chem. Sci.* **2016**, *7*, 5827–5832.

[215] L. E. Kreno, K. Leong, O. K. Farha, M. Allendorf, R. P. Van Duyne, J. T. Hupp, *Chem. Rev.* **2012**, *112*, 1105–1125.

[216] D. Farrusseng, S. Aguado, C. Pinel, *Angew. Chemie - Int. Ed.* **2009**, *48*, 7502–7513.

[217] C. Silva, I. Luz, X. Llabres, A. Corma, H. Garcia, *Chemistry* **2010**, *16*, 11133–11138.

[218] P. Horcajada, R. Gref, T. Baati, P. K. Allan, G. Maurin, P. Couvreur, G. Férey, R. E. Morris, C. Serre, *Chem. Rev.* **2012**, *112*, 1232–1268.

[219] R. C. Huxford, J. Della Rocca, W. Lin, *Curr. Opin. Chem. Biol.* **2010**, *14*, 262–268.

[220] V. L. Rechac, F. G. Cirujano, A. Corma, F. X. i Xamena, *Eur. J. Inorg. Chem.* **2016**, *2016*, 4512–4516.

[221] P. Ji, K. Manna, Z. Lin, A. Urban, F. X. Greene, G. Lan, W. Lin, *J. Am. Chem. Soc.* **2016**, *138*, 12234–12242.

[222] A. Phan, A. U. Czaja, F. Gándara, C. B. Knobler, O. M. Yaghi, *Inorg. Chem.* **2011**, *50*, 7388–7390.

[223] M. I. Gonzalez, J. Oktawiec, J. R. Long, *Faraday Discuss.* **2017**, *201*, 351–367.

[224] M. Kømurcu, A. Lazzarini, G. Kaur, E. Borfecchia, S. Øien-Ødegaard, D. Gianolio, S. Bordiga, K. P. Lillerud, U. Olsbye, *Catal. Today* **2020**, 1–10.

[225] G. C. Shearer, S. Forselv, S. Chavan, S. Bordiga, K. Mathisen, M. Bjørgen, S. Svelle, K. P. Lillerud, *Top. Catal.* **2013**, *56*, 770–782.

[226] M. Nakamura, M. Tanaka, M. Ito, O. Sakata, *J. Chem. Phys.* **2005**, *122*, 224703.

[227] M. Nakamura, M. Ito, *Chem. Phys. Lett.* **2004**, *384*, 256–261.

[228] T. Ikuno, S. Grundner, A. Jentys, G. Li, E. Pidko, J. Fulton, M. Sanchez-Sanchez, J. A. Lercher, *J. Phys. Chem. C* **2019**, *123*, 8759–8769.

[229] M. J. Frisch, G. W. Trucks, H. B. Schlegel, G. E. Scuseria, M. A. Robb, J. R. Cheeseman, G. Scalmani, V. Barone, G. A. Petersson, H. Nakatsuji, et al., **2016**.

[230] D. Andrae, U. Häußermann, M. Dolg, H. Stoll, H. Preuß, *Theor. Chim. Acta* **1990**, *77*, 123–141.

[231] I. M. Alecu, J. Zheng, Y. Zhao, D. G. Truhlar, *J. Chem. Theory Comput.* **2010**, *6*, 2872–2887.

[232] D. Yang, V. Bernales, T. Islamoglu, O. K. Farha, J. T. Hupp, C. J. Cramer, L. Gagliardi, B. C. Gates, *J. Am. Chem. Soc.* **2016**, *138*, 15189–15196.

[233] K. Hadjiivanov, H. Knözinger, M. Mihaylov, *J. Phys. Chem. B* **2002**, *106*, 2618–2624.

[234] M. Kermarec, D. Olivier, M. Richard, M. Che, F. Bozon-Verduraz, *J. Phys. Chem.* **1982**, *86*, 2818–2827.

[235] A. Zecchina, C. Lamberti, G. Spoto, L. Carnelli, C. O. Arehn, **1994**, 9577–9582.

[236] S. M. T. Almutairi, B. Mezari, E. A. Pidko, P. C. M. M. Magusin, E. J. M. Hensen, *J. Catal.* **2013**, *307*, 194–203.

[237] K. Hadjiivanov, M. Mihaylov, D. Klissurski, P. Stefanov, N. Abadjieva, E. Vassileva, L. Mintchev, *J. Catal.* **1999**, *185*, 314–323.

[238] B. I. Mosqueda-Jiménez, A. Jentys, K. Seshan, J. A. Lercher, *J. Catal.* **2003**, *218*, 348–353.

[239] M. Sano, T. Maruo, H. Yamatera, M. Suzuki, Y. Saito, *J. Am. Chem. Soc.* **1987**, *109*, 52–55.

[240] H. Guesmi, P. Massiani, *Catal. Today* **2011**, *177*, 25–30.

[241] Y. Ganjkhanlou, E. Groppo, S. Bordiga, M. A. Volkova, G. Berlier, *Microporous Mesoporous Mater.* **2016**, *229*, 76–82.

[242] S. Contarini, J. Michalik, M. Narayana, L. Kevan, *J. Phys. Chem.* **1986**, *90*, 4586–4590.

[243] B. Pawelec, J. L. G. Fierro, J. F. Cambra, P. L. Arias, J. A. Legarreta, G. Vorbeck, J. W. De Haan, V. H. J. De Beer, R. A. Van Santen, *Zeolites* **1997**, *18*, 250–259.

[244] R. Cid, J. L. G. Fierro, A. López Agudo, *Zeolites* **1990**, *10*, 95–100.

[245] H. Förster, U. Hatje, *Solid State Ionics* **1997**, *101–103*, 425–430.

[246] M. Crespin, P. Levitz, L. Gatineau, *J. Chem. Soc. Faraday Trans. 2 Mol. Chem. Phys.* **1983**, *79*, 1181–1194.

[247] L. R. Furenlid, M. W. Renner, E. Fujita, *Phys. B Phys. Condens. Matter* **1995**, *208–209*, 739–742.

[248] U. Deka, A. Juhin, E. A. Eilertsen, H. Emerich, M. A. Green, S. T. Korhonen, B. M. Weckhuysen, A. M. Beale, *J. Phys. Chem. C* **2012**, *116*, 4809–4818.

[249] S. M. Maier, A. Jentys, J. A. Lercher, *J. Phys. Chem. C* **2011**, *115*, 8005–8013.

[250] R. Khare, A. Jentys, J. A. Lercher, *Phys. Chem. Chem. Phys.* **2020**, *22*, 18891–18901.

[251] N. Fairley, "Copyright © 2005 Casa Software Ltd," can be found under http://www.casaxps.com/, **n.d.**

[252] B. C. Lippens, B. G. Linsen, J. H. d. Boer, *J. Catal.* **1964**, *3*, 32–37.

[253] U. Bergmann, P. Glatzel, *Photosynth. Res.* **2009**, *102*, 255–266.

8 Appendix

8.1 List of publications

L. Löbbert, S. Chheda, J. Zheng, N. Khetrapal, J. Schmid, R. Zhao, C.A. Gaggioli, D.M. Camaioni, R. Bermejo-Deval, O. Gutiérrez, Y. Liu[a], M. Neurock, J.I. Siepmann, L. Gagliardi, J.A. Lercher, *Influence of adsorption on butene dimerization activity of single metal cations on UiO-66 nodes* in preparation.

J. Zheng,‡ L. Löbbert,‡ S. Chheda, N. Khetrapal, C.A. Gaggioli, J. Schmid, B. Yeh, O.Y. Gutiérrez, R. Bermejo-Deval, R.K. Motkuri, J.L. Fulton, M. Balasubramanian, J.I. Siepmann, M. Neurock, L. Gagliardi, J.A. Lercher, *Metal–organic framework supported single-site Ni catalysts for butene dimerization*, **J.Catal.**, 2021, submitted.

B. Yeh, S. Vicchio, S. Chheda, J. Zheng, J. Schmid, L. Löbbert, R. Bermejo-Deval, O. Gutiérrez, J. A. Lercher, C. Lu, M. Neurock, R. Getman, L. Gagliardi, A. Bhan, *Site Densities, Rates, and Mechanism of Stable Ni/UiO-66 Ethylene Oligomerization Catalysts*, **J. Am. Chem. Soc.**, 2021, accepted.

A. Ehrmaier, L. Löbbert, M. Sanchez-Sanchez, R. Bermejo-Deval, J. A. Lercher *Impact of alkali and alkali-earth cations on Ni-catalyzed dimerization of butene,* **ChemCatChem**, 2020, 12 (14), 3705-3711.

8.2 Conference contributions

FEZA 2021 – The 8th Federation of European Zeolite Associations Conference, United Kingdom (online)

Presentation: *Study of Ni-exchanged FAU, MFI and CHA catalysts shows impact of zeolite properties on the activity of Ni single sites for selective butene dimerization*

54. Jahrestreffen Deutscher Katalytiker 2021, Weimar (online)

Poster: *Effect of Ni loading and Brønsted acidity on the performance of Ni-FAU catalysts in butene dimerization*

ICC 2020 – the 17th International Congress on Catalysis, San Diego, USA

Presentation: *Effect of different zeolitic environments on the performance of Ni-clusters in butene dimerization* (cancelled due to the Covid19 pandemic)

53. Jahrestreffen Deutscher Katalytiker 2019, Weimar

Presentation: *Influence of the zeolitic environment on the efficiency of Ni-sites in butene dimerization* (cancelled due to the Covid19 pandemic)

52. Jahrestreffen Deutscher Katalytiker 2019, Weimar

Poster & Short presentation: *Designing zeolite constraints for butene dimerization into linear octenes - Influence of different constraint sizes*

DGMK Conference 2018 – Challenges for Petrochemicals and Fuels, Berlin

Poster: *Selective linear dimerization of 1-butene over zeolitic catalysts*